

# Performance Analytics for Electron Beam Powder Bed Fusion of Ti-6Al-4V

by

Gitanjali Shanbhag

A thesis  
presented to the University of Waterloo  
in fulfillment of the  
thesis requirement for the degree of  
Doctor of Philosophy  
in  
Mechanical and Mechatronics Engineering

Waterloo, Ontario, Canada, 2021

© Gitanjali Shanbhag 2021

## Examining Committee Membership

The following people served on the Examining Committee for this thesis. The decision of the Examining Committee is by majority vote.

External Examiner            Dr. Farzaneh Farhang-Mehr, Director of the Additive Manufacturing Lab  
Dept. of Materials Engineering  
University of British Columbia, Canada

Supervisor                    Dr. Mihaela Vlasea, Assistant Professor  
Dept. of Mechanical and Mechatronics Engineering  
University of Waterloo, Canada

Internal Member            Dr. Ehsan Toyserkani, Professor  
Dept. of Mechanical and Mechatronics Engineering  
University of Waterloo, Canada

Internal Member            Dr. Stewart McLachlin, Assistant Professor  
Dept. of Mechanical and Mechatronics Engineering  
University of Waterloo, Canada

Internal-External Member    Dr. Karim S Karim, Professor  
Dept. of Electrical and Computer Engineering  
University of Waterloo, Canada

## **Author's Declaration**

This thesis consists of materials all of which I authored or co-authored: see Statement of Contributions included in the thesis. This is a true copy of the thesis, including any required final revisions, as accepted by my examiners.

I understand that my thesis may be made electronically available to the public.

## Statement of Contributions

Chapters 1,2,3,6,7 and 8 of this thesis were authored by myself under the supervision and mentorship of my direct supervisor, Dr. Mihaela Vlasea.

Chapter 4 and Chapter 5 of this thesis consists of content that was authored by myself, my supervisor, Evan Wheat and Dr. Shawn Moylan. The following provides a detailed description of my direct contribution, as well as the co-authors' diverse contributions for these two chapters.

**Gitanjali Shanbhag:** Conceptualization, methodology, validation, investigation, formal analysis – tensile data, formal analysis – computed tomography data, visualization, project administration, writing- original draft preparation, reviewing and editing.

**Evan Wheat:** Conceptualization, methodology, formal analysis – computed tomography data, validation, software, visualization, writing – reviewing and editing.

**Dr. Shawn Moylan:** Supervision, resources, writing – reviewing and editing.

**Dr. Mihaela Vlasea:** Conceptualization, funding acquisition, supervision, resources, writing – reviewing and editing.

## Abstract

Titanium alloys are widely used in biomedical, aerospace, marine, energy and chemical industries because of their unique properties. Ti-6Al-4V, an  $\alpha+\beta$  alloy, offers desirable properties such as high strength-to-weight ratio, low coefficient of thermal expansion, metallurgical stability, excellent corrosion resistance, high tissue and bone integration and excellent biocompatibility. The advent of electron beam powder bed fusion (EB-PBF) additive manufacturing (AM) has made it possible to fabricate titanium alloy components directly from three-dimensional computer aided design (CAD) models. AM is an innovative manufacturing process that offers near-net shape fabrication of highly complex components, resulting in a much-needed reduction in lead-time, waste, and cost. The increasing demand for manufacturing functional and custom-designed components via EB-PBF is the driving force for achieving a deep understanding of the process-structure-properties relationship. This thesis specifically aims to advance the scientific body of knowledge in understanding the interconnected relationships between the powder properties, bulk powder behavior, in-situ performance, and part properties by (i) understanding the effect of reuse on powder properties and the EB-PBF process, (ii) understanding the tensile behavior and pore space characteristics of EB-PBF components, and (iii) understanding the in-situ powder cake properties and its effects on the surface topography, geometric dimensional deviations and de-powdering, in the EB-PBF process.

Upon robust investigation of the effect of reuse on powder properties and the EB-PBF process, it was found that there is an increase in measured response in powder size distribution, tapped density, Hausner ratio, Carr index, basic flow energy and specific energy, dynamic angle of repose, oxygen and nitrogen content, while the bulk density remained largely unchanged. The morphology of the powder showed extensive physical changes with powder reuse as a result of the powder recovery process, tumbling process, as well as the high temperature conditions leading to overheating and smelting of particles and satellites. Powder characteristics such as the flow properties (basic flow energy and specific energy) and packing properties (tap density, Hausner ratio and Carr index) deteriorated with increasing the degree of powder reuse as a result of the mechanical interlocking and friction between particles. Lastly, the chemical composition (oxygen and nitrogen concentration) remained below the limits outlined by ASTM F2924-14, however, a gradual increase with increasing degree of powder reuse, was observed. From the trends, it was concluded that the powder may be deemed unusable after 5-6 reuse cycles, according to the ASTM F2924-14 standard. Based on the observations, a unified powder quality score called the EB-PBF Suitability Factor was established to help compare the degree of deterioration of the reused powder.

Upon in-depth analysis of the tensile behavior and pore characteristics of the EB-PBF components, it was found that changes in specimen geometry, specimen size, build orientation, and the internal porous defects have significant effects on the tensile properties. The horizontally-built specimens had higher yield and tensile strength, but lower elongation compared to vertically built specimens. Furthermore, the horizontally-built specimens had the highest variability in layer-wise pore fraction, with occurrence of large unevenly-distributed defects. As such, a single tensile specimen size and geometry may not accurately represent the mechanical properties of all features of a component, which has a significant impact on part qualification criteria. It was observed that all vertically-built specimens only displayed pores  $< 200 \mu\text{m}$ , whereas all horizontally-built specimens had additionally much larger pores (up to  $1200 \mu\text{m}$ ). The pore space  $< 100 \mu\text{m}$  was very similar across specimens manufactured in both orientations. Additionally, an increase in cross-sectional area led to an increase in the yield, tensile strength, and elastic modulus. The subsurface pore population was observed to be significantly less for the horizontal specimens having the largest and smallest cross-sectional area whereas it was quite similar for all vertical specimens. An increase in surface area to volume ratio, led to a decrease in the yield and tensile strength; indicating that cylindrical specimens with a smaller diameter and flat specimens with a larger width and/or smaller thickness will have decreased performance. The average solid fraction of the specimens had no influence on any measured tensile properties. Furthermore, with an increase in maximum pore size, the elongation of the specimen decreased. The % elongation was linked to the pore equivalent diameter such that specimens that showed an absence of pores  $> 500 \mu\text{m}$  had higher elongation values.

Upon detailed experimental characterization of the powder cake properties and its effects on surface topography, geometric dimensional deviations, and de-powdering, it was found that an increase in preheating temperature led to a linear increase in packing density, contact size ratio, coordination number, effective thermal conductivity of the powder cake, and surface roughness of manufactured parts. Logarithmic regression equations were established from the empirically-derived thermal conductivity data and the measured surface roughness data. These equations can be used to predict the powder cake properties and the surface roughness of parts when using preheating temperatures between  $650 \text{ }^\circ\text{C}$  and  $730 \text{ }^\circ\text{C}$ . The current study shows that a decrease of  $80 \text{ }^\circ\text{C}$  in the preheating temperature led to a 13% and 18% decrease in the  $R_a$  and  $S_a$  values, respectively with a mere change of 3% in the layer-wise density and 12% in the effective thermal conductivity. Therefore, a decrease in the preheating temperature can improve surface roughness without dramatic changes in the packing density of the powder cake. Furthermore, it was found that a decrease in the preheating temperature led to a decrease in partially-fused powder particles onto the solidified structure, leading to better de-powdering and increased geometric fidelity of manufactured parts.

## Acknowledgements

There are numerous people I would like to thank for their support during my PhD journey and journey at the University of Waterloo.

First and foremost, I would like to thank my supervisor, Dr. Mihaela Vlasea for her guidance, support, and above all her encouragement. She has taught me what compassionate mentorship looks like. Her kindness and generosity have helped me through the difficult phases of my degree.

I would like to thank Dr. Ehsan Toyserkani for not only being my thesis committee member, but also for being my course instructor for the Manufacturing Processes course that focused on Additive Manufacturing. His graduate course is what inspired me to pursue a PhD in the field of AM.

I would like to acknowledge my thesis examining committee members Dr. Karim S. Karim and Dr. Stewart McLachlin from the University of Waterloo and Dr. Farzaneh Farhang-Mehr from the University of British Columbia, for taking the time to review my thesis.

I would like to extend a special acknowledgement for the funding received from the NSERC Network for Holistic Innovation in Additive Manufacturing (NSERC HI-AM) for supporting my research, for providing me with the opportunity to present at various conferences, and for sponsoring my internship at National Institute of Standard & Technology (NIST). I would like to thank Dr. Alkan Donmez for giving me the opportunity to work in the Engineering Lab at NIST. A huge thanks to Dr. Shawn Moylan for his supervision and mentorship during the projects I undertook at NIST. In the brief span of three months, I had the invaluable opportunity to learn so much from him and the team, with special mention to Brandon Lane, Jason Fox, and Bill Luecke.

I feel so fortunate to have met many kind people at the University of Waterloo, who I now call my friends, family, and mentors. Firstly, many thanks to Sera Ertay and Sagar Patel for their friendship and support. I am so glad to have found you and have created such a deep bond with the two of you. Secondly, I would like to thank Jerry Ratthapakdee and Karl Rautenberg for all their help with my experimental work, but most of all, their kind and cheerful nature. I am very grateful for the casual conversation, humor, and constant encouragement. Thirdly, I would like to thank Dr. Paola Russo and Dr. Lokesh Narsineni for their friendship, support, and love. Paola, thank you for transitioning from my friend to my sister. Lokesh, thank you for always being there no matter the distance. Lastly, I would like to thank Dr. Christine Zaza for her mentorship, friendship, and trust in me. I am so glad I took your course, and I am grateful that you trusted me (and still do) with AHS 105. Teaching this course has been such a pleasure and one of the most gratifying part of my life at the University of Waterloo.

I would be remiss if I did not thank my Centre for Teaching Excellence (CTE) family (specifically Dr. Svitlana Taraban-Gordon and Monika Soczewinski) and Student Success Office (SSO) family (specifically Nasim Shojayi and Dr. Andrea Prier). I am very grateful that I got the chance to work with all of you over the past four years. Working at CTE and SSO was one of the biggest joys of my life at the University of Waterloo.

Last but not the least, I would like to thank my family - my parents, my grandmother, my brother, and Evan. To my Mum, thank you for being my best friend, my cheerleader, and my rock. Everything that I am today is because of you. Thank you for always pushing me to be the best version of myself. Despite the 10- hour time difference, you were always just one phone call away. To Abhimanyu, thank you for your silly jokes, the bizarre WhatsApp messages, and your love. Thinking about you always makes me smile. To Dadi, thank you for the daily phone calls, for the daily health and news updates and for everything you have done for me since I was born. I am very grateful for your blessings and the infinite love that you shower upon me. To my beloved Evan, thank you for your patience, care, kindness, motivation, affection, and friendship. Your confidence in me is the reason I am able to finish this PhD today. I feel so fortunate that you entered my life and became part of my family.



## Dedication

*This thesis is dedicated to my late grandfather, Shri. Amritlal Adhikari, who always believed that education is the first stepping stone to becoming a successful person. Thank you for your endless love, encouragement, and support. Thank you for everything you have done for me from taking me to my first school ever to teaching me English, Hindi, and Sanskrit. Thank you for choosing me as your granddaughter.*

*Dada, I wish you were here to see me finish my PhD, but I know that you are watching over me, and I hope this makes you proud.*

## Table of Contents

<b>List of Figures</b> .....	<b>xiv</b>
<b>List of Tables</b> .....	<b>xxi</b>
<b>List of Abbreviations</b> .....	<b>xxii</b>
<b>Chapter 1 Introduction</b> .....	<b>1</b>
1.1 Background.....	1
1.2 Motivations .....	2
1.3 Thesis Objectives .....	4
1.4 Organization of Chapters .....	6
<b>Chapter 2 Literature Review</b> .....	<b>8</b>
2.1 Fundamentals of Electron Beam Powder Bed Fusion (EB-PBF) .....	8
2.1.1 History & Development.....	8
2.1.2 EB-PBF Description of Principles & Operation .....	9
2.1.3 EB-PBF Operating Procedure .....	14
2.1.4 EB-PBF areas of applications, advantages, and limitations.....	16
2.2 Relationship between process-structure-properties in EB-PBF of Ti-6Al-4V.....	16
2.2.1 The effect of the EB-PBF process on phase transformations and microstructure.....	17
2.2.2 The effect of powder properties on EB-PBF process outcomes .....	20
2.2.3 The surface roughness characteristics of EB-PBF components.....	20
2.2.4 The pore space characteristics of EB-PBF components .....	21
2.2.5 The tensile behavior of EB-PBF components.....	22
2.2.6 Complex designs and their implementation to biomedical applications.....	23
<b>Chapter 3 Understanding the effect of reuse on powder properties and the EB-PBF process</b> .....	<b>25</b>
3.1 <i>Part I: Preliminary study</i> .....	26
3.1.1 Preface.....	26
3.1.2 Introduction.....	26
3.1.3 Materials and Methods.....	27
3.1.4 Results and Discussion.....	28
3.1.5 Conclusions.....	32
3.2 <i>Part II: Comprehensive study</i> .....	32
3.2.1 Preface.....	32

3.2.2 Introduction.....	33
3.2.3 Materials and Methods.....	38
3.2.4 Results and Discussion.....	40
3.2.5 Conclusions.....	54
<b>Chapter 4 Effect of specimen geometry and orientation on tensile properties of Ti-6Al-4V manufactured by electron beam powder bed fusion.....</b>	<b>56</b>
4.1 Preface.....	57
4.2 Introduction.....	58
4.3 Review of EB-PBF Tensile Studies and Challenges in Data Usability .....	59
4.4 Materials and Methods.....	64
4.4.1 Ti-6Al-4V Powder .....	64
4.4.2 Specimen Preparation and Build Layout.....	65
4.4.3 Additive manufacturing process .....	66
4.4.4 X-ray Computed Tomography analysis .....	67
4.4.5 Surface roughness analysis .....	68
4.4.6 Tensile testing of specimens .....	69
4.5 Results and Discussion .....	69
4.5.1 X-ray Computed Tomography .....	69
4.5.2 Surface Roughness.....	74
4.5.3 Tensile Properties.....	76
4.5.4 Conclusions.....	85
4.6 Addendum (Data in Brief) .....	86
4.6.1 Preface.....	86
4.6.2 Specifications Table.....	87
4.6.3 Value of the Data .....	88
4.6.4 Data Description .....	88
4.6.5 Experimental Design, Materials and Methods .....	91
<b>Chapter 5 Effect of specimen geometry and orientation on pore space characteristics of Ti-6Al-4V manufactured by electron beam powder bed fusion.....</b>	<b>92</b>
5.1 Preface.....	92
5.2 Introduction.....	93
5.3 Materials and Methods.....	95

5.3.1 Additive manufacturing and X-ray computed tomography analysis .....	95
5.3.2 Pore Space Analysis.....	96
5.3.3 Pore cut-off value determination.....	97
5.4 Results and Discussion .....	97
5.4.1 Effect of specimen orientation on pore space characteristics .....	97
5.4.2 Effect of specimen cross-sectional area on pore space characteristics .....	105
5.4.3 Effect of specimen surface area to volume ratio on pore space characteristics .....	111
5.4.4 Effect of pore equivalent diameter on tensile properties.....	114
5.5 Conclusions.....	119
<b>Chapter 6 Effect of varying preheating temperatures in electron beam powder bed fusion: Part I</b>	
<b>Assessment of the effective powder cake thermal conductivity .....</b>	<b>121</b>
6.1 Preface.....	122
6.2 Introduction.....	122
6.3 Preheating studies in EB-PBF of Ti-6Al-4V .....	124
6.4 Thermal conductivity studies of Ti-6Al-4V powder bed.....	126
6.5 Assessing the in-situ powder cake properties using powder-capture artefacts .....	129
6.6 Materials and methods .....	130
6.6.1 CAD file preparation, specimen design, and build layout .....	130
6.6.2 Additive manufacturing of samples .....	132
6.6.3 X-ray computed tomography (XCT).....	133
6.6.4 Analysis of XCT data to extract particle coordination number, packing density, contact size ratio and sinter neck size .....	134
6.6.5 Inferred effective thermal conductivity.....	135
6.7 Results and Discussion .....	136
6.7.1 Packing density of powder layer, $p$ .....	136
6.7.2 Average Equivalent diameter of powder particles in the powder cake.....	140
6.7.3 Contact size ratio, $x$ .....	141
6.7.4 Effective thermal conductivity, $\lambda_{eff}$ .....	144
6.7.5 Correlation between the preheating temperatures and density, contact size ratio and effective thermal conductivity of the powder capsules, respectively.....	146
6.8 Conclusions.....	148

<b>Chapter 7 Effect of varying preheating temperatures in electron beam powder bed fusion: Part II</b>	
<b>Assessment of the surface topography and geometric fidelity .....</b>	<b>149</b>
7.1 Preface.....	149
7.2 Surface topography of EB-PBF parts.....	150
7.3 Lattice architectures produced by EB-PBF and challenges in geometric fidelity.....	152
7.4 Materials and methods .....	154
7.4.1 Additive manufacturing of the part-quality artefacts .....	154
7.4.2 Surface topography evaluation for the part-quality artefacts .....	154
7.4.3 Additive manufacturing of TPMS structures .....	156
7.4.4 Geometric fidelity evaluation of the TPMS structures.....	158
7.5 Results and Discussion .....	158
7.5.1 Analysis of the part-quality artefacts .....	158
7.5.2 Analysis of the TPMS structures .....	164
7.6 Conclusions.....	168
<b>Chapter 8 Conclusions and Future Work.....</b>	<b>170</b>
8.1 Thesis Conclusions and recommendations for future work.....	170
8.2 Research Contributions .....	174
8.2.1 Articles in peer-reviewed journals .....	174
8.2.2 Conference proceedings, presentations, posters, magazines, and AM awards .....	175
<b>References.....</b>	<b>177</b>
<b>Appendices.....</b>	<b>210</b>
<b>Appendix A. Chapter 4 Pore space analytics code .....</b>	<b>210</b>
<b>Appendix B. Chapter 5 Formatting code .....</b>	<b>224</b>
<b>Appendix C. Chapter 5 Plotting code .....</b>	<b>230</b>
<b>Appendix D. MATLAB code for thresholding and converting a grayscale image stack to a B&amp;W image stack</b>	<b>253</b>
<b>Appendix E. Python code for obtaining preheated powder bed analytics .....</b>	<b>256</b>
<b>Appendix F. Chapter 6 Supplementary Data .....</b>	<b>262</b>
<b>Appendix G. MATLAB code for Ra and Sa plot creation .....</b>	<b>266</b>
<b>Appendix H. Engineering stress-strain curves for Chapter 4 tensile specimens.....</b>	<b>270</b>

## List of Figures

Figure 1.1 Powder properties, bulk powder behavior, in-situ performance, and part properties relationship studied in this thesis. ....	5
Figure 2.1 Schematic of an Arcam A2X EB-PBF machine.....	10
Figure 2.2 Depiction of (a) PH1 and PH2 regions (b) Extent to which powder particles are sintered in the PH1 stage .....	11
Figure 2.3 Scan strategy for Melt Theme .....	13
Figure 2.4 Figure depicts a completed build showing the sintered powder cake. This cake will be taken to the PRS to extract final parts. ....	15
Figure 2.5 A schematic illustrating the sequence of diffusion-controlled phase transformation in Ti-Al-4V. Figure created by author but adapted from Kelly [95].....	18
Figure 2.6 Cooling path and critical cooling rates for Ti-6Al-4V in EB-PBF. Reprinted with permission from Galarraga et al. [91].....	19
Figure 3.1 Schematic illustrating the powder reuse cycle.....	27
Figure 3.2 SEM micrographs of powder defects (a) $G_0$ at 481X depicting satellites in as-received powder; (b) $G_1$ at 150X depicting clip-clap defect in reused powder; (c) $G_1$ at 100X depicting broken particle in reused powder; (d) $G_1$ at 150X depicting shattered particle in reused powder; (e) $G_1$ at 750X depicting agglomerates in reused powder; (f) $G_2$ at 1000X depicting particles with molten specks in reused powder; (g) $GB_{12}$ at 750X depicting elongated particle in reused powder; (h) $GB_{12}$ at 1000X depicting deformed particle in reused powder. Nomenclature as per [188] . ....	28
Figure 3.3 Comparisons between powder generations based on (a) PSD, (b) Density vs. no. of taps, (c) BFE vs. no. of trials, (d) Sphericity vs. $x_{c\ min}$ particle size .....	30
Figure 3.4 Graphical abstract depicting the manufacturing process, results, and observations.....	33
Figure 3.5 Example of compaction curve obtained by GranuPack - illustrating bulk density ( $\rho_0$ ), tap density ( $\rho_{500}$ ), Hausner ratio ( $Hr$ ), and Carr index ( $C$ ) .....	40
Figure 3.6 SEM micrographs for all powder types depict (a) Satellites in $G_0$ powder; (b), (f) Deformed particle in $G_1$ and $GB_{13}$ powders respectively; (c) Elongated particle in $GB_{12}$ powder; (d) Particle with molten specks in $G_2$ ; (e) Clip-Clap in $GB_{13}$ powder; (g), (h), (i), (k) Broken particles in $GB_{13}$ , $GB_{23}$ and $G_3$ powders; (j) Agglomerate in $GB_{23}$ powder, and (l) Shattered particle in $G_3$ powder. Nomenclature used to describe these micrographs was first defined by Popov et al. [188]. A Zeiss Ultra SEM instrument was used to capture the image shown in (a); all other images were captured using the Tescan VEGA3 instrument.	41

Figure 3.7  $D_{10}$ ,  $D_{50}$  and  $D_{90}$  values for all powder types. Error bars represent the standard deviation. .... 43

Figure 3.8 (a)  $\rho_0$  and  $\rho_{500}$  values (b) Hr and C values; for all powder types. Error bars represent the standard deviation..... 45

Figure 3.9 (a) BFE vs. SE (b) BFE and SE values, for all powder types. Error bars represent the standard deviation..... 47

Figure 3.10 (a) AOR vs. speed of drum rotation for all powder types; (b) CI vs. speed of drum rotation for all powder types; (c) AOR at 2 and 60 rpm vs. number of reuse cycles; (d) CI at 2 and 60 rpm vs. number of reuse cycles; (e) AOR at 2 rpm vs. particle size (D values) for individual genesis powder types; (f) AOR at 60 rpm vs. particle size (D values) for individual genesis powder types; (g) relationship between drum rotating speed and surface flow speed (Redrawn from [217]). Note than  $G_0$  powder is considered an anomaly due to the fact that it has not undergone any processing, blasting, or sieving procedure. .... 49

Figure 3.11 (a) Oxygen and (b) Nitrogen concentration for  $G_0$ ,  $G_1$ ,  $G_2$ , and  $G_3$  powder types along with linear (in red) and logarithmic (in black) trendlines. Error bars represent the standard deviation..... 51

Figure 3.12 Radar diagram comparing the performance of  $G_0$ ,  $G_1$ ,  $G_2$ , and  $G_3$  powders w.r.t the D values, SE, BFE, Nitrogen (in wt.%), Oxygen (in wt.%), Hr, C, CI, and AOR..... 53

Figure 4.1 Graphical abstract depicting the manufacturing process, results, and observations..... 57

Figure 4.2 Comparison of YS, UTS, and % EL values for (a) rectangular and (b) cylindrical specimens from published literature [4], [5], [125], [146], [149]–[152], [197], [229]–[231], [35], [232]–[241], [43], [242]–[251], [69], [252], [71], [85], [104], [106], [123]. Error bars represent the reported min-max range. The green line, red line, blue line correspond to the minimum UTS, YS, and % EL values respectively, for a bar of wrought Ti-6Al-4V in annealed condition according to AMS 4928W [253]..... 61

Figure 4.3 Comparison of YS, UTS, and % EL values for vertically-built and horizontally-built specimens from published literature [4], [35], [239], [241], [245]–[247], [43], [85], [123], [146], [150], [235], [237], [238] Error bars represent the reported min-max range. The green line, red line, blue line correspond to the minimum UTS, YS, and % EL values respectively, for a bar of wrought Ti-6Al-4V in annealed condition according to AMS 4928W [253]..... 62

Figure 4.4 Depiction of all specimen types and placement of their replicates inside the bounding box (a) E8-3 (b) E8M -2 (c) E8M-3 (d) E8M-4 (e) E8M-5 (f) Flat (Large) (g) Flat (Small). For E8M-4 and E8M-5, three extra specimens were built in the Z (vertical) direction to maintain uniform part distribution such that the beam scans the entire build platform until the very last layer..... 66

Figure 4.5 (a) Minimum layer-wise solid fraction (b) Average layer-wise solid fraction for all specimens ..... 70

Figure 4.6 Layer-wise density for E8-3 vertical and horizontal specimens along with the XCT image of the least dense layer for the full gauge specimen. The gray line represents the Full Gauge sample, and the green and red lines represent the Single FOV samples..... 71

Figure 4.7 Layer-wise density for E8M-2 vertical and horizontal specimens along with the XCT image of the least dense layer for the full gauge specimen. The gray line represents the Full Gauge sample, and the green and red lines represent the Single FOV samples..... 71

Figure 4.8 Layer-wise density for E8M-3 vertical and horizontal specimens along with the XCT image of the least dense layer for the full gauge specimen. The gray line represents the Full Gauge sample, and the green and red lines represent the Single FOV samples..... 72

Figure 4.9 Layer-wise density for E8M-4 vertical and horizontal specimens along with the XCT image of the least dense layer for the full gauge specimen. The gray line represents the Full Gauge sample, and the green and red lines represent the Single FOV samples..... 72

Figure 4.10 Layer-wise density for E8M-5 vertical and horizontal specimens along with the XCT image of the least dense layer for the full gauge specimen. The gray line represents the Full Gauge sample, and the green and red lines represent the Single FOV samples..... 73

Figure 4.11 Layer-wise density for Flat (Large) vertical and horizontal specimens along with the XCT image of the least dense layer for the full gauge specimen. The gray line represents the Full Gauge sample, and the green and red lines represent the Single FOV samples. .... 73

Figure 4.12 Layer-wise density for Flat (Small) vertical and horizontal specimens along with the XCT image of the least dense layer for the full gauge specimen. The gray line represents the Full Gauge sample, and the green and red lines represent the Single FOV samples. .... 74

Figure 4.13 Surface roughness (Ra and Sa) values for all specimen types for (a) vertical and (b) horizontal specimens. Error bars represent the min-max range. .... 75

Figure 4.14 (a) Ultimate tensile strength (UTS) and Yield strength (YS) (b) Elastic Modulus (E) (c) Elongation at fracture (% EL) values for the Vertical (V) and Horizontal (H) specimen types. Error bars represent the min-max range..... 77

Figure 4.15 (a) Ultimate Tensile Strength (UTS) (b) Yield Strength (YS) (c) Elongation at fracture (% EL) (d) Elastic Modulus (E) vs. cross-sectional area for all specimens..... 78

Figure 4.16 (a) Minimum layer solid fraction (b) Maximum pore size vs. cross-sectional area for all specimens..... 79

Figure 4.17 Surface area/volume ratio vs. (a) Ultimate Tensile Strength (UTS) (b) Yield Strength (YS) (c) Elongation at fracture (% EL) (d) Elastic Modulus (E) vs. cross-sectional area for all specimens. .... 81



Figure 4.18 Surface area/volume ratio vs. (a) Minimum layer solid fraction (b) Maximum pore size for all specimens.....	82
Figure 4.19 Minimum layer solid fraction vs. (a) UTS and YS (b) Elastic modulus (E) (c) elongation at fracture (% EL); Average solid fraction vs. (d) UTS and YS (e) Elastic modulus (E) (f) elongation at fracture (% EL) where V=vertically and H=horizontally-built specimens. ....	83
Figure 4.20 Maximum pore size vs. (a) UTS and YS (b) Elastic modulus (E) (c) Elongation at fracture (% EL) where V=vertically and H=horizontally-built specimens.....	84
Figure 5.1 Build layout (for simplicity, support structures have not been shown).....	95
Figure 5.2 Workflow schematic showing how the data passes from one code module to the other.....	96
Figure 5.3 Depiction of the principal axes of the pore.....	97
Figure 5.4 Pore equivalent diameter vs. the total pore volume for all specimens, where (a) and (b) represent the compilation on the pore space data for all vertical and horizontal specimens, respectively.....	98
Figure 5.5 Specimen type vs. pore equivalent diameter for all pores > 50 $\mu\text{m}$ , where (a) and (b) are the vertical and horizontal specimens, respectively.....	99
Figure 5.6 Specimen type vs. pore equivalent diameter for all pores between 50 $\mu\text{m}$ and 200 $\mu\text{m}$ where (a) and (b) are the vertical and horizontal specimens, respectively.....	100
Figure 5.7 Pore equivalent diameter vs. frequency for all pores between 50 $\mu\text{m}$ and 200 $\mu\text{m}$ for both vertical and horizontal specimens.....	101
Figure 5.8 Pore equivalent diameter vs. sphericity for all pores > 50 $\mu\text{m}$ , where (a) and (b) are the vertical and horizontal specimens, respectively.....	102
Figure 5.9 Pore equivalent diameter vs. aspect ratio for all pores > 50 $\mu\text{m}$ , where (a) and (b) are the vertical and horizontal specimens, respectively.....	103
Figure 5.10 Number of pores for all pore classes, for all specimen types, where (a) and (b) are the vertical and horizontal specimens, respectively.....	104
Figure 5.11 Specimen cross-sectional area vs. pore equivalent diameter for all pores > 50 $\mu\text{m}$ , where (a) and (b) are the vertical and horizontal specimens, respectively.....	105
Figure 5.12 Specimen cross-sectional area vs. pore equivalent diameter for all pores between 50 $\mu\text{m}$ and 200 $\mu\text{m}$ where (a) and (b) are the vertical and horizontal specimens, respectively. ....	106
Figure 5.13 Radial distance of the pores from the center of the specimen vs. pore equivalent diameter for E8M-2 specimens for V and H orientations. Pore radial position is with respect to the center of the part; E8M-2 components have a nominal radius of 4.5 mm. ....	107

Figure 5.14 Radial distance of the pores from the center of the specimen vs. pore equivalent diameter for E8M-3 specimens for V and H orientations. Pore radial position is with respect to the center of the part; E8M-3 components have a nominal radius of 3 mm. ....	108
Figure 5.15 Radial distance of the pores from the center of the specimen vs. pore equivalent diameter for E8M-4 specimens for V and H orientations. Pore radial position is with respect to the center of the part; E8M-4 components have a nominal radius of 2 mm. ....	109
Figure 5.16 Radial distance of the pores from the center of the specimen vs. pore equivalent diameter for E8M-5 specimens for V and H orientations. Pore radial position is with respect to the center of the part; E8M-5 components have a nominal radius of 1.25 mm. ....	109
Figure 5.17 Radial distance of the pores from the center of the specimen vs. pore equivalent diameter for E8-3 specimens for V and H orientations. Pore radial position is with respect to the center of the part; E8-3 components have a nominal radius of 3 mm.....	110
Figure 5.18 Number of pores, for all pore classes, with respect to the cross-sectional area, where (a) and (b) are the vertical and horizontal specimens, respectively. ....	111
Figure 5.19 Specimen surface area to volume ratio vs. pore equivalent diameter for all pores > 50 $\mu\text{m}$ , where (a) and (b) are the vertical and horizontal specimens, respectively. ....	112
Figure 5.20 Specimen surface area to volume ratio vs. pore equivalent diameter for all pores between 50 $\mu\text{m}$ and 200 $\mu\text{m}$ where (a) and (b) are the vertical and horizontal specimens, respectively. ....	113
Figure 5.21 Number of pores, for all pore classes, with respect to the specimen surface area to volume ratio, where (a) and (b) are the vertical and horizontal specimens, respectively. ....	114
Figure 5.22 Specimen ultimate tensile strength (UTS) vs. pore equivalent diameter for all pores > 50 $\mu\text{m}$ , where (a) and (b) are the vertical and horizontal specimens, respectively. ....	116
Figure 5.23 Specimen yield strength (YS) vs. pore equivalent diameter for all pores > 50 $\mu\text{m}$ , where (a) and (b) are the vertical and horizontal specimens, respectively. ....	117
Figure 5.24 Specimen elastic modulus (E) vs. pore equivalent diameter for all pores > 50 $\mu\text{m}$ , where (a) and (b) are the vertical and horizontal specimens, respectively.....	118
Figure 5.25 Specimen elongation (% EL) vs. pore equivalent diameter for all pores > 50 $\mu\text{m}$ , where (a) and (b) are the vertical and horizontal specimens, respectively. ....	119
Figure 6.1 Illustration of where the PH1 and PH2 theme regions are in effect, with respect to a part slice within a layer. PH1 and PH2 are applied to sinter the powder cake. The Melt Theme is applied to melt the cake and create the part layer. ....	123
Figure 6.2 (a) Wireframe diagram of the powder-capture artefact (b) Solid view of the cylindrical .....	131

Figure 6.3 (a) Top view of the build plate depicting powder-capture artefacts and part-quality artefacts (left) and Labeling strategy for all specimens based on their location on the build plate (right table) (b) Modeler view of Materialise Magics showing powder-capture artefacts and part-quality artefacts on the build plate. .... 132

Figure 6.4 Depiction of the cropped internal section from the original XCT scanned ROI ..... 134

Figure 6.5 (a) Grayscale image of a slice of powder artefact obtained by XCT reconstruction (b) Segmented image of a slice obtained by employing thresholding in MATLAB..... 135

Figure 6.6 Layer-wise density (in %) vs. Layer number for LUC, C, and RBC samples. The solid lines, dashed lines and dotted lines represent the behavior of the capsules processed at 730 °C, 690 °C, and 650 °C, respectively. .... 137

Figure 6.7 Depiction of the solid part of the powder-capture artefact that was cropped and analyzed to obtain layer-wise density ..... 139

Figure 6.8 Layer-wise density (in %) vs. Layer number C samples. The solid lines, dashed lines and dotted lines represent the behavior of the solid part, of the powder-capture artefact, processed at 730 °C, 690 °C, and 650 °C, respectively. .... 139

Figure 6.9 Layer-wise average equivalent powder particle diameter (in  $\mu\text{m}$ ) vs. Layer number for LUC, C, and RBC samples. The solid lines, dashed lines and dotted lines represent the behavior of the capsules processed at 730 °C, 690 °C, and 650 °C, respectively. .... 141

Figure 6.10 Layer-wise average sinter neck diameter to particle equivalent diameter ratio vs. Layer number for LUC, C, and RBC samples. The solid lines, dashed lines and dotted lines represent the behavior of the capsules processed at 730 °C, 690 °C, and 650 °C, respectively..... 142

Figure 6.11 Possible solid-state sintering mechanisms: non-densifying mechanisms (left) and densifying mechanisms (right). Reprinted with permission from Wheat et al. [328]..... 143

Figure 6.12 Average (a) density (b) Coordination number vs. average contact size ratio for all experiments with linear trendlines and R-squared values. Error bars represent the standard deviation. .... 144

Figure 6.13 Layer-wise average effective thermal conductivity vs. Layer number for LUC, C, and RBC samples. The solid lines, dashed lines and dotted lines represent the behavior of the capsules processed at 730 °C, 690 °C, and 650 °C, respectively..... 145

Figure 6.14 Average (a) density (b) contact size ratio (c) coordination number vs. average effective thermal conductivity for all experiments with linear trendlines and R-squared values. Error bars represent the standard deviation. .... 146

Figure 6.15 Average (a) density, (b) contact size ratio, (c) coordination number, and (d) effective thermal conductivity, vs. preheating temperature for all experiments with linear trendlines and R-squared values. Error bars represent the standard deviation.....	147
Figure 7.1 Schematic describing the (a) Ra and (b) Sa measurements for calculating surface roughness [359] .....	155
Figure 7.2 Flowchart showing the steps for the main operations for acquisition of surface roughness parameters .....	155
Figure 7.3 Schematic showing an example a 2D surface profile and 3D topographic map, used to calculate the Ra and Sa values; respectively.....	156
Figure 7.4 Depiction of the start plate containing the TPMS structures partially embedded in the powder cake .....	157
Figure 7.5 Flowchart showing the steps for qualitative assessment of geometrical deviations.....	158
Figure 7.6 Average Ra values (in $\mu\text{m}$ ) for all skins (for all fabricated part-quality artefacts) across the build plate where (a), (b), and (c) represent artefacts manufactured at 650 °C (Experiment 1), 690 °C (Experiment 2), and 730 °C (Experiment 3), respectively. The colors green, red, blue, and yellow represent Skin 1, Skin 2, Skin 3, and Skin 4, respectively.....	159
Figure 7.7 Average Sa values (in $\mu\text{m}$ ) for all skins (for all fabricated part-quality artefacts) across the build plate where (a), (b), and (c) represent artefacts manufactured at 650 °C (Experiment 1), 690 °C (Experiment 2), and 730 °C (Experiment 3), respectively. The colors green, red, blue, and yellow represent Skin 1, Skin 2, Skin 3, and Skin 4, respectively.....	161
Figure 7.8 Average (a) Ra and (b) Sa values for every skin for all experiments with linear trendlines. Error bars represent the standard deviation. ....	163
Figure 7.9 2D and 3D XCT visualizations of Diamond 4 TPMS structures manufactured during Experiment 1 ((a), (b), (c)), Experiment 2 ((d), (e), (f)), and Experiment 3 ((g), (h), (i)). ....	165
Figure 7.10 2D and 3D XCT visualizations of Diamond5 TPMS structures manufactured during Experiment 1 ((a), (b), (c)), Experiment 2 ((d), (e), (f)), and Experiment 3 ((g), (h), (i)). ....	166
Figure 7.11 2D and 3D XCT visualizations of Diamond 6 TPMS structures manufactured during Experiment 1 ((a), (b), (c)), Experiment 2 ((d), (e), (f)), and Experiment 3 ((g), (h), (i)). ....	167

## List of Tables

Table 2.1 Arcam A2X Technical Data.....	14
Table 3.1 (a) Powder performance metrics for all powder types, (b) Powder flowability metric comparison based on the Carr index (C) and the Hausner ratio (Hr) [200].....	31
Table 3.2 Powder suitability criteria for use in the EB-PBF process.....	36
Table 3.3 Nomenclature and description of the various powder types investigated for the current study .	38
Table 4.1 Chemical composition of Ti-6Al-4V powder obtained from supplier.....	64
Table 4.2 ASTM E8/E8M tensile specimen types along with their dimensions [228].....	65
Table 4.3 Table summarizing XCT parameters such as the voxel resolution, FOV dimensions, and minimum detectable pore diameter .....	68
Table 4.4 ASTM E8/E8M tensile specimen types along with their dimensions [228].....	88
Table 4.5 Build orientation, location, and naming scheme for all specimen replicates as per ASTM 52921:2013 [275].....	89
Table 4.6 Anomalous stress-strain curves.....	90
Table 5.1 Pore classification according to pore equivalent diameter.....	103
Table 6.1 Thermal conductivity values for powder ( $W m^{-1} K^{-1}$ ), as-built parts, wrought rods and for wrought Ti-6Al-4V material extracted from representative plots presented by Arce [55], Cheng et al. [88], [192] and Boivineau et al. [317]. PREP = Plasma Rotating Electrode Process and GA = Gas Atomized.....	128
Table 6.2 Preheat Theme process parameters.....	133
Table 6.3 Table summarizing the average values and standard deviation for packing density, contact size ratio, eff. thermal conductivity and particle equivalent diameter, for all powder capsules .....	138
Table 7.1 TPMS Diamond specimen types and their associated dimensions .....	157

## List of Abbreviations

2D	Two Dimension(al)
3D	Three Dimension(al)
$\rho_0$	Bulk density
$\rho_{500}$	Tapped density after 500 taps
% EL or % el	% Elongation
AM	Additive manufacturing
AOR	Angle of Repose
ASTM	American Society for Testing and Materials
BFE	Basic Flow Energy
C	Carr Index
CAD	Computer Aided Design
CI	Cohesive Index
E	Elastic Modulus
EB-PBF or EPBF	Electron Beam Powder Bed Fusion
$H_r$	Hausner Ratio
PBF	Powder Bed Fusion
SE	Specific Energy
SEM	Scanning Electron Microscope or Microscopy
STL	Stereolithography File Format
Ti	Titanium
TPMS	Triply Periodic Minimal Surfaces
UTS	Ultimate Tensile Strength
XCT	X-ray Computed Tomography
YS	Yield Strength

# Chapter 1

## Introduction

### 1.1 Background

Additive manufacturing (AM), also known as layered manufacturing (LM), solid freeform fabrication (SFF), or more commonly 3D printing, has proved to be a disruption in the manufacturing industry. AM techniques enable users to manufacture physical parts directly from computer aided design (CAD) models, without any tooling and secondary fixtures. The Stereolithography (STL) file, also called a standard tessellation language file, is obtained from the CAD model, and describes the surface geometry of a 3D object. The STL is sliced into a series of cross-sectional layers by a software package, with each layer describing the geometry at that specific location. The layer-by-layer information is merged with machine-specific parameters and transferred to an AM system for execution. The part is then fabricated in a layer-by-layer fashion on a build plate or platform [1], [2]. According to the American Society for Testing and Materials (ASTM), the established AM processes can be divided into 7 categories: VAT photopolymerization, material jetting, binder jetting, material extrusion, powder bed fusion (PBF), sheet lamination, and directed energy deposition [3]. The three main PBF processes are: electron beam powder bed fusion (EB-PBF or EPBF), laser powder bed fusion (LPBF), and selective laser sintering (SLS). These methods use either a laser or electron beam to melt and/or fuse powder material together [3].

This thesis explores scientific discoveries in the EB-PBF AM technology class. EB-PBF is a process which makes use of a high-power focused electron beam as a heat source to selectively melt the metal powder to create 3D parts in a layer-by-layer fashion. This process has demonstrated the capability of printing parts with alloys such as Ti-6Al-4V [4]–[6], Ti-48Al-2Cr-2Nb [7]–[9], Co-Cr alloys [10], [11], H13 and 316L steel [12], [13], nickel and nickel-iron alloys [14]–[19], copper [20], [21], etc. EB-PBF is used in emerging industrial applications such as turbine blade production [22], engine valves and turbine wheels for turbochargers [23], and induction coils [20]. More commonly, EB-PBF is used in commercial manufacturing of implants and surgical tooling for bone replacement and augmentation in knees, hips, elbows, fingers, spine, shoulders, and maxillofacial applications, with components ranging from fixation devices, plates, spinal cages, acetabular cup implants, to jaw reconstruction components [24]–[32].

The EB-PBF process offers distinct advantages when compared to other metal PBF processes. In EB-PBF, components are manufactured under a controlled vacuum and at an elevated temperature [33]. This environment is beneficial as it has the potential of having minimal impact on the chemical composition of the powders and is suitable for reactive materials such as titanium alloys [34], and it furthermore results in

lower residual stresses in the deposited material by virtue of the elevated process temperature [35]. In addition, the EB-PBF process enables faster build rates owing to the high-power and fast beam scanning [36]. It is also a “tool-less” fabrication technology which requires neither fixtures nor tooling to obtain a custom part geometry, within tolerance limits. EB-PBF technology also permits blends of used and new powders to be recycled back into the system, therefore this technology has the potential to be an environmentally friendly process.

To continually improve the process, it is important to identify, address, and overcome some of the process limitations. Sames [37] and Antonysamy [38] have identified a few limitations such as high process waste leading to increased costs, lack of quality control due to absence of testing standards, and inadequate repeatability and reproducibility of part quality due to limited understanding of the process-structure-property relationship. This thesis will look at addressing and overcoming some of these limitations, with further insights captured below.

## **1.2 Motivations**

The EB-PBF process has enabled manufacturing of functional, highly complex, and highly customized metallic parts much more conveniently when compared to traditional manufacturing methods such as milling, metal forming, and press-and-sinter [37]. Manufacturing functional and custom-designed parts in EB-PBF requires careful consideration of processing conditions and a deep understanding of the nature of the additive process and its effect on the physical and mechanical properties of the fabricated specimens. This is the driving force for achieving a deep understanding of the process-structure-properties relationship.

The first step in the EB-PBF process is preheating. The build plate is heated by the electron beam from room temperature to a temperature  $\approx 475$  °C [39]. Once this temperature is achieved, degassing is performed for 10 minutes to remove species such as water vapor from the surface of the build platform, moisture from the powder stored in the hoppers, etc. After degassing, the temperature of the build platform is increased to a pre-defined initial preheating temperature. The temperature of the build plate is monitored by a thermocouple that is affixed at the bottom of this plate. In the Arcam A2X machine, the thermocouple lies on top of the powder bed and the build plate is positioned such that the thermocouple is touching the build plate in the centre. Once the preheat temperature is reached ( $\approx 730$  °C), the build table is moved downwards by 1-layer thickness, and a layer of powder is spread homogeneously. This is followed by a step where powders are pre-sintered into a powder cake, followed by the melting step where the material is selectively melted to create the part layer. This is repeated until all the specimens are built by sequential exposure of the powder cake to the preheating and melting steps, respectively. Lastly, the parts are cooled from  $\approx 730$



°C to room temperature once the build is completed. The specimens are then retrieved from a partly sintered cake by blasting in the Powder Recovery System (PRS) where the powder cake is blasted with the same powder raw material used for fabrication, circulated in a stream of air. This allows for recovery of the solid specimens from the cake [11], [40]–[43]. A detailed description of the process is presented in Chapter 2.

The entire process is quite complex, with the powder quality and the process parameters, as they pertain to the preheat and the melt stage, influencing the as-built product quality outcomes. This thesis aims at advancing the scientific body of knowledge for the following problem statements.

**Problem statement 1:** There is a need for lowering the economic barriers in EB-PBF AM processes. One way to achieve this is to increase the process efficiency and reduce the waste by implementing feedstock powder re-use and recycling strategies<sup>1</sup>. The challenge with doing so is that mechanical properties of metal parts, manufactured by PBF processes, are strongly influenced by the characteristics of the metal powder (particle size, size distribution, particle shape, flowability, etc.). It is also known that powders influence the packing behavior, powder organization in the powder bed, and the kinetics of melting and sintering, thereby impacting properties such as density, dimensional fidelity, and surface topography of the final component. Despite the fact that there have been a considerable number of studies on correlating powder properties (i.e., basic physical or chemical property of the individual particle) with bulk powder behavior (i.e., the behavior of the powder ensemble as a whole) in different branches of powder processing, the link to the specific behavior of powders as a function of powder reuse in the EB-PBF domain is still weak. Therefore, there is a need to delve into quantifying the effect of powder reuse on the powder quality, which may lead to informing future research on powder layer organization and part properties.

**Problem statement 2:** Final part performance in AM is usually quantified based on the tensile behavior of components. As such, tensile specimens are often used to qualify builds; however, there is currently no single standard specimen geometry that is in widespread use for PBF processes. While there is already work demonstrating the difference in measured properties between tensile specimens produced in different build orientations, this does not extend to different specimen geometries. It is currently not well-understood whether a difference in measured tensile properties between different specimen geometries exists. As a result, it is imperative to expand the understanding of the relationship between specimen geometry, specimen build location, and pore characteristics (size, density, and spatial distribution), within a component. The scientific outcomes of such studies are expected to translate to a direct and immediate

---

<sup>1</sup> In the context of this thesis, powder re-use implies the recirculation of powders or powder blends back into the EB-PBF process, while re-cycling implies the modification (chemical, mechanical, thermal) of spent powders in an attempt to recover the initial virgin powder properties.

value to the standards community and to industry towards addressing the knowledge gap in quality assessment of the EB-PBF process.

**Problem statement 3:** One of the major barriers in adapting the existing EB-PBF process parameters to a new powder material system is controlling the preheating conditions of the powder such that every layer results in enough partial sintering to create a coherent powder cake. A coherent powder cake not only results in low-defect components, but also influences the surface quality and de-powdering of complex geometries. To be able to understand the powder sintering process and to furthermore adapt this understanding to other materials, the degree of sintering and the effective thermal conductivity of the powder bed must be investigated. An in-depth understanding of these characteristics will help tailor the preheating temperature. This will enable strategies to improve the de-powdering process for intricate parts after build completion, while leveraging the preheating phenomenon to create a coherent powder cake. EB-PBF is viewed as a one-step fabrication process for custom porous titanium implants and scaffolds, however, easy de-powdering is essential for manufacturing intricate geometries such that they have minimum deviations from the intended geometrical models. Appropriate control of the preheat stage is expected to have a significant impact on de-powdering of such complex geometries.

### 1.3 Thesis Objectives

This thesis specifically aims to advance the scientific body of knowledge in understanding the interconnected relationships between the powder properties, bulk powder behavior, in-situ performance, and part properties (as shown in Figure 1.1).

**Objective 1: Understanding the effect of reuse on powder properties and the EB-PBF process:** To address the concerns highlighted under Problem Statement 1, and to better understand the powder-process-part quality relationships, this thesis looks into a systematic reusability study to evaluate the performance of powders for use over extended periods of time, as well as the relationship between the powder characteristics, build chemistries and rheological behavior for various generations of powders. The effect of the differences between various generations of powders and powder blends on the various powder characteristics such as the morphology, size distribution, flow properties (basic flow energy, specific energy, cohesive index, and angle of repose), packing properties (bulk density and tap density, Hausner ratio, and Carr index) and chemical composition (oxygen and nitrogen content), was evaluated. The work done highlights the powder characteristics that are the most likely to change with powder reuse.

**Objective 2: Understanding the tensile behavior and pore space characteristics of EB-PBF components:** To address the concerns highlighted under Problem Statement 2, this thesis investigated the effect of varying sample geometries on tensile properties, along with the development of analytical tools to evaluate pore characteristics (such as total volume, equivalent diameter, frequency, sphericity, aspect ratio, radial position) and their effect on part mechanical properties. The knowledge obtained from the pore space analysis helps in understanding the tensile behavior of EB-PBF components and the occurrence and types of porosity that influenced this behavior. Such tools are expected to be generalizable in nature and can be leveraged for other materials and powder bed fusion processes.

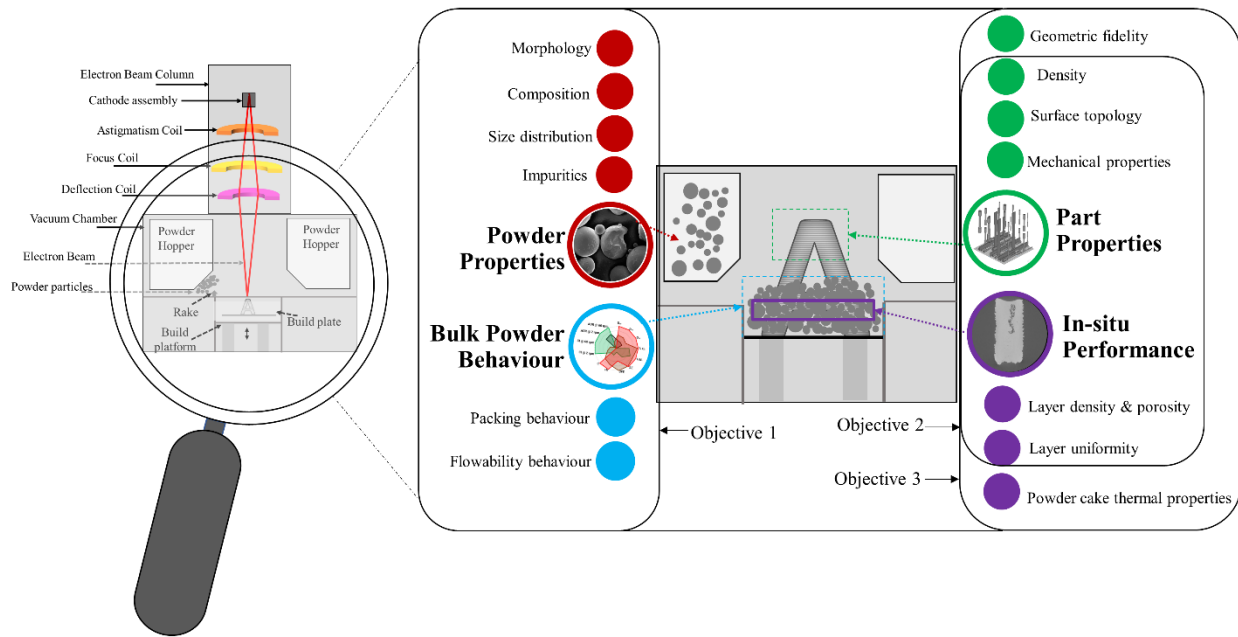


**Figure 1.1 Powder properties, bulk powder behavior, in-situ performance, and part properties relationship studied in this thesis.**

**Objective 3: Understanding the in-situ powder cake properties and its effects on the surface topography, geometric dimensional deviations and de-powdering, in the EB-PBF process:** To address the concerns highlighted under Problem Statement 3, this thesis looks to develop an empirically-derived thermal conductivity model for the powder cake, to evaluate the impact of preheating temperature on the in-situ powder cake properties, and to study the resulting effects on surface topography, geometric fidelity, and de-powdering capabilities for complex design architectures. Unique powder-capture artefacts and analogous part-quality artefacts were created, wherein the powder-capture artefacts were used to analyze

the in-situ powder cake properties (such as coordination number, thermal conductivity, packing density of the powder cake) and inform the powder cake empirical model, and the analogous part-quality artefacts were used to quantify the surface topography. As a proof of concept, triply periodic minimal surface (TPMS) Ti-6Al-4V structures with varying cell sizes and solid volume fraction were manufactured to study the impact of varying the preheating temperature on dimensional deviations and de-powdering.

## **1.4 Organization of Chapters**

This thesis includes eight chapters. Chapter 1 presents the general literature background, thesis motivations outlining the driving force behind furthering the process-structure-properties relationship understanding, objectives, and organization of this thesis. Chapter 2 presents a literature review of the EB-PBF process and the relationship between process-structure-properties in EB-PBF of Ti-6Al-4V with a specific focus on the effect of phase transformations, microstructure, powder properties, surface topography, pore space characteristics and tensile properties on the EB-PBF process outcomes. Chapter 3 is divided into 2 parts and addresses Objective 1 of this thesis. Part I is a preliminary study that was conducted to evaluate the effect of powder reuse on particle size, flow properties, and rheometry. Part II is a comprehensive study that was conducted to evaluate the influence of multiple reuse cycles, as well as powder blends created from reused powder, on various powder characteristics such as the morphology, size distribution, flow properties, packing properties, and chemical composition. This chapter highlights the powder characteristics that are the most likely to change with powder reuse. In addition, a unified powder quality score to understand the relative change of powder characteristics with reuse, is presented. Chapter 4 and Chapter 5 address Objective 2 of this thesis. Chapter 4 presents a systematic investigation of tensile properties for EB-PBF as-built Ti-6Al-4V by evaluating, assessing, and reporting the impact on tensile test results with respect to the changes in specimen geometry, size, build orientation, and the internal porous defects observed via X-ray computed tomography. Chapter 5 aims at advancing the study conducted by the authors in Chapter 4, by employing X-ray computed tomography techniques to address the deeper correlations between the pore space and specimen geometry, orientation, cross-sectional area, surface area to volume ratio, and the tensile behavior. Chapter 6 and Chapter 7 address Objective 3 of this thesis. Chapter 6 presents the investigation on the impact of preheating temperatures on the in-situ powder cake properties through unique powder-capture artefacts that enabled capturing of the immobilized powder cake. The powder cake was exposed to different preheat strategies and the inter-dependency of the thermal conductivity on the contact size ratio and density was quantified. An empirically-derived model for thermal conductivity of the powder cake was established as a function of changing the preheating temperatures. The

findings for this work were applied in Chapter 7 to assess and to correlate the effects of different powder conductivity and preheat temperatures on the surface topography and geometric fidelity of components with simple and complex lattice geometries. Chapter 8 provides a summary of the key findings from the work presented in this thesis, identifies the directions for future research, and outlines the author's scientific contributions.

## Chapter 2

### Literature Review

This chapter is divided into 2 sections: Section 2.1 focuses on the Fundamentals of EB-PBF – history and development, description of components in the system, operating principles, and areas of application, advantages, and limitations and Section 2.2 focuses on relationship between process-structure-properties in EB-PBF of Ti-6Al-4V alloy.

#### 2.1 Fundamentals of Electron Beam Powder Bed Fusion (EB-PBF)

##### 2.1.1 History & Development

The EB-PBF technology was developed by Arcam AB, a Sweden-based company, which was founded in 1997. The technology stemmed through a collaboration with Chalmers University of Technology in Gothenburg, Sweden. The principle of melting the electrically conductive material was patented in 1993 [44], and in 2002 the technology was ready for commercialization, and two units of first production model, S12, were displayed at Euromold in Frankfurt. The technology uptake in the research domain [41], [45] and industry domains shortly followed, with EB-PBF technological gaps being continuously addressed. As such, up to now, eight different system iterations of this technology have been released, each addressing a specific issue or niche capability [46]–[48]. In 2007, the Arcam A2 was released for manufacturing of large structural parts, specifically for the aerospace industry. In the Arcam A2 system, a double stage vacuum system was implemented, which provided a vacuum pressure of  $10^{-7}$  mbar, which falls under the high-vacuum performance pressure rating. As a result, the main advantage of this vacuum system is that less oxidation and contamination exists in the final part and powder [11]. In 2009, the A1 model and afterwards A2X model were developed for the volume production of orthopaedic implants and for materials' research and development, respectively. In these models, the patented MultiBeam™ technology has been used. This technology maintains several melt pools simultaneously at multiple locations. The Arcam A2X is designed for processing materials that require elevated process temperatures [46]. In 2012, the Arcam A2XX was developed, and this model had a bigger build chamber, as compared to the previous models, while targeting similar technological capabilities as the A2X. The development of EB-PBF AM equipment then progressed, where in 2013, another two generations of this equipment (Arcam Q10 and Arcam Q20) were released specifically for fabrication of biomedical-related parts such as orthopedic implants [24]–[32], and aerospace-related [22], [49], [50] parts such as turbine blades and structural airframe components, respectively. These two generations were succeeded by Arcam Q10+ and Arcam Q20+ models respectively.

The newest models in line are the Spectra H and Spectra L. The newest electron beam gun provides both better resolution and higher productivity. The other important feature of these recently-developed systems is having the benefit of in-process monitoring detectors, capturing both visible and near infrared signatures from the process window; this camera-based monitoring system is available for data analysis for inline quality verification of the process [47]. The accelerated interest from industry has prompted innovation in this sector. There are emerging new technologies which target research and development capabilities [51] rather than production, as well as new production systems [52].

### 2.1.2 EB-PBF Description of Principles & Operation

The EB-PBF technology is composed of an electron beam that selectively melts metal powder layer-by-layer (schematic in Figure 2.1). In order to understand the process, knowledge of the electron beam column, build chamber and powder recovery system (which is a separate machine) are required. Furthermore, on the software process side, it is important to know how to generate a build file, and what process/build conditions can be optimized. As such, a description of these above-mentioned technological elements, the hardware and the process are briefly presented below.

**Electron Beam Column:** This column contains a cathode assembly, a drift tube-anode assembly, and three magnetic coils as shown in Figure 2.1. The cathode assembly contains a tungsten filament and a grid cup. During operation, the tungsten filament is electrically heated to approximately 2600 °C. A potential difference between the cathode and anode is created and this leads to the acceleration of electrons from the cathode to the anode [53]. The electrons that do not get absorbed by the anode, pass through the drift tube, and reach the substrate. The three magnetic coils control the electron beam. First, the astigmatism coil provides assistance with changing the spot shape, secondly the focus coil provides focus of the beam to the required diameter, and thirdly, the deflection coil provides deflection of the focused beam to the required spot on the build table [12]. When the high energy electrons strike the powder particles, the kinetic energy is transformed into thermal energy, liquefying/melting the powder particles (as shown in Figure 2.1).

**Build Chamber:** All components are manufactured in the build chamber, also known as the vacuum chamber. The chamber contains the build platform, raking system and powder hoppers (as shown in Figure 2.1). There is a small viewport in the build chamber which is made of leaded glass. The interaction between the emitted electrons and powder surface can cause X-ray emissions. The build chamber is designed in a way to prevent exposure of X-ray emissions out of the chamber. The build platform, also known as the build plate or start plate, is typically comprised of a 316L stainless steel plate, floating onto a leveled powder

substrate acting as a thermal insulator buffer between the build plate and a piston-driven build platform assembly.

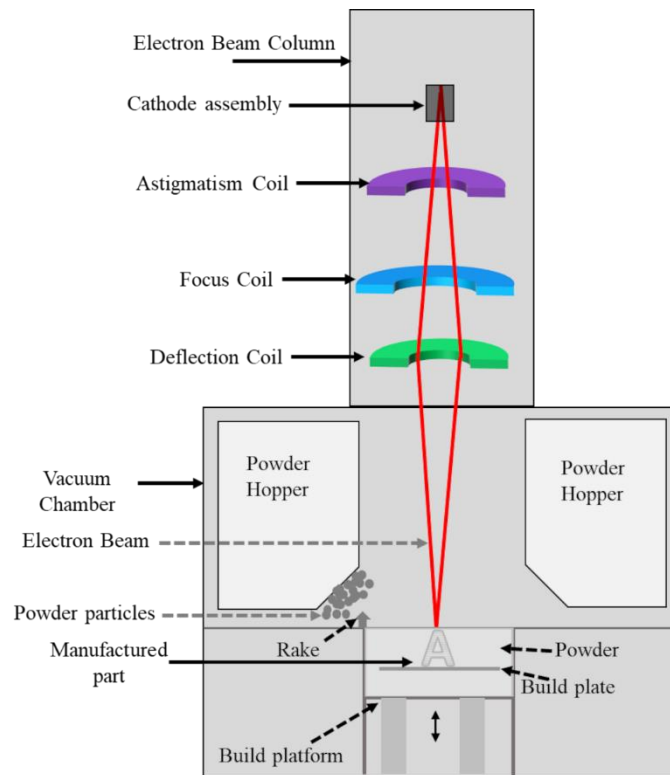


**Figure 2.1 Schematic of an Arcam A2X<sup>2</sup> EB-PBF machine**

The build plate is the surface onto which the powder is sequentially spread, layer upon layer. The build platform is capable of moving in the Z direction, thus actuating the build plate motion. Squared build plates with sizes (between 150 mm and 210 mm are used in the A2X machine) are used, and the maximum build height varies for each EB-PBF system (with a 380 mm height for the A2X machine). The build plate is heated, before the start of a build, to reach a predetermined temperature by repeated exposure to the electron beam. The temperature feedback is provided by a thermocouple that is attached to the bottom of the build plate; when the build plate reaches the predetermined value, the build can start. The entire process takes place under vacuum (build chamber  $\approx 10^{-4}$  mbar and electron beam column  $\approx 10^{-7}$  mbar). A constant flux of helium ( $10^{-3}$  mbar) is introduced into the build chamber, but only during the powder melting process. The powder is stored inside hoppers located in the build chamber (as shown in Figure 2.1). The raking

<sup>2</sup> The relevant technical details on the mode of operation enclosed in this document focus on the Arcam A2X machine, as this is the system used for this research.



system picks up a select amount of powder, from the hoppers, and spreads a thin layer of powder on the build plate. The rakes that assist with spreading of powder on the build plate are made of spring steel.

**Powder Recovery System:** The Powder Recovery System (PRS) is an enclosed cabinet intended for powder removal and recovery, where the powder cake resulting from the process is blasted under a high pressure. The blasting material is the powder used for manufacturing (Ti-6Al-4V powder for the current work) circulated in a stream of air. This allows the user to break the sinter necks in the powder cake that result from the preheating stage (discussed below) and further to recover the solid components. The remaining powder is sieved and reused for future builds.

**Process-specific requirements for the generation of a build:** The CAD model is processed into an STL file format and imported to the Build Assembler (Arcam AB, Sweden) software. This software slices the model into a stack of two-dimensional (2D) cross-sections based on the predefined layer thicknesses, pre-assigns build parameters for each layer to create a build file and transfers it to the EB-PBF system for execution. The process parameters in the build file are driven by “Themes” and are defined in the EBM Control (Arcam AB, Sweden) software for fabrication of the final parts. A "Theme" is a set of process parameters, compensation functionalities, and beam scanning strategies. The standard themes typical for EB-PBF (with nomenclatures inspired from the A2X machine) are the “Preheat”, “Melt”, “Net”, and “Wafer”. To better understand the process and challenges, all these themes are explained in detail below.

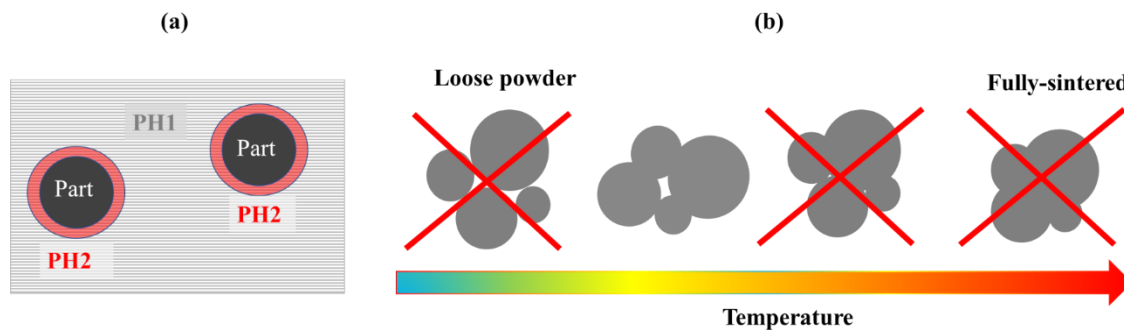


**Figure 2.2** Depiction of (a) PH1 and PH2 regions (b) Extent to which powder particles are sintered in the PH1 stage

***Preheat Theme:***

The Preheat Theme uses the electron beam in a defocused mode to preheat the build plate and sinter the powder to create a powder cake. The electron beam interaction with metallic powder develops a charge distribution around the build plate. If this charge exceeds a critical limit, the repulsive forces between the negatively-charged powder particles can cause particle motion and result in an avalanche effect, also known as “smoke” or “smoking effect” [53]. In order to avoid this smoking effect, the powder needs to be partially

sintered [54]. This powder sintering is performed by using the Preheat Theme. There are two steps in preheating, Preheating 1 (PH1) and Preheating 2 (PH2). PH1 is required for securing the powder particles strongly such that the electron beam is able to sweep over the powder bed without the formation of any smoke. PH1 covers the entire build plate and enables the electron beam to jump between melt areas; making the electron beam jump safe. PH2 is required to facilitate the melting of powder particles in select regions corresponding to the part cross-section at that layer and to prevent swelling in parts. PH2 covers each individual melt region (as shown in Figure 2.2 (a)) and uses a higher energy electron beam to provide mechanical anchoring of parts and supports (if any) [55]. For the very first layer, the Preheat Theme heats the build plate to the predetermined temperature ( $\approx 730$  °C for Ti-6Al-4V). After this step, each time the Preheat Theme occurs, its main purpose is to partially sinter the powder into a so-called cake (as shown in Figure 2.2 (b)).

Studies have shown that preheating can increase the mechanical strength, electrical and thermal conductivity of the sintered powder, as well as improve the beam-powder interaction efficiency [56]–[59]. Preheating has also been shown to reduce the formation of balling phenomena [56], [60] and lower the thermal gradient during melting, thus reducing distortion and warpage in the manufactured components [12], [58], [61]. However, Sigl et al. [62] identified a few drawbacks. They mentioned that (i) preheating increases the total build time and energy consumption (ii) a powder recovery system (PRS) is required break up the powder cake to retrieve the final parts, and (iii) preheating may limit the small details in complex internal geometries as it is difficult to remove the partially sintered powder particles. The presence of partially sintered powder particles in intricate or complex internal geometries and features may lead to an increase in surface roughness of the part as well. There is a need for identifying a suitable preheating strategy in order to address the disadvantages presented by Sigl et al. [62] and influence the powder cake properties for easy powder removal after the build has been completed. In order to do this, it is important to understand the effect of preheating and sintering on the powder particles and their thermal properties. This research avenue is explored as part of this thesis.

#### ***Melt Theme:***

The Melt Theme is used for melting the 2D slice corresponding to the part geometry manufactured within the specific layer. There are 2 different types of melting modes: Contour and Hatch. Contour controls the surface finish, geometric dimensioning, tolerancing, and acts as an interface between the sintered powder cake and the areas exposed to the hatch scanning. The hatch pattern melts the bulk of the part. Figure 2.3 shows a single slice, corresponding to one melt layer of a cylindrical component. The powder cake surrounding the part is ignored in this depiction. The boundary of the CAD is represented by the black

line and illustrates the theoretical geometric dimension of the part. The outer path of the beam trajectory (called outer contour) is a certain distance away from the boundary and this distance is known as the outer contour offset. The beam then scans an inner contour which is at a certain distance away from the outer contour and this distance is known as the inner contour offset. The area inside the inner contour is melted by a strategy called hatching. The hatching deploys a raster scan, which uses a line-by-line melting strategy that is defined by the heat-model. The distance between each line is the line offset.

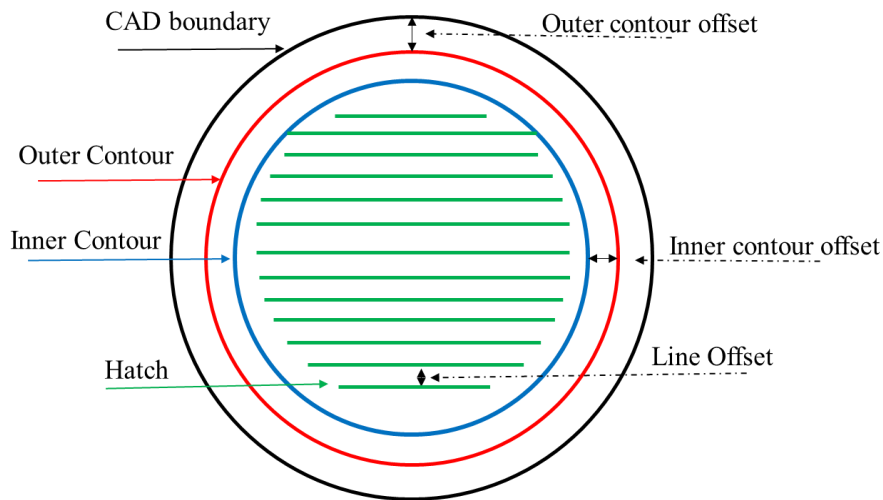


**Figure 2.3 Scan strategy for Melt Theme**

Carlsson et al. [63] have studied the effect of changing the number of contours as well as the contour offset parameters on the surface roughness of Ti-6Al-4V parts. They picked contour offset values of 0.20 mm, 0.25 mm and 0.30 mm and line offset values of 0 mm and 0.7 mm. They also varied the speed and current in these contours. However, effects of the process parameters in this study had a probability of changing the surface roughness values to an order of 1-2  $\mu\text{m}$ . The authors have noted that these parameters are insufficient in trying to optimize the surface roughness values for Ti-6Al-4V based on application needs. Gong et al. [64] demonstrated the effects of line offset in EB-PBF and found that porosity increased when the line offset value increased above 0.17 mm for Ti-6Al-4V parts. Tammam -Williams et al. [65] found that using contour only scanning strategy resulted in fewer defects in comparison to hatch settings. In this thesis, the relevant interest resides in assessing strategies for improving geometric fidelity and surface qualities, with the core property optimization out of scope.

***Net Theme:***

This theme is used specifically for thin structures (such as lattices) as it follows only contour paths. A high-resolution sharp beam is used with the same settings as the contour settings in order to enable the production of lattice structures. Suard [66] studied the use of Net theme for manufacturing thin struts for applications in lattice structures. They concluded that the Net theme should only be used for features  $\leq 1$  mm since features larger than these do not melt completely in the center, thereby causing large lack-of-fusion pores. Studies on optimization of the net theme are out of scope for this thesis.

***Wafer Theme:***

This theme is specifically used for partially melting support structures [67]. Support structures act as a heat sink, to prevent swelling, and to mechanically support parts. Studies on optimization of the wafer theme are out of scope for this thesis.

**2.1.3 EB-PBF Operating Procedure**

In EB-PBF, the beam operates at 60 kV accelerating voltage to provide an energy density greater than 100 kW/cm<sup>2</sup>. Table 2.1 illustrates the technical capabilities for the system used in this work.

**Table 2.1 Arcam A2X Technical Data**

Parameter	A2X values
Beam Power	50 – 3000 W
Scan Speed	Up to 8000 mm/s
Build Rate	55/80 cm <sup>3</sup> /h (for Ti-6Al-4V)
CAD Interface	Standard STL
Max. Build Size	200*200*380 mm

The beam current varies between 0 and 50 mA. The process takes place in a vacuum environment which prevents scattering of the electron beam as a result of collisions with gas atoms. A base pressure of  $1 \times 10^{-5}$  mbar or better needs to be achieved before the filament can be heated up. Once this vacuum is achieved, the tungsten filament is heated up by an electrical current. During normal operation, the first step is to preheat the build plate, using the Preheat Theme, to a predetermined temperature. For this step, the electron beam is defocused by increasing the offset focus parameter. This defocused beam scans lines that are parallel and offset to each other and continues to do so until the predetermined temperature is reached. For builds that have progressed in layers, the preheating helps decrease the thermal gradient between the currently melting layer and other previously solidified layers [38], and secondly, it helps to sinter the

powder material into a powder cake to prevent smoking [59]. The required current and speed are automatically calculated by themes. As a second step, a layer of metal powder (50  $\mu\text{m}$  thickness for the A2X machine) is spread over the build plate. A rake is used to evenly distribute this powder. The third step is to melt the parts by using the Melt Theme. The electron beam is focused (by decreasing the offset focus parameter) for this step. When the focused beam scans this layer, it melts the outline of the part by virtue of the outer and inner contour, then the part is filled in using a hatching pattern (as in Figure 2.3). After every layer has been melted by the electron beam, the build platform is lowered by the thickness of one layer. The powder sintering into a powder cake and powder melting into the part layer, provide supports for the overhanging structures of the component throughout the process. During the entire process, each point that is melted undergoes at least two cooling cycles: a rapid cooling rate from the melting state to the process-maintained temperature (730 °C) and a second slow cooling from 730 °C to room temperature when the part is completed and ready to be recovered from the powder cake (as shown in Figure 2.4). This slow cooling from 730°C to room temperature reduces the final residual stresses in the finished part [66]. More information on the cooling cycles is presented in Section 2.2.1: The effect of phase transformations and microstructure in the EB-PBF process.



**Figure 2.4** Figure depicts a completed build showing the sintered powder cake. This cake will be taken to the PRS to extract final parts.

The process of preheating, melting, and lowering of the build platform, and spreading a new layer of powder is repeated until the component(s) are created. Once the build is complete, it needs to be cooled to 50 °C before retrieving the component(s). Upon cooling, the entire build (powder cake + component(s)) is taken to the PRS where components(s) are retrieved. During the entire process, a partial pressure of Helium is introduced to  $2 \times 10^{-3}$  mbar.

### **2.1.4 EB-PBF areas of applications, advantages, and limitations**

EB-PBF is used in emerging industrial applications such as turbine blade production [22], engine valves and turbine wheels for turbochargers [23], induction coils [20] and biomedical implants with components ranging from fixation devices, plates, spinal cages, acetabular cup implants, to jaw reconstruction components [24]–[32].

The process offers distinct advantages when compared to other metal PBF processes. In EB-PBF, components are manufactured under a controlled vacuum and at an elevated temperature [33]. This environment is beneficial as it has the potential of having minimal impact on the chemical composition of the powders and is suitable for reactive materials such as titanium alloys [34] and it results in lower residual stresses in the deposited material by virtue of the elevated process temperature [35]. In addition, the EB-PBF process enables faster build rates owing to the high-power and fast beam scanning [36]. It is also a “tool-less” fabrication technology which requires neither fixtures nor tooling to obtain a custom part geometry, within tolerance limits. EB-PBF technology also permits blends of used and new powders to be recycled back into the system, therefore this technology has the potential to be an environmentally friendly process.

In contrast, there are many limitations to this process as well. For instance, the part properties may be influenced by the geometry and therefore it can be concluded that no optimal process parameters can be created that cover all instances [68], [69]. The orientation, height, location on the build plate and building angle of a part can influence the thermal history and material properties, and furthermore lead to formation of defects and residual stresses [4], [5]. In addition, EB-PBF parts have a poor surface roughness and geometric fidelity [70]–[74]. Lastly, defects such as cracks, inclusions, porosity, shrinkage, delamination are common and not well studied [37].

## **2.2 Relationship between process-structure-properties in EB-PBF of Ti-6Al-4V**

Ti-6Al-4V (an  $\alpha+\beta$  alloy) is one of the most prevalent titanium (Ti) alloys presently utilized in metal AM. At room temperature, the  $\alpha$ -phase dominates, and when heated to above the  $\beta$  transus [75], [76], it exists as a single  $\beta$  phase [77]. The presence of aluminum increases the strength and the presence of vanadium improves the room temperature ductility of the alloy [75]. Ti-6Al-4V exhibits a high strength-to-weight ratio, excellent corrosion resistance, wear resistance and biocompatibility [78]–[84]. Due to these properties, this alloy is a desirable material for use in airframes, aero-engines, petrochemical applications, bio-medical industry and many more [45], [85]. Therefore, it is necessary to understand and assess the process-structure-properties relationship to be able to tailor and predict the physical, mechanical, and

thermal properties of EB-PBF manufactured Ti-6Al-4V components. The scope of this thesis is limited to EB-PBF of Ti-6Al-4V and on understanding the above-mentioned relationships.

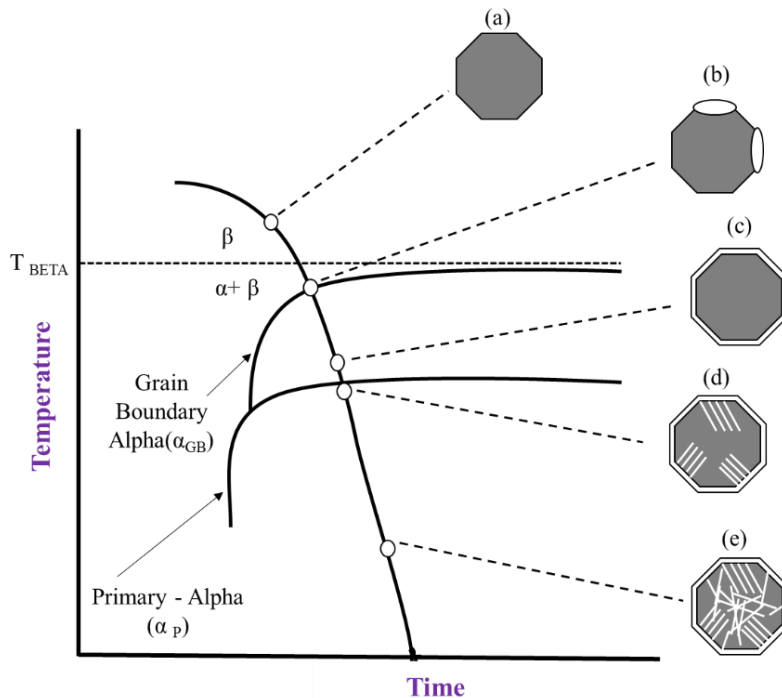
### **2.2.1 The effect of the EB-PBF process on phase transformations and microstructure**

Pure Ti is an allotropic element thereby exhibiting two different crystallographic structures with change in temperature [45]. Pure Ti exists in a hexagonal-close-packed (HCP) form (known as  $\alpha$ -phase) at room temperature, and transforms to a body-centered-cubic (BCC) form (known as  $\beta$ -phase) at high temperatures ( $> 882\text{ }^{\circ}\text{C}$ ), until reaching the melting temperature of about  $1670\text{ }^{\circ}\text{C}$  [86]. This temperature (i.e.,  $882\text{ }^{\circ}\text{C}$ ) is known as the  $\beta$ -transus temperature as this is when Ti transforms to the  $\beta$ -phase [87]. The  $\beta$ -transus temperature is very important, since processing and heat treatment conditions are based on this temperature. However, the  $\beta$ -transus temperature of titanium can be changed by the addition of alloying elements. The alloying elements that increase the  $\beta$ -transus temperature by stabilizing the  $\alpha$ -phase at higher temperatures are referred to  $\alpha$  stabilizers (examples are aluminum, oxygen, nitrogen) and those that decrease the  $\beta$ -transus temperature by stabilizing the  $\beta$ -phase at a lower temperature are referred to as  $\beta$  stabilizers (examples are vanadium, molybdenum, niobium). Depending on the stabilizer content, the alloy is considered either a fully  $\alpha$  alloy, a near  $\alpha$  alloy, a two phase  $\alpha + \beta$  alloy or fully  $\beta$  alloy [86]. The  $\alpha + \beta$  alloys contain a combination of one or more  $\alpha$  stabilizers and one or more  $\beta$  stabilizers. The composition of these alloys allows for the full transformation to  $\beta$  phase when heating is applied, and at lower temperatures, it can transform back to  $\alpha$  phase. The most well-known and currently the most used titanium alloy, Ti-6Al-4V, is categorized in this group. Ti-6Al-4V contains a volume fraction of approximately 15 %  $\beta$  phase at an equilibrium temperature of about  $800\text{ }^{\circ}\text{C}$  [75]. It consists of 6.1 wt. % Al, 4.3 wt. % V, 0.16 wt. % Fe, and balance Ti. For Ti-6Al-4V, the  $\alpha$ -phase dominates at room temperature, but once heated above the  $\beta$  transus temperature ( $\sim 992\text{ }^{\circ}\text{C}$  [75], [76]) it exists as a single  $\beta$  phase [77].

The melt pool temperature values in the EB-PBF process are estimated to be between  $1900\text{ }^{\circ}\text{C}$  and  $2700\text{ }^{\circ}\text{C}$  [88]–[91]. As described by Safdar [89], the phase transformation from the liquefied temperature ( $>1900\text{ }^{\circ}\text{C}$ ), to room temperature is a three-step process: rapid cooling from  $\sim 1900\text{ }^{\circ}\text{C}$  to  $\sim 650\text{ }^{\circ}\text{C}$  (chamber temperature) at a cooling rate in the order of  $10^3\text{--}10^5\text{K/s}$  [92], holding at the chamber temperature of  $\sim 650\text{ }^{\circ}\text{C}$ , and slow cooling from chamber temperature to room temperature after all parts have been built. This phase transformation can take place in 2 ways:

(i) Diffusion-controlled transformation: Figure 2.5 is a schematic illustrating the sequence of diffusion-controlled phase. Below the  $\beta$ -transus temperature, high temperature prior  $\beta$  phase ( $\beta_p$ ) is transformed into  $\alpha+\beta$  microstructure. This transformation occurs during the isothermal hold at the chamber temperature.

Firstly, the grain boundary (GB)  $\alpha$  phase ( $\alpha_{GB}$ ) nucleates heterogeneously on the prior  $\beta$  columnar grains as shown in Figure 2.5(b) (a single  $\beta$  grain is shown in Figure 2.5(a)) [75], [93]. This  $\alpha_{GB}$  grows in directions normal to the grain boundaries to form an  $\alpha$  layer (Figure 2.5(c)). After the formation of  $\alpha_{GB}$ , the Widmanstätten plates start nucleating along the  $\alpha_{GB}$  inside the prior  $\beta$  columnar grains (Figure 2.5(d)). In the case of EB-PBF parts, very fine Widmanstätten  $\alpha$  singular platelets are observed (Figure 2.5(e)) [94].



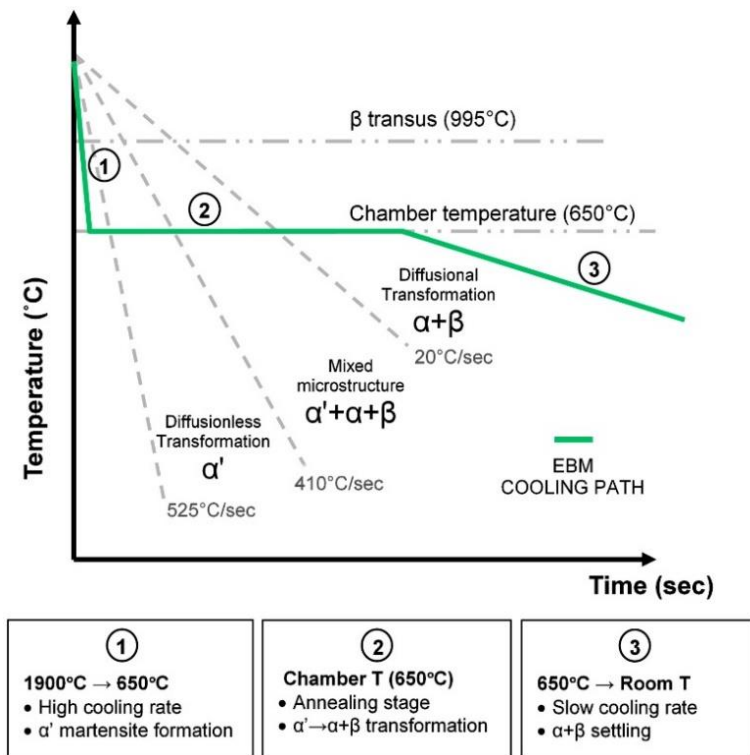
**Figure 2.5** A schematic illustrating the sequence of diffusion-controlled phase transformation in Ti-Al-4V.

Figure created by author but adapted from Kelly [95]

(ii) Transformation involving martensite formation: Ahmed et al. [77] and Safdar [42] have stated that a rapid cooling (cooling rate  $> 410$  °C/s) of Ti-6Al-4V leads to the formation of a fully martensitic phase ( $\alpha'$ ). Since EB-PBF is a manufacturing method where rapid cooling occurs due to fast melting and solidification thermal cycles, the initial cooling rate from  $\sim 1900$  °C to 650 °C is very high which may lead to formation of martensitic microstructures. Gaytan et al. [96], Murr et al. [79], and Bermani et al. [92] have reported the formation of martensitic phase for Ti-6Al-4V. Zeng et al. [97] explain how two transformations are feasible during the hold at the chamber temperature. The first one is when the hexagonal close packed martensite,  $\alpha'$  decomposes to form  $\alpha+\beta$  and the second is when the  $\alpha'$  decomposes to form  $\alpha''$  (orthorhombic martensite)  $+\beta$ . However, the lattice difference between  $\alpha$  and  $\alpha'$  phase is relatively small and therefore the first transformation is more favorable. It has been noted that the transformation from a  $\alpha'$  to  $\alpha+\beta$  phase at



~650 °C in Ti-6Al-4V takes about 30 minutes [98]. This is a much shorter duration than the hold time during the build. Therefore, it can be conclusively stated that during the hold at chamber temperature,  $\alpha'$  transforms to  $\alpha+\beta$  phase [91]. Figure 2.6 shows the cooling path and critical cooling rates for Ti-6Al-4V microstructure formation in EB-PBF.



**Figure 2.6 Cooling path and critical cooling rates for Ti-6Al-4V in EB-PBF. Reprinted with permission from Galarraga et al. [91]**

EB-PBF process parameters such as beam power, beam diameter, scan speed, focus offset, and preheating temperature can affect the solidification microstructure (grain and morphology). While this thesis did not include in scope the in-depth microstructural investigation; the deep understanding of this theory helped inform conclusions in Chapter 4 that looks at investigating the tensile properties of EB-PBF as-built components and Chapter 6 that looks at investigating the effective thermal conductivity of the EB-PBF powder cake.

### **2.2.2 The effect of powder properties on EB-PBF process outcomes**

Most powders for AM are manufactured with atomization methodologies. Almost all the current atomization processes use energy sources such as plasma torches and/or induction coils with nozzles to melt a metal in wire feedstock which then forms spherical droplets and solidifies into powder particles [99], [100]. Typically, powders used in EB-PBF are manufactured via Plasma Atomization. Plasma Atomization (PA) is the process of melting a wire spool feedstock of metal with a plasma torch and cooling it in an inert tower. The PA process environment operates in a vacuum to minimize metal oxidation levels and reduce the amount of entrapped gas within particles. In general, PA powder particles exhibit the following characteristics [101]: particles have a spherical shape, with minimal satellites or internal pores, particles also possess good flow and packing properties required for EB-PBF process. In general, the EB-PBF process uses a nominal Particle Size Distribution (PSD) between 45–106  $\mu\text{m}$ ; a similar PSD was used in this thesis.

The performance of the process strongly depends on the characteristics and properties of the powder [102]. Such properties include morphology, size distribution, flow properties (basic flow energy, specific energy, cohesive index, and angle of repose), packing properties (bulk density and tap density, Hausner ratio and Carr index) and chemical composition (oxygen and nitrogen content) [103]. A detailed literature review capturing the research efforts in understanding powder characteristics, their observed changes with powder re-use, as well as their impact on part quality is presented in Chapter 3. This thesis highlights the powder characteristics that are the most likely to change with powder reuse.

### **2.2.3 The surface roughness characteristics of EB-PBF components**

The influence of surface roughness, of EB-PBF as-built parts, on part mechanical properties have been reported by many authors [104]–[106]. The as-built parts for EB-PBF have relatively rough surfaces as compared to conventionally machined surfaces or parts produced by other AM processes [70]–[74]. This high level of roughness leads to increased crack initiation zones [106]. Chan et al. [107] and Edwards et al. [108] have indicated that the fatigue life of Ti-6Al-4V parts fabricated by AM techniques can be diminished due to these high surface roughness values. In industrial applications, rough surfaces lead to corrosion and fracture of pipes [109]. A study observed that reducing the roughness of as-fabricated Ti-6Al-4V specimens from an Ra value of 17.9 $\mu\text{m}$  to an Ra value of 0.3 $\mu\text{m}$  can increase the fatigue strength of components from 300 MPa after  $3 \times 10^7$  cycles (as built) to 775 MPa after  $3 \times 10^7$  cycles. [106]. Therefore, EB-PBF complex geometries or components might have to resort to post processing to obtain a better surface finish for fatigue driven applications.

However, for biomedical applications, studies have shown that rougher surfaces promote attachment of fibrin that acts as a matrix enabling the migration of stem cells to the surface and lead to a greater absolute contact between the bone and implant that might improve the biomechanical behavior of the implant [110]–[113]. Cells grown on rougher surfaces also exhibited increased production of prostaglandin E<sub>2</sub>, collagen, and transforming growth factor  $\beta$  [114], [115].

There is a need to further understand the relationship between process-structure-properties and the resulting effect on the surface topography of simple reference geometries and complex-shaped components [116], [117]. A detailed literature review describing the methodologies for assessing surface topography features, the range of achievable performance in EB-PBF, reasons behind the high surface roughness of as-built EB-PBF surfaces, as well as research efforts in decreasing the surface roughness is presented in Chapter 7. This thesis highlights ways of reducing and furthermore controlling the surface roughness of as-built components without the need of additional post-processing techniques.

## **2.2.4 The pore space characteristics of EB-PBF components**

There has been a growing interest in the determination of material porosity in AM manufactured parts [118]–[120]. There are two major types of internal defects in EB-PBF: (i) insufficient powder melting (or lack-of-fusion porosity) [121], [122] between successive layers or within a layer that is usually attributed to insufficient energy input, and (ii) entrapment of gas in the melt pool (gas pores) that is usually attributed to excessive energy input [123]–[125]. Such defects have been shown to influence the tensile strength, among other mechanical properties [4], [65], [126]. Lack-of-fusion pores are more detrimental to the performance of manufactured components, when compared to gas pores [106].

It is also well-known that such pores influence mechanical properties of manufactured parts and, consequently, their performance [120], [127]–[130]; most studies reporting on tensile properties do not assess the defect population. Many studies have mentioned that optimizing process parameters can ensure a reduction of porosity; however, it is extremely difficult for these to be completely removed due to technology limitations and prohibitive costs in parameter optimization [119], [131]–[134].

There are multiple ways of evaluating such pores, such as methods based on relative density measurements (e.g., Archimedes' method) to evaluate the amount of porosity, microscopic analysis of specimens' cross sections to evaluate sizes of defects [119], [135], and ultrasonic testing [118]. Although these methods are useful for inferring bulk density estimates, it is difficult to extract the 3D spatially-resolved information about porous defects (shape, size, distribution) required for proper assessment of mechanical properties for defect-prone material systems [125], [136], [137]. X-ray computed tomography

(XCT) is widely used for spatially-resolving, characterizing, and classifying defects in additively manufactured components due to its capabilities to visualize and detect external/internal features that are normally not accessible non-destructively [138]–[141]. Measuring and characterizing each internal defect from the XCT data can be a daunting task due to the massive quantity of data that resides in the high-resolution, volumetric XCT datasets. A few tools are mentioned in literature for assisting in the measurement and analysis of large quantities of internal defects [142]–[144]. Automated defect recognition algorithms are increasingly being implemented to speed up analysis, and such analytics have the potential to become commonplace.

There is a need to further understand the relationship between process-structure-properties and the resulting effect on the part porosity. A detailed literature review describing the methodologies for assessing the pore characteristics in EB-PBF, the range of achievable performance in EB-PBF for Ti-6Al-4V, as well as research efforts in assessing porosity of EB-PBF parts is presented in Chapter 4 and Chapter 5. This thesis highlights the development and adoption of XCT tools to evaluate porous defects, both qualitatively and quantitatively, to understand their impact on mechanical properties and performance.

### **2.2.5 The tensile behavior of EB-PBF components**

There are multiple studies in EB-PBF literature that focus on the tensile properties of Ti-6Al-4V specimens. These studies focus on evaluating the difference and/or similarities in properties with respect to build orientation, specimen geometry, location on build platform, height of specimen, comparison with the cast and wrought counterpart, post-processing technique, etc. However, the results presented are inconsistent [38], [85], [145]–[151]. There is a significant amount of mechanical property data scatter for a single material system (Ti-6Al-4V). It is important to note that, due to a lack of information on build parameters, it is difficult to definitively explain why there is such a broad range and inconsistency in results. For the same reason, it is also difficult to make accurate quantitative comparisons between the observations and results of different published literature. In the context of the present thesis, the build parameters include (i) information about the powder such as chemistry, particle size distribution, powder manufacturing process (gas-atomized, plasma-atomized), and powder reuse cycles (ii) information about the specimen such as shape, orientation, location on the build platform, dimensions, use of supports, post-processing techniques such as machining, heat-treatment, cooling rates for heat-treatment, and (iii) information on process parameters such as layer thickness, preheat temperature, scanning strategy, rotation angle between consecutive hatches, build theme version, and machine model type. Of note, although the operation of all machine models is similar, improvements have been made with every generation [152]. All the above-

mentioned build parameters can have a significant effect on tensile properties and therefore should be provided, along with the specimen performance data, to be able to draw robust conclusions and draw comparisons in performance.

There is a need to further understand the relationship between process-structure-properties and the resulting effect on the mechanical properties. A detailed literature review describing the methodologies for assessing the mechanical properties in EB-PBF, the range of achievable performance in EB-PBF for Ti-6Al-4V, as well as research efforts in assessing the tensile properties of EB-PBF as-built and machined parts is presented in Chapter 4. This thesis highlights the impact of specimen geometry, specimen size, build orientation, and the internal porous defects observed on the tensile properties of EB-PBF components.

## **2.2.6 Complex designs and their implementation to biomedical applications**

In the last decade, many medical applications of AM have been developed and reported [153], however, this research area presents challenges because the leaps in development require an interdisciplinary process and includes work related to medical imaging, 3D modeling, design optimization, medical treatment, and the actual deployment of the AM technology. Tuomi et al. [154] classified the spectrum of medical applications of AM in the following categories: medical models for preoperative planning, education and training, surgical tools and instruments, medical aids, supportive guides, splints and prostheses, bio-manufacturing and inert implants.

With the advent of AM technologies, there has been renewed interest in fabrication of structures with controllable internal pore architectures to be used in biomedical applications, to be able to mimic the complex architecture of tissues and organs [155]. Porous structures have been proven to have enhanced cell adhesion, migration, and proliferation as well as tissue ingrowth, nutrient delivery, and vascularization [156]–[158] when used as implants and scaffolds. There have been many studies on fabrication of porous structures for biomedical applications using EB-PBF techniques. Harrysson et al. [29] stated that EB-PBF is capable of manufacturing porous implants and scaffolds that can be used for knees, hips, elbows, fingers, shoulders, and bone plates. The majority of these works focus on regular lattice-based geometries, such as diamond [159]–[161], cubic [147], [162], [163], octahedral [164], [165], and rhombic dodecahedron [166], [167]. There have been several studies in literature specifically focusing on manufacturing porous Ti-6Al-4V structures using EB-PBF. Cansizoglu et al. [168] successfully fabricated non-stochastic hexagonal lattices with varying densities ranging from 5 % to 11% of solid Ti-6Al-4V. Parthasarathy et al. [147], [169] manufactured porous cellular cranioplasty plates which had up to 60% porosity. Murr et al. [170] manufactured knee implants with an inner dense material and an outer lattice structure. This geometry

promoted cell propagation onto the implant. Heintz et al. [171] produced freeform open-cell structures and also demonstrated the possibility of locally varying the density of lattices. Horn et al. [166] manufactured open-cell rhombic dodecahedron structures with varying densities.

Another type of porous structures that are biologically desirable, due to the ease of controllability of the internal pore architectures, are triply periodic minimal surfaces (TPMS) [172], [173]. TPMS structures can be periodic along three independent directions and have zero mean curvature of the surface [174], [175]. Porous TPMS architectures are manufactured by using repeating unit cells with the minimum possible area [155]. TPMS structures have several advantages, over strut-based lattices, such as high surface area-to-volume ratio [155], improved mechanical and biological properties due to the geometrical continuity and topological smoothness [176], enhanced cell adhesion, migration, and proliferation [177], and superior fatigue properties [178]. These advantages make them ideal for use as scaffolds [155], [163]. Despite all these advantages, there have not been many studies on the fabrication of TPMS using Ti-6Al-4V EB-PBF. Some of the reasons for the limited number of studies could be that (i) TPMS structures consist of curved inner channels and therefore powder removal is a challenging task when dealing with such intricate structures [179] and (ii) it is very challenging to produce intricate geometries that have high dimensional accuracy and low deviations from the intended geometrical models, especially since rough surfaces and dross are commonly observed in intricate geometries. These topographical defects are caused due to heat trapping and over melting of the thermally insulating powder cake that surrounds and supports these structures [180], [181]. The as-built surfaces of EB-PBF components are relatively rough. Partly fused and loosely attached powder particles are always present on the surfaces if no post-processing is performed. Even with parameter optimization, thin and porous structures may have significantly rough surfaces [116].

There is a need to further understand the relationship between process-structure-properties and the resulting effect on the surface topography and geometric fidelity of simple reference geometries and complex-shaped components [116], [117]. A detailed literature review describing the research efforts on assessing surface topography features and geometrical fidelity is presented in Chapter 7. This thesis highlights ways of reducing and furthermore controlling the geometric dimensional deviations of complex geometries. Such geometries may be applicable for use in biomedical applications.

## Chapter 3

# Understanding the effect of reuse on powder properties and the EB-PBF process

This chapter is published as follows:

### **Part I (Preliminary study):**

Shanbhag G, Vlasea M. “The effect of reuse cycles on Ti-6Al-4V powder properties processed by electron beam powder bed fusion.” *Journal of Manufacturing Letters*. August 2020.

<https://doi.org/10.1016/j.mfglet.2020.07.007>

Reprinted with permission © Elsevier

### **Part II (Comprehensive study):**

Shanbhag G, Vlasea M. “Variation of Powder Properties Induced by Reuse Cycles in Electron Beam Powder Bed Fusion.” *Journal of Materials, Special Issue: Materials Research Considerations for Metal Powder and Wire-Based Additive Manufacturing Processing*. August 2021.

<https://doi.org/10.3390/ma14164602>

Reprinted from the open-access article published in MDPI

## **3.1 Part I: Preliminary study**

### **3.1.1 Preface**

Electron beam powder bed fusion can offer advantages in terms of powder reuse by virtue of larger layer thickness and flexible recoater, thus lowering the economic barrier by reducing material waste. Systematic studies focused on quantifying the effect of reuse on powder performance metrics such as size, rheometry and flowability remain scarce. This work presents results on the influence of the process on Ti-6Al-4V powder, by comparing virgin powder to reused powders over two processing cycles, benchmarking the most sensitive powder characteristics. Particle size, flow properties and rheometry are compared. It was observed that morphology, size distribution, flowability and spreadability were degraded due to partial sintering and powder recovery.

### **3.1.2 Introduction**

Electron beam powder bed fusion (EB-PBF) is an additive manufacturing (AM) technology that uses a high-power electron beam as an energy source to melt metal powder and create 3D components layer-by-layer. The high cost of metal AM components has been prohibitive for technology adoption. The feedstock powder accounts for 10-25% of the total cost of producing an AM component [182], [183]. One path to lowering the economic barrier can be achieved by reducing the waste via implementing powder reuse strategies (powder cycled back into the process, either blended with virgin powder, or with other reuse generations). In EB-PBF, almost 95 - 98% of the powder that is not melted could be used again after blasting and sieving [184] to lower the production costs. However, one of the key issues is to guarantee that the reused powder is comparable to virgin powder [185]. It is also essential to verify that any differences that may appear between virgin and reused powder do not interfere with the performance of the as-built components.

The performance of the process strongly depends on the characteristics and properties of the powder. The flowability of the powder is very important, to ensure uniform layer characteristics when dispensed, distributed, or spread onto the build area. Cohesive powders that exhibit poor flow properties are more difficult to deploy in terms of obtaining layers with homogenous density throughout the build, compared to powders which are comparatively free flowing [99]. Particle size also has a significant influence on flow [186]; larger particles are more free-flowing than smaller particles. Flow properties also show a dependency on packing density [187]. Therefore, it is imperative to assess the powder properties before conducting experiments to develop and optimize parameters for an EB-PBF system.



There is a need for systematic studies to demonstrate the effect of reuse on powder properties for EB-PBF. The present study aims at benchmarking powder characteristics and achieving preliminary data by extracting and comparing the particle size, morphology, flow properties and rheometry of virgin and reused powders over two EB-PBF processing cycles.

### 3.1.3 Materials and Methods

Four powder types were assessed for this study. The virgin (Genesis 0 or  $G_0$ ) plasma-atomized Ti-6Al-4V Grade 5 powder was obtained in a pre-alloyed condition with a size range of 45-105  $\mu\text{m}$ . Powder that was used once (Genesis 1 or  $G_1$ ), was passed through a vibrating sieve to recover the powder for reuse (as shown in Figure 3.1). Genesis 2 ( $G_2$ ) powder was similarly obtained after printing parts with  $G_1$  powder.  $G_1$  and  $G_2$  powders were blended in equal wt.% of powder constituents to obtain a Genesis Blend ( $GB_{12}$ ). In order to ensure that a consistent beam scanning strategy is used for all builds; the parts built, and the parameters used (Theme 5.2.52, Arcam A2X, GE Additive) were identical across both build cycles.

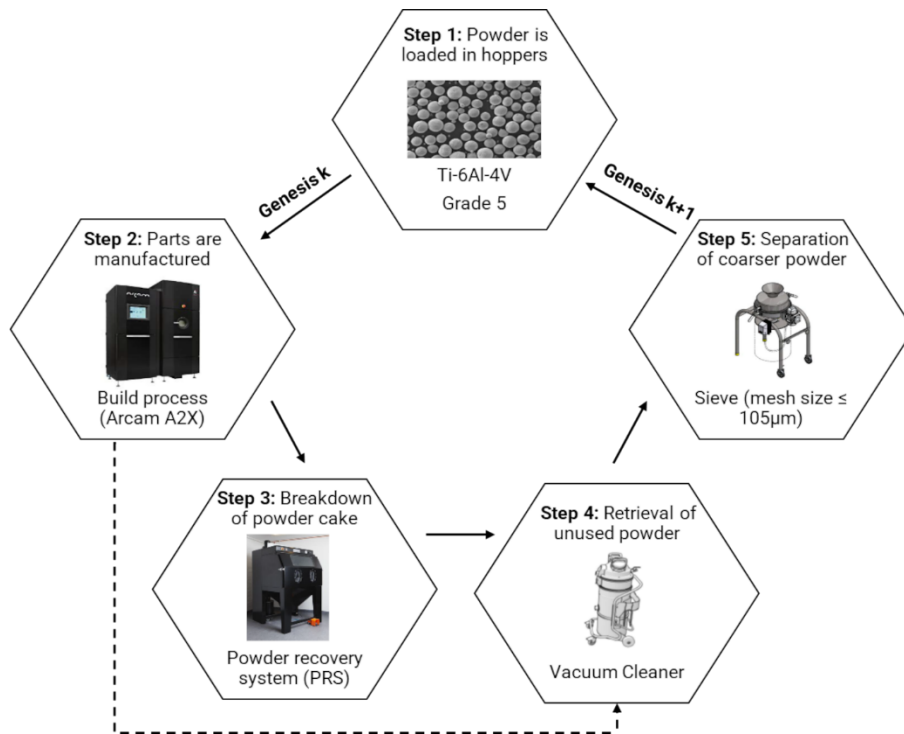


**Figure 3.1 Schematic illustrating the powder reuse cycle**

Field emission microscopy (SEM, Zeiss Ultra & Tescan VEGA3) was performed to assess the morphology (shape of the particles, the presence of satellites, foreign particles/contamination and defects), dynamic image analysis was used (Camsizer X2, Retsch) to assess the particle size distribution (PSD) and

sphericity, powder flow properties were investigated (FT4 Rheometer, Freeman Technology; GranuPack, Granutools) to assess performance metrics such as basic flow energy (BFE), specific energy (SE), bulk density (BD), tap density after 500 taps (TD), Hausner ratio (Hr) and Carr index (C) and elemental analysis was performed (LECO TCH 600, Leco Corporation) to analyze the oxygen content for all powder types. All experiments were performed in triplicate.

### 3.1.4 Results and Discussion

The SEM micrographs of all powder types indicate that reusing powder has introduced defects in the powder. These defects are classified as clip-clap, broken particles, shattered particles, particles with molten satellites, elongated particles and deformed particles according to the classification created by Popov et al. [188]. All images indicate that the particles are mostly spherical for all powder types however,  $G_0$  includes a large amount of satellites (Figure 3.2(a)).

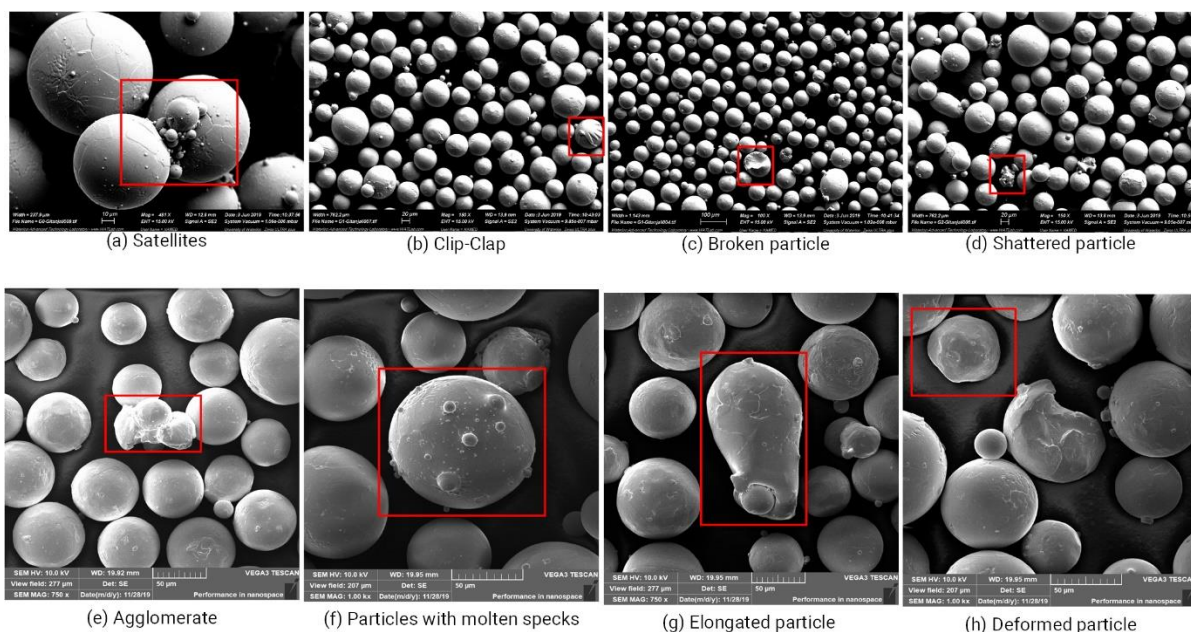


**Figure 3.2 SEM micrographs of powder defects (a)  $G_0$  at 481X depicting satellites in as-received powder; (b)  $G_1$  at 150X depicting clip-clap defect in reused powder; (c)  $G_1$  at 100X depicting broken particle in reused powder; (d)  $G_1$  at 150X depicting shattered particle in reused powder; (e)  $G_1$  at 750X depicting agglomerates in reused powder; (f)  $G_2$  at 1000X depicting particles with molten specks in reused powder; (g)  $GB_{12}$  at 750X depicting elongated particle in reused powder; (h)  $GB_{12}$  at 1000X depicting deformed particle in reused powder. Nomenclature as per [188].**

These satellites appear to have been eliminated in  $G_1$  (Figure 3.2(b), (c), (d), and (e)) likely from blasting during recovery from the powder cake (Step 3 in Figure 3.1). Very small satellite specks, however,

are more readily observed to be bonded onto large spherical particles (Figure 3.2(f)) for  $G_2$ . Due to the higher surface energy of small particles, they are melted quickly and bond to larger particles as soon as they are heated. Figure 3.2(c), (d), (g) and (h) depict broken, shattered, elongated, and deformed particles, respectively. Based on previous studies [184], [188], [189] these deformations can be attributed to the impact between particles during powder recovery, the sieving procedure, and overheating and smelting of the particles and satellites. Figure 3.2(e) depicts an agglomerate of particles. This can be attributed to the heat transfer from the electron beam. The observed defects may decrease powder flowability, which further leads to non-homogeneity in layer thickness and lack-of-fusion porosity.

The PSD for all powder types is plotted in Figure 3.3(a) and the  $D_{10}$ ,  $D_{50}$  and  $D_{90}$  values are indicated in Table 3.1(a). It is observed that the  $G_1$  and  $GB_{12}$  have a narrower size distribution whereas  $G_2$  is slightly broader when compared to  $G_0$ , however more iterations are required for conclusive results. The  $D_{10}$ ,  $D_{50}$ ,  $D_{90}$  values for  $G_1$  and  $GB_{12}$  are lower than  $G_0$ , whereas the values for  $G_2$  are closer to  $G_0$ . This similarity between  $G_2$  and  $G_0$  is attributed to defects such as agglomeration and particles with molten specks (as seen in Figure 3.2(e) and (f)) that lead to formation of larger particles. The PSD influences layer densities such that a wider PSD may lead to a higher density, as finer particles fill the vacancies between larger particles [190], [191]. Therefore, PSD is an important powder characteristic and needs to be carefully tailored [192].

The quality of the part built via EB-PBF is directly related to the powder flowing properties [193]–[195]. Higher bulk densities are preferred, as they provide better heat conduction and reduce the risk of sample overheating. The BD values for the powder types (Table 3.1(a)) are the same; however there is a change in the TD values (Table 3.1(a) and Figure 3.3(b)) attributed to the change in PSD as seen in Figure 3.3. BFE is a measure of how easily a powder will flow in a constrained environment, whereas SE evaluates the powder flow in an unconstrained environment. For both metrics, a higher value indicates increased mechanical interlocking and friction – leading to poor flowability [194]. The BFE (Table 3.1(a) and Figure 3.3(c)) values for  $G_1$ ,  $G_2$  and  $GB_{12}$  are observed to be higher than  $G_0$  and the SE values have an increasing trend (Table 3.1(a)) such that  $GB_{12} > G_2 > G_1 > G_0$ . This suggests that the  $G_1$ ,  $G_2$  and  $GB_{12}$  powders would not flow as freely as  $G_0$  due to changes in morphology resulting in more angular powders, thus contributing to increased particle interlocking. The sphericity plots in Figure 3.3(d) illustrate that the particles with lower  $x_{c\ min}$  are becoming less spherical, potentially contributing to this effect; more in-depth studies are required.

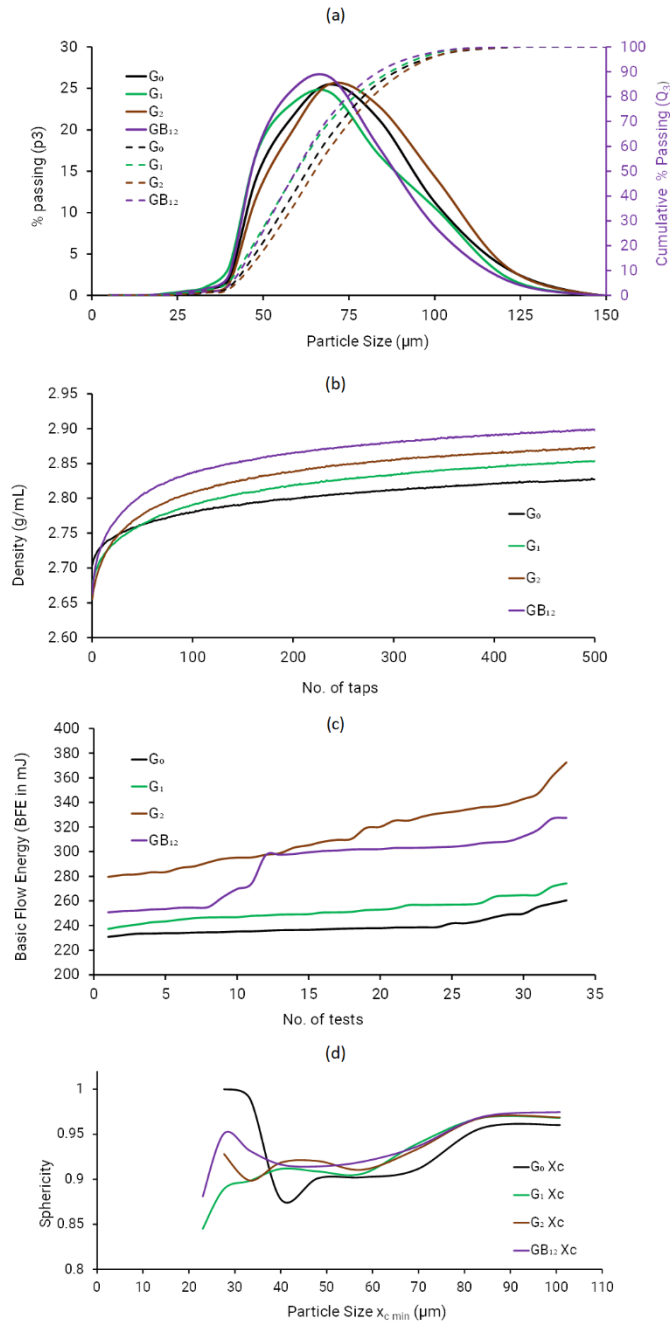


**Figure 3.3 Comparisons between powder generations based on (a) PSD, (b) Density vs. no. of taps, (c) BFE vs. no. of trials, (d) Sphericity vs.  $X_{c \min}$  particle size**

Another method to quantify flowability and compressibility of the powder is the Hr and C values respectively [102]. The C and Hr values for all powder types (Table 3.1(a)) are indicative that they still have excellent flowability (when compared to the optimal values given in Table 3.1(b)). However, it is

observed that the Hr and C values also follow an increasing trend where  $GB_{12} > G_2 > G_1 > G_0$ . This is attributed to the reduction in spherical particles and increased irregular particles in  $G_1$ ,  $G_2$  and  $GB_{12}$  as compared to  $G_0$ .

In general, the powder recovered from the build may contain splatter from the melt pool in the form of satellite particles, or the particles may have acquired surface contaminants during sieving or storage; in addition, powders may have broken or remained fused together despite blasting in the PRS. Thus, it is concluded that  $G_0$  has a better flowability than all other powder types. The concentration of Oxygen remains between 0.13-0.17 wt.% (Table 3.1(a)) which is below the limit of 0.20 wt.% as outlined by ASTM F2924-14 [196]. However, the increase in oxygen pickup is pretty swift across the powder reuse cycles. This increase is attributed to the fact that the powder is exposed to the ambient atmosphere when transferred from the machine to the PRS and then the transfer from PRS to the sieve. This exposure can act as a source for moisture that results in oxidation [16], [197]. Another factor is mechanical deformation during blasting and sieving, leading to acceleration of the oxidation process through production of new surfaces that become prone to oxidation [198]. An increase in the oxygen content can lead to decrease in ductility [86] and powder flowability [184], [199].

**Table 3.1 (a) Powder performance metrics for all powder types, (b) Powder flowability metric comparison based on the Carr index (C) and the Hausner ratio (Hr) [200]**

(a) Powder performance metrics					(b) Powder flowability from the Carr index (C) and Hausner ratio (Hr) [200]		
Parameter	$G_0$	$G_1$	$G_2$	$GB_{12}$	C	Flowability	Hr
$D_{10}$ ( $\mu\text{m}$ )	48.73 $\pm$ 0.64	46.83 $\pm$ 0.99	49.93 $\pm$ 0.63	47.93 $\pm$ 1.61	$\leq 10$	Excellent	1.00 – 1.11
$D_{50}$ ( $\mu\text{m}$ )	68.39 $\pm$ 1.45	65.13 $\pm$ 0.38	70.95 $\pm$ 0.40	64.85 $\pm$ 2.58	11 – 15	Good	1.12 – 1.18
$D_{90}$ ( $\mu\text{m}$ )	97.4 $\pm$ 2.45	94.65 $\pm$ 1.43	99.28 $\pm$ 0.42	91.45 $\pm$ 2.13	16 – 20	Fair	1.19 – 1.25
BFE (mJ)	239.46 $\pm$ 7.29	252.61 $\pm$ 8.10	313.47 $\pm$ 14.52	289.72 $\pm$ 7.96	21 – 25	Passable	1.26 – 1.34
SE (mJ/g)	1.40 $\pm$ 0.01	1.54 $\pm$ 0.03	1.69 $\pm$ 0.08	1.82 $\pm$ 0.12	26 – 31	Poor	1.35 – 1.45
BD (g/mL)	2.67 $\pm$ 0.004	2.67 $\pm$ 0.005	2.66 $\pm$ 0.004	2.65 $\pm$ 0.001	32 – 37	Very poor	1.46 – 1.59
TD (g/mL)	2.83 $\pm$ 0.001	2.85 $\pm$ 0.003	2.87 $\pm$ 0.003	2.90 $\pm$ 0.002	$> 38$	Awful	$> 1.60$
Hr	1.06 $\pm$ 0.001	1.07 $\pm$ 0.001	1.08 $\pm$ 0.002	1.09	-	-	-
C	5.65 $\pm$ 0.11	6.32 $\pm$ 0.08	7.32 $\pm$ 0.20	8.62 $\pm$ 0.03	-	-	-
Oxygen (%)	0.13 $\pm$ 0.001	0.15 $\pm$ 0.005	0.17 $\pm$ 0.015	0.17 $\pm$ 0.002	-	-	-

An important overall finding in this work is the consistent trend that a blend (GB<sub>12</sub>) can have a poorer flow performance than the individual powder constituents. In addition, it is suggested that powder reuse can have a deteriorating effect on powder properties. Further studies are planned to investigate blends of reused and virgin powder.

### **3.1.5 Conclusions**

The spherical morphology of G<sub>0</sub> powder was partially degraded by sintering and melting, followed by the blasting process during powder recovery. Multiple defects such as clip-clap, broken particles, shattered particles, deformed particles, elongated particles, agglomerates, and particles with molten specks are observed in G<sub>1</sub>, G<sub>2</sub> and GB<sub>12</sub> powder types. The PSD curves indicate that the distribution for G<sub>1</sub> and GB<sub>12</sub> has narrowed when compared to G<sub>0</sub>. The BFE, SE, TD, Hr, and C values indicated that the G<sub>0</sub> powder had better flowability and spreadability as compared to G<sub>1</sub>, G<sub>2</sub> and GB<sub>12</sub>, respectively. It is also suggested that reusing can lead to an increase in oxygen pickup and further deterioration of the powder.

## **3.2 Part II: Comprehensive study**

### **3.2.1 Preface**

A path to lowering the economic barrier associated with the high cost of metal additively manufactured components is to reduce the waste via powder reuse (powder cycled back into the process) and recycling (powder chemically, physically, or thermally processed to recover the original properties) strategies. In electron beam powder bed fusion, there is a possibility of reusing 95–98% of the powder that is not melted. However, there is a lack of systematic studies focusing on quantifying the variation of powder properties induced by number of reuse cycles. This work compares the influence of multiple reuse cycles, as well as powder blends created from reused powder, on various powder characteristics such as the morphology, size distribution, flow properties, packing properties, and chemical composition (oxygen and nitrogen content). It was found that there is an increase in measured response in powder size distribution, tapped density, Hausner ratio, Carr index, basic flow energy, specific energy, dynamic angle of repose, oxygen, and nitrogen content, while the bulk density remained largely unchanged. Figure 3.4 is a graphical abstract depicting the manufacturing process, results, and observations.

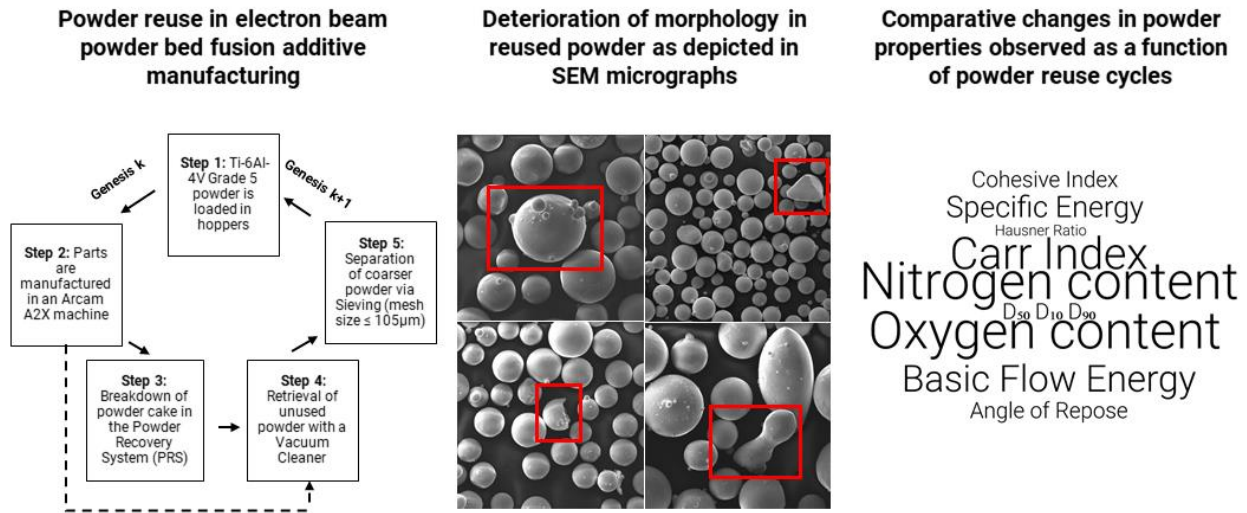


**Figure 3.4 Graphical abstract depicting the manufacturing process, results, and observations**

### 3.2.2 Introduction

The performance of a powder-based additively manufactured part highly relies on the quality of the powder feedstock properties. Vock et al. [102] stated that the correlation between bulk powder behavior, powder layer organization and final part quality is still not well understood. To improve the understanding of the powder-process-part relationship, there is a need to delve into quantifying the variability in powder properties, either as a function of print cycles, handling, or batch-to-batch variability and investigate their effects on the resulting part properties.

#### 3.2.2.1 Powder parameters of interest for electron beam powder bed fusion (EB-PBF) processes

When looking at powder feedstock for powder bed fusion (PBF) processes, Popov et al. [117] identified that some of the fundamental powder characteristics that need to be assessed include shape, particle size, composition, gas inclusions, flowability, tendency to oxidize and sintering/melting conditions.

Particle morphology has a considerable influence on the powder bed packing density, and consequently on the final component density, where the more irregular the particles, the lower the final density [201]. Higher apparent densities are preferred, as they provide better heat conduction, reducing the risk of sample swelling and overheating [36] in the EB-PBF process. In terms of powder morphology, spherical or regular equiaxed particles, are less cohesive and tend to flow freely, arrange and pack more efficiently than irregular or angular particles [195]. As shape deviates from spherical, the interparticle friction increases and

furthermore detrimentally affects the powder flowability and packing efficiency. Powder morphology can also affect the mechanical properties, microstructure, and surface finish of the final component. Consequently, Medina [202] emphasizes that powder morphology examination should be performed to identify particle shape, the presence of satellites, foreign particles, or contamination. Most powders for PBF processes are manufactured via atomization. Powders used in the EB-PBF process are typically manufactured via plasma atomization (PA). PA is the process of melting a wire spool feedstock of metal with a plasma torch and cooling it in an inert tower [203]. Powder particles manufactured by PA are usually spherical with minimal satellites and pores.

Particle Size Distribution (PSD) is a significant parameter in determining the minimum layer thickness, the minimum achievable feature size in final parts; and affects the powder-energy source interaction. The EB-PBF process uses a nominal PSD between 45  $\mu\text{m}$  to 105  $\mu\text{m}$ . Simchi [204] explained that a deviation in the PSD can lead to in-situ powder segregation and layer streaking due to coarser particles being pushed away from the powder bed. This could lead to variations in build quality.

The flowability of the powder is also highly important, to ensure uniform layers when dispensed, distributed, and/or spread onto the build area. It is generally understood that in order to obtain powder layers with homogeneous density, it is important to ensure that the powders are free-flowing and exhibit good flow properties. Powder flowability behavior can be correlated to the size, shape, moisture content, and packing efficiency of the powder particles [186]. For example, larger and spherical particles tend to flow better than smaller and irregular particles. The Angle of Repose (AOR) can be used to characterize the flowability of powders [102]. The AOR is affected by various cohesive forces: Van der Waals, electrostatic and capillary, as well as the contact forces between powder particles. Teferra [205] states that powders that show a low AOR are categorized as non-cohesive, highly flowable powders and can be transported using gravitational force or extremely little energy. Powders with high AOR values are characteristic of cohesive powders and may lead to sporadic or intermittent flow. Powder rheometry characterization provides a suite of in-depth powder performance metrics such as tap density, apparent density, dynamic flow testing, dynamic angle of repose, shear index, and cohesiveness.

Inert gas fusion analysis (i.e., LECO) provides quantitative data on the absolute oxygen and nitrogen content in the powders. This analysis is essential to understand whether the evolution of the oxygen and nitrogen content in the reused Ti-6Al-4V powder is within the allowable concentration limits defined by ASTM 2924-14 [196] ( i.e. < 0.20 wt.% for oxygen and < 0.05 wt.% for nitrogen).

It is of interest to quantify the effect of powder morphology, PSD, powder flowability, oxygen, and nitrogen content on the EB-PBF processes as a function of powder reuse.



### 3.2.2.2 Powder parameter studies in EB-PBF of Ti-6Al-4V

There has been an increasing interest in fabricating parts using EB-PBF. To continually improve the process, it is important to identify, address, and overcome some of the process limitations. Debroy et al. [183] have identified that the cost of a manufactured part, in PBF processes, is essentially contributed by the additive manufacturing equipment, feedstock material, manufacturing and indirect costs [206]. Specifically, when looking at the cost of 1 build via EB-PBF, Baumers et al. [207] have identified that the feedstock powder makes up to ~ 28% of the total cost of the build. Therefore, we can conclude that the cost of the EB-PBF process heavily relies on the reusability of powders and may not be cost-affordable for complex applications if the un-melted powder in the build bed is not reused. Thus, the evaluation of the maximum number of allowable powder reuse cycles is an essential factor to assess process affordability for a specific part or application. Reusing Ti-6Al-4V powder in EB-PBF can result in changes in the chemical composition, powder morphology, powder size distribution, and flowability, resulting in changes in the properties of the solidified material. material [208]–[210].

Powder morphology has been observed to be modified after reusing Ti-6Al-4V powders in EB-PBF. Tang et al. [197] observed that the particles became less spherical, had fractures, protrusions, and concave sites after reusing. They also observed an increase in surface roughness and distortions in the final part. Strondl et al. [195] observed irregularities, impact marks, satellites, and stacked particles in the recycled powder. Similar findings were reported by Mohammadhosseini et al. [82], where satellites and aggregation of particles in the reused powder were observed.

Some studies also reported flowability results for virgin and reused powders. Tang et al. [197] observed that the reused powder showed lower flowability when measured by Hall flowmeter and attributed this to the blasting process, which led to irregular particle morphology and impact marks on the particle surface. Contradictory to this, Mohammadhosseini et al. [82] observed no change in the flowability when measured by Hall flowmeter and Carney funnel after reuse.

Studies on the effect of reusing powder on chemical composition showed that reusing Ti-6Al-4V can lead to an increase in oxygen content. Sun et al. [211] observed that after 30 reuses, there was a 35% increase in oxygen content in the reused powder, from 0.15 wt. % in virgin powder to 0.20 wt.%. Petrovic and Niñerola [184] observed that the oxygen content exceeded the 0.20 wt.% limit after 12 reuse cycles, where the initial oxygen content in the virgin powder was 0.14 wt.%. They attributed this increase to the humidity pickup from the inner walls of the machine. Similarly, Tang et al. [197] observed that the oxygen content increased from 0.08 wt.% to 0.19 wt.% after 21 reuse cycles. They attributed this oxygen increase to exposure of powder to the air, including processing in the powder recovery system and sieving. An

increase in oxygen content typically results in an increase in the strength but lowers the toughness and ductility of the final part [208]. Furthermore, Leung et al. [212] observed that the oxides in an oxidized powder may enable pore formation (and subsequently stabilize the pores) during the manufacturing process. Therefore, the mechanical properties of the parts will be varying with the number of reuse cycles.

Based on these studies, a powder suitability criteria can be created for reused powders (see Table 3.2), for use in the EB-PBF process, to understand what type of powder performance metric behavior is suitable with respect to the morphology, size distribution, sphericity, basic flow energy, specific energy, density, Hausner ratio, Carr index, cohesive index, angle of repose, oxygen content, and nitrogen content.

EB-PBF machines store about 100 – 250 kg of powder (depending on the machine model) in the hoppers and it is often impossible to refill these hoppers with powder from the same reuse cycle. Hence blends of powders, either a mixture of virgin and reused or a mixture of different reuse cycles, are frequently used for manufacturing parts and such blend performances also need to be evaluated. These practices often pose challenges in isolating the effects of powder reuse in the above-mentioned studies. In addition, most published studies focus on assessing the effect of powder reuse on only a few specific powder performance metrics. Therefore, there is a need to assess the different powder characterization techniques and obtain the various powder performance metrics associated with these techniques. This needs to be done by precisely isolating the powder blends used in the build, as well as performing a comprehensive study on effects of powder reuse on powder properties. Thus, the current comprehensive manuscript aims at advancing the authors’ preliminary study [103], by assessing different powder characterization techniques and obtaining the various powder performance metrics associated with these techniques to identify the key performance features of reused powder and powder blends.

**Table 3.2 Powder suitability criteria for use in the EB-PBF process**

<b>Powder characteristic</b>	<b>Requirements</b>	<b>What other characteristics does this property have an influence on</b>	<b>Performance metrics that can help assess the powder property</b>	<b>Should this performance metric be maximized (↑), minimized (↓) or kept constant (↔)</b>
Morphology	Spherical and equiaxed to increase flowability and avoid interparticle friction	Powder bed packing density and the final component density, surface finish	Sphericity	↑

	and mechanical interlocking			
Apparent density	Should be high for improved heat conduction in the EB-PBF process	Heat conduction, Sample swelling and Overheating	$\rho_0$	↑
Compressibility	High compressibility is desirable to be able to achieve higher packing density in the powder bed	Powder bed packing density, layer thickness, heat conduction	Carr Index ( $C$ )	↓
Particle Size distribution (PSD)	Stay within the manufacturer's size range and not drastically increase in order to obtain small feature sizes and thinner powder layers	Minimum layer thickness, Minimum achievable feature size, build quality, surface finish	$D_{10}$ , $D_{50}$ and $D_{90}$ values	↔
Chemical composition	The oxygen and nitrogen concentration should stay within allowable concentration limits	Mechanical properties such as toughness, ductility of final parts, embrittlement	Oxygen (in wt.%) and nitrogen (in wt.%)	↓
Spreadability	A dynamic cohesive index closer to zero corresponds to a non-cohesive powder. A cohesive powder leads to a sporadic or intermittent flow while a non-cohesive powder leads to a regular flow	Powder bed packing density, powder layer uniformity, rake-ability, easy flow in the hoppers (i.e., powder storage). Decreased spreadability and flowability may contribute to more defects in the final part	Cohesive Index (CI)	↓
Flowability	Highly flowable powder minimizes the risk of mechanical interlocking and friction between particles and allows for smooth operation while raking and for uniform and homogenous distribution over the build plate		Hausner ratio ( $H_r$ )	↓
			Basic Flow energy (BFE)	↓
			Specific Energy (SE)	↓
			Angle of repose (AOR)	↓

### 3.2.3 Materials and Methods

The Grade 5 plasma-atomized powder (Batch number: P1321, Advanced Powders and Coatings, Montreal, Quebec, Canada) was obtained in its pre-alloyed form with a size range of 45  $\mu\text{m}$  to 105  $\mu\text{m}$ . The chemical composition of the powder conforms to ASTM F2924 for a Grade 5 Ti-6Al-4V powder (according to batch information provided by powder supplier). A total of seven powder types were assessed for this study. The powder obtained from the supplier is referred to as the virgin powder (henceforth known as Genesis 0 or  $G_0$ ). It should be noted that  $G_0$  powder did not undergo any processing in the EB-PBF machine, blasting in the powder recovery system and sieving to remove the fine powder particles. Therefore, this powder type may be considered an anomaly for the various powder characterization. Nevertheless, the results for  $G_0$  are presented in order to compare the results for all other powder types and use  $G_0$  as the baseline. Powder that was used once (Genesis 1 or  $G_1$ ), was passed through a vibrating sieve (mesh size -140+325, i.e., 44  $\mu\text{m}$  to 105  $\mu\text{m}$ ) to recover the powder for reuse. Genesis 2 ( $G_2$ ) and Genesis 3 ( $G_3$ ) powders were similarly obtained after printing parts with  $G_1$  and  $G_2$  powder, respectively. For every powder type, approximately 500 grams of powder was collected in a metal can. These cans were subsequently sealed and rolled/tumbled, on a jar-mill (Labmill 8000, Gardco, Pompano Beach, Florida, USA), at 40 revolutions per minute (RPM), for 24 hours in order to homogenize the sample before conducting any characterization.  $G_1$  and  $G_2$  powders were blended in equal wt.% to obtain the  $GB_{12}$  blend and compare its properties with the other powder types. Similarly,  $GB_{13}$  and  $GB_{23}$  blends were obtained based on equal wt.% of powder constituents. Table 3.3 summarizes the nomenclature and description of the various powder types investigated for the current study. The individual powder genesis were first collected in metal cans and rolled for 24 hours as mentioned earlier. These were then mixed in equal parts to create the respective blends. This blended powder was also collected in metal cans, sealed, and rolled for another 24 hours to ensure homogeneity and proper mixing in the blend. Therefore, the blended powders see a total rolling/tumbling time of 48 hours as compared to 24 hours for the unblended powders. All printing was done on an Arcam A2X machine using the default parameters provided for Ti-6Al-4V (Theme 5.2.52, Arcam A2X, GE Additive, Gothenburg, Sweden). To ensure that a consistent beam scanning strategy was used for all builds, the parts built were constant across the 3 printing cycles.

**Table 3.3 Nomenclature and description of the various powder types investigated for the current study**

Powder type	Description
$G_0$	Virgin powder
$G_1$	Powder that was used 1 time
$G_2$	Powder that was used 2 times
$G_3$	Powder that was used 3 times

GB <sub>12</sub>	50% G <sub>1</sub> + 50 % G <sub>2</sub>
GB <sub>13</sub>	50% G <sub>1</sub> + 50 % G <sub>3</sub>
GB <sub>23</sub>	50% G <sub>2</sub> + 50 % G <sub>3</sub>

In order to assess the powder particle morphology, field emission microscopy (SEM, Zeiss Ultra & Tescan VEGA3, Munich, Germany and Pittsburgh, Pennsylvania, USA, respectively) observations were performed. A Camsizer X2 (Retsch GmbH, Düsseldorf, Germany) was used to measure the PSD of the various powder types. 2 grams of powder was used for each test performed on the Camsizer. The system uses the principle of digital image processing [213], where the dispersed particles pass in front of LED light sources and their shadows are captured with two digital cameras. The Retsch software (Version 6.7, Retsch GmbH, Düsseldorf, Germany) analyzes the size of each particle captured by the camera and calculates the respective distribution curves.

Powder rheology was investigated using a powder rheometer (FT4, Freeman Technology, Gloucestershire, UK), rotating drum (Granudrum; Granutools, Liège, Belgium) and an automated tap density instrument (GranuPack; Granutools, Liège, Belgium). Performance metrics were collected, such as the basic flow energy (BFE), specific energy (SE), bulk density ( $\rho_0$ ), tap density after 500 taps ( $\rho_{500}$ ), Hausner ratio ( $H_r$ ), and Carr index ( $C$ ). To characterize the resistance to flow, eleven test cycles were run with a condition cycle run between each test. 25 grams of powder was used for each test performed on the FT4. During the tests, the precision blade was rotated downwards and upwards through the fixed volume of powder to establish a flow pattern, where the resistance of the powder to the blade yielded the bulk flow properties. The BFE is defined as the energy required to displace a powder when the blade is moving downward, and the powder is constrained. As described by Freeman and Fu [214], the SE measures the powder's flowability as the blade rotates upward and the powder is unconfined as there is no enclosure at the top of the vessel. The GranuPack measures the evolution of the powder density as a function of the tap number to obtain a compaction curve (as shown in Figure 3.5), which is used to calculate the  $H_r$  and  $C$  values. 35 grams of powder was used for each test performed on the GranuPack.  $H_r$  is a number that is correlated to the flowability of a powder and is calculated using the formula  $H_r = \rho_{500} / \rho_0$  where  $\rho_{500}$  is the tapped density of the powder after 500 taps and  $\rho_0$  is the initial bulk density of the powder.  $C$  is related to the compressibility of a powder and is calculated by the formula  $100 (\rho_{500} - \rho_0) / \rho_{500}$ , where  $\rho_0$  is the initial bulk density of the powder and  $\rho_{500}$  is the final tapped density of the powder after 500 taps.

The GranuDrum instrument (Granutools, Liège, Belgium) is used to determine the dynamic angle of repose and the cohesive index. The GranuDrum is composed of a horizontal drum half-filled with powder that rotates around its axis at an angular velocity ranging from 2 rpm to 60 rpm. 50 grams of powder was

used for each test performed on the GranuDrum. In total 17 velocities were tested, from 2 rpm to 20 rpm at increments of 2 rpm followed by 25 rpm to 60 rpm at increments of 5 rpm. To minimize internal sequence effects, a different velocity sequence was used for each replicate (3 replicates in total) such that the sequences for all replicates are minimally correlated. A camera takes snapshots for each angular velocity and the software calculates the flowing angle of powder (or AOR) and the cohesive index (CI) values.

Chemical analysis for the various powders were performed using inert gas fusion on a LECO TCH 600 (Leco Corporation, St. Joseph, Michigan, USA) instrument to analyze the oxygen and nitrogen content in the powders. 3 grams of powder was used for each test performed on the LECO TCH 600. All powder characterization experiments were performed in triplicate and the average values are reported in this manuscript.

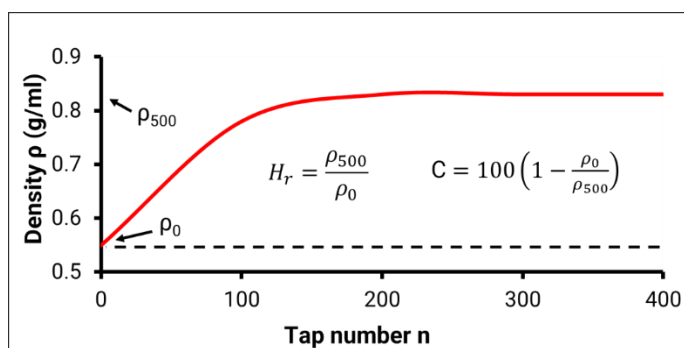


**Figure 3.5 Example of compaction curve obtained by GranuPack - illustrating bulk density ( $\rho_0$ ), tap density ( $\rho_{500}$ ), Hausner ratio ( $H_r$ ), and Carr index ( $C$ )**

### 3.2.4 Results and Discussion

As the number of reuse cycles increases, properties such as chemical composition, surface features (e.g., surface roughness and overall particle roundness), and physical and thermal properties are expected to change. Therefore, understanding the powder behavior with reuse is important for both cost and quality control.

#### 3.2.4.1 Observations of Changes in Powder Properties with Reuse Cycles

The powder is predominantly spherical in its as-received (or virgin) condition. Figure 3.6 presents the high magnification SEM micrographs for all different powder types. These micrographs help define and depict defects such as satellites (Figure 3.6(a)), elongated particles (Figure 3.6(c)), broken particles (Figure 3.6(g),(h),(i) and (k)), deformed particles (Figure 3.6(b) and (f)), particle with molten specks (Figure 3.6(d)), clip-clap (Figure 3.6(e)), shattered particles (Figure 3.6(l)), and agglomerates (Figure 3.6(j)). The

nomenclature and morphology of  $G_0$ ,  $G_1$ ,  $G_2$  and  $GB_{12}$  powder types has been previously described in [103], [188]. Other authors have also reported defects such as non-spherical particles and presence of agglomerates after reusing. Sun et al. [211] observed noticeable deformations and distortions on the surface of reused EB-PBF powder particles. Cordova et al. [215] observed that reused powder, in laser PBF processes, exhibits a deformation towards a teardrop shape and a rougher surface due to remelting.

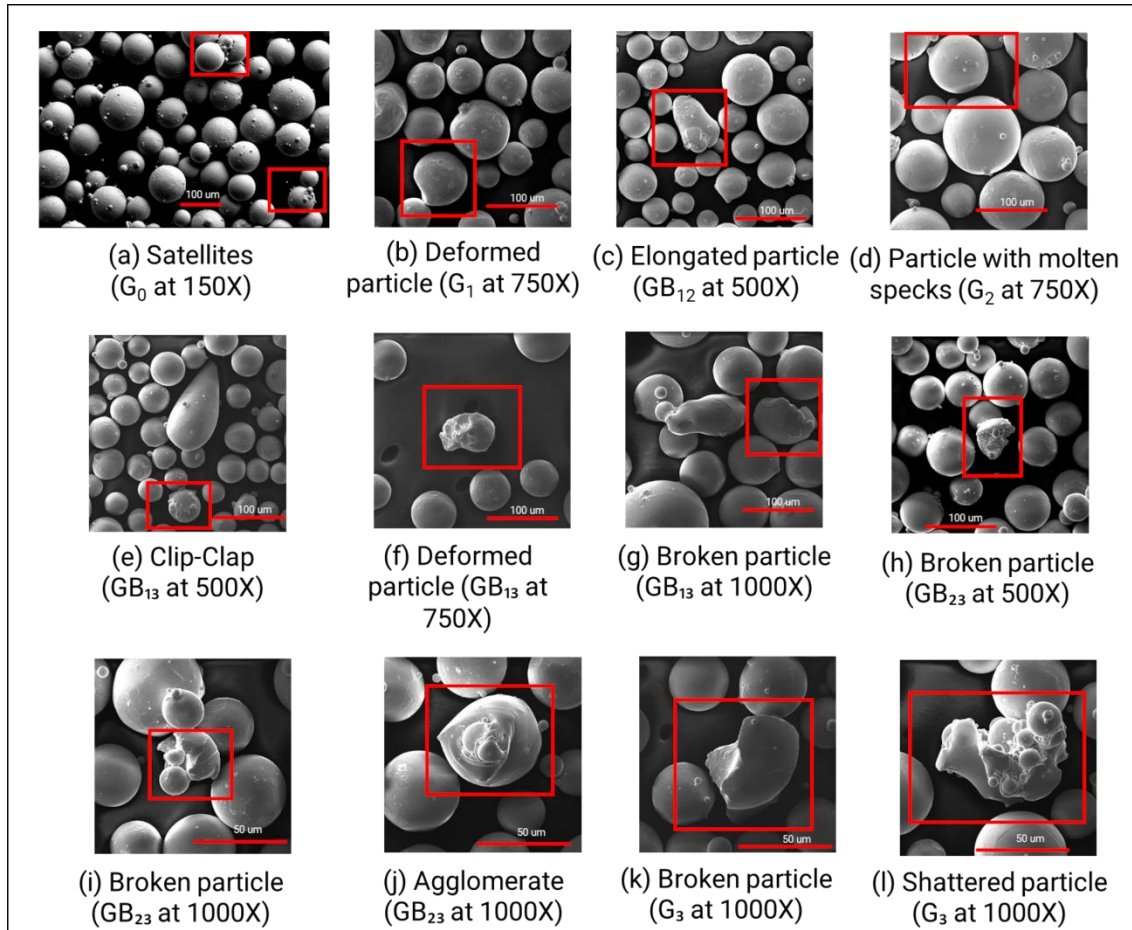


**Figure 3.6 SEM micrographs for all powder types depict (a) Satellites in  $G_0$  powder; (b), (f) Deformed particle in  $G_1$  and  $GB_{13}$  powders respectively; (c) Elongated particle in  $GB_{12}$  powder; (d) Particle with molten specks in  $G_2$ ; (e) Clip-Clap in  $GB_{13}$  powder; (g), (h), (i), (k) Broken particles in  $GB_{13}$ ,  $GB_{23}$  and  $G_3$  powders; (j) Agglomerate in  $GB_{23}$  powder, and (l) Shattered particle in  $G_3$  powder. Nomenclature used to describe these micrographs was first defined by Popov et al. [188]. A Zeiss Ultra SEM instrument was used to capture the image shown in (a); all other images were captured using the Tescan VEGA3 instrument.**

The deformed, broken, clip-clap and shattered particle defects are attributed to the recovery via the blasting procedure. The homogenization of powder via tumbling on a jar-mill, may result in numberless collisions between particles, and in friction and wear in presence of air and therefore the tumbling procedure may be another reason for these defects. The particles with molten specks and elongated particles are attributed to the temperature conditions that lead to overheating and smelting of the particles and satellites [188]. The agglomeration of powders is attributed to the high temperature of the process. Agglomerated particles result from the diffusion bonding obtained during preheating (to allow charge dissipation through the powder bed and reduce particle ejections resulting from the interaction of the electron beam during melting). The SEM micrographs (Figure 3.6) make it qualitatively evident that recovering and reusing the powder from the powder cake has changed the powder morphology significantly.

Figure 3.7 shows the  $D_{10}$ ,  $D_{50}$  and  $D_{90}$  values of the different powders investigated. The  $D_{50}$  (median value), is described as the diameter where half of the population lies below this value. Similarly, 90% and 10% of the distribution lies below the  $D_{90}$  and  $D_{10}$ , respectively. It is worth noting that the  $G_0$  powder has not undergone any processing in the EB-PBF machine, nor blasting or recovery through the sieve. This contributes to the discrepancies below  $44\ \mu\text{m}$  in the PSD of  $G_0$  when compared to the other powder types. As expected, the  $D_{10}$ ,  $D_{50}$ ,  $D_{90}$  values for  $GB_{12}$ ,  $GB_{13}$ , and  $GB_{23}$  lie between their respective genesis powders. This is because the authors ensured that the powder blends were made from equal wt.% of powder constituents and mixed thoroughly before characterization. The  $D_{10}$ ,  $D_{50}$ ,  $D_{90}$  values for the individual genesis powders (i.e.,  $G_1$ ,  $G_2$ ,  $G_3$ ) show an increasing trend (Figure 3.7). In other words, one can say that the  $D_{10}$ ,  $D_{50}$ ,  $D_{90}$  values increase with an increase in number of reuse cycles. Specifically, a 7%, 10%, and 7% increase was observed in the  $D_{10}$ ,  $D_{50}$ ,  $D_{90}$  values, respectively, for  $G_3$  powder when compared to the  $G_0$  powder.



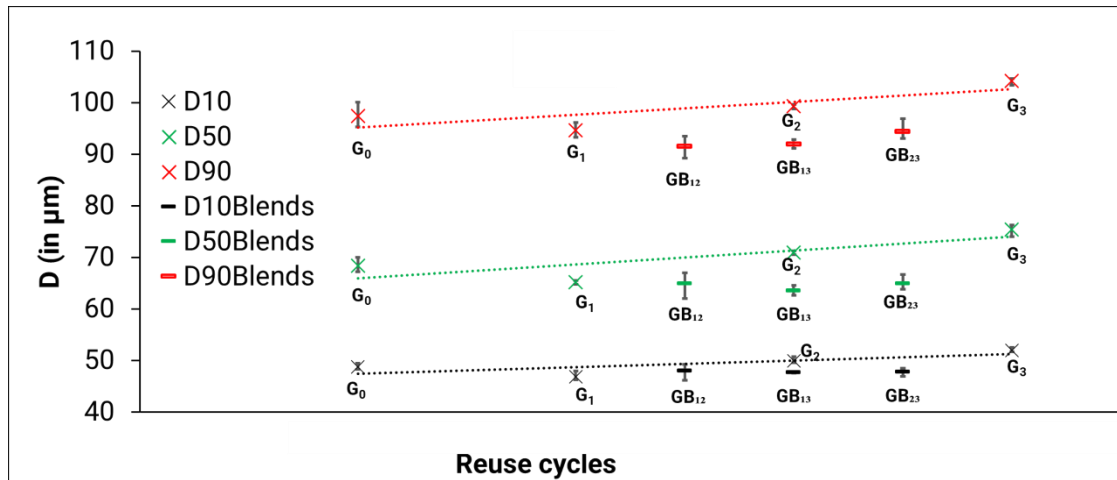


**Figure 3.7 D<sub>10</sub>, D<sub>50</sub> and D<sub>90</sub> values for all powder types. Error bars represent the standard deviation.**

Slotwinski et al. [193] also reported an increase in particle size with increasing number of reuse cycles in laser powder bed fusion (LPBF). They associated this observation to the consolidation and loss of the small particles. Grainger [216] also noticed a disappearance of smaller particles with an increase in number of powder reuse cycles in LPBF. Although the LPBF process does not use the same energy source, nor result in a powder cake after sintering, the powders are exposed to sputter and undergo a sieving process to recover the powders for reuse; similarities in trends with EB-PBF are observed in the present work.

The bulk density ( $\rho_0$ ) measured with the GranuPack instrument indicate that the values for the individual genesis powders and the powder blends do not significantly change with reuse (as seen in Figure 3.8(a)). Similar results were observed by Tang et al. [197] where the  $\rho_0$  remained unchanged after 21 reuse cycles. A powder with good flowability is usually characterized by a high  $\rho_0$  value. This is because free flowing particles (with minimum interparticle adhesion) would be able to find an optimum arrangement and pack densely, therefore corresponding to a higher  $\rho_0$  value. For such a powder, the possibility of a density increase during tapping is limited and therefore the ratio of tap density ( $\rho_{500}$ ) to  $\rho_0$  (also known as the Hausner ratio) would be close to unity.

The  $\rho_{500}$  values are presented in Figure 3.8(a). It is observed that the tap density increases with the number of reuse cycles. Specifically, a 3% increase was observed in the  $\rho_{500}$  value for G<sub>3</sub> powder when compared to the G<sub>0</sub> powder. For the most part, the tap density values for the powder blends lie between their respective genesis powders. The difference between the bulk and tapped densities is significant and increases with an increase in number of reuse cycles. Interparticulate interactions are usually larger for

poorly flowing powders and therefore a greater difference between the bulk and tapped densities is observed [215]. This suggests that the powder flowability is reduced when the number of reuse cycles increases.

The Carr index ( $C$ ) is the measure of the extent to which a powder can be compressed (without deforming the particles). The compressibility of the powder is expected to affect the continuity and uniformity of the powder layer, with lower  $C$  values in favor of the formation of denser layers. As mentioned earlier,  $H_r$  is an index that helps assess the flowability of the powder. According to Goyal et al. [200], for excellent compressibility and flowability, the  $C$  (%), and  $H_r$  should be lower than 10 % and 1.11, respectively. The  $H_r$  and  $C$  values measured in this study, are presented in Figure 3.8(b)). When looking at all powder types, a good correlation is observed between the  $H_r$  values and number of reuse cycles as well as Carr index and number of reuse cycles such that an increase in these metrics is observed with an increase in number of reuse cycles. For the most part, the  $H_r$  and  $C$  values for the powder blends lie between their respective genesis powders. All the values indicate that the flowability and compressibility is excellent (as defined by Goyal et al. [200]), however, the increasing trend suggests a degradation in the powder flowability characteristics. These plots strongly indicate that the powder has deteriorated from its virgin state. Specifically, a 3% and 30% increase was observed in the  $H_r$  and  $C$  values, respectively, for  $G_3$  powder when compared to the  $G_0$  powder. This observation is also supported by the general increase of PSD and changes in powder morphology observed as a function of increased reuse cycles.

This degradation of flow properties of the powder blends, as well as the reused individual genesis powders is attributed to the deviation in the powder morphology as observed in the SEM micrographs (Figure 3.6). Such deviations from the spherical morphology are expected to not only decrease flowability but may also lead to uneven layer formation during raking and ultimately may result in powder bed non-uniformity across the build bed as mentioned in Table 3.2. On the other hand, the virgin (or  $G_0$ ) powder is observed to be more spherical and therefore flows easily due to lower surface friction and mechanical interlocking, thus displaying a lower value for  $H_r$  and  $C$  metrics. The packing ability of powder particles influences the sintering of the powder layer [41]. As Neira-Arce [55] describes, uniform and homogeneous layers are crucial to ensure that there is proper heat conduction and for achieving dimensional accuracy, which in turn reduces the risk of swelling or overheating in EB-PBF parts.

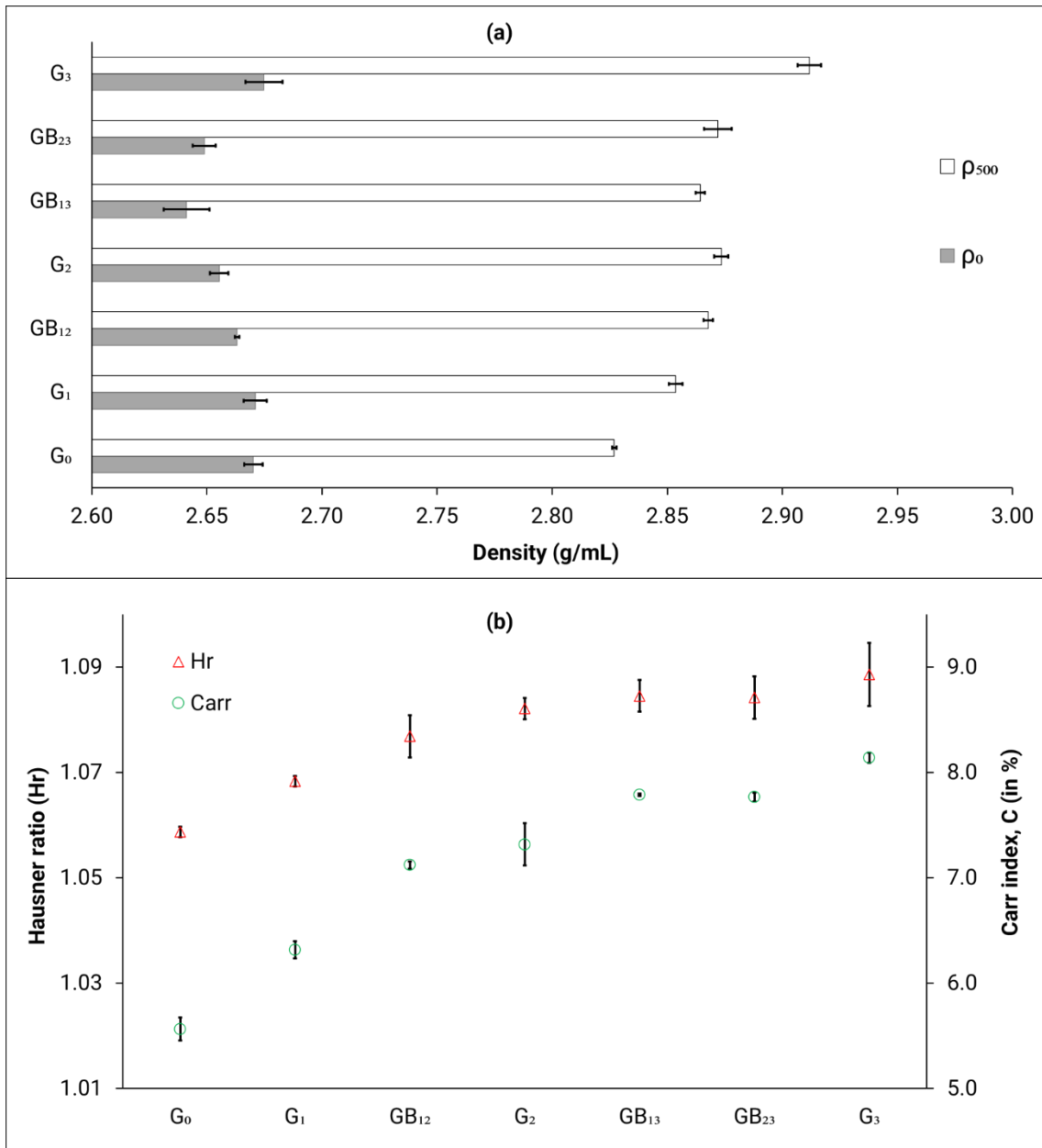


**Figure 3.8 (a)  $\rho_0$  and  $\rho_{500}$  values (b) Hr and C values; for all powder types. Error bars represent the standard deviation.**

The BFE and SE (Figure 3.9(b)) values for the reused powders and blends have also increased with an increase in number of reuse cycles. Specifically, an 18% and 15%, increase was observed in the BFE and SE values, respectively, for G<sub>3</sub> powder when compared to the G<sub>0</sub> powder. The effect of larger BFE and smaller bulk density of the powder blends might result in a more uneven layer distribution. When looking

at the individual genesis powders (Figure 3.9(b)), it can be concluded that both BFE and SE show an increase in values with an increase in number of reuse cycles, with  $G_3$  being an exception. Similarly, there is a good correlation between BFE and SE (Figure 3.9(a)), for all powder types, where an increase in BFE leads to an increase in the SE values.

Strondl et al. [195] observed similar results in EB-PBF powders where the BFE and SE values increased after reusing. Clayton et al. [194] also compared the BFE results for virgin and reused powders and concluded that processing significantly increases the BFE values for reused powders.

Both BFE and SE results suggest that the reused powders and blends would not flow as freely as  $G_0$ . The energy to move the blade in the rheometer is increasing for the reused powders and blends mainly due to their deviation from an overall spherical shape (affected by the pre-heating, blasting and sieving procedures) which causes greater interparticle interactions during testing of the powder samples in the FT4 instrument. As explained by Clayton et al. [194], a higher SE indicates increased mechanical interlocking and friction between particles that may potentially lead to flow problems. An interesting observation is that the BFE and SE values for the  $G_3$  powder is lower than the  $G_2$  powder. The reason behind this behavior is not well understood and therefore this powder type needs to be studied more extensively. The authors also speculate that the blends have a much higher concentration of non-spherical particles when compared to their respective genesis powders. This may be due to the fact that these powders were exposed to rolling/tumbling over a cumulative time of 48 hours. This tumbling procedure may have caused increased physical deformation to the blended powders when compared to the individual genesis powders.

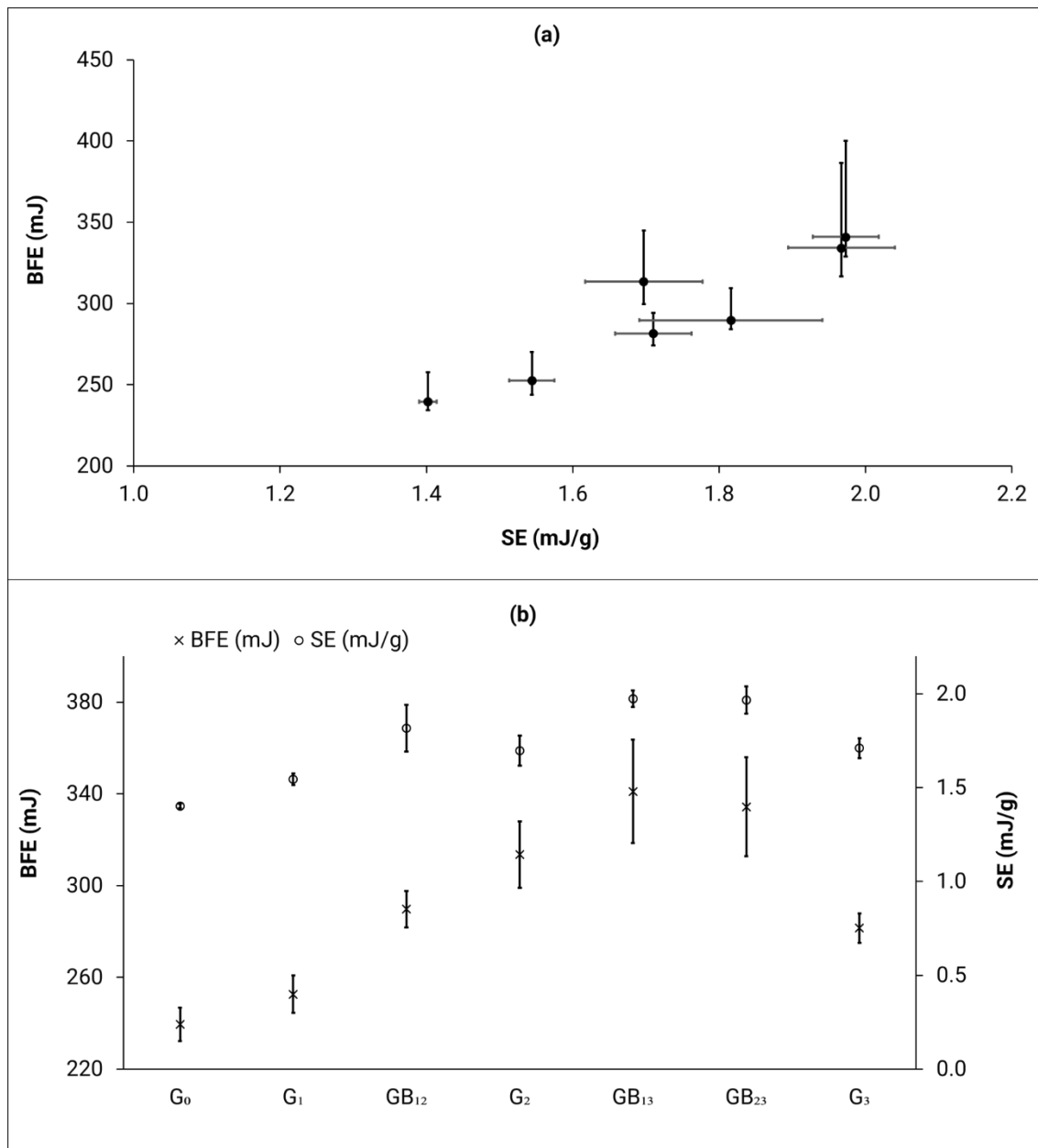


**Figure 3.9 (a) BFE vs. SE (b) BFE and SE values, for all powder types. Error bars represent the standard deviation.**

Figure 3.10(a) presents a plot of the dynamic angle of repose vs. rotating drum speed for all powder types. It is observed that below 25 rpm, it is difficult to make a differentiation between the various powders and all powder have excellent flowability at 2 rpm. Above 25 rpm, the AOR decreases with an increase in number of reuse cycles. As an example, from Figure 3.10(c), it can be observed that at the highest speed

(i.e., 60 rpm), the AOR decreases from  $G_1$  to  $G_3$ . It should be noted that  $G_0$  stands out, probably because this powder has not undergone any processing in the machine (pre-heating, blasting, sieving).

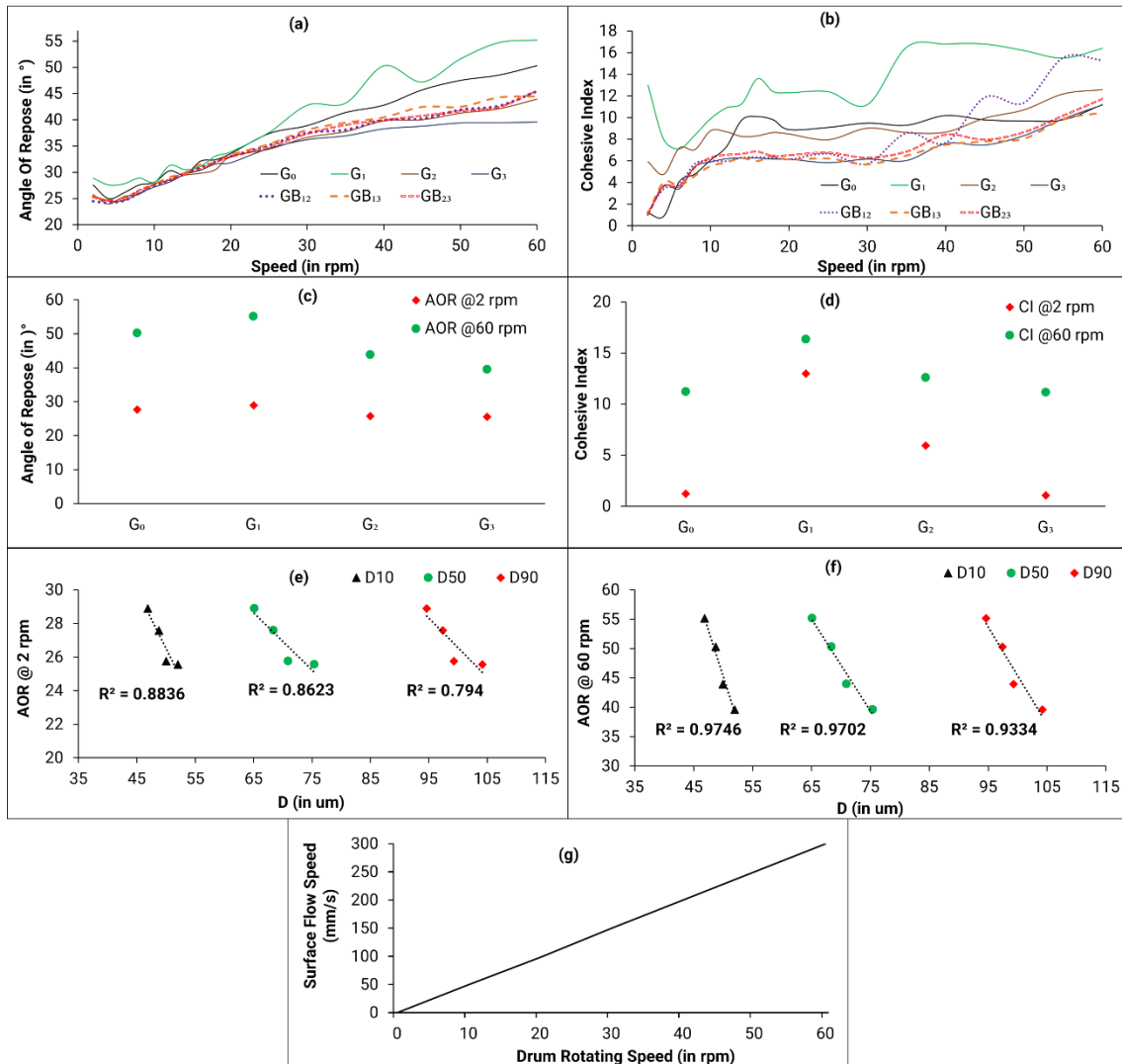
The AOR values at the lowest and highest drum rotation speed (i.e., 2 rpm and 60 rpm, respectively) were correlated with the particle size  $D_{10}$ ,  $D_{50}$  and  $D_{90}$  values. As can be seen from Figure 3.10(e) and (f), an excellent correlation is observed where an increase in particle size leads to a decrease in the AOR value. It is recognised that larger particles tend to flow more easily than finer powder. It has been observed that the  $D_{10}$ ,  $D_{50}$  and  $D_{90}$  values increase with an increase in number of reuse cycles. Therefore, this increase in particle size is leading to a better flow in the rotating drum, thus suggesting that the flowability of the reused powders is better in this instrument.

Figure 3.10(b) presents the Cohesive Index (CI) at various drum rotation speeds for all powder types. The CI metric is linked to the fluctuations of the interface between the powder and air. The dynamic cohesive index of a powder depends on the magnitude of the cohesive forces between the particles. Therefore, a value closer to zero corresponds to a non-cohesive powder. Per the flow guidelines provided in the GranuDrum instrument software (Version 4.07, Granutools, Liège, Belgium), threshold values for cohesive index are: < 5 very good, 5-10 good, 10-20 fair, 20-30 passable, 30-40 poor, > 40 very poor. The CI follows the same trend (as observed in Figure 3.10(b) and (d)) as the AOR curves, where an increase in number of reuse cycles lead to a decrease in the CI value (except  $G_0$ ).

The GranuDrum data interpretation guide mentions that the flowability of a powder is measured as a function of the shearing rates, and therefore rheological properties like shear thinning or shear thickening could be evaluated with this instrument. If the powder AOR and CI increase with an increase in drum speed, the powder is said to show a shear-thickening behavior. All powders in this study show a shear-thickening behavior (Figure 3.10(a) and (b)). A powder material that shows a constant shear-thickening behavior is known to be a poor candidate for a dynamic process. That being said, there are portions in the CI vs. drum rotation speed curve (Figure 3.10(b)) where a somewhat constant cohesive index can be observed between speeds of 15 rpm and 40 rpm. The GranuDrum instrument (Granutools, Liège, Belgium) helps identify an optimum raking/re-coating speed. The relationship between the drum rotating speed and surface flow speed (i.e., raking speed in mm/s) is displayed in Figure 3.10(g). It has been mentioned by the machine manufacturer [217], [218], that when selecting raking speeds, one should look at areas that display a constant cohesive index.

As mentioned earlier, drum rotating speeds between 15 rpm and 40 rpm (corresponding to 75 mm/s and 175 mm/s respectively, according to Figure 3.10(g)) show a constant cohesive index. Therefore, raking speeds between 75 mm/s and 175 mm/s should be considered when using powders for EB-PBF processes.

The effect of powder reuse on interparticle cohesion is contrary to the measurements done with FT4 instrument (higher BFE and SE with reuse). It is not clear at the moment whether the increase of the PSD with reuse is only associated with the agglomeration, the sieving, or a combination of both. Difference in flow regime and the sensitivity of the flowability to multiple powder modifications may explain the discrepancy in these results.



**Figure 3.10** (a) AOR vs. speed of drum rotation for all powder types; (b) CI vs. speed of drum rotation for all powder types; (c) AOR at 2 and 60 rpm vs. number of reuse cycles; (d) CI at 2 and 60 rpm vs. number of reuse cycles; (e) AOR at 2 rpm vs. particle size (D values) for individual genesis powder types; (f) AOR at 60 rpm vs. particle size (D values) for individual genesis powder types; (g) relationship between drum rotating speed and surface flow speed (Redrawn from [217]). Note that G<sub>0</sub> powder is considered an anomaly due to the fact that it has not undergone any processing, blasting, or sieving procedure.

As mentioned by Brika et al. [209], powder flowability is not an inherent material property and is the ability of the powder to flow in a desired manner in a particular instrument. A powder may perform well in a certain instrument/piece of equipment while may perform poorly in another. Thus, additional tests are required to better understand which regime better represents the behavior of the powder in an additive manufacturing (AM) machine.

Figure 3.11(a) and (b) show that the average values for oxygen and nitrogen concentration increases with number of reuse cycles. Specifically, a 37% and 44% increase was observed in the oxygen and nitrogen concentration, respectively, for  $G_3$  powder when compared to the  $G_0$  powder. However, the oxygen concentration remains lower than 0.18 wt.% and below the limit outlined by ASTM F2924-14 [196]. A logarithmic trendline seems to better fit the results when compared to the linear trendline (Figure 3.11(a)). From the logarithmic trendline, it can be deduced that the  $O_2$  concentration will exceed the 0.2 wt.% limit by 5-6 reuse cycles. The nitrogen concentration remains between 0.016 wt.% and 0.023 wt.% (Figure 3.11(b)) which is well below the 0.05 wt.% limit outlined by ASTM 2924-14 [196]. Increase of nitrogen concentration with the number of reuse cycles is observed; the logarithmic trend line suggest that this nitrogen pick-up may reach a saturation level, suggesting that this is a surface contamination (formation of nitride or local concentration at the surface). The trend suggests that the maximum (i.e., 0.05 wt.%) will not be reached before a large number of reuse cycles.

Some other studies have also looked at the increase in oxygen and nitrogen content with increase in number of reuse cycles. Ghods et al. [198] showed that the oxygen content was > 0.20 wt.% after 11 reuse cycles. Grainger [216] observed a linear increase in oxygen and nitrogen concentrations in Grade 23 Ti-6Al-4V powder after reusing in the laser PBF process. However, after 30 builds, the oxygen concentration remained below 0.20 wt.%. These values are attributed to the fact that the starting oxygen concentration in Grade 23 Ti-6Al-4V is much lower than that of Grade 5 Ti-6Al-4V. Nandwana et al. [16] observed an increase in the oxygen concentration from 0.13 wt.% to 0.18 wt.%, however their nitrogen concentration remained the same over 5 reuse cycles for a Ti-6Al-4V powder.

There are numerous factors which contribute to oxygen pickup in Ti-6Al-4V powders processed through EB-PBF. One of the possible reasons for the increase of oxygen pickup is the fact that the powder is exposed to the ambient atmosphere and moisture when transferred from the machine to the PRS for part recovery, and then transferred from the PRS to the sieve. A study performed by Vluttert [219] shows that Ti-6Al-4V can pick up about 0.2 wt. % moisture (relative to dry weight) when left in an environment that was set to 25 °C and 90% humidity. Therefore, the presence of water vapor in the air may have a reasonable impact on oxygen pickup. Montelione et al. [220] compare the EB-PBF process to gas tungsten arc welding



and suggest that when the powder is exposed to air, the water molecules adsorbed on the particle surface may dissociate during heating, allowing the oxygen to diffuse in the metal alloy. In addition, the deformation caused by blasting and sieving can also lead to an acceleration of the oxidation due to creation of new oxidation prone surfaces. Shvab et al. [221] describe that this will lead to a passive oxide layer formation that may diffuse inward and reform during heating cycles. This oxide layer may also translate into the melt pool upon melting, and cause instabilities that form balling defects, thus hindering part consolidation [222]. Furthermore, oxygen pickup can also occur if the machine is not under vacuum, when the powder is stored in the hoppers, in between the builds. Finally, the major source of oxygen pickup is the reaction of titanium at high temperature with residual oxygen in the atmosphere of the machine. In addition, Mizuno et al. [223] noted that all oxides in titanium alloys dissolve above 400 °C and the oxygen diffuses into the bulk through the bulk diffusion process.

The EB-PBF process takes place at a relatively high temperature where the titanium can react with residual oxygen. Moreover, the high temperature can also result in oxygen diffusion as described by Attalla et al. [224] (build chamber  $\approx 10^{-4}$  mbar and electron beam column  $\approx 10^{-7}$  mbar). The oxygen and nitrogen can dissolve interstitially into the titanium lattice during solidification of the melt pool, and form oxides and nitrides [198]. Such oxides and nitrides are known to be detrimental to the fatigue performance of manufactured parts [225]. As stated by Donachie [86], an increase in the oxygen and nitrogen content in solution can lead to an increase in the strength and decrease in the ductility which further leads to embrittlement.

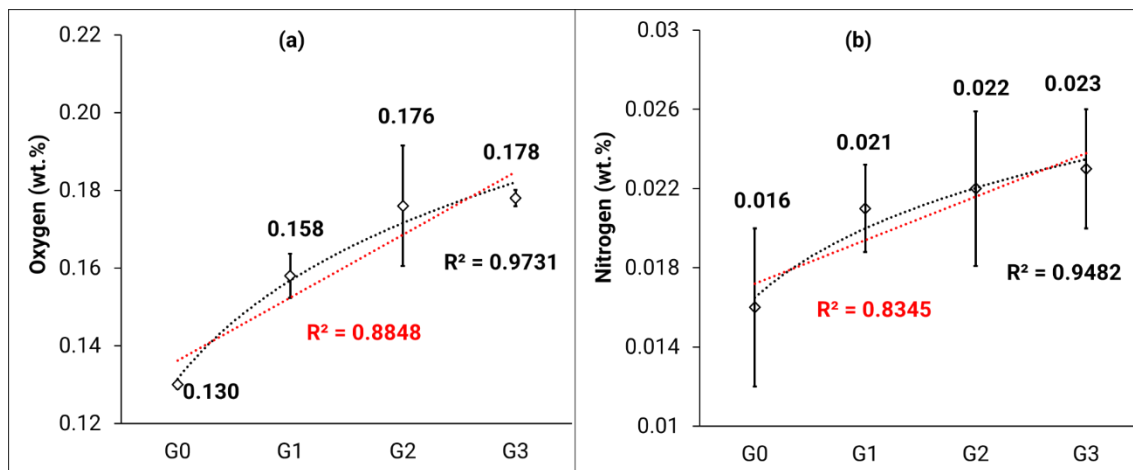


**Figure 3.11 (a) Oxygen and (b) Nitrogen concentration for G<sub>0</sub>, G<sub>1</sub>, G<sub>2</sub>, and G<sub>3</sub> powder types along with linear (in red) and logarithmic (in black) trendlines. Error bars represent the standard deviation.**

### 3.2.4.2 Evaluation of the relative performance of powders

It is quite challenging to deploy a unified metric to capture the absolute suitability of powders for PBF AM processes. The powder metrics measured are very different in nature and may impact the PBF process and final part properties in different ways. For instance, powder metrics variations may have opposite effects, i.e., some characteristics may lead to an improved behavior in the AM process, others may lead to a deterioration of the AM process behavior, while some powder metrics may have limited effect. In the context of the current study, process behavior means raking in the system, flowability in the powder hoppers, spreadability of the powder on the build plate, etc. In literature, this is poorly understood at the moment. Variability is still relatively high for some of the powder measurement techniques, and are influenced by the testing equipment type, the testing conditions, the powder storage and handling conditions, the operator skill, the calibration of instruments, and many other factors. Care must be exercised in interpreting each powder metric result individually. Although it is challenging to capture the absolute suitability of powders for PBF AM processes via a consolidated index, there is a potential to describe the relative change in powder properties with respect to a reference state, if such reference should exist. A reference state, for instance, is often considered to be the virgin powder. Two examples of calculations of relative changes from a reference state are presented below.

#### 3.2.4.2.1 Relative Performance Evaluated via Radar Diagrams

To understand the sensitivity of response to change of the various powder characteristics, from a reference powder ( $G_0$  in this work), the various properties measured were normalized to a range of 0 to 1 and a radar diagram of the normalized indices for the  $G_0$ ,  $G_1$ ,  $G_2$ , and  $G_3$  powders was plotted in Figure 3.12. The normalization was done to transform the data into a dimensionless data sequence for ease of comparability. For this study, the approach used for normalizing all metrics was taken from Mehat et al. [226]:

$$x_i^*(k) = \frac{x_i^{(0)}(k) - \min x_i^{(0)}(k)}{\max x_i^{(0)}(k) - \min x_i^{(0)}(k)} \quad \text{Equation 3.1}$$

where  $x_i^{(0)}(k)$  is the measurement of the quality characteristic,  $\max x_i^{(0)}(k)$  is the largest value of  $x_i^{(0)}(k)$ , and  $\min x_i^{(0)}(k)$  is the smallest value of  $x_i^{(0)}(k)$ .

In accordance with the powder suitability criteria created in Table 3.2, the smaller the area covered by the radar diagram, the higher the powder suitability for the EB-PBF process. It is observed that the  $G_0$

powder has the smallest area, followed by G<sub>1</sub>, G<sub>2</sub> and G<sub>3</sub>, indicating that the powder is becoming less-suitable with increasing number of reuse cycles.

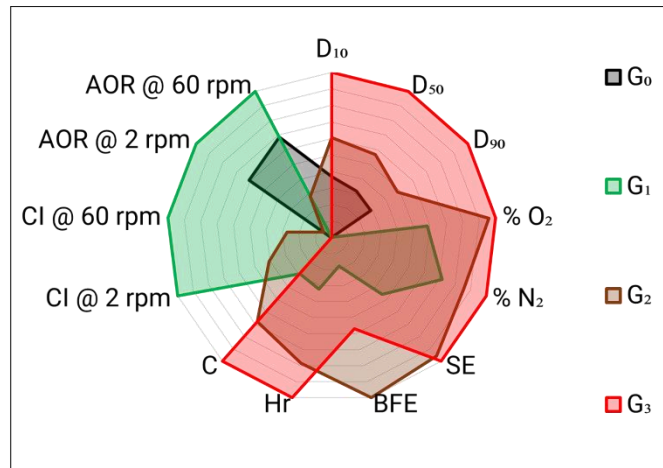


**Figure 3.12 Radar diagram comparing the performance of G<sub>0</sub>, G<sub>1</sub>, G<sub>2</sub>, and G<sub>3</sub> powders w.r.t the D values, SE, BFE, Nitrogen (in wt.%), Oxygen (in wt.%), Hr, C, CI, and AOR**

In this study the authors evaluate the reused powders through various performance metrics such as morphology, size distribution, basic flow energy, specific energy, bulk density, tap density, Hausner ratio, Carr index, cohesive index, angle of repose, oxygen content, and nitrogen content. Each metric contributes additional knowledge and information regarding the powders, as per Table 3.2. However, performing all of these tests can be very time consuming and expensive. Furthermore, acquiring results for all these metrics may not necessarily be relevant to a specific user or application. Therefore, it is up to the user to determine which tests are relevant for their own work based on the information that is provided for each characterization technique (Table 3.2 may be used for this purpose). For example, a user looking at manufacturing parts for aerospace applications will need to adhere by ASTM F2924-14 and therefore this user must evaluate the % O<sub>2</sub> and % N<sub>2</sub>. Conversely, if a user is looking at manufacturing medical models solely for the purpose of education and training, then they may require good dimensional accuracy and surface finish for their model. Therefore, they must evaluate the particle size distribution (D values) and flowability metrics (e.g., BFE and SE) as these affect the layer homogeneity, proper spreading upon raking, minimum feature size, surface finish as described in Table 3.2.

#### 3.2.4.2.2 Relative Performance Evaluated via Performance Index

Efforts in assessing powder suitability for powder bed fusion were undertaken by Brika et al. [209]; they differentiated powders and assessed three powder types by calculating a figure of merit called AMS

(Additive Manufacturing Suitability). While in this present study, the authors are not assessing an absolute suitability criteria due to challenges aforementioned, this approach is deployed herein to assess if this index can be used to quantify the relative changes in powder properties with respect to a reference state ( $G_0$  in this work). Since the current study focuses on EB-PBF powder suitability, the index will be referred as “ESF” (Electron-beam powder bed fusion Suitability Factor) and is inspired from Brika et al. [209]. As such, for each powder reuse cycle, a cumulative sum of the normalized index presented in Figure 3.12 will provide an objective function:

$$ESF = \frac{(D_{10} + D_{50} + D_{90} + O_2 + N_2 + SE + BFE + H_r + C + CI @ 2 \text{ rpm} + CI @ 60 \text{ rpm} + AOR @ 2 \text{ rpm} + AOR @ 60 \text{ rpm})}{13} \quad \text{Equation 3.2}$$

The ESF values for  $G_0$ ,  $G_1$ ,  $G_2$ , and  $G_3$  powders are 0.176, 0.504, 0.609, and 0.659, respectively. It is assumed that the lower deviation from the ESF value with respect to  $G_0$ , the more the properties of the powder will depart from the reference state. This is another example of efforts towards expressing the relative change in powder characteristics.

As a conclusion, this study looked into comparing the influence of multiple reuse cycles, as well as powder blends created from reused powder, through various performance metrics such as morphology, size distribution, basic flow energy, specific energy, bulk density and tap density after 500 taps, Hausner ratio and Carr index, cohesive index, angle of repose, oxygen content, and nitrogen content. In accordance with the authors’ hypotheses established in Shanbhag and Vlasea [103], it was observed that reusing modifies the powder significantly when assessing the various performance metrics. While parts were printed during this study, no significant differences were observed during the different build cycles or general appearance of the printed components. The evaluation of the reuse of the powder on the microstructure and properties of the parts was beyond the scope of this study. Future research efforts will rely on this present study and will look into assessing the microstructure and mechanical properties of the parts to be able to understand the impact of reusing powders on part performance.

### 3.2.5 Conclusions

Investigation into the effect of plasma-atomized Grade 5 Ti-6Al-4V powder reuse on the powder properties as well as properties of powder blends led to the following conclusions:

- (1) The SEM micrographs of the various powder types show extensive physical modification to the surface of the particles, with increasing degree of powder reuse. The micrographs depict features such as elongated particles, broken particles, clip-clap, deformed particles, particle with molten specks and

agglomerates. The broke, shattered, clip-clap and deformed particles are attributed to the powder recovery process (i.e., blasting, sieving) and tumbling process; and the particles with molten specks, elongated particles and agglomerated particles are attributed to the high temperature conditions leading to overheating and smelting of particles and satellites.

- (2) The  $D_{10}$ ,  $D_{50}$  and  $D_{90}$  values increase with increasing degree of powder reuse. Specifically, a 7%, 10%, and 7% increase was observed in the  $D_{10}$ ,  $D_{50}$ ,  $D_{90}$  values, respectively, for  $G_3$  powder when compared to the  $G_0$  powder. This observation is attributed to the agglomeration of powder particles.
- (3) The  $\rho_0$  remained unchanged for all powders; however, the  $\rho_{500}$  increases with increasing degree of powder reuse. Specifically, a 3% increase was observed in the  $\rho_{500}$  value for  $G_3$  powder when compared to the  $G_0$  powder. The  $H_r$  and  $C$  values show an increase with an increase in number of reuse cycles. Specifically, a 3% and 30% increase was observed in the  $H_r$  and  $C$  values, respectively, for  $G_3$  powder when compared to the  $G_0$  powder. This trend indicates modification of reused powders from their virgin state. These observations have been attributed to the deviations from spherical morphology, for the reused powder, as observed in the SEM micrographs. Due to these deviations, uneven raking and non-homogenous layers may be obtained.
- (4) The BFE and SE values measured using powder rheology increase with increasing degree of powder reuse. This suggests that the reused powder is more cohesive than the virgin powder. Specifically, an 18% and 15%, increase was observed in the BFE and SE values, respectively, for  $G_3$  powder when compared to the  $G_0$  powder. This behavior is attributed to the mechanical interlocking and friction between particles (caused by the non-spherical morphology).
- (5) The dynamic AOR and CI values decrease with an increase in number of reuse cycles. This behavior is attributed to the agglomeration and increase of the  $D_{10}$ ,  $D_{50}$  and  $D_{90}$  with the number of reused cycles. The variations of the metrics with drum rotating speed may help identify a range of optimum raking speeds that can be used for these powders when being used in the EB-PBF machine.
- (6) The  $O_2$  and  $N_2$  concentration remain below the limits outlined by ASTM F2924. However, a gradual increase has been observed with increasing degree of powder reuse. Specifically, a 37% and 44% increase was observed in the  $O_2$  and  $N_2$  concentration, respectively, for  $G_3$  powder when compared to the  $G_0$  powder. From the logarithmic trendline, it can be deduced that the  $O_2$  concentration will exceed the 0.2 wt.% limit by 5-6 reuse cycles.
- (7) A unified powder quality score or powder quality metric was established to compare the effect of powder reuse on the various powder performance metrics.

## **Chapter 4**

### **Effect of specimen geometry and orientation on tensile properties of Ti-6Al-4V manufactured by electron beam powder bed fusion**

This chapter is considered for publication as follows:

Section 4.1 to Section 4.5.4:

Shanbhag G, Wheat E, Moylan S, Vlasea M. “Effect of specimen geometry and orientation on tensile properties of Ti-6Al-4V manufactured by electron beam powder bed fusion.” *Journal of Additive Manufacturing. (Under Review)*

Section 4.6:

Shanbhag G, Wheat E, Moylan S, Vlasea M. “Data related to the Effect of specimen geometry and orientation on tensile properties of Ti-6Al-4V manufactured by electron beam powder bed fusion.” *Journal of Data in Brief. (Under Review)*

## 4.1 Preface

Tensile testing is often proposed as the preferred methodology to qualify builds and materials produced through additive manufacturing. While there is already work demonstrating the difference in measured properties between tensile specimens produced in different build orientations, this does not extend to different specimen geometries. In addition, the body of knowledge in this domain is typically made up of studies that utilize custom combinations of specimen geometries, part finishing, and post-processing, making it challenging to compare results. To study the impact of geometry of tensile specimens on tensile testing results, a selection of standard specimen types provided in ASTM E8/E8M was prepared in Ti-6Al-4V using an electron beam powder-bed fusion additive manufacturing machine. These specimens were characterized to observe any porosity defects, dimensional deviations, and surface topography that could impact performance. It was found that changes in specimen geometry, specimen size, build orientation, and the internal porous defects; have significant effects on the tensile properties of the specimens. The horizontally built specimens had higher yield and tensile strengths, but lower elongation compared to vertically built specimens. With an increase in cross-sectional area, an increase in the yield, tensile strength, and elastic modulus was observed. With an increase in surface area to volume ratio, there was a decrease in the yield and tensile strength. The average solid fraction of the specimens had no influence on any measured tensile properties. Furthermore, with an increase in maximum pore size, the elongation of the specimen decreased. Figure 4.1 is a graphical abstract depicting the manufacturing process, results, and observations.

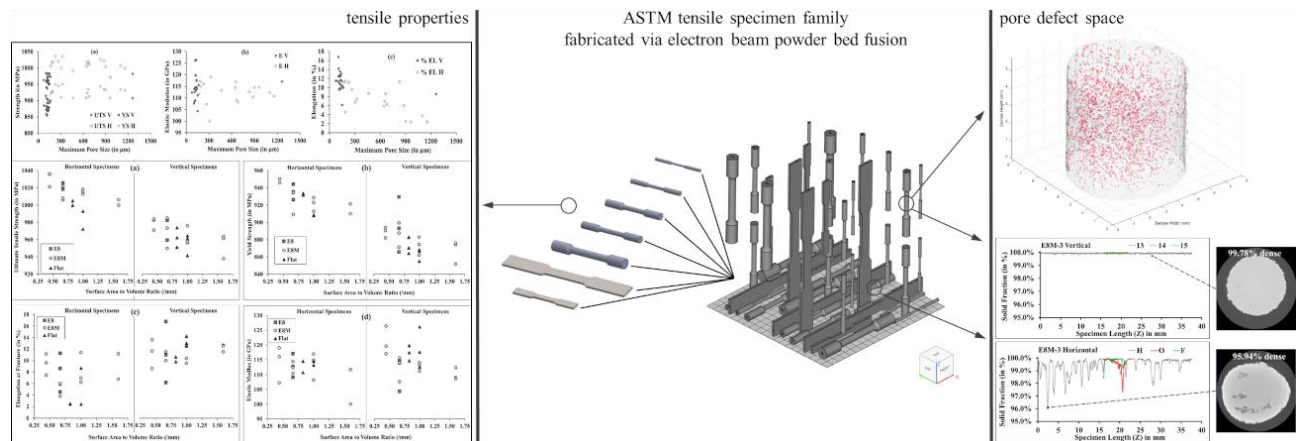


Figure 4.1 Graphical abstract depicting the manufacturing process, results, and observations

## 4.2 Introduction

Electron beam powder bed fusion (EB-PBF) additive manufacturing (AM) is a process that uses a high-energy electron beam to selectively melt a conductive metal powder bed at an elevated temperature ( $\approx 750$  °C) in a vacuum [33]. This process is capable of producing fully dense and near-net-shape complex parts with superior mechanical properties, when compared to other powder bed fusion processes [41]. The elevated temperature inside the machine helps to minimize thermally-induced residual stresses and non-equilibrium microstructures [227]. The powder is first preheated to reduce the possibility of oxygen pickup and to lower the moisture content. Preheating also evens out the temperature gradient between consecutive layers and therefore helps reduce residual stress buildup. The preheating step is followed by the melting step. Lastly, the parts are cooled from  $\approx 750$  °C to room temperature once the build is completed. A detailed description of the process can be found elsewhere [11], [40]–[43]. EB-PBF is used in emerging industrial applications [20], [22], [23], as well as commercial manufacturing of implants and medical devices [24]–[32]. The most common alloy deployed in EB-PBF for the biomedical sector is Ti-6Al-4V, also referred to as Ti64.

Ti-6Al-4V (an  $\alpha+\beta$  alloy) is one of the most prevalent titanium alloys presently utilized in metal AM. At room temperature, the  $\alpha$ -phase dominates, and when heated to above the  $\beta$  transus [75], [76], it exists as a single  $\beta$  phase [77]. The presence of aluminum increases the strength and the presence of vanadium improves the room temperature ductility of the alloy [75]. Ti-6Al-4V exhibits a high strength-to-weight ratio, excellent corrosion resistance, wear resistance, and biocompatibility [78]–[84]. Due to these properties, this alloy is a desirable material for use in airframes, aero-engines, petrochemical applications, bio-medical industry, and many more [45], [85]. Due to cyclic thermal fluctuations during the layer-by-layer manufacturing process, the EB-PBF built Ti-6Al-4V has different properties when compared to wrought and cast Ti-6Al-4V. In order to use these EB-PBF fabricated parts in critical load-bearing applications, their mechanical properties must be qualified. Tensile testing is one of the fundamental testing methods deployed to evaluate the mechanical properties of the parts. Depending on the area of application, to be considered adequate, EB-PBF parts should meet or exceed the tensile properties exhibited by manufacturing via conventional methods.

To perform tensile tests and draw robust conclusions, one needs to establish the specimen geometry to be used for fabrication of tensile specimens. The ASTM E8/E8M-16a [228] standard provides more than 30 specimen geometries. The specimen geometry selection is usually based on the manufacturing method. For example, to qualify powder metallurgy materials, a ‘flat unmachined’ or ‘round machined’ specimen type should be used. Similarly, there is a fixed geometry, outlined in the standard, for qualifying specimens



made of malleable iron, die castings, large and heavy steel castings, etc. There is currently no clear direction on the specimen size and geometry, part orientation and build location, and ideal part finishing that should be used for testing additively manufactured materials. For instance, in order to ensure a more homogeneous microstructure, it is typical to manufacture monolithic blocks via AM [150], [152] and then machine these blocks to the desired final tensile specimen shape. Testing of these specimens may provide accurate information about the material properties, however, they do not provide accurate information on the part performance if the parts are to be used as-built [229].

There is a need for a robust evaluation of the effect of specimen size and geometry, as well as specimen build orientation in the as-built (as-fabricated) condition to understand their effects on the tensile properties. It is important to understand the mechanical properties of as-built specimens for four significant reasons: (i) this may capture the performance of the process and variability for quality assurance purposes, without the interference from downstream post-processing, (ii) this may reduce the cost of performance testing as it eliminates other costly post-processing, (iii) this may act as a better match to mechanical properties of parts where the surfaces are not finished, and (iv) this may enable an un-modified part library stored with every build as a source for future troubleshooting, as needed. Therefore, this study aims at assessing the as-built mechanical properties for a range of tensile specimen geometries selected from the ASTM E8/E8M-16a [228].

### **4.3 Review of EB-PBF Tensile Studies and Challenges in Data Usability**

There are multiple studies in EB-PBF literature that focus on the tensile properties of Ti-6Al-4V specimens. These studies focus on evaluating the difference and/or similarities in properties with respect to build orientation, specimen geometry, location on the build platform, height of the specimen, comparison with the cast and wrought counterpart, post-processing technique, etc. However, the results presented are inconsistent [38], [85], [145]–[151].

For example, when considering part orientation, Rafi et al. [146] investigated the effect of build orientation in EB-PBF and reported that specimens built in the *XY* direction (also known as horizontally built specimens) have marginally higher strength values when compared to specimens built in the *Z* direction (also known as vertically built specimens). Ackelid et al. [145] reported no difference in the yield strength (YS), an increase in the ultimate tensile strength (UTS), and decrease in the % elongation (% EL) for horizontally built specimens. Contrary to these, Zhao et al. [85] observed higher YS, UTS, and % EL values for vertically built specimens in comparison with those built horizontally.

Similarly, when comparing the performance of EB-PBF parts to conventional cast or wrought, results seem to be inconsistent. Parthasarathy et al. [147] compared the tensile properties of Ti-6Al-4V EB-PBF specimens to cast Ti-6Al-4V ones. Facchini et al. [148] compared the tensile properties of as-built and heat treated Ti-6Al-4V EB-PBF specimens to wrought and annealed Ti-6Al-4V. Both these studies concluded that EB-PBF specimens performed better than conventional ones. However, Zhao et al. [85] reported that the tensile properties of Ti-6Al-4V EB-PBF specimens were worse than their wrought counterparts. Koike et al. [151] also reported that as-built Ti-6Al-4V ELI (Extra Low Interstitials) EB-PBF specimens performed worse than their cast and wrought counterparts.

Another inconclusive topic is the effect of specimen thickness on the tensile properties. Antonysamy [38] has mentioned that with an increase in thickness, heat dissipation via the already built volume and substrate becomes challenging due to the poor thermal conductivity of Ti-6Al-4V [75] and this leads to a decrease in strength. Contrary to this, Machry et al. [149] have concluded that thicker specimens that are in direct contact with the build platform, can efficiently conduct heat downwards in the direction of the build platform due to the high contact area. Thinner specimens, where the conduction is less due to the smaller area in contact with the platform, show a decrease in strength. Kircher et al. [150] presented a few case studies that investigated the effects of specimen geometries (flat and round) on the tensile properties of EB-PBF manufactured Ti-6Al-4V specimens. They observed that the tensile properties of the round ASTM E8 specimens had comparable YS, UTS, and % EL values to wrought Ti-6Al-4V specimens. Their preliminary results on the flat specimens showed that when compared to the round ones, the flat specimens exhibited lower YS and UTS values. However, the authors extracted the necessary specimens out of large blocks of EB-PBF produced Ti-6Al-4V making it difficult to compare with other studies.

In an effort to undergo a robust evaluation of the body of knowledge in this area, forty-one published articles were evaluated in this present work to understand the range of tensile property (YS, UTS, and % EL) values [4], [5], [125], [146], [149]–[152], [197], [229]–[231], [35], [232]–[241], [43], [242]–[251], [69], [252], [71], [85], [104], [106], [123] for EB-PBF of Ti-6Al-4V. The values were plotted, based on the tensile specimen shape type (rectangular vs. cylindrical), and are presented in Figure 4.2. The rationale for dividing the data between rectangular (R) and cylindrical (C) is to have a better frame of reference for the current study, which focuses on the effect of specimen geometry on properties.

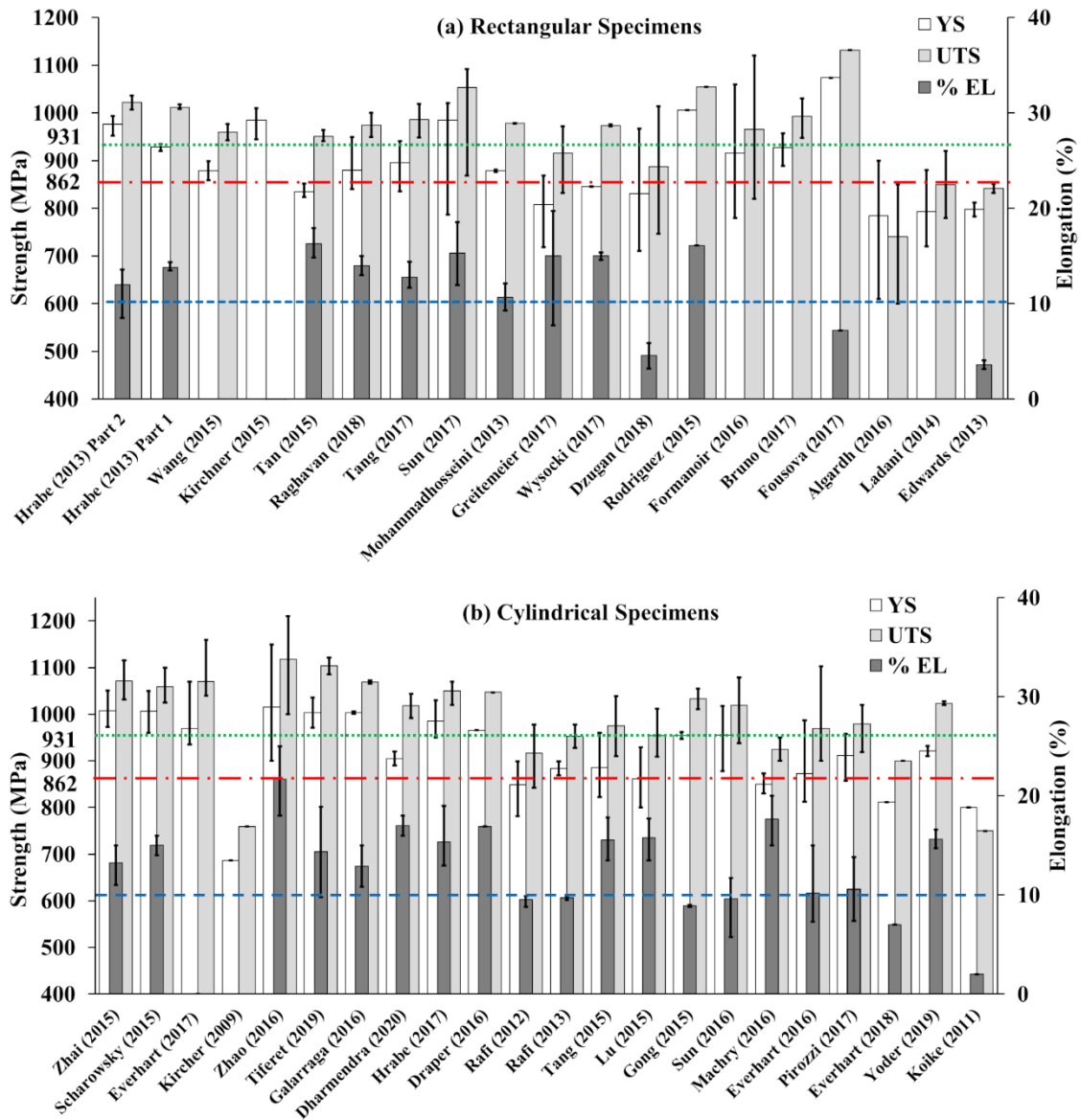


**Figure 4.2 Comparison of YS, UTS, and % EL values for (a) rectangular and (b) cylindrical specimens from published literature [4], [5], [125], [146], [149]–[152], [197], [229]–[231], [35], [232]–[241], [43], [242]–[251], [69], [252], [71], [85], [104], [106], [123]. Error bars represent the reported min-max range. The green line, red line, blue line correspond to the minimum UTS, YS, and % EL values respectively, for a bar of wrought Ti-6Al-4V in annealed condition according to AMS 4928W [253]**

This is not an exhaustive review of literature, but simply meant to serve as a guide for comparison and reference. Due to lack of available data points, the elastic modulus (E) was not plotted. From Figure 4.2 (a) and (b), it can be observed that the reported range of YS = 610 MPa to 1150 MPa, UTS = 600 MPa to 1210

MPa, and % EL = 2 % to 25 %. Upon comparing the R and C specimens, it can be observed that the values range for  $YS_R = 610$  MPa to 1074 MPa and  $YS_C = 686$  MPa to 1150 MPa. The value range for  $UTS_R = 600$  MPa to 1132 MPa and  $UTS_C = 750$  MPa to 1210 MPa. Lastly, the value range for  $\% EL_R = 2.5$  % to 18 % and  $\% EL_C = 2$  % to 25 %. From this data, one may conclude that the cylindrical specimens have higher performance values.

A few studies compared the tensile properties of horizontally-built (H) specimens with vertically-built (V) specimens manufactured via EB-PBF in Ti-6Al-4V. Figure 4.3 indicates the differences in performance between each orientation. It can be observed that for 8 of the 15 studies, the YS and UTS values for H are higher than for V. Zhao et al. [85] observed higher strength and % elongation values for V in comparison with H. Zhai et al. [241] observed that the YS and UTS values for V were higher than H. Galarraga et al. [123] observed that the UTS was higher for V, but the YS was higher for H. They also observed noticeable differences in % EL (10 % for V and 15 % for H). Dharmendra et al. [246] observed that the YS, UTS, and % EL are higher for V specimens. Edwards et al. [35] observed that the YS and UTS are higher for V specimens. Draper et al. [245] noticed a slight increase in YS for V but the UTS for H is higher than for V.

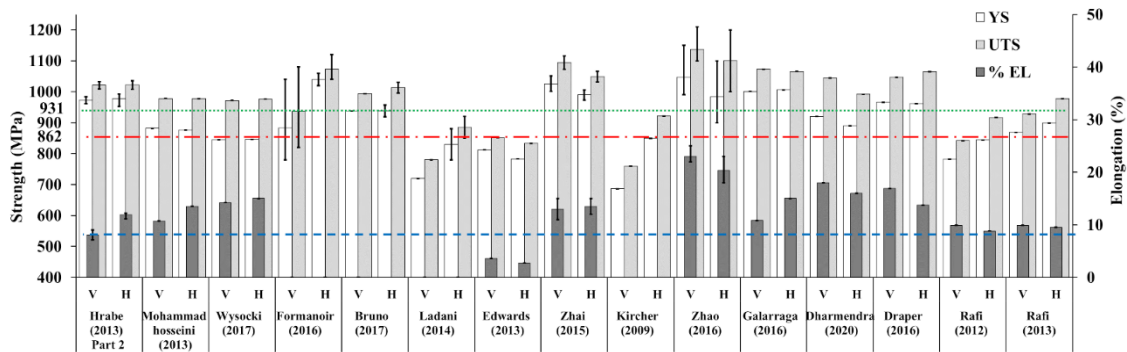


**Figure 4.3 Comparison of YS, UTS, and % EL values for vertically-built and horizontally-built specimens from published literature [4], [35], [239], [241], [245]–[247], [43], [85], [123], [146], [150], [235], [237], [238] Error bars represent the reported min-max range. The green line, red line, blue line correspond to the minimum UTS, YS, and % EL values respectively, for a bar of wrought Ti-6Al-4V in annealed condition according to AMS 4928W [253]**

The paramount takeaway from Figure 4.2 and Figure 4.3 is that there is a significant amount of mechanical property data scatter, for a single material system (Ti-6Al-4V). It is important to note that, due to a lack of information on build parameters, it is difficult to definitively explain why there is such a broad range (Figure 4.2) and discrepancies in results (Figure 4.3). For the same reason, it is also difficult to make accurate quantitative comparisons between the observations and results of different published literature. In the context of the present work, the build parameters include (i) information about the powder such as

chemistry, particle size distribution, powder manufacturing process (gas-atomized, plasma-atomized), and powder reuse cycles (ii) information about the specimen such as shape, orientation, location on the build platform, dimensions, use of supports, post-processing techniques such as machining, heat-treatment, cooling rates for heat-treatment, and (iii) information on process parameters such as layer thickness, preheat temperature, scanning strategy, rotation angle between consecutive hatches, build theme version, and machine model type. Of note, although the operation of all machine models is similar, improvements have been made with every generation [152]. All the above-mentioned build parameters can have a significant effect on tensile properties and therefore should be provided, along with the specimen performance data, to be able to draw robust conclusions and draw comparisons in performance.

It is also well-known that internal defects influence mechanical properties of manufactured parts and, consequently, their performance [120], [127]–[130]; most studies reporting on tensile properties do not assess the defect population. Many studies have mentioned that optimizing process parameters can ensure a reduction of internal defects; however, it is extremely difficult for these to be completely removed due to technology limitations and prohibitive costs in parameter optimization [119], [131]–[134]. Therefore, to properly assess the tensile performance, the mechanical performance data needs to be accompanied by an estimate of the part bulk density (at minimum) and by a measure of the pore space properties (ideally).

There are two major types of internal defects in EB-PBF: (i) insufficient powder melting (or lack-of-fusion porosity) [121], [122] between successive layers or within a layer that is usually attributed to insufficient energy input, and (ii) entrapment of gas in the melt pool (gas pores) that is usually attributed to excessive energy input [123]–[125]. Such defects have been shown to influence the tensile strength, among other mechanical properties [4], [65], [126]. There are multiple ways of evaluating such defects, such as methods based on relative density measurements (e.g., Archimedes' method) to evaluate the amount of porosity, microscopic analysis of specimens' cross sections to evaluate sizes of defects [119], [135], and ultrasonic testing [118]. Although these methods are useful for inferring bulk density estimates, it is difficult to extract the 3D spatially-resolved information about porous defects (shape, size, distribution) required for proper assessment of mechanical properties for defect-prone material systems [125], [136], [137]. X-ray computed tomography (XCT) is widely used for spatially-resolving, characterizing, and classifying defects in additively manufactured components due to its capabilities to visualize and detect external/internal features that are normally not accessible non-destructively [138]–[141]. Ultimately, whether or not to pass or fail an AM component will need to rely upon comprehensive knowledge of the relationship between defects, material properties, and process parameters [254]. This study aims at adopting and developing tools for analyzing internal defects with the help of XCT and correlating these to the specimen tensile properties.

As such, this study aims to perform a systematic investigation of tensile properties for EB-PBF by evaluating, assessing, and reporting the impact on tensile properties with respect to (i) the changes in specimen geometry, (ii) the change in specimen size, (iii) the change in build orientation, and (iv) the internal porous defects observed via XCT. This study specifically looks at tensile specimens because of their high use for qualifying and certifying parts produced in AM. Therefore the changes in geometry, size, and orientation are being varied within the context of the specimens outlined in the ASTM E8/E8M-16a [228].

## 4.4 Materials and Methods

### 4.4.1 Ti-6Al-4V Powder

The Ti-6Al-4V powder used, for manufacturing the tensile specimens, was supplied by Advanced Powders & Coatings<sup>3</sup> (AP&C), Canada. The Grade 5 plasma-atomized powder (Batch number: P1321) was obtained in its pre-alloyed form with a size range of 45  $\mu\text{m}$  to 105  $\mu\text{m}$ . The powder was used in its virgin form. D10, D50, and D90 of the powder were measured to be 48.73  $\mu\text{m} \pm 0.64 \mu\text{m}$ , 68.39  $\mu\text{m} \pm 1.45 \mu\text{m}$ , and 97.4  $\mu\text{m} \pm 2.45 \mu\text{m}$ , respectively. More information on the properties of this powder can be found elsewhere [103]. The chemical testing was carried out by Luvak Inc. (Boylston, USA) and the chemical composition of the powder conforms to ASTM F2924 for a Grade 5 Ti-6Al-4V powder (shown in Table 4.1).

**Table 4.1 Chemical composition of Ti-6Al-4V powder obtained from supplier**

Powder chemical composition (in % mass fraction)			
Element	ASTM F2924	Measured	Testing method
Carbon (C)	< 0.08	0.02	ASTM E1941
Oxygen (O)	< 0.20	0.13	ASTM E1409
Nitrogen (N)	< 0.05	0.02	ASTM E1409
Hydrogen (H)	< 0.015	0.001	ASTM E2371
Iron (Fe)	< 0.30	0.19	ASTM E2371
Aluminum (Al)	5.50 – 6.75	6.48	ASTM E2371
Vanadium (V)	3.50 – 4.50	4.00	ASTM E2371
Yttrium (Y)	< 0.005	< 0.001	ASTM E2371
Titanium	Balance	Balance	ASTM E2371

<sup>3</sup> Certain commercial equipment, instruments, or materials are identified in this paper to foster understanding. Such identification does not imply recommendation or endorsement by the National Institute of Standards and Technology, nor does it imply that the materials or equipment identified are necessarily the best available for the purpose.

#### 4.4.2 Specimen Preparation and Build Layout

A range of tensile specimen types provided for ASTM E8/E8M was selected. Table 4.2 provides the gauge length, width, thickness, and diameter information for these specimens as per ASTM E8/E8M- 16a [228]. In order to see if there is any influence of the orientation of the stacked layers on densification behavior and the tensile properties, specimens were fabricated in two orientations: (i) in the first orientation class, the long axis of the specimens was oriented perpendicular to the powder-stacked layers (Z direction), these are the vertically-built (V) specimens, and (ii) in the second orientation class, the long axis of the specimens was oriented parallel to the powder stacked layers (X direction), these are known as the horizontally-built (H) specimens.

**Table 4.2 ASTM E8/E8M tensile specimen types along with their dimensions [228]**

	Specimen Type						
	Flat (Large)	Flat (Small)	E8-3	E8M-2	E8M-3	E8M-4	E8M-5
G (Gauge length in mm)	50.0 ± 0.1	25.0 ± 0.1	24.0 ± 0.1	45.0 ± 0.1	30.0 ± 0.1	20.0 ± 0.1	12.5 ± 0.1
W (Width in mm)	12.5 ± 0.2	6.0 ± 0.1	-	-	-	-	-
D (Diameter in mm)	-	-	6.0 ± 0.1	9.0 ± 0.1	6.0 ± 0.1	4.0 ± 0.1	2.5 ± 0.1
T (Thickness in mm)	3	3	-	-	-	-	-
Vertically-built (V) Replicate 1	1B	4	7	1	13	17	28
Vertically-built (V) Replicate 2	2B	10	8	5	14	20	27
Vertically-built (V) Replicate 3	3B	11	9	6	15	22	29
Horizontally-built (H) Replicate 1	E	C	G	A	H	K	B
Horizontally-built (H) Replicate 2	J	T	N	M	O	P	D
Horizontally-built (H) Replicate 3	R	Q	I	U	F	S	L

Additional information regarding details on the specimen locations, specimen replicate information, and a downloadable stereolithography (STL) build file can be provided by the authors upon request. Once the STL file was created using SolidWorks (Dassault Systèmes, France), file preparation for manufacturing was then performed using Materialise Magics version 25.0 (Materialise, Belgium). The software was used for scaling, positioning of specimens on the start/build platform, and support structure creation, where required. To account for thermal shrinkage after melting, the specimens were scaled, as recommended by the machine manufacturer, by 1.0092 for X and Y directions and 1.1032 for Z direction. Slicing the files was then executed by the Arcam Build Processor version 3.2 (Arcam plug-in for Materialise Magics), which

converts the information into an Arcam build file (.abf) that is imported to the machine. A total of three replicates per specimen type were tested. Table 4.2 provides the specimen designation for all replicates.

Figure 4.4 depicts all specimen types and placement of their replicates on the build platform. The specimens analyzed in this study were fabricated using an Arcam A2X (Arcam AB, Sweden) electron beam powder bed fusion system. Some vertical specimens were built with support structures that were removed manually with pliers. All horizontal specimens were built with support structures and these supports were first removed manually using pliers and the remaining nubs were gently removed using a 150 mm (6 in.) flat file, with care, by the same technician.

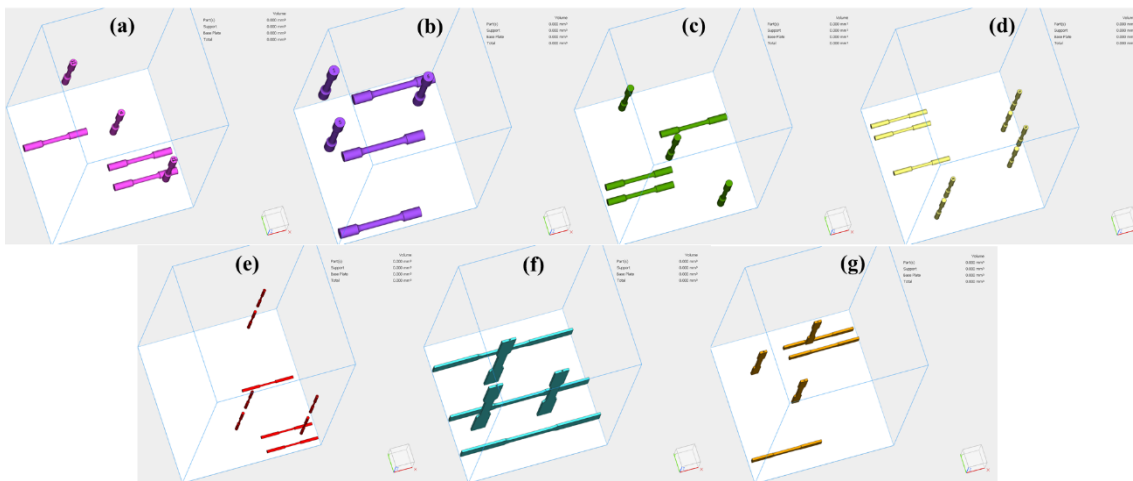


**Figure 4.4 Depiction of all specimen types and placement of their replicates inside the bounding box (a) E8-3 (b) E8M-2 (c) E8M-3 (d) E8M-4 (e) E8M-5 (f) Flat (Large) (g) Flat (Small). For E8M-4 and E8M-5, three extra specimens were built in the Z (vertical) direction to maintain uniform part distribution such that the beam scans the entire build platform until the very last layer.**

#### 4.4.3 Additive manufacturing process

At the beginning of the additive manufacturing process, the build platform was heated by the electron beam from room temperature to a temperature  $\approx 475$  °C. Once this temperature was achieved, degassing was performed for 10 minutes to remove species such as water vapor from the surface of the build platform, moisture from the powder stored in the hoppers, etc. After degassing, the temperature of the build platform was increased to the pre-defined initial preheating temperature (730 °C for Ti-6Al-4V). The temperature of the build platform was monitored by a thermocouple that is attached to the bottom of this platform. Once the preheat temperature was reached, the build table moved downwards by 1-layer thickness (50  $\mu$ m), and a layer of Ti-6Al-4V powder was spread homogeneously. This was repeated until all the specimens were



built by sequential exposure of the powder cake to the Preheat Theme recipe and the part to the Melt Theme recipe, respectively. After the build was completed, the specimens were retrieved from a partly sintered cake by powder blasting in the Powder Recovery System (PRS). This blasting is required to retrieve parts in the EB-PBF process, and thus is not considered a post-processing step. In the PRS, the powder cake is blasted with the same raw material used for fabrication (virgin Ti-6Al-4V powder for the current study) circulated in a stream of air. This allows for powder removal (from the cake) and recovery of the solid specimens. The build height for this experiment was 200 mm. The build area used was 200 mm x 200 mm. The specimens were built on a 10 mm thick 316L stainless steel platform. The manufacturing parameters were defined by an internal algorithm of the Arcam A2X machine (Theme 5.2.52). The accelerating voltage was 60 kV, vacuum was set to  $1.0 \times 10^{-4}$  mbar, beam current was 12 mA, scanning line offset was 0.2 mm, and focus offset was 25 mA. In these default parameters, the contours are processed in the multibeam mode such that up to a 100 contour positions are melted in a quasi-simultaneous manner to optimize scan lengths and reduce the number of scan lines. The Arcam heat model determines the current required at the processed layer to maintain an adequate surface temperature considering energy losses by radiation and conduction. To keep the melt profile constant, the current is adjusted in function of the scan line length. All testing was conducted on the as-fabricated tensile specimens and no post-processing was performed.

#### **4.4.4 X-ray Computed Tomography analysis**

For this study, XCT was performed using an Xradia 520 Versa system (Zeiss, Germany). The entire gauge length was scanned for all specimens that are mentioned under Replicate 1 (as per Table 4.2). For the remaining specimens (i.e., Replicate 2 and Replicate 3 mentioned in Table 4.2), a single field of view (FOV) in the center of the gauge length was scanned to ensure each class of specimens has similar internal defect architectures. The FOV dimensions vary for each specimen and therefore the exact FOV dimensions and resolution are mentioned in Table 4.3. Since all specimens had different gauge widths, they were scanned at different voxel sizes; Table 4.3 presents the various voxel sizes used. The vertical stitching feature (Vertical Stitch software by Zeiss, Germany) was used to stitch multiple image segments into one continuous volume. Once the scan was complete, reconstruction of the projection images was completed using the Zeiss Scout-and-Scan version 14.0.1 (Zeiss, Germany) software package.

The top and bottom 100 slice images of the XCT reconstructions were discarded because of X-ray cone-beam imaging artifacts. A gray-scale threshold value to isolate the solid portion of the specimen (white = solid, black = pore) was chosen such that the thresholded images had a qualitative visual match to the gray-scale data pore structure. The layer-wise solid fraction (conversely pore fraction) and bulk density

(conversely porosity) estimations were obtained with this technique. Another metric obtained was the true cross-sectional area of each image slice, and the average cross-sectional area of the specimens. The true cross-sectional area is the area of the white pixels in each image slice, with the specimen cross-sectional area being an average of these. This average area is used to calculate the tensile stress. Defect space analysis along the specimen gauge length was conducted with the XCT data. Based on the voxel size used, some pores cannot be detected during analysis. According to Plessis et al. [255] the typical diameter of the minimum detectable pore that can be identified with a high degree of confidence is at least 3x3x3 voxels (27 voxel-neighborhood in 3D). Table 4.3 shows the typical diameter of the minimum detectable pore for the various specimen types based on the feasible resolution achieved during scanning.

**Table 4.3 Table summarizing XCT parameters such as the voxel resolution, FOV dimensions, and minimum detectable pore diameter**

Specimen Type	Voxel sizes used for XCT scanning ( $\mu\text{m}$ )	FOV (mm) (Length x Width)	Minimum detectable pore diameter ( $\mu\text{m}$ )
Flat (Large)	14	14.33 x 14.33	42
Flat (Small)	8	8.1 x 8.1	24
E8-3	8	8.1 x 8.1	24
E8M-2	10.5	10.7 x 10.7	32
E8M-3	8	8.1 x 8.1	24
E8M-4	6.5	6.6 x 6.6	20
E8M-5	3.5	3.5 x 3.5	11

The MATLAB R2017b function “regionprops” and “regionprops3” were used to evaluate the 2D and 3D volumetric images obtained from the XCT data to retrieve pore information, respectively. A bilateral filter was used before thresholding any data. The input used for regionprops3 is a volumetric binary image. When given a black and white image, it automatically determines the properties of each contiguous white region that is 8-connected. Various properties such as the volume, centroid, orientation, equivalent spherical diameter, surface area, and sphericity of pores, were extracted. A detailed description of the regionprops and regionprops3 function can be found elsewhere [256]. The MATLAB code used to extract pore space analytics is presented in 0.

#### 4.4.5 Surface roughness analysis

Surface roughness was determined using a coaxial laser confocal microscope (VK-X250, Keyence, Japan). Surface roughness is usually represented by  $Ra$  and  $Sa$ , where the  $Ra$  is the arithmetic average of the absolute values of the profile deviations from the mean line of the roughness profile and  $Sa$  is the extension

of  $Ra$  to a surface [257]. Both these parameters are represented in micrometers ( $\mu\text{m}$ ). A surface scanning area of  $1400 \mu\text{m}$  by  $1000 \mu\text{m}$  was scanned for every specimen. The vertical ( $Z$ ) resolution was set to  $1 \mu\text{m}$ . All measurements were performed with the 20x objective. The surface roughness analysis, to obtain the  $Ra$  and  $Sa$  values for all tensile specimens, was performed using the VK-X Multifile Analyzer software (Keyence, VK-X250, Japan). A surface shape correction for the curvature was employed for all cylindrical specimens as the surface of these specimens was curved. The correction method used was Plane Tilt and the entire measurement area was selected. The measurements were conducted on the gauge lengths of the specimens. For the horizontal specimens, the up-facing surface was characterized. A total of three, equally spaced, measurements were taken across the entire cross-section of the gauge length. No other adjustments (such as outlier removals, use of filters) were performed.

#### **4.4.6 Tensile testing of specimens**

All tensile tests were conducted according to the ASTM E8/E8M -16a Control Method C, by a NADCAP certified testing laboratory (IMR Test Labs, NY, USA). The elongation at fracture (% EL), 0.2 % offset yield strength (YS), ultimate tensile strength (UTS), and elastic modulus (E) were obtained from the engineering stress-strain curves for each specimen. Specimens E8M-5 B, Flat (Large) R, and Flat (Small) Q were reported to have failed outside the gauge and therefore their tensile properties have not been included in the results. The raw stress-strain data can be obtained through the authors upon request. The engineering stress-strain curves are presented in Appendix H.

### **4.5 Results and Discussion**

#### **4.5.1 X-ray Computed Tomography**

Figure 4.5 (a) and (b) depicts the minimum and average layer-wise solid fraction (in %) respectively and was obtained by XCT, for all specimens. In the figures, the symbols encode whether the scan encompasses the full reduced parallel section (“Full Gauge”) or only the center single FOV as described in Section 4.4.4 (“Single FOV”). It can be observed from these figures that the horizontal specimens have a lower minimum and average layer-wise solid fraction. The average solid fraction values lie between 99.83 % to 99.99 % for vertical specimens and 99.28 % to 99.95 % for horizontal specimens. It can also be observed that the minimum layer solid fraction for the Full Gauge H specimens is lower than the Single FOV. This would indicate that the single FOV’s are not fully representative of the entire specimen gauge length for H specimens. The Full Gauge and Single FOV scans for the minimum layer solid fraction for V specimens

are in closer agreement with each other. This is because V specimens have fewer large defects and have a more uniform pore distribution. This can also be seen from Figure 4.6 to Figure 4.12.

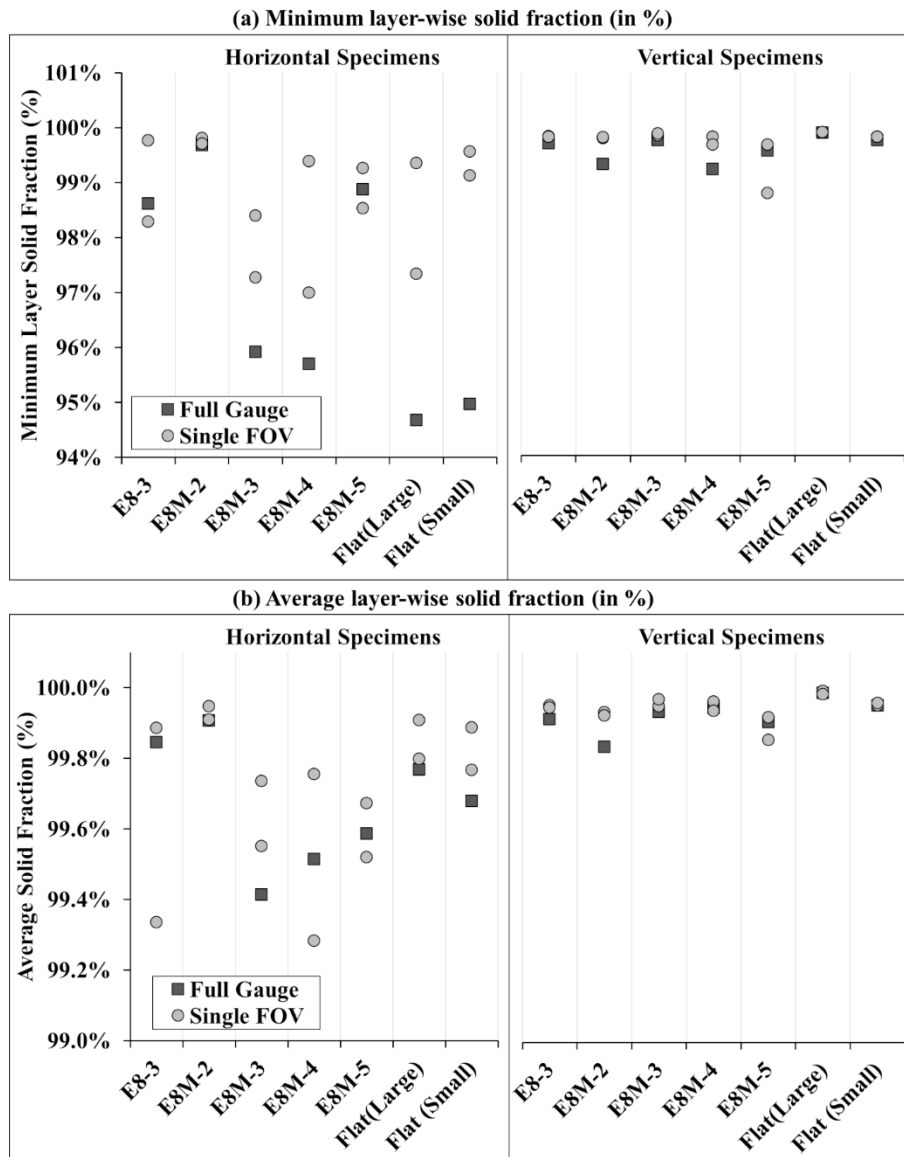


**Figure 4.5 (a) Minimum layer-wise solid fraction (b) Average layer-wise solid fraction for all specimens**

For better clarity over the defect space, the detailed layer-wise solid fraction plots for the Full Gauge of all specimens under Replicate 1 and Single FOV for all specimens under Replicate 2 and 3 (Table 4.2) are presented in Figure 4.6 (E8-3), Figure 4.7 (E8M-2), Figure 4.8 (E8M-3), Figure 4.9 (E8M-4), Figure 4.10 (E8M-5), Figure 4.11 (Flat-Large), and Figure 4.12 (Flat-Small), along with the XCT image of the

least dense layer (for the full gauge specimens) as the worst-case scenario illustration of the pore space distribution.

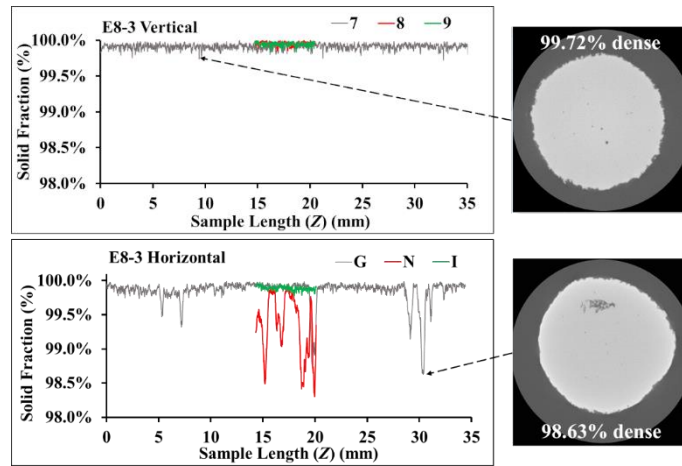


**Figure 4.6** Layer-wise density for E8-3 vertical and horizontal specimens along with the XCT image of the least dense layer for the full gauge specimen. The gray line represents the Full Gauge sample, and the green and red lines represent the Single FOV samples.

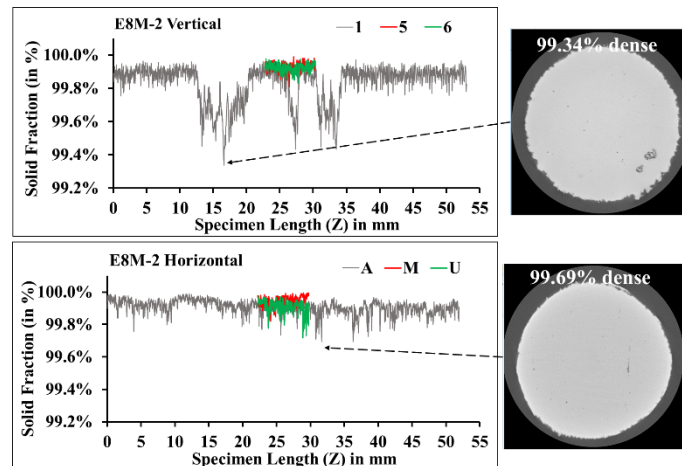


**Figure 4.7** Layer-wise density for E8M-2 vertical and horizontal specimens along with the XCT image of the least dense layer for the full gauge specimen. The gray line represents the Full Gauge sample, and the green and red lines represent the Single FOV samples.

Based on these figures, as well as selectively looking at the slices with the lowest density, the main defect type found in the tensile specimens was predominately lack-of-fusion defects. Lack-of-fusion defects are usually irregularly shaped and can contain internal un-melted zones or partially sintered powder particles. It has been reported in literature [8], [255], [258] that these lack-of-fusion defects may be caused

by process systematic biases such as powder re-coating influences, random events such as material ejections, as well as improper process parameter selection.

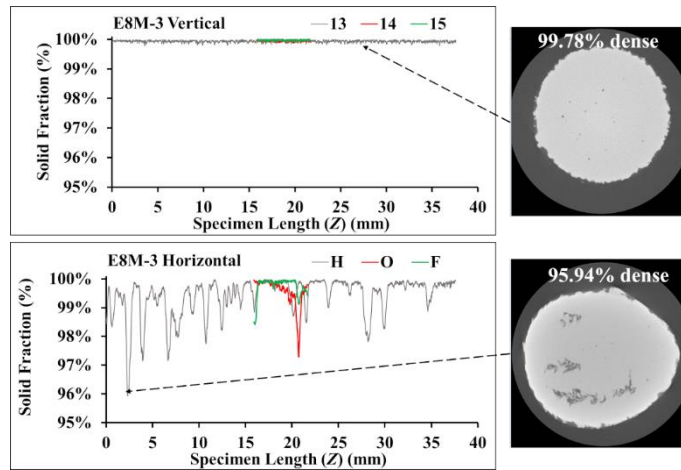


**Figure 4.8** Layer-wise density for E8M-3 vertical and horizontal specimens along with the XCT image of the least dense layer for the full gauge specimen. The gray line represents the Full Gauge sample, and the green and red lines represent the Single FOV samples.

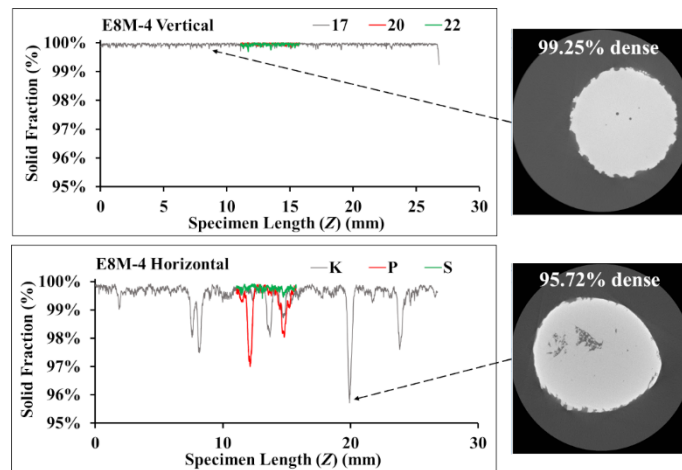


**Figure 4.9** Layer-wise density for E8M-4 vertical and horizontal specimens along with the XCT image of the least dense layer for the full gauge specimen. The gray line represents the Full Gauge sample, and the green and red lines represent the Single FOV samples.

A common instability in the EB-PBF systems that may lead to lack-of-fusion defects are arc trips [64]. Whenever an arc trip occurs during the Melt Theme, the printing of that layer restarts by raking of powder and re-melting the entire cross-sectional area. It should be noted no optimization of parameters was carried

out in this study; the default parameters defined by Arcam EBM Control Theme 5.2.52 were used. It can be noted from Figure 4.6 to Figure 4.12 that the horizontal specimens show a larger variability in porosity, and contain larger defects, while the vertical specimens show a much more consistent porosity level and contain smaller defects.

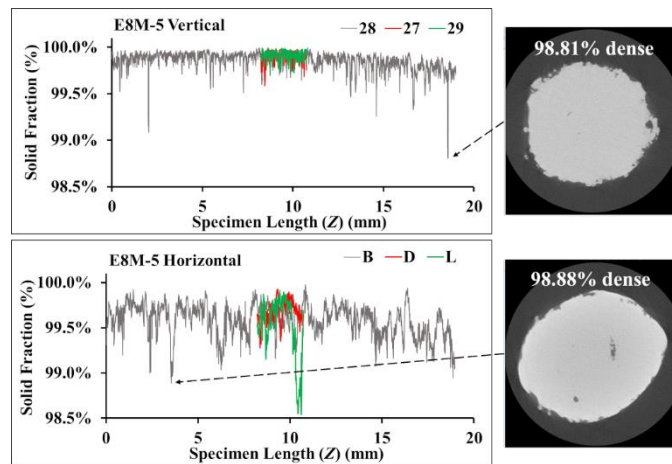


**Figure 4.10** Layer-wise density for E8M-5 vertical and horizontal specimens along with the XCT image of the least dense layer for the full gauge specimen. The gray line represents the Full Gauge sample, and the green and red lines represent the Single FOV samples.

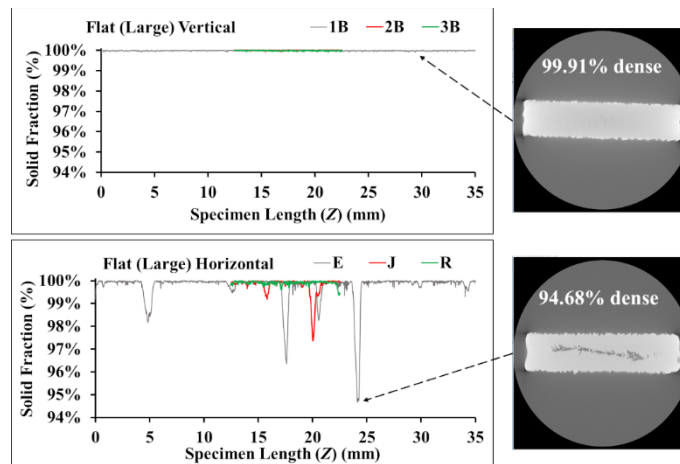


**Figure 4.11** Layer-wise density for Flat (Large) vertical and horizontal specimens along with the XCT image of the least dense layer for the full gauge specimen. The gray line represents the Full Gauge sample, and the green and red lines represent the Single FOV samples.

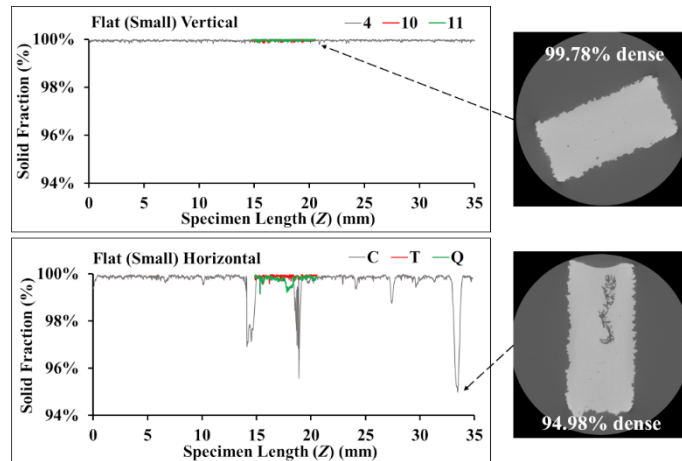


**Figure 4.12** Layer-wise density for Flat (Small) vertical and horizontal specimens along with the XCT image of the least dense layer for the full gauge specimen. The gray line represents the Full Gauge sample, and the green and red lines represent the Single FOV samples.

#### 4.5.2 Surface Roughness

The surface roughness measurements were carried out on all specimens. Figure 4.13 (a) and (b) depicts the surface roughness values ( $Ra$  and  $Sa$ ). The range of  $Ra$  values of as-fabricated EB-PBF parts has been reported as 20  $\mu\text{m}$  to 50  $\mu\text{m}$  in literature [63], [72], [73], [123] and the values seen here also fall in this range. The  $Ra$  values for the H specimens lie between 25  $\mu\text{m}$  to 35  $\mu\text{m}$  with the exception of E8M-5 specimens (B, D, L) where the  $Ra$  values lie between 18  $\mu\text{m}$  to 23  $\mu\text{m}$ . The same trend is observed for the  $Sa$  values for the horizontal specimens where the values lie between 30  $\mu\text{m}$  to 40  $\mu\text{m}$ , however for the E8M-5 specimens, these values lie between 22  $\mu\text{m}$  to 28  $\mu\text{m}$ . For vertical specimens, all  $Ra$  values lie between 25  $\mu\text{m}$  to 40  $\mu\text{m}$  and  $Sa$  values lie between 25  $\mu\text{m}$  to 42  $\mu\text{m}$ . This trend indicates that the roughness values for vertical specimens are slightly higher than the horizontal specimens. In general, the resulting surface topology of the EB-PBF produced parts after selectively melting each powder layer can be attributed to the sintered powder adhered to the boundary or contours of the parts. A high energy density enhances the sintering phenomenon. Powder particles located in the vicinity of the molten pool experience a partial melting that result in the attachment of the powder to the solidified area. Therefore, the partial sintering of powder particles could be the main cause of a highly rough surface [259], [260]. The staircase effect is another factor that influences the surface roughness of EB-PBF parts. EB-PBF uses a higher particle size distribution (usually 45  $\mu\text{m}$  to 150  $\mu\text{m}$ ) when compared to other AM processes. Therefore, the minimum layer thickness that can be used is 50  $\mu\text{m}$ . The staircase effect is dependent on the curvature of the part's surface and the deposition layer thickness that normally ranges from 50  $\mu\text{m}$  to 200  $\mu\text{m}$  for EB-PBF [261].



Hence, the use of finer powders will lead to an improved surface finish [262]. Lastly process parameters such as beam current, focus offset, and scan speed can also affect the surface roughness [263]. Assessing the reasoning behind the variability of surface roughness for this study is deemed as out of scope.

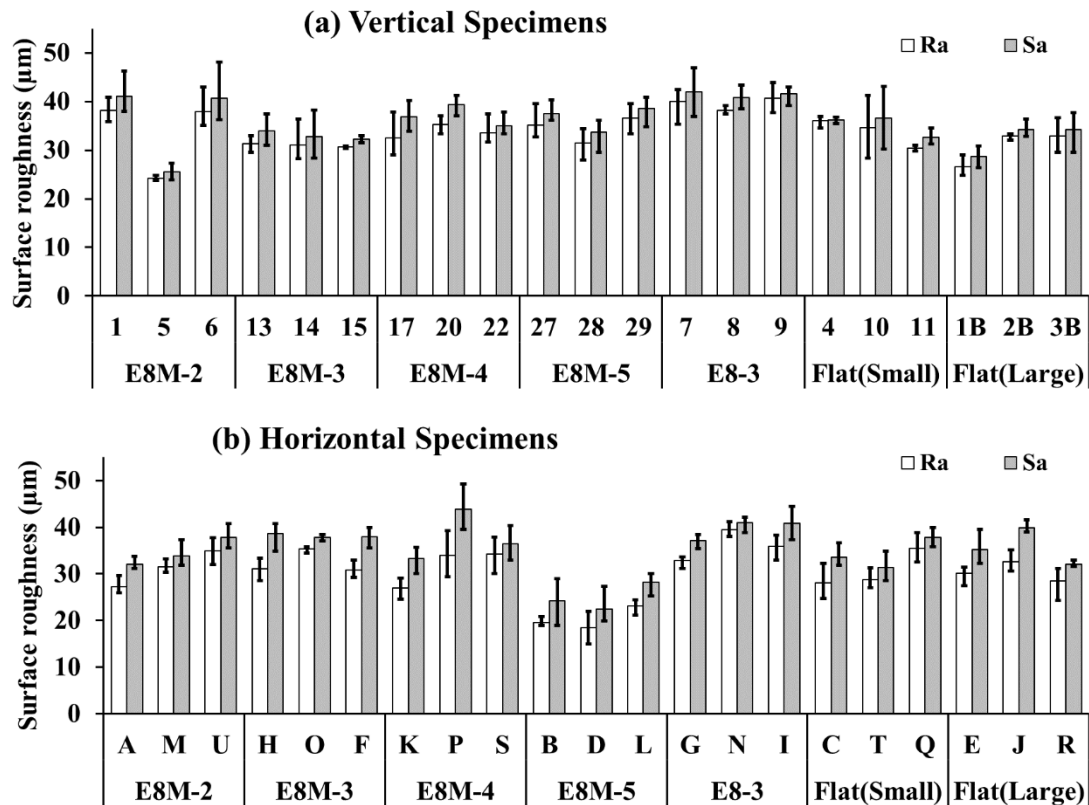


**Figure 4.13** Surface roughness (*Ra* and *Sa*) values for all specimen types for (a) vertical and (b) horizontal specimens. Error bars represent the min-max range.

The topology of the as-built surfaces, as well as sub-surface defects, play an important role in the development of surface stress concentrations, as these specimens will tend to fail earlier during applied stress, in comparison to their machined surface counterparts. The roughness of parts produced through the EB-PBF process has been associated with detrimental effects on mechanical properties [71], [264]. From this study, no trend was observed between the surface roughness and specimen size and shape and the resultant tensile properties. The authors hypothesize that since the *Ra* and *Sa* values are consistent for all the specimen types; the effects of the roughness are consistent for all specimens and therefore is not the cause of the difference in measured tensile properties.

### 4.5.3 Tensile Properties

#### 4.5.3.1 Effect of specimen orientation on tensile properties

The values obtained from the tensile test for YS, UTS, E, and % EL, are summarized in the Figure 4.14 below. The YS values range from 854.63 MPa to 951.83 MPa for V specimens and 907.98 MPa to 950.26 MPa for H specimens. The UTS values range from 937.93 MPa to 985.20 MPa for V specimens and 972.26 MPa to 1036.20 MPa for H specimens. Similarly, the % EL values range from 6.16 % to 16.78 % for V specimens and 2.41 % to 11.38 % for H specimens.

It can be observed that the given values lie between the ranges provided in literature in Figure 4.2. The E values range from 104.35 GPa to 126.34 GPa for vertical specimens and 100.00 GPa to 119.01 GPa for horizontal specimens. For specimen E8M-5 L, the stress-strain curve was observed to be unconventionally shaped due to which the YS and E values were calculated manually. Despite the deviation of the tensile properties for this specimen, it was still found to be representative of the E8M-5 H specimens.

The mechanical properties depend on the microstructure, thus warranting a closer look at the microstructural features observed in literature for EB-PBF manufactured Ti-6Al-4V to understand the differences between H and V specimens. Ti-6Al-4V processed by EB-PBF shows an ordered lamellar microstructure, consisting of small fine grains [249]. A columnar prior- $\beta$  phase morphology is observed parallel to the build direction [89]. Dharmendra et al. [246] have outlined three major reasons for the evolution of columnar  $\beta$ -grains during solidification. Reasoning (i) is the facilitation of epitaxial growth due to the narrow liquid/solid phase region for Ti-6Al-4V [265]. Reasoning (ii) is the high thermal gradient and heat dissipation along build direction leads to acceleration of epitaxial growth of the solid phase along the principal heat loss direction [180]. There are two significant heat losses in EB-PBF: radiation off the top surface and conduction through the sintered powder from the surrounding surface of the part and build platform [266]. In EB-PBF, previous layers usually undergo a longer annealing period, when compared to successive layers and therefore cooling rates change as a function of build height. This behavior has been seen to influence the strain hardening effect such that a more pronounced effect occurs in the upper part [230]. This is because annealing effectively reduces the number of dislocations, eliminating the strain hardening effect [267]. Reasoning (iii) is due to overheating of the melt pool via the electron beam, which results in epitaxial growth of coarse columnar  $\beta$ -grains [268]. Safdar et al. [89] reported Widmanstätten  $\alpha$ -platelets with rod-like  $\beta$  phase at the interface of the fine  $\alpha$ -grains in the columnar prior- $\beta$  grains.  $\beta$ -rod interspacing and  $\beta$ -grain width were found to increase as build layers increased [230].

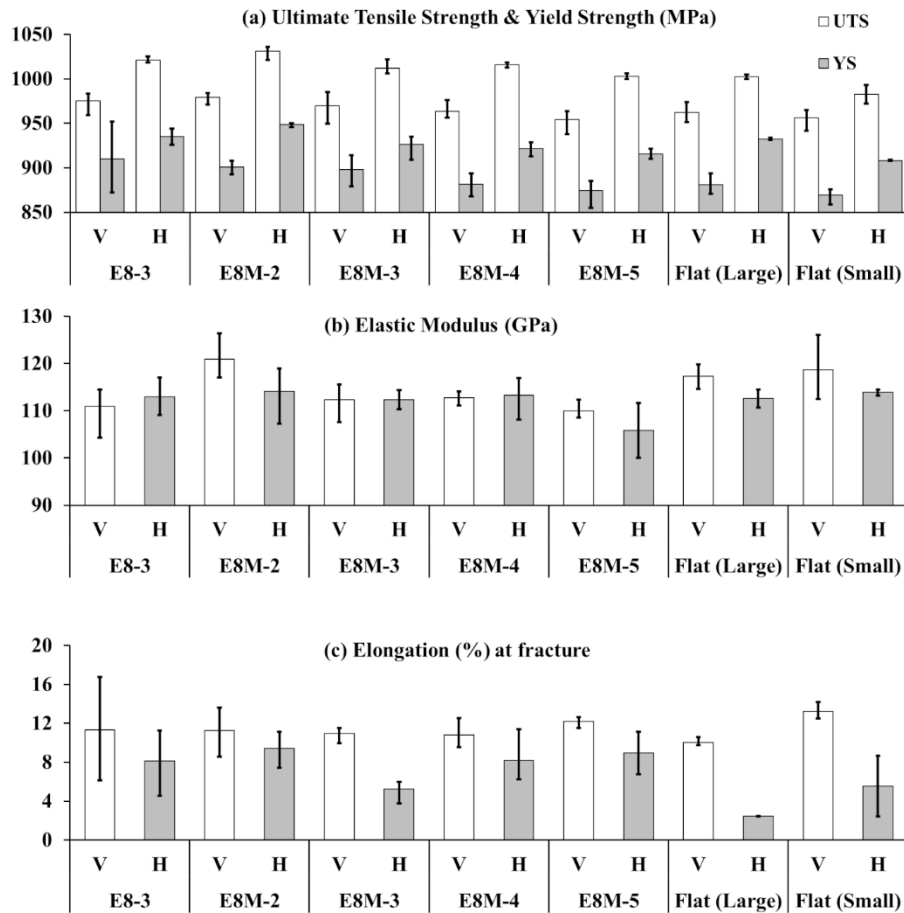


**Figure 4.14 (a) Ultimate tensile strength (UTS) and Yield strength (YS) (b) Elastic Modulus (E) (c) Elongation at fracture (% EL) values for the Vertical (V) and Horizontal (H) specimen types. Error bars represent the min-max range.**

According to the Hall-Petch equation [269], the strength is indirectly proportional to the square root of the grain size. Therefore, with an increase in grain size, the strength will decrease. Tan et al. [230] suggest that a graded microstructure is seen along the build direction. They observed that due to the graded microstructure, the materials' ductility improves along the gradient direction. Therefore, the vertically manufactured specimens have a higher average elongation value than horizontally manufactured specimens. As observed from the results in this study, the UTS and YS values of vertically-built specimens are lower than the horizontally-built specimens. This variation with respect to orientation can be attributed to the orientation of defects as a function of loading axis [270]. It has been mentioned by Liu et al. [45] that the short axis of lack-of-fusion pores is aligned in the building direction (Z). Under a uniaxial tensile load, parallel to the building direction, the sharp tips of the lack-of-fusion pores are prone to concentrated local

stresses, putting the lack-of-fusion defect into a mode I opening stress [270], [271]. Rafi et al. [146] have mentioned that microscopic discontinuity will exist where the two ends of columnar grains meet (perpendicular to the tensile loading axis). Horizontally built specimens are aligned parallel to the tensile loading axis and therefore it is not as prone to opening up a defect present in the *XY* plane [272].

#### 4.5.3.2 Effect of specimen cross-sectional area on tensile properties

Figure 4.15 shows the variation of (a) UTS and (b) YS with the specimen cross-sectional area for both V and H specimens. It can be observed that, as the specimen effective cross-sectional area increases, the YS and UTS values increase.

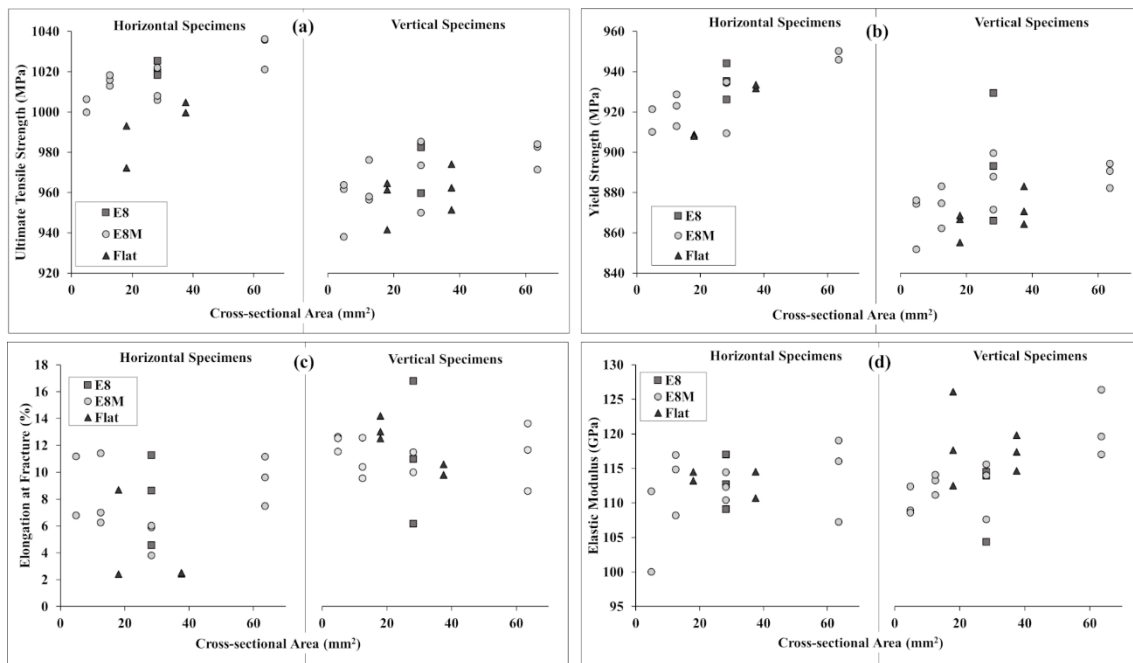


**Figure 4.15 (a) Ultimate Tensile Strength (UTS) (b) Yield Strength (YS) (c) Elongation at fracture (% EL) (d) Elastic Modulus (E) vs. cross-sectional area for all specimens.**

A decrease in the  $\alpha$ -plate spacing with an increase in diameter may be the cause of the higher strength values. According to [273] decreasing the  $\alpha$ -colony size will improve tensile properties such as YS, UTS, ductility, and crack propagation resistance. The  $\alpha$ -colony size is limited by the cooling rate from the  $\beta$ -phase field and prior- $\beta$  grain size [149]. The presence of finer  $\alpha$ -plate in thicker specimens can be attributed to a more efficient cooling of the specimen during the process. This efficient dissipation of heat will lead to better mechanical properties. According to [274] the semi-sintered powder cake that surrounds the EB-

PBF parts acts as a thermal insulator when compared to the properties of solidified material. Therefore, conductivity is restricted to the specimen itself and along the build direction. An increasing gauge diameter/area thus translates to increased heat dissipation and consecutively an increase in strength. Figure 4.15 (d) shows the variation of elastic modulus with cross-sectional area and shows that as the area increases, the elastic modulus of the V specimens increases. However, no clear trend is observed for the horizontal specimens, which is in part due to the presence of pores which introduced more noise in the material response trends. Similarly, no significant influence was observed on the % EL values, for the vertical specimens, as seen in Figure 4.15 (c). The H specimens show a trend where the % EL is highest for the E8M-5 and E8M-2 specimens. This behavior appears to be influenced by the minimum layer solid fraction and maximum pore size (Figure 4.16).

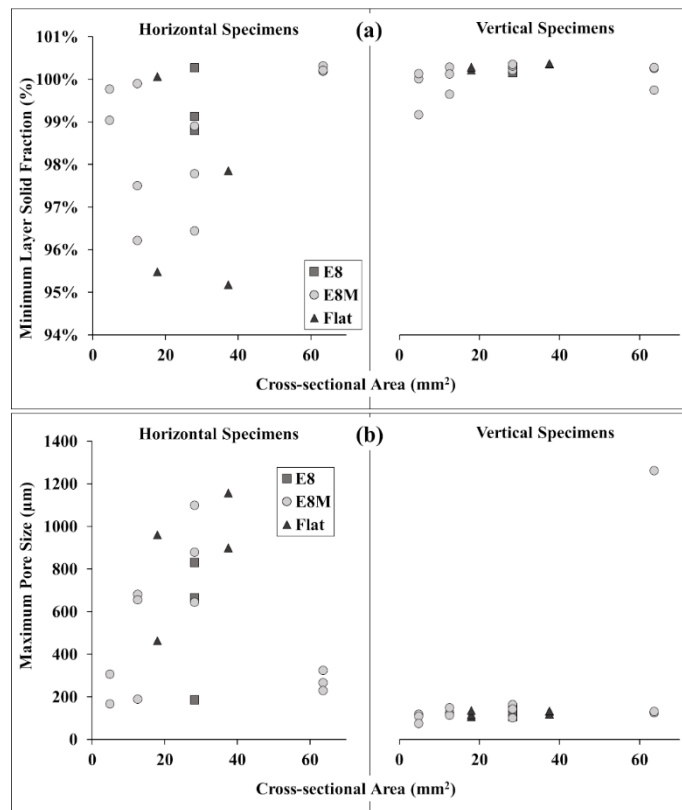


**Figure 4.16 (a) Minimum layer solid fraction (b) Maximum pore size vs. cross-sectional area for all specimens.**

The minimum layer solid fraction and the maximum pore size start out at good values (high solid fraction and low pore size respectively) for the lowest cross-sectional area (E8M-5), worsen as the area

increases (decrease and increase respectively), and then return to the same good values for the largest cross-sectional area (E8M-2). Similar to % EL (Figure 4.15), the minimum layer solid fraction and maximum pore size effectively stays the same for all of the vertically built specimens. The trends seen in Figure 4.16 show that the E8M-5 and E8M-2 specimens have a smaller maximum pore size as well as a higher minimum layer solid fraction. However, the average density for all of the specimen types is approximately the same. This means that the porosity in E8M-5 and E8M-2 specimens is made up of smaller, and more evenly spaced pores compared to E8M-4 and E8M-3.

Unfortunately, it is not fully understood why the specimens show very different maximum pore sizes and minimum layer solid fractions. The most likely cause is how the system hatches and scans the horizontal parts. Typically to optimize the speed of the scanning process, the Arcam system will break up larger parts (larger print area in the layer), rather than print the area of a single part all at once. The pores could be forming at areas where scanning stops and starts. It could also be how the different tensile specimen cross-sections are hatched in each layer, which causes the different specimens to have different pore distributions. The cause appears to be more to do with the scan strategy rather than something inherent to the geometries, otherwise it would be expected that the same trends would be seen in the vertical specimens. It is not possible to evaluate the reasoning behind the difference in the defects between the different specimen types because all the specimens were manufactured with a single build parameter set.

#### 4.5.3.3 Effect of surface area to volume ratio on tensile properties

In order to observe the influence of surface area to volume ratio on the various tensile properties, the surface area of the specimens was calculated based on the designed gauge diameter for the cylindrical specimens and based on the designed thickness and width for the flat specimens. The volume was then calculated using the gauge length. Figure 4.17 depicts (a) UTS, (b) YS, (c) % EL, and (d) E versus surface area to volume ratio, for both vertical and horizontal specimens. A clear trend is observed in Figure 4.17 (a) and (b), where an increase in surface area to volume ratio leads to a decrease in the YS and UTS values. This explains the lower values for the Flat (Large) and Flat (Small) specimens. It can be seen that the samples having surface area to volume ratio between 0.5 /mm to 1.25 /mm exhibit lower elongation values as seen in Figure 4.17 (c).

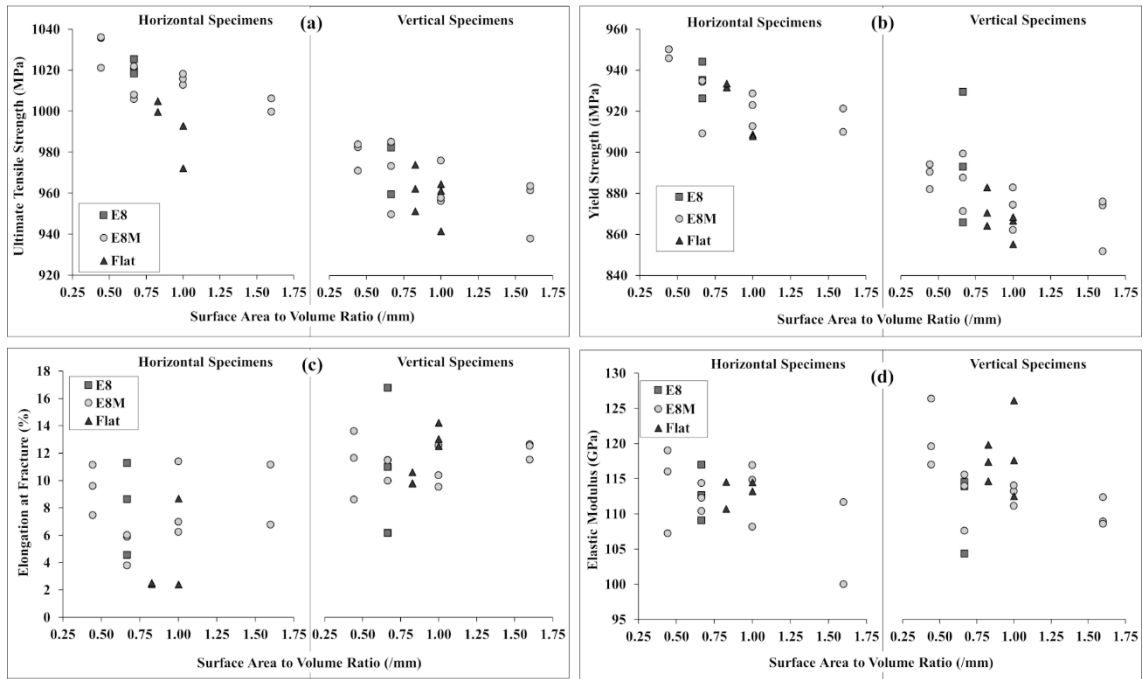


**Figure 4.17 Surface area/volume ratio vs. (a) Ultimate Tensile Strength (UTS) (b) Yield Strength (YS) (c) Elongation at fracture (% EL) (d) Elastic Modulus (E) vs. cross-sectional area for all specimens.**

This change in elongation values is caused by the change in maximum pore size (Figure 4.18) and is the same as what was seen when comparing just the effects of cross-sectional area in the previous section. This again indicates that the largest (E8M-2) and smallest (E8M-5) specimens, which correspond to the lowest and highest surface area to volume ratio, have smaller and more evenly spaced pores, giving them better elongation values. No clear trend is observed for the elastic modulus observed in Figure 4.17 (d). Overall, these results indicate that caution must be exercised when interpreting tensile properties, as there is a clear dependency on geometric properties.

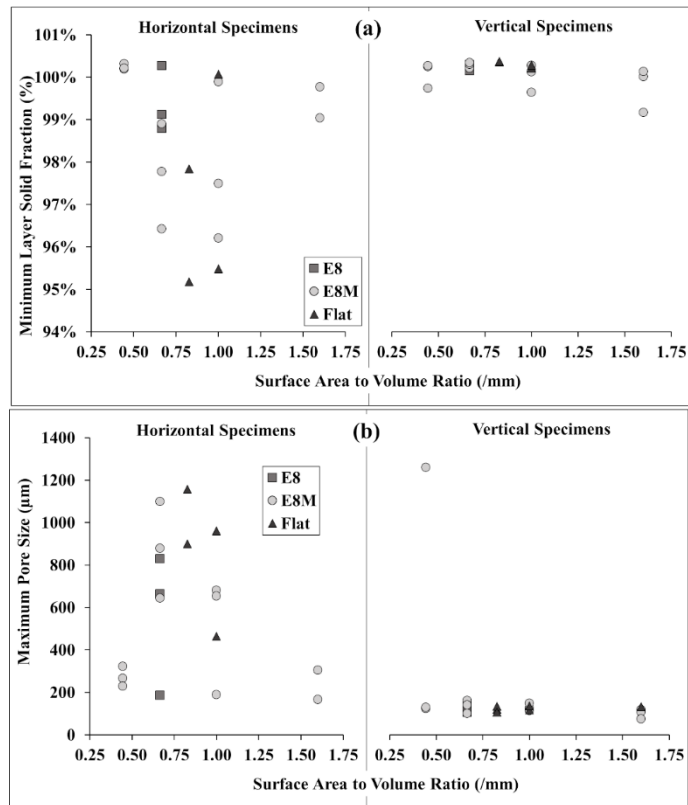


**Figure 4.18 Surface area/volume ratio vs. (a) Minimum layer solid fraction (b) Maximum pore size for all specimens.**

#### 4.5.3.4 Effect of % solid fraction on tensile properties

An important observation from the XCT data was the solid fraction (in %) obtained for the vertical and horizontal specimens. It is important to assess how the minimum and average layer-wise solid fraction (shown in Figure 4.5 (a) and (b)) affects the tensile properties. It can be seen that there is little correlation between the minimum layer solid fraction seen in a specimen, and UTS and YS (Figure 4.19 (a)), E (Figure 4.19 (b)). There appears to be a trend where an increasing minimum layer solid fraction is related to the increase in elongation for H specimens (Figure 4.19 (c)). No correlation is seen when the minimum layer solid fraction is replaced with the average solid fraction (shown in Figure 4.19 (d), (e), and (f)). All of this indicates that the average solid fraction fluctuations in the specimens (ranging from 99.99 % to 99.28 %) have a negligible impact on measured performance. While the bulk solid fraction seems to have little impact on performance, the authors suspect that pore morphology and location in the specimen have a significant impact (for example, 1% porosity being evenly distributed with many small pores vs. the 1% porosity being a single large pore). An extension of the current work will look into the pore space analysis information to



deduce such correlations in more depth to leverage the full potential of XCT analytical datasets in the interpretation of tensile performance.

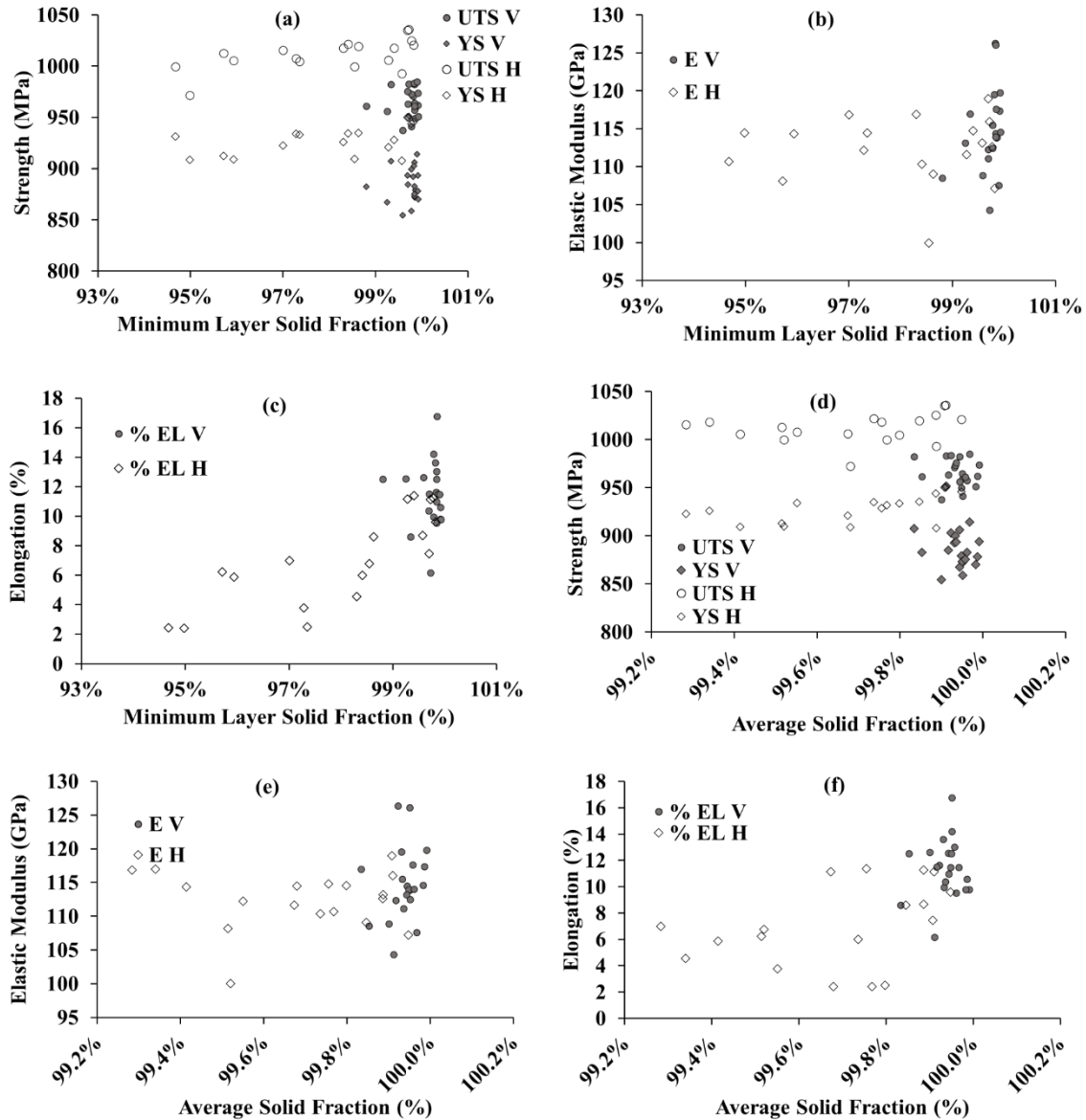


**Figure 4.19** Minimum layer solid fraction vs. (a) UTS and YS (b) Elastic modulus (E) (c) elongation at fracture (% EL); Average solid fraction vs. (d) UTS and YS (e) Elastic modulus (E) (f) elongation at fracture (% EL) where V=vertically and H=horizontally-built specimens.

#### 4.5.3.5 Effect of maximum pore size on tensile properties

In Figure 4.6 to Figure 4.12, horizontal specimens have fluctuating layer-wise densities and the images representing the worst layers showed big lack-of-fusion pores. There is little to no correlation between the

maximum pore size and the tensile strength (YS and UTS as shown in Figure 4.20 (a)) as well as E (as shown in Figure 4.20 (b)).

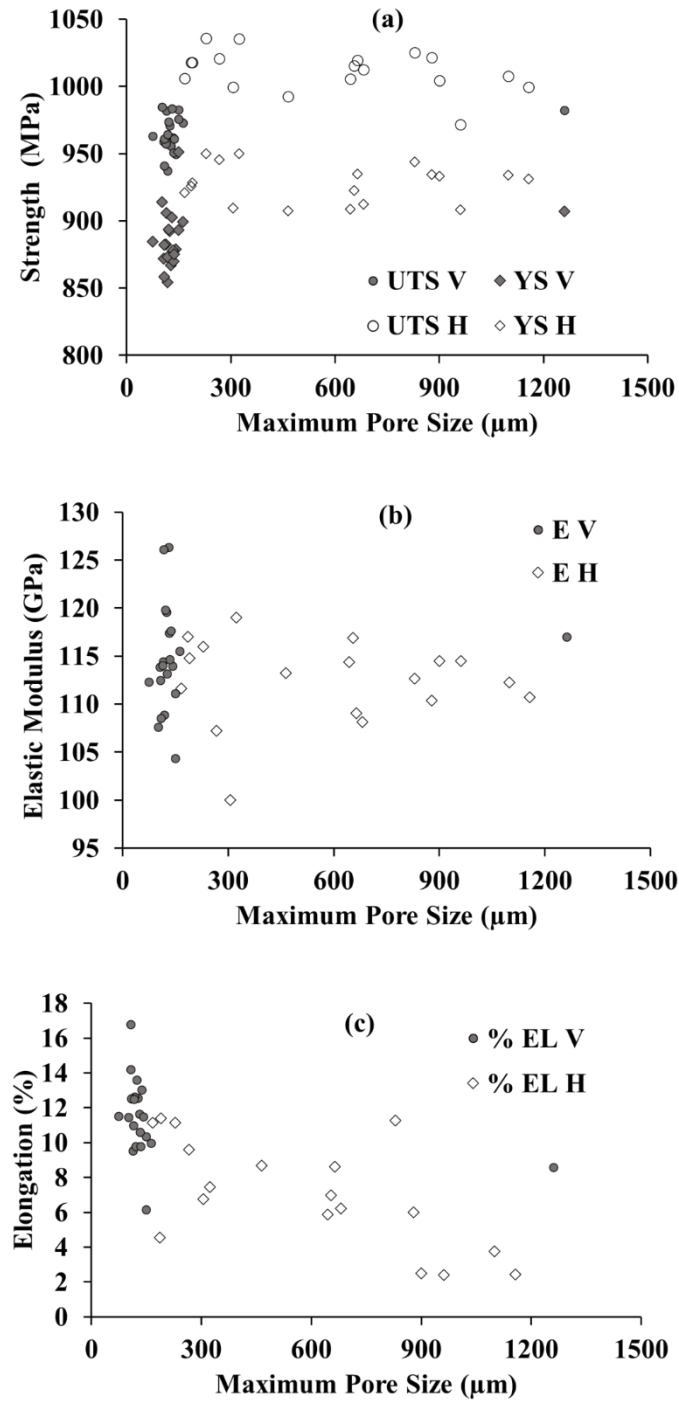


Figure 4.20 Maximum pore size vs. (a) UTS and YS (b) Elastic modulus (E) (c) Elongation at fracture (% EL) where V=vertically and H=horizontally-built specimens.

However, there is a correlation between the maximum pore size and % EL (as shown in Figure 4.20 (c)) for horizontal specimens such that an increase in pore size leads to a decrease in % EL. It is likely that the maximum pore seen in a part corresponds to the minimum layer density and this may explain why the effect is seen with both properties. The trend seen here seems likely as large pores act as crack initiation sites and thus lead to early failure and low % EL.

From all the above observations, it can be concluded that the specimen build orientation, cross-sectional area, surface area to volume ratio, % solid fraction and maximum pore size can have a significant impact on the tensile properties of as-built EB-PBF Ti-6Al-4V specimens. It is therefore very important to take these properties into account when comparing results in literature and assessing the performance of tensile specimens.

While these conclusions hold true for these specimens, it is difficult to extrapolate the results to other materials in EB-PBF and other AM processes. The thermal history of the specimen changes with a change in size, shape, and orientation, and these differing thermal histories are one of the major reasons for the difference in mechanical properties. It is expected that other materials would react differently to these varying thermal histories and therefore their mechanical properties may not follow the same trends as seen here. The thermal history seen in a specimen will also vary for a different combination of build parameters as well as for a different AM process. Therefore, these conclusions should not be extrapolated for other materials and AM processes.

#### **4.5.4 Conclusions**

This present study focused on a systematic investigation of tensile properties for EB-PBF as-built Ti-6Al-4V by evaluating, assessing, and reporting the impact on tensile test results with respect to (i) the changes in specimen geometry, (ii) the change in specimen size, (iii) the change in build orientation, and (iv) the internal porous defects observed via XCT. The findings in this study support the following conclusions:

1. The solid volume fraction of the specimens ranged from 99.83 % to 99.99 % and 99.28 % to 99.95 % for V and H specimens, respectively. H specimens have the highest variability in layer-wise pore fraction. It was also observed the Single FOV scans for H specimens were not representative of the Full Gauge due to the presence of large unevenly distributed defects.
2. For H specimens, those with a very low, or very high (E8M-2 and E8M-5 respectively) surface area to volume ratio had a lower maximum pore size, which resulted in higher elongation values. These specimens also had higher minimum layer solid fractions, indicating that they have smaller, more evenly spaced pores compared to the other specimen types.

3. The surface topography of specimens had minimal variation between the V ( $Ra$ : 25  $\mu\text{m}$  to 40  $\mu\text{m}$ ,  $Sa$ : 25  $\mu\text{m}$  to 42  $\mu\text{m}$ ) and H ( $Ra$ : 18  $\mu\text{m}$  to 35  $\mu\text{m}$ ,  $Sa$ : 22  $\mu\text{m}$  to 40  $\mu\text{m}$ ) specimens.
4. H specimens showed higher UTS (972.26 MPa to 1036.20 MPa) and YS (907.98 MPa to 950.26 MPa), and lower % EL values (2.41 % to 12.36 %) when compared to Vertically-built (V) specimens (UTS: 937.93 MPa to 985.20 MPa; YS: 854.63 MPa to 951.83 MPa; %EL: 6.16 % to 16.78 %). No specific trends were observed for the E values (H specimens: 100.00 GPa to 119.01 GPa and V specimens: 104.35 GPa to 126.34 GPa).
5. An increase in specimen cross-sectional area led to an increase in the UTS, YS, and E values for the E8M specimens.
6. An increase in the specimen surface area to volume ratio led to a decrease in the UTS and YS values. This indicates that cylindrical specimens with a smaller diameter and flat specimens with a larger width and/or smaller thickness, will have decreased performance. For H specimens, those with a very low, or very high surface area to volume ratio had a lower maximum pore size, which resulted in higher elongation values. These specimens also had higher minimum layer solid fractions, indicating that they have smaller, more evenly spaced pores compared to the other specimen types.
7. The specimen maximum pore size did not affect the UTS, YS and E. However, a strong correlation was observed between the % EL and the maximum pore size for horizontal specimens, such that with the % EL decreases with an increase in maximum pore size.
8. From this work it can also be concluded that a single tensile specimen size and geometry may not accurately represent the mechanical properties of all features of an EB-PBF as-built Ti-6Al-4V component. This has impact on part qualification since a load-bearing feature from a part would not necessarily have the same mechanical properties if the qualifying tensile specimen differed from it in overall size, shape, and orientation.

## **4.6 Addendum (Data in Brief)**

### **4.6.1 Preface**

Additive manufacturing quality assessment often relies on tensile testing as the preferred methodology to qualify builds and materials. The data included in this article provides additional supporting information on our work, described in earlier sections, on the effect of specimen geometry and orientation on tensile properties of Ti-6Al-4V manufactured by electron beam powder bed fusion. As such, the data in brief provides in-depth details on the tensile specimen specifications, the tensile specimen build layout and

replicate notations, and the tensile testing datasets. The information presented herein complements the manuscript.

#### 4.6.2 Specifications Table

<b>Subject</b>	Engineering, Materials Science
<b>Specific subject area</b>	Additive Manufacturing
<b>Type of data</b>	Tabulated data Microsoft Excel worksheet (XLSX) file Stereolithography (STL) file
<b>How data were acquired</b>	An Arcam A2X <sup>4</sup> electron beam powder bed fusion additive manufacturing system was used to fabricate the tensile specimens using the build STL file and an Instron MTS Criterion tensile test instrument was used by an external certified lab to extract all tensile data that is provided in the XLSX file.
<b>Data format</b>	Raw Stereolithography file (STL) Microsoft excel worksheet (XLSX)
<b>Parameters for data collection</b>	As described in the earlier sections of this thesis. Additional support data is included in this Data in Brief manuscript.
<b>Description of data collection</b>	Test specimens were fabricated in vertical and horizontal directions via the electron beam powder bed fusion (EB-PBF) technique. Tensile testing was performed at an external NADCAP certified lab, and these tests were conducted following ASTM E8/E8M-16a guidelines.
<b>Data source location</b>	Multi-Scale Additive Manufacturing Laboratory, University of Waterloo, Waterloo, ON, Canada
<b>Data accessibility</b>	With the article

<sup>4</sup> Certain commercial equipment, instruments, or materials are identified in this paper to foster understanding. Such identification does not imply recommendation or endorsement by the National Institute of Standards and Technology and the University of Waterloo, nor does it imply that the materials or equipment identified are necessarily the best available for the purpose.

<b>Related research article</b>	G. Shanbhag, E. Wheat, S. Moylan, M. Vlasea. Effect of specimen geometry and orientation on tensile properties of Ti-6Al-4V manufactured by electron beam powder bed fusion, J. Addit. Manuf. (Under Review)
---------------------------------	--

#### 4.6.3 Value of the Data

- The tensile specimen dimensions (Table 4.4), location (Table 4.5), and STL build file provides the readers with the opportunity to replicate these experiments and compare the data they may generate with the data presented in the earlier sections of this chapter. The raw tensile data XLSX file provides the readers the opportunity to plot stress-strain curves and examine the behaviour of the tensile specimens based on the executed experiments.
- The information presented and appended with this article is beneficial to be able to replicate the experiments, re-iterate on data analysis using other analytical tools, and compare results.
- The tensile specimen information, build file, and tensile test results from the present study on Ti-6Al-4V can be used for comparison purposes with other material systems that can be deployed in EB-PBF additive manufacturing.

#### 4.6.4 Data Description

There are three tables and two supplementary data files that are described in this article.

(1) For this work, a single build consisting of 48 tensile specimens with different geometries and orientations was manufactured using an Arcam A2X (GE Additive) electron beam powder bed fusion (EB-PBF) additive manufacturing system. SolidWorks (Dassault Systèmes, France) was first used to create the specimen stereolithography (STL) file. Supplementary Stereolithography (STL) data file named “Ti6Al4V Tensile Build.stl” can be provided by the authors upon request.

(2) A range of tensile specimen types provided for ASTM E8/E8M were selected for manufacturing via the EB-PBF process. Table 4.4 provides details of these specimens, along with their nominal design dimensions and nomenclature as per ASTM E8/E8M- 16a [228].

**Table 4.4 ASTM E8/E8M tensile specimen types along with their dimensions [228]**

	Specimen Type						
	Flat (Large)	Flat (Small)	E8-3	E8M-2	E8M-3	E8M-4	E8M-5
<b>G (Gauge length in mm)</b>	50.0 ± 0.1	25.0 ± 0.1	24.0 ± 0.1	45.0 ± 0.1	30.0 ± 0.1	20.0 ± 0.1	12.5 ± 0.1

<b>W (Width in mm)</b>	12.5 ± 0.2	6.0 ± 0.1	-	-	-	-	-
<b>D (Diameter in mm)</b>	-	-	6.0 ± 0.1	9.0 ± 0.1	6.0 ± 0.1	4.0 ± 0.1	2.5 ± 0.1
<b>T<sub>max</sub> (Maximum thickness)</b>	19	6	-	-	-	-	-
<b>T (Thickness used in the current work in mm)</b>	3	3	-	-	-	-	-
<b>R (Radius of fillet in mm)</b>	12.5	6	6	8	6	4	2
<b>L (Overall Length in mm)</b>	200	100	88.57	115.98	94.57	79.71	73.12
<b>A (Length of reduced parallel section, min in mm)</b>	57	32	30	54	36	24	20
<b>B (Length of grip section used in the current work in mm)</b>	62.5	29.5	25	25	25	25	25
<b>C (Width of grip section, approximate in mm)</b>	20	10	9.6	14.4	9.6	6.4	4

(3) Six replicates of every specimen type were manufactured, with three in each orientation. For specimen types E8M-4 and E8M-5, an extra specimen was built on top of the previous specimen in the Z (vertical) direction to maintain uniform part distribution such that the beam scans the entire build platform until the very last layer. However, tensile tests were only performed for three specimens each, selected at random. Table 4.5 provides information on the naming scheme, orientation, and location of the specimens as per ASTM 52921:2013 [275]. A total of 48 specimens were fabricated and the placement of these specimens was randomized.

**Table 4.5 Build orientation, location, and naming scheme for all specimen replicates as per ASTM 52921:2013 [275]**

Specimen Type	Orientation	Specimen Replicate					
		Replicate 1		Replicate 2		Replicate 3	
		Specimen designation	Location (X, Y, Z) mm	Specimen designation	Location (X, Y, Z) mm	Specimen designation	Location (X, Y, Z) mm
Flat (Large)	YZX	E	0.0, -61.4, 15.0	J	0.0, -9.9, 15.0	R	0.0, 62.6, 15.0
Flat (Small)	YZX	C	-46.1, -70.3, 10.0	T	44.8, 70.2, 10.0	Q	47.9, 54.7, 10.0
E8-3	Y	G	47.9, -47.9, 9.8	N	-52.3, 36.6, 9.8	I	48.9, -19.5, 9.8

E8M-2	Y	A	-37.3, -87.3, 12.2	M	0.4, 15.0, 12.2	U	38.7, 88.0, 12.2
E8M-3	Y	H	-46.7, -19.1, 9.8	O	48.5, 31.9, 9.8	F	-50.9, -39.9, 9.8
E8M-4	Y	K	-45.7, -0.1, 8.2	P	-55.5, 54.1, 8.2	S	-55.5, 71.4, 8.2
E8M-5	Y	B	60.8, -90.9, 7.0	D	59.0, -69.7, 7.0	L	54.3, 0.2, 7.0
Flat (Large)	ZYX	1B	29.9, -34.0, 100.0	2B	-63.8, -29.4, 100.0	3B	-26.7, 27.3, 100.0
Flat (Small)	ZYX	4	11.3, 45.0, 149.9	10	-73.9, 24.4, 149.9	11	-32.5, -29.3, 149.9
E8-3	Z	7	-36.3, 84.4, 154.9	8	4.5, 0.6, 154.9	9	52.7, -80.5, 154.9
E8M-2	Z	1	-71.9, 87.3, 141.9	5	-86.7, 15.2, 141.9	6	50.3, 44.1, 141.9
E8M-3	Z	13	36.3, 84.4, 47.2	14	4.5, 0.6, 47.2	15	52.7, -80.5, 47.2
E8M-4	Z	17	75.3, 15.1, 160.0	20	67.9, -35.4, 59.1	22	-50.4, -77.9, 59.1
E8M-5	Z	28	49.6, 78.9, 163.3	27	-10.4, -53.4, 163.3	29	73.4, -83.5, 163.3

(4) All tensile tests were conducted according to the ASTM E8/E8M -16a Control Method C [228], by a NADCAP certified testing laboratory (IMR Test Labs, NY, USA) using an Instron MTS Criterion test instrument. The crosshead speed for all specimens was 0.005 mm/mm/min up to yield. All tensile data (elongation at fracture, ultimate tensile strength, yield strength, elastic modulus) was obtained from the engineering stress-strain curves for each specimen. The post-yield strain was calculated from the actuator displacement and the length of the reduced parallel section. The raw tensile data containing raw stress-strain data and average true-cross section value for every specimen can be provided by the authors upon request.

(5) Table 4.6 summarizes the engineering stress-strain curves that showed anomalous behavior.

**Table 4.6 Anomalous stress-strain curves**

Type	Orientation	Designation	Notes
E8M-5	Horizontal	B	Failed outside gauge length as per testing laboratory
Flat (Large)	Horizontal	R	Failed outside gauge length as per testing laboratory
Flat (Small)	Horizontal	Q	Failed outside gauge length as per testing laboratory



E8-3	Vertical	7	Odd shape, suspected early failure
E8M-3	Horizontal	O	Odd shape, suspected early failure
E8M-5	Horizontal	L	Odd shape, Suspected sample slippage in the grips
Flat (Large)	Horizontal	E	Odd shape, suspected early failure
Flat (Large)	Horizontal	J	Odd shape, suspected early failure
Flat (Small)	Horizontal	C	Odd shape, suspected early failure

#### **4.6.5 Experimental Design, Materials and Methods**

The details are enclosed in the earlier sections presented in this chapter.

## **Chapter 5**

### **Effect of specimen geometry and orientation on pore space characteristics of Ti-6Al-4V manufactured by electron beam powder bed fusion**

#### **5.1 Preface**

Quantitative examination of the defect space is imperative for reliable quality control assessment. The current work looks at quantitative evaluation of porosity defects in Ti-6Al-4V as-built EB-PBF specimens as a function of geometry, dimension, and build configuration. The occurrence of internal and subsurface pores is highly detrimental to the fatigue performance of manufactured parts, as they act as stress raisers and can eventually lead to premature failure. The effects of bulk and spatially-distributed pore properties on quasi-static tensile properties are not well understood. The current work looks at advancing the study conducted by the authors in prior work (Chapter 4), by employing X-ray computed tomography to assess the pore space characteristics of specimens built for tensile testing. The efforts will focus on establishing deeper correlations between the pore space characteristics (such as total volume, equivalent diameter, frequency, sphericity, aspect ratio, and radial position) and the tensile specimen characteristics (such as geometry, orientation, cross-sectional area, surface area to volume ratio, and tensile behavior). It was observed that all Vertical (V) specimens only displayed pores  $< 200 \mu\text{m}$ , whereas all Horizontal (H) specimens had additionally much larger pores (in some cases up to  $1200 \mu\text{m}$ ). The pore space  $< 100 \mu\text{m}$  was very similar across specimens manufactured in both orientations. The majority of the pores  $< 100 \mu\text{m}$  for both orientations showed a sphericity value  $> 0.8$  and therefore were categorized as gas pores, whereas majority of the pores  $> 200 \mu\text{m}$  showed a sphericity value  $< 0.6$  and therefore were categorized as lack-of-fusion pores. The subsurface pore population was observed to be significantly less for the H specimens having the largest and smallest cross-sectional area, whereas it was quite similar for all V specimens. Lastly, the ultimate tensile strength, yield strength, and elastic modulus were not affected by the pore equivalent diameter. The % elongation was linked to the pore equivalent diameter such that specimens that showed an absence of pores  $> 500 \mu\text{m}$  had higher elongation values. This work is expected to inform the scientific community about the true impact that porosity defects can have on the mechanical properties of EB-PBF specimens.

## 5.2 Introduction

Electron beam powder bed fusion (EB-PBF) is an additive manufacturing (AM) process which makes use of a high-power focused electron beam as a heat source to selectively melt the metal powder to create 3D parts in a layer-by-layer fashion. This process has demonstrated the capability of printing parts with alloys such as Ti-6Al-4V [4]–[6], Ti-48Al-2Cr-2Nb [7]–[9], Co-Cr alloys [10], [11], H13 and 316L steel [12], [13], nickel and nickel-iron alloys [14]–[19], copper [20], [21], to name a few. EB-PBF is used in emerging applications such as turbine blade production [22], engine valves and turbine wheels for turbochargers [23], and induction coils [20] and biomedical implants [24]–[32]. EB-PBF is also a “tool-less” fabrication technology which requires neither fixtures nor tooling to obtain a custom near-net part geometry. The process offers distinct advantages when compared to other metal PBF processes. In EB-PBF, components are manufactured under a controlled vacuum and at an elevated temperature [33]. The vacuum environment is beneficial as it has the potential of having minimal impact on the chemical composition of the powders and is suitable for reactive materials such as titanium alloys [34]. The EB-PBF also results in lower residual stresses in the deposited material by virtue of the elevated process temperature [35]. In addition, the EB-PBF process enables faster build rates owing to the high-power and fast beam scanning capabilities [36]. EB-PBF technology also permits blends of used and new powders to be recycled back into the system, therefore this technology has the potential to be an environmentally friendly process. In contrast, there are many limitations to this process as well. For instance, the part properties may be influenced by the geometry and therefore it can be concluded that no optimal process parameters can be created that cover all design space instances [69], [276]. The orientation, height, location on the build plate, and building angle of a part can influence the thermal history characteristics and material properties, and furthermore can lead to formation of defects and residual stresses [4], [5]. In addition, EB-PBF parts can have a poor surface roughness and geometric fidelity [70]–[74]. Lastly, defects such as cracks, inclusions, porosity, shrinkage, delamination, as a function of specimen geometry, are common and not well studied [37].

Most studies in literature talk about the progress in the EB-PBF manufacturing process and reflect on the experimental analysis of strength parameters; the topic of quantitative evaluation of defects is rarely considered [277]. However, it is very important to quantitatively examine the defect space across a family of geometries for reliable quality control assessment. Usually, parts manufactured for industrial applications need to be accompanied by witness specimens for tensile testing, fatigue testing, metallurgical analysis, hardness testing, and surface topography analysis [278]. This is because assessment and verification of these witness specimens is extremely important for traceability, for quality control purposes, and to examine

the extent to which the unavoidable defects prove to be detrimental to the strength and lifecycle of critical areas of the components [279].

A detailed approach is followed in the current work to quantitatively evaluate porosity defects in Ti-6Al-4V as-built EB-PBF specimens as a function of geometry, dimension, and build configuration. There are two types of process-induced pores commonly observed in EB-PBF parts. Lack-of-fusion pores stem from insufficient powder melting between successive layers or within a layer, while gas pores stem from the entrapment of gas in the melt pool. The two types of pores can be distinguished by their shape; gas pores being spherical and lack-of-fusion pores being elongated and irregular in shape. Lack-of-fusion pores are more detrimental to the performance of manufactured components, when compared to gas pores [106], [277]. There have been some efforts towards reducing and, ideally, fully eliminating these pores, using hot isostatic pressing [85], [244], [280]; however, at the moment such pore defects cannot be completely eliminated [281].

The fatigue life of AM components can be influenced by factors such as the component size, surface topography, microstructure, internal porosity, and subsurface porosity [282]. The occurrence of internal and subsurface pores is highly detrimental to the fatigue performance of manufactured parts as they act as stress raisers and eventually lead to failure [283]. It has been shown that the pores in Ti-6Al-4V EB-PBF specimens, despite occupying only 0.1% to 0.5% of the volume [64], are highly detrimental to the high cycle fatigue life. The pore size, location, and shape are important in determining its influence on crack initiation [35], [38], [281].

Researchers in the AM domain have turned to X-ray computed tomography (XCT), to assess simple and complex geometries, as it enables robust evaluation of internal defects and furthermore assess their effects on part performance. Pathasarathy et al. [147] examined the interconnected pores in porous Ti-6Al-4V EB-PBF structures, using micro-CT scan data. Saâdaoui et al. [284] analyzed zirconia parts to identify and quantify defects and furthermore predict defect formation sites using XCT. Romano et al. [279] investigated the defect population in AlSi10Mg parts, using XCT, to be able to estimate the fatigue life of specimens. Leuders et al. [281] analysed crack growth behavior and porosity of Ti-6Al-4V specimens using XCT. Gong et al. [285] investigated inclusions and defects, using XCT, in Ti-6Al-4V specimens and furthermore created an empirical model to estimate the porosity using reconstructed models of the XCT scans. Ortega et al. [286] used XCT to detect porosity and geometrical fidelity of In718 parts.

It was identified that many studies in literature look at the effect of bulk porosity on mechanical properties and furthermore use this to determine optimal processing parameters [73], [123], [124], [163], [287]. In prior work (Chapter 4) it was found that the bulk porosity had no appreciable effects on the tensile

properties of the specimens. Therefore, it is essential to look at the distribution of the pores (known as pore space distribution from here on) and analyse its effects (if any) on mechanical properties. The current work looks at advancing the study conducted by the authors in Chapter 4, by employing XCT to assess the pore space characteristics of specimens built for tensile testing, in order to address the deeper correlations between the pore space characteristics and the tensile specimen geometry, orientation, cross-sectional area, surface area to volume ratio, and the tensile behavior. This work is expected to inform the scientific community about the true impact that porosity defects can have on the tensile properties of EB-PBF specimens.

### 5.3 Materials and Methods

#### 5.3.1 Additive manufacturing and X-ray computed tomography analysis

The current work extensively analyses the XCT data collected as described in Chapter 4. Therefore, all details regarding the specimen preparation, build layout, additive manufacturing of samples, XCT scanning, and tensile testing can be found in Chapter 4 Section 4.4. Figure 5.1 depicts the build layout for all tensile specimens manufactured using Ti-6Al-4V EB-PBF.

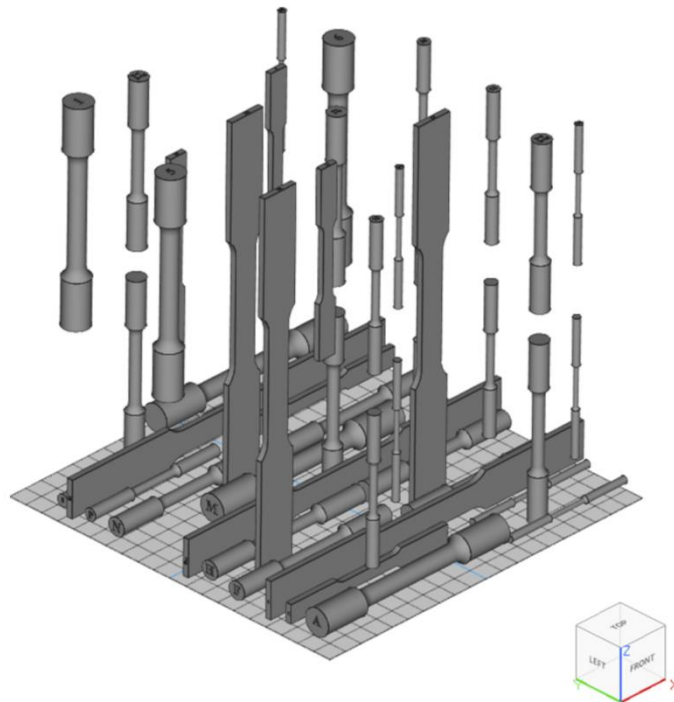


**Figure 5.1 Build layout (for simplicity, support structures have not been shown)**

### 5.3.2 Pore Space Analysis

The MATLAB R2017b function “regionprops” and “regionprops3” [256] were used to evaluate the 2D and 3D volumetric images obtained from the XCT data to retrieve pore information, respectively. The information extracted is mentioned in Figure 5.2 under “pore space analytics code”.

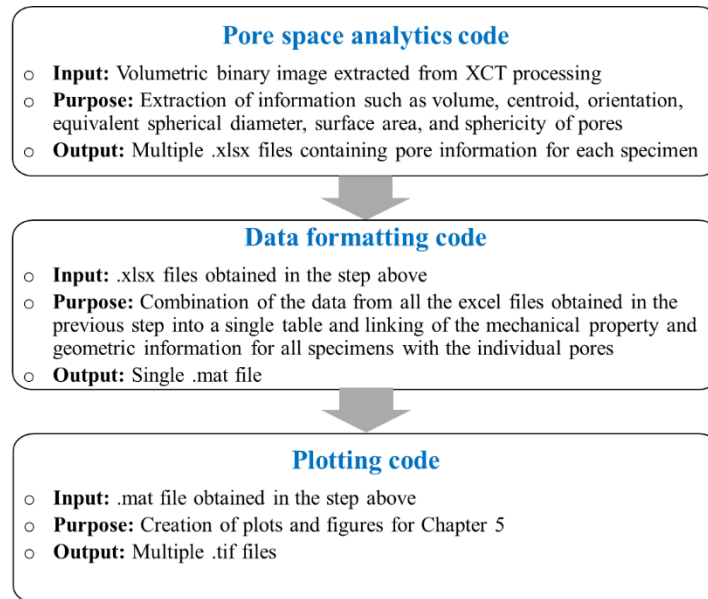


**Figure 5.2 Workflow schematic showing how the data passes from one code module to the other**

The output .xlsx files from the “pore space analytics code” were used as the input for the “data formatting code” as shown in Figure 5.2. Lastly, the output .mat file from the “data formatting code” was used as the input for the “plotting code” as depicted in Figure 5.2. The “pore space analytics code”, “data formatting code”, and “plotting code” are presented in 0, Appendix B, and Appendix C, respectively. The sphericity and aspect ratio are derived from the three principal axes of the pore (Figure 5.3) [288] and are calculated as:

$$Sphericity = \sqrt[3]{c^2/ab} \quad \text{Equation 5.1}$$

$$Aspect\ Ratio = c/a \quad \text{Equation 5.2}$$

where a = dL (longest axis), b = dI (intermediate axis) and c = dS (shortest axis).

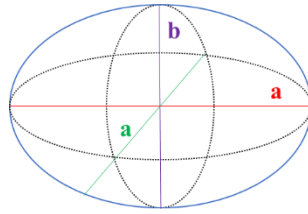


**Figure 5.3 Depiction of the principal axes of the pore**

### 5.3.3 Pore cut-off value determination

As mentioned in Chapter 4, the minimum detectable pore that can be identified with a high degree of confidence is at least  $3 \times 3 \times 3$  voxels (27 voxel-neighborhood in 3D) [255]. Previous work (Chapter 4 Table 4.3) shows that for the Flat (Large) specimens, the minimum detectable pore size is  $42 \mu\text{m}$ . However, for the E8M-5 specimens, the minimum detectable pore size is  $11 \mu\text{m}$ . Therefore, it is not reasonable to compare the pore space characteristics if very small pores can be identified in some specimens (e.g., E8M-5) but not in others (e.g., Flat (Large)) due to the limitations of the XCT scanning voxel resolution. Hence, to accurately compare the pore space characteristics of all specimens,  $50 \mu\text{m}$  was determined as a cut-off value for all subsequent comparisons.

## 5.4 Results and Discussion

### 5.4.1 Effect of specimen orientation on pore space characteristics

In prior work (Chapter 4) it was noted that the specimen orientation had a substantial impact on the tensile properties such that the Horizontally-built (H) specimens showed higher Ultimate Tensile Strength (UTS) and Yield Strength (YS), and lower elongation at fracture (% EL) values when compared to Vertically-built (V) specimens. To understand whether this observation is linked to the pore space characteristics, this chapter looks at the impact of specimen orientation on the pore space characteristics. Figure 5.4 depicts the pore equivalent diameter vs. total pore volume, for all specimens in the V and H orientations. It can be observed that all pores for V specimens (Figure 5.4(a)) are  $< 200 \mu\text{m}$ , with the exception of E8M-2 specimen that has few pores  $> 600 \mu\text{m}$ . Contrary to this, Figure 5.4(b) depicts that H specimens have a considerably larger number of pores that are  $> 200 \mu\text{m}$ . In addition to this, it can be observed that for H specimens, although there are many pores  $< 200 \mu\text{m}$ , the pores  $> 200 \mu\text{m}$  contribute a much larger overall proportion of the pore volume (despite forming a minor fraction, in terms of number of the pore population).

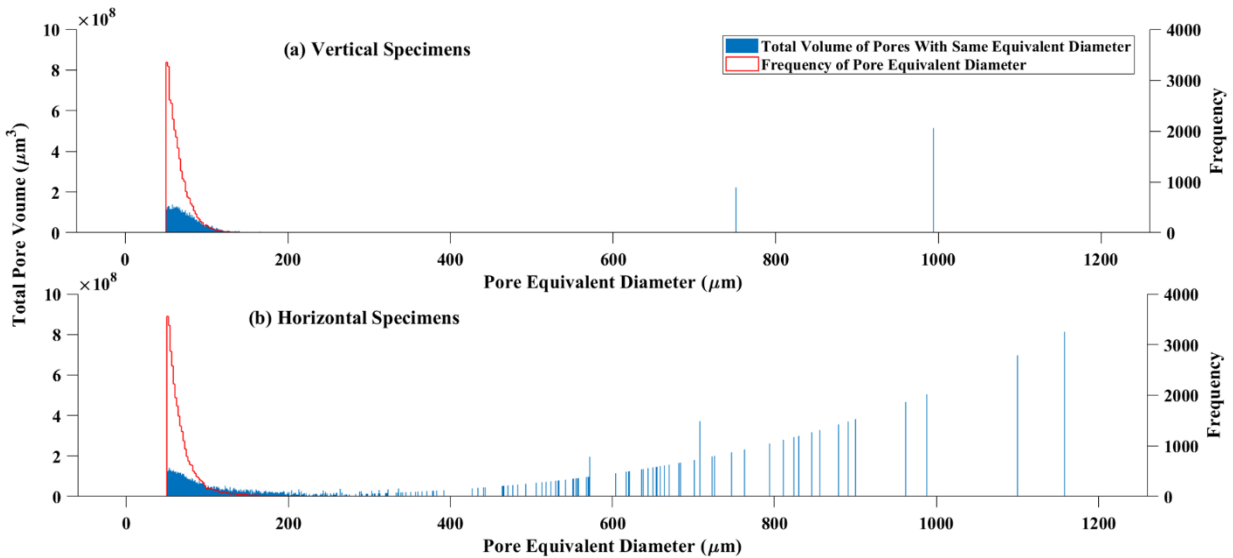


**Figure 5.4 Pore equivalent diameter vs. the total pore volume for all specimens, where (a) and (b) represent the compilation on the pore space data for all vertical and horizontal specimens, respectively.**

To further segregate the pore defect distribution by specimen type, Figure 5.5 was created. On each box in this figure, the central mark indicates the median, and the bottom and top edges of the box indicate the 25th and 75th percentiles, respectively. The whiskers extend to the most extreme data points not considered outliers, and the outliers are plotted individually using the '+' symbol. Taking a closer look at the pores between 50  $\mu\text{m}$  and 200  $\mu\text{m}$  (in Figure 5.6) it is observed that the mean, 25<sup>th</sup> percentile, and extreme data points appear to be very similar for both V (Figure 5.6(a)) and H (Figure 5.6(b)) specimens. From Figure 5.5 and Figure 5.6 it can be concluded that the pore frequency, for pores < 100  $\mu\text{m}$ , across all specimen types and orientations is the same. Furthermore, for H specimens (Figure 5.5(b)) the pores > 200  $\mu\text{m}$  do not show any specific trends across the specimen types.



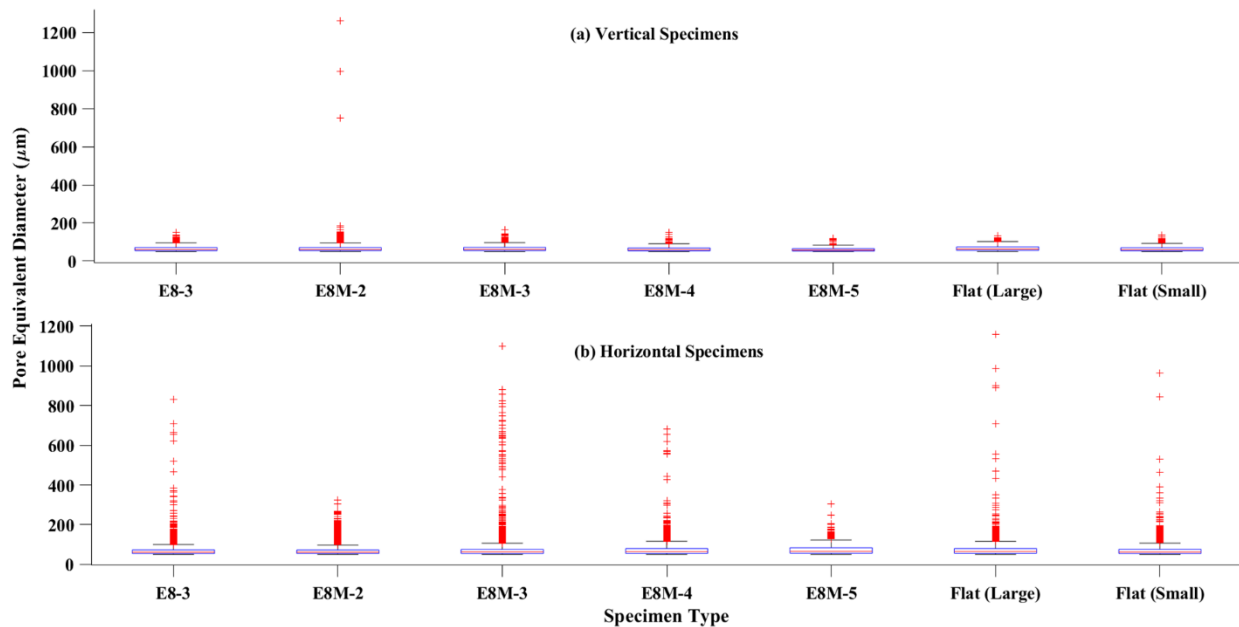


**Figure 5.5 Specimen type vs. pore equivalent diameter for all pores > 50 μm, where (a) and (b) are the vertical and horizontal specimens, respectively.**

Many studies in literature have mentioned that the most common pores observed in AM parts, upon conducting metallographic investigations, have a circular profile and are < 100 μm in size [4], [5], [289]. These defects have been classified as gas pores and are presumed to be caused by trapped bubbles during melt pool solidification. In laser powder bed fusion (LPBF), that uses an inert atmosphere, these bubbles are expected to originate from the shielding gas that is trapped during powder densification [290]. However, the EB-PBF process takes place under a vacuum environment and therefore this is unlikely to be the cause for pores < 100 μm. A detailed investigation on the circular pores in EB-PBF Ti-6Al-4V conducted by Tammam-Williams [291] shows that gas pores in manufactured part are caused due to the trapped gas in the powder feedstock, during the atomization (gas or plasma) process. When these powders are used in the process, they melt, and the entrapped gas is released in the melt pool and allowed to expand by the reduced pressure in the build chamber. The authors believe that this may be part of the reason why both H and V specimens show similar pore space for pores < 100 μm. Therefore, the authors suspect that, if the process parameters are kept constant, these pores will appear in specimens of any size and geometry, irrespective of their build orientation and dimension. If the porosity is influencing the tensile properties, then it is hypothesized that the influence on tensile properties would be caused due to the pores > 100 μm since the distribution for pores < 100 μm is similar for both orientations.

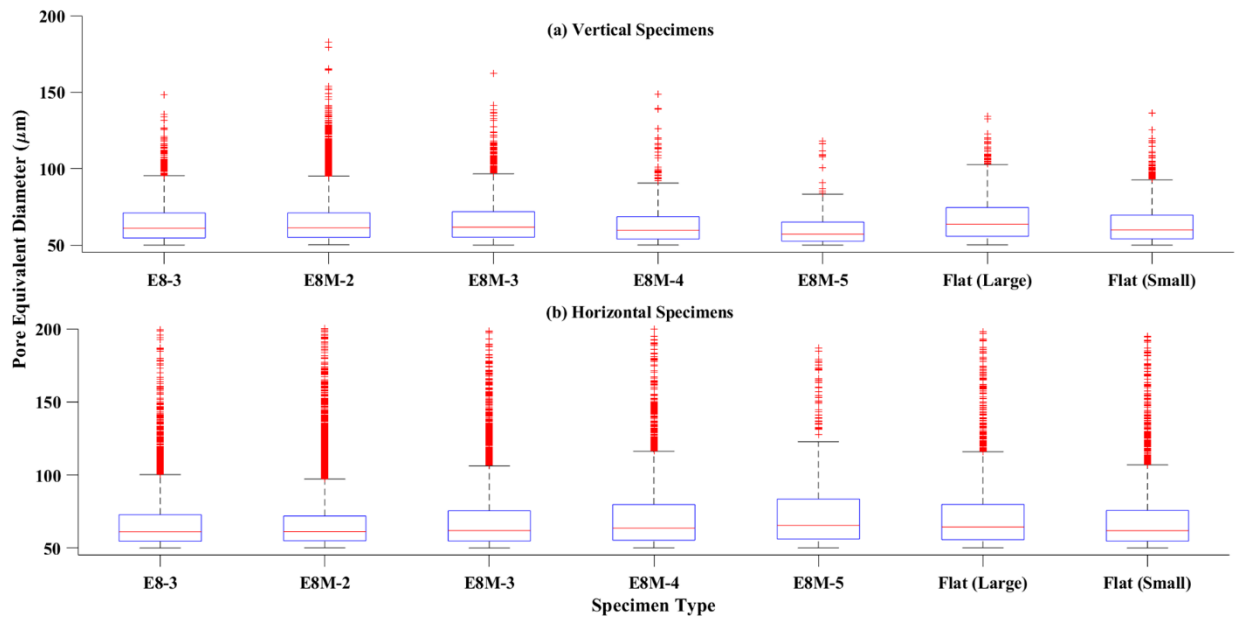


**Figure 5.6 Specimen type vs. pore equivalent diameter for all pores between 50 µm and 200 µm where (a) and (b) are the vertical and horizontal specimens, respectively.**

Figure 5.7 was created to further confirm the observation that the defect space is similar for H and V specimens for pores < 100 µm. From this figure, it can be conclusively stated that the number of pores < 100 µm is the same for specimens manufactured in both orientations. The H and V specimens show similar pore size distributions from 100 µm to 200 µm, however the H specimens have a larger number of pores within this range. The actual difference in the number of pores per specimen is low since the total number of pores (for all H specimens) has a low absolute value.

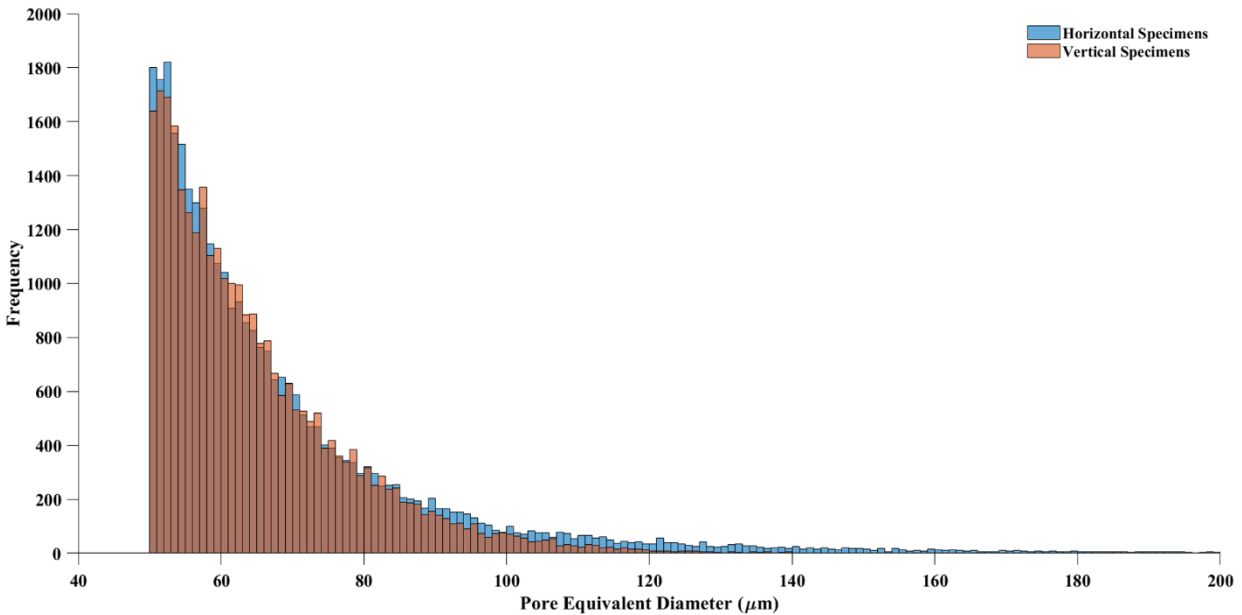


**Figure 5.7 Pore equivalent diameter vs. frequency for all pores between 50  $\mu\text{m}$  and 200  $\mu\text{m}$  for both vertical and horizontal specimens**

The next characteristic to investigate is the sphericity of the pores. From Figure 5.8, it can be observed that majority of the pores  $< 100 \mu\text{m}$  for V (Figure 5.8(a)) and H (Figure 5.6(b)) specimens have a sphericity  $> 0.8$ . Pores with such high sphericity values are categorized as gas pores [123], [126], [291]; therefore, it can be stated that pores  $< 100 \mu\text{m}$  in this study are gas pores. Conversely, the majority of the pores  $> 200 \mu\text{m}$ , for H specimens, have a sphericity value  $< 0.6$  and therefore are categorized as non-spherical pores. There were only three pores  $> 200 \mu\text{m}$  in the V specimens all of which had a sphericity value  $< 0.6$ . Many studies in literature have mentioned that undesirable process conditions, such as un-optimized process parameters can lead to insufficient melting between powder layers or between adjacent beam passes [122], [126]. This insufficient melting between layers is known as lack-of-fusion. Lack-of-fusion defects are characterized by their elongated and non-spherical shape, and these are usually  $> 200 \mu\text{m}$  in size [122], [126], [292]. Therefore, it can be inferred that pores  $> 200 \mu\text{m}$  in this study are lack-of-fusion pores. Additionally, there are pores between  $100 \mu\text{m}$  and  $200 \mu\text{m}$  that the authors suspect fall within a transitional range where there are a large number of pores that are both spherical and non-spherical as observed in Figure 5.8. It should be noted that many of the pores at the very low end of the range (closer to  $50 \mu\text{m}$ ) show a wide range in sphericity values and this is attributed to the pixelation of the pores when analyzing the XCT data. It is not that the sphericity values are incorrect, however they might not be entirely accurate in representing the pore and its sphericity because of the low resolution; data in this range (close to  $50 \mu\text{m}$ )

is considered to have some uncertainty. It is important to quantify the sphericity of the pores since it is known that the sphericity is an indication of the type of defect (e.g., gas pores, lack-of-fusion pores). Additionally, large non-spherical pores are observed to be sources of preferential crack nucleation and propagation [293] and therefore recognizing these pores can help in further finding ways of eliminating them. The type of metric illustrated in Figure 5.8 provides visibility into the origins of pores and may help to infer strategies to mitigate defects via process parameter optimization.

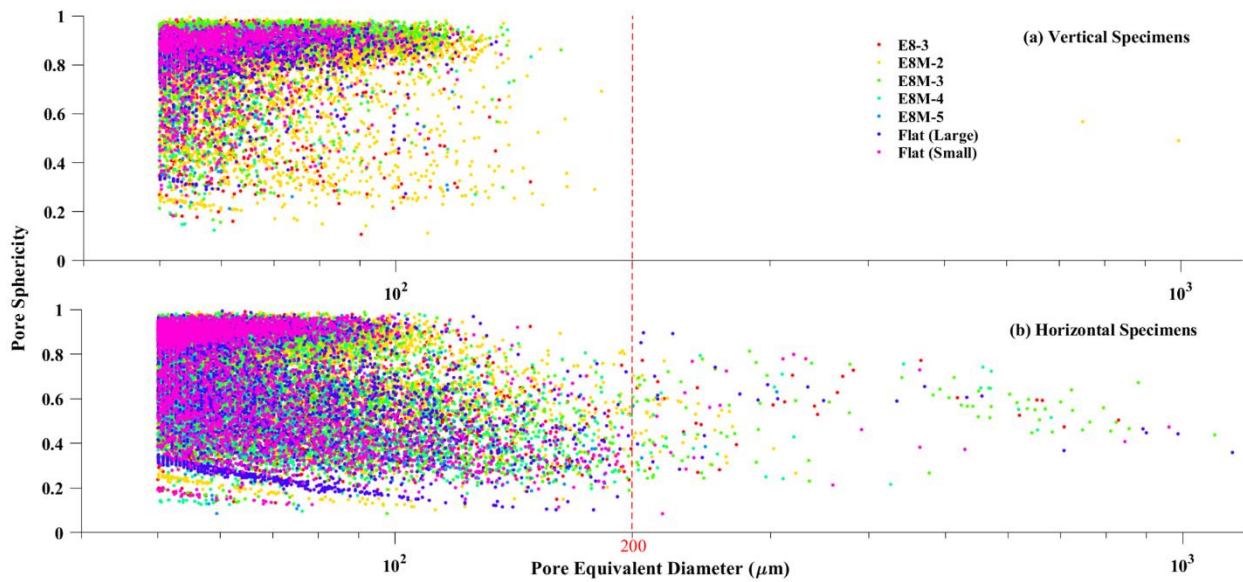


**Figure 5.8 Pore equivalent diameter vs. sphericity for all pores > 50  $\mu\text{m}$ , where (a) and (b) are the vertical and horizontal specimens, respectively.**

To further strengthen the conclusion on lack-of-fusion pores, a new visualization methodology was created, as detailed in Figure 5.9. This figure shows that the aspect ratio for majority of the pores for V specimens is  $> 0.6$  whereas that for H specimens is  $< 0.6$ . It has been stated by many researchers that pores  $> 200 \mu\text{m}$  in EB-PBF are lack-of-fusion pores [65], [126], [294] and furthermore, the more pronounced the lack-of-fusion defect, the smaller the sphericity and aspect ratio values. The irregularly shaped lack-of-fusion pores can create higher stress concentrations and therefore prove to be more damaging to the mechanical properties of the specimens [293]. It is important to report both sphericity and aspect ratio values as sphericity accounts for the intermediate axis of the pore (see Section 5.3.2 for more details), whereas the aspect ratio is more indicative of a worst-case scenario where it is only comparing the longest to the shortest axis. Similar to Figure 5.8, Figure 5.9 provides visibility into types of pores towards parameter optimization.

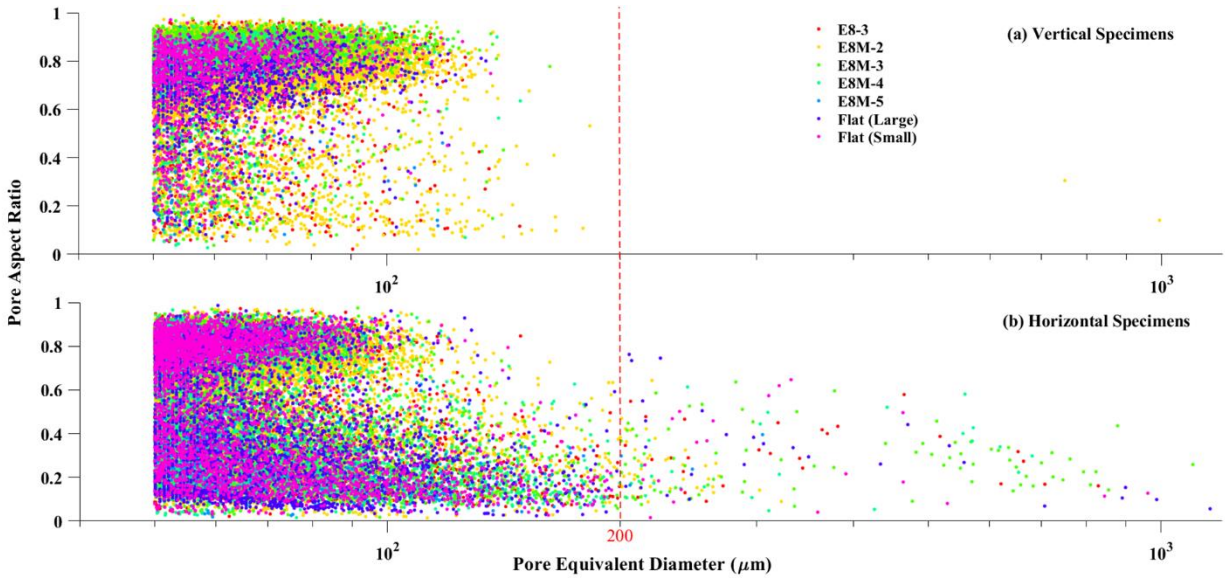


**Figure 5.9 Pore equivalent diameter vs. aspect ratio for all pores > 50  $\mu\text{m}$ , where (a) and (b) are the vertical and horizontal specimens, respectively.**

Lastly, the authors created five categories (or classes) of pores (Class A, Class B, Class C, Class D, and Class E) according to Table 5.1 to divide the pores based on their size, as measured by XCT. The classification range for Class E is defined based on the cut-off value (as described earlier in Section 5.3.3) going up to the maximum equivalent pore diameter suggested for gas pores (i.e., 100  $\mu\text{m}$ ). The Class D pores are a transitional range spanning from the maximum diameter for gas pores (101  $\mu\text{m}$ ) to the minimum diameter for the lack-of-fusion pores (200  $\mu\text{m}$ ). After the 200  $\mu\text{m}$  diameter range, the number of pores decreases significantly, however, these would be the most detrimental pores [126], [292] and therefore it is important to break up the range to ensure that proper correlations can be made between the effect of specimen geometry and orientation on the pore equivalent diameter. Figure 5.10 depicts the number of pores for all pore classes for all specimen types where (a) and (b) are the vertical and horizontal specimens, respectively. This figure demonstrates that the Class D and Class E pores form a major proportion, in terms of number, of the pore population for all specimens irrespective of their build orientation.

**Table 5.1 Pore classification according to pore equivalent diameter**

Class of pores	Pore equivalent diameter
A	> 500 $\mu\text{m}$
B	301 $\mu\text{m}$ to 500 $\mu\text{m}$

C	201 $\mu\text{m}$ to 300 $\mu\text{m}$
D	101 $\mu\text{m}$ to 200 $\mu\text{m}$
E	50 $\mu\text{m}$ to 100 $\mu\text{m}$

The major difference between the specimens built in both orientations is that the H specimens display Class A, Class B and Class C pores, but the V specimens do not (with the exception of E8M – 2 V specimen). Despite the fact that H specimens contain a significant number of lack-of-fusion pores, they show higher UTS, YS values when compared to V specimens. Therefore, it can be concluded that the UTS and YS behavior does not depend on the pore size of the specimens. However, a reduction in % EL was observed in the H specimens. This can be correlated to the presence of lack-of-fusion pores, as large pores act as fracture initiation sites and thus lead to early failure of the specimen leading to a lower % EL value, as explained in Chapter 4.

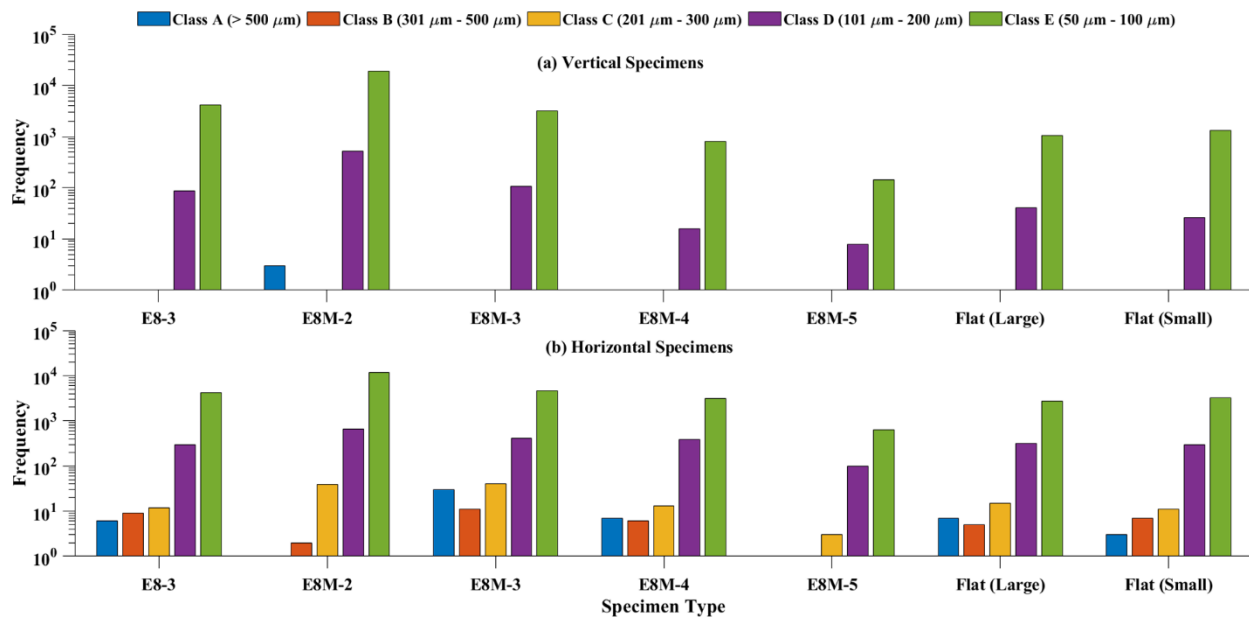


**Figure 5.10** Number of pores for all pore classes, for all specimen types, where (a) and (b) are the vertical and horizontal specimens, respectively.

Another observation (in Chapter 4 Section 4.5.3.4) was that the % EL for E8M-2 H and E8M-5 H specimens was higher than all other H specimen types. The authors hypothesized that this occurrence may be due to the fact that the porosity in E8M-2 and E8M-5 specimens is made up of smaller, and more evenly-spaced pores compared to all other specimen types. From Figure 5.10 this hypothesis can be

verified. It is observed that the E8M-2 H and E8M-5 H specimens are the only 2 H specimen types that do not have Class A pores. This can lead us to the conclusion that Class A pores are the most detrimental pores when it comes to the elongation behavior of the specimens. More comprehensive pore classification methods have been proposed (see example here [295]), however, this was deemed out of scope for the current work. More robust classifiers may show groups or classes of pores that are not inherently obvious when looking at equivalent diameter and it is important to explore this further to ensure all classes of pores can be correlated to mechanical properties.

### 5.4.2 Effect of specimen cross-sectional area on pore space characteristics

In prior work (Chapter 4) it was noted that an increase in specimen cross-sectional area led to an increase in the UTS, YS and Elastic Modulus (E) values and no change in the % EL values. To understand whether this observation is linked to the pore space characteristics, this section looks at the impact of specimen cross-sectional area on the pore space characteristics. It is worth mentioning again that the E8M-3 and E8-3 sample types have the same gauge diameter (i.e., 6 mm) and therefore have the same cross-sectional area. To categorize the pore defect distribution by specimen cross-sectional area, the assessment captured in Figure 5.11 was created.

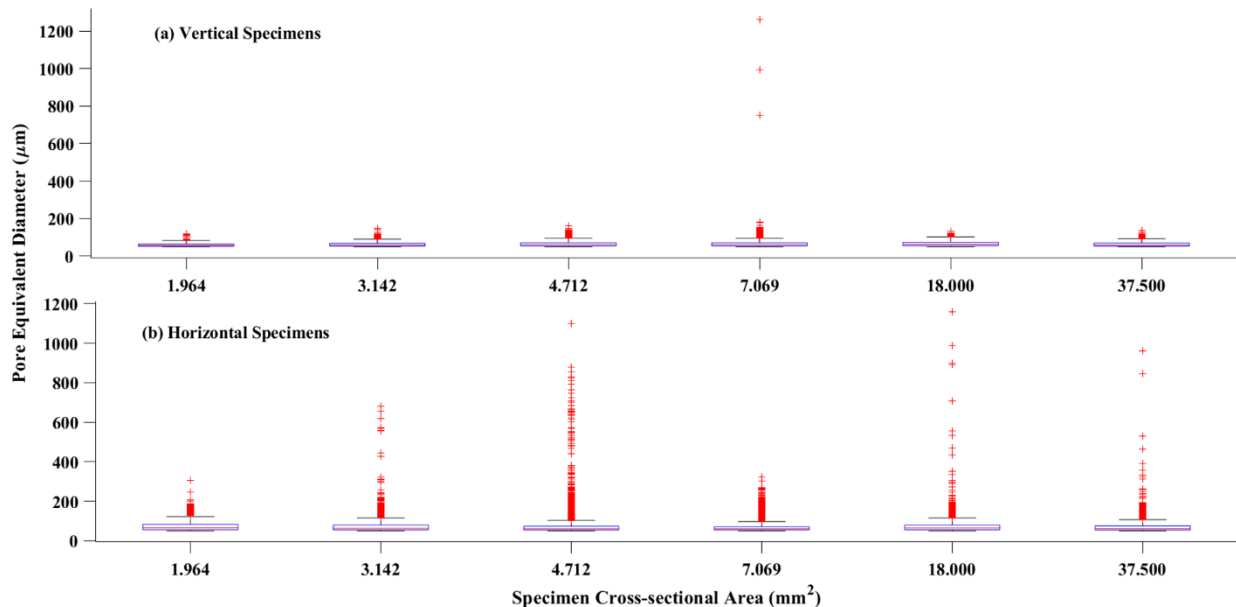


**Figure 5.11 Specimen cross-sectional area vs. pore equivalent diameter for all pores > 50  $\mu\text{m}$ , where (a) and (b) are the vertical and horizontal specimens, respectively.**

When looking at Figure 5.11, no trends in the pore frequency, with respect to specimen cross-sectional area, are observed. The only observation, previously established in Figure 5.5, is that all pores for V specimens (Figure 5.11(a)) are  $< 100 \mu\text{m}$ , and H specimens (Figure 5.11(b)) have a considerably larger number of pores that are  $> 200 \mu\text{m}$ .

Upon investigating the pores between  $50 \mu\text{m}$  and  $100 \mu\text{m}$  (Figure 5.12), similar observations can be made, i.e., there are no trends in the pore space distribution with respect to the specimen cross-sectional area. Therefore, it can be conclusively stated that the change in the tensile properties (UTS, YS, and E) seen in prior work (Chapter 4) is not caused by the pores  $< 100 \mu\text{m}$ .

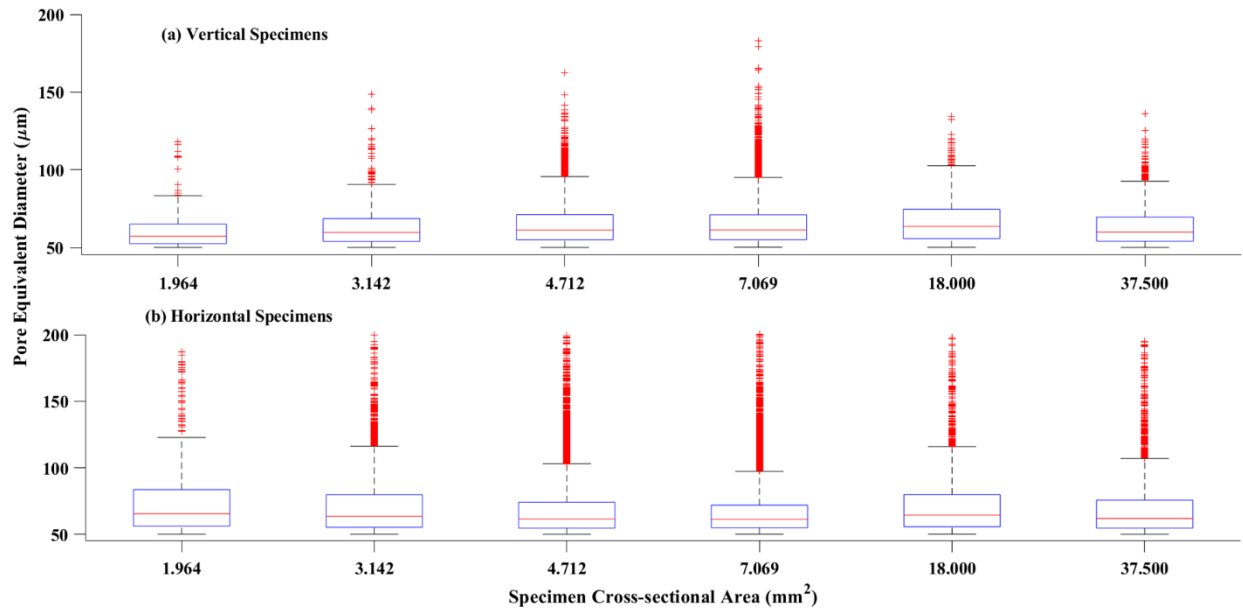


**Figure 5.12 Specimen cross-sectional area vs. pore equivalent diameter for all pores between  $50 \mu\text{m}$  and  $200 \mu\text{m}$  where (a) and (b) are the vertical and horizontal specimens, respectively.**

The analyses thus far relied on the bulk pore characteristics, rather than their spatial location. It has been concluded by many researchers that apart from the shape and size; the location of pores is also essential in determining the impact they have on the reduction in mechanical properties such as elongation at fracture or fatigue life [281], [292], [296]. Specifically, it is important to assess and evaluate the surface, sub-surface, and internal pore defects. Wycisk et al. [296] demonstrated that the surface pores affect the low cycle fatigue tests and the internal pores affect the high cycle tests. They also observed that internal pores  $> 500 \mu\text{m}$  significantly reduced the number of cycles to failure, thus causing premature failure of the part. As such, an important characteristic to assess is the radial distance of the pores from the center of the specimen vs. pore equivalent diameter. Figure 5.13, Figure 5.14, Figure 5.15, Figure 5.16, and Figure 5.17 depicts the



radial distance of the pores from the center of the specimen vs. pore equivalent diameter for E8M-2, E8M-3, E8M-4, E8M-5, and E8-3 specimens, respectively. The E8M-2, E8M-3, E8M-4, E8M-5, and E8-3 cylindrical specimens have a diameter of 9 mm, 6 mm, 4 mm, 2.5 mm, and 6 mm, respectively. From these figures it can be observed that there is an increase in the number of pores and pore equivalent diameter in the subsurface region for all specimens. It is worth mentioning again that for the purpose of XCT analysis, only closed pores were evaluated. Upon careful investigation, it is observed that this increase, for cylindrical specimens, depends on the specimen cross-sectional area and build orientation. The subsurface pore density for all V specimens is quite similar such that effective elimination of the subsurface pores by machining  $\sim 0.5$  mm off the surface, is possible. The subsurface pore density for H specimens has a high degree of variability, requiring geometry-specific machining cutting depth to address such defects. The pores in the core of all V and H specimens show a similar defect distribution.

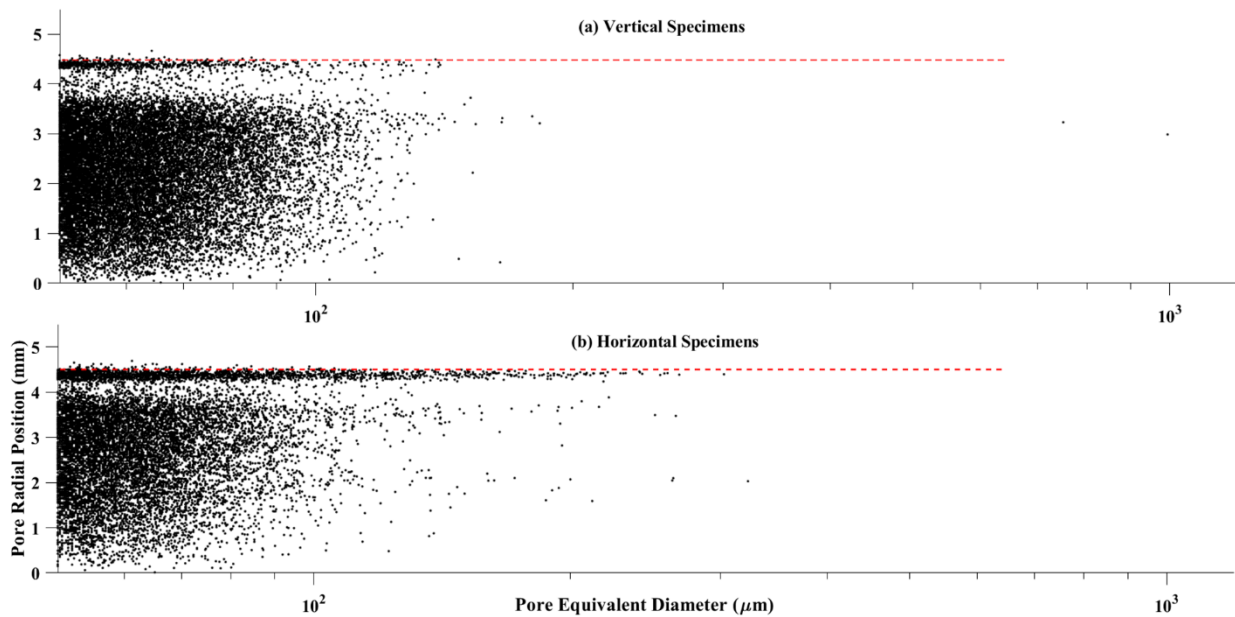


**Figure 5.13 Radial distance of the pores from the center of the specimen vs. pore equivalent diameter for E8M-2 specimens for V and H orientations. Pore radial position is with respect to the center of the part; E8M-2 components have a nominal radius of 4.5 mm.**

For the E8M-2 H (Figure 5.13) and E8M-5 H (Figure 5.16) specimens, i.e., specimens having the largest and smallest cross-sectional area, the population of the subsurface pores is significantly less when compared to all other H specimens (Figure 5.14, Figure 5.17, and Figure 5.15). In previous work (Chapter 4 Section 4.5.3.2), it was noted that the H specimens showed a trend where the % EL was highest for the E8M-5 and

E8M-2 specimens. This behavior was linked to the maximum pore size. The values for maximum pore size for E8M-2 H and E8M-5 H specimens were much lower than that for the E8M-3 H, E8-3 H, and E8M-4 H specimens. Although the subsurface pore density for E8M-2 and E8M-5 specimens is different; the overwhelming majority of the pores  $> 200 \mu\text{m}$  lie in the core of the specimens and not the subsurface region. Furthermore, the maximum pore size outlined in prior work (Chapter 4) is  $323.5 \mu\text{m}$  and  $305.4 \mu\text{m}$  for E8M-2 H and E8M-5 H specimens, respectively. These are clearly observed to be in the core or internal region of the pore space when looking at Figure 5.13 and Figure 5.16. Therefore, it can be conclusively stated that the % EL of the specimens is linked to the internal porosity and not the subsurface porosity.

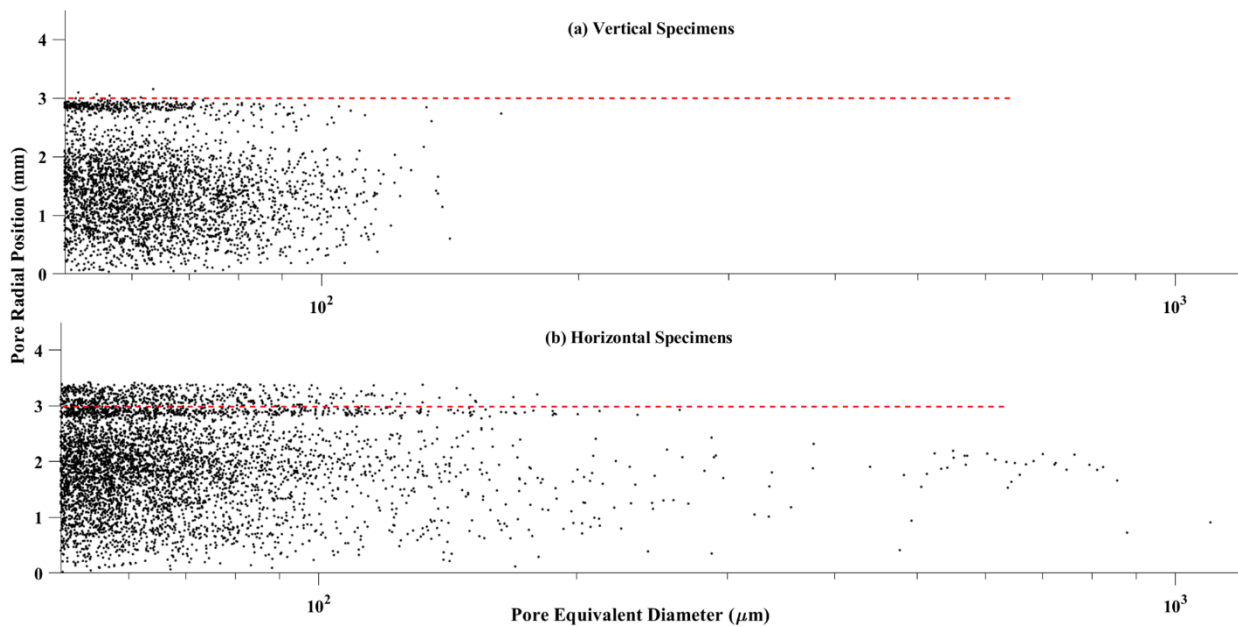


**Figure 5.14 Radial distance of the pores from the center of the specimen vs. pore equivalent diameter for E8M-3 specimens for V and H orientations. Pore radial position is with respect to the center of the part; E8M-3 components have a nominal radius of 3 mm.**

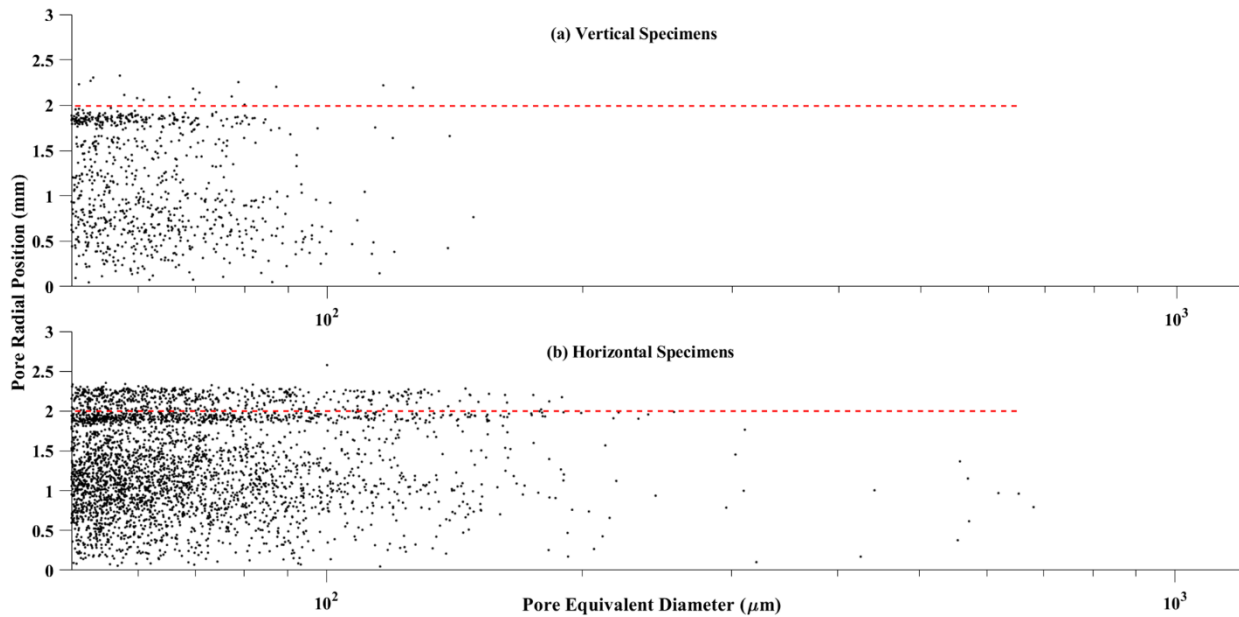


**Figure 5.15 Radial distance of the pores from the center of the specimen vs. pore equivalent diameter for E8M-4 specimens for V and H orientations. Pore radial position is with respect to the center of the part; E8M-4 components have a nominal radius of 2 mm.**

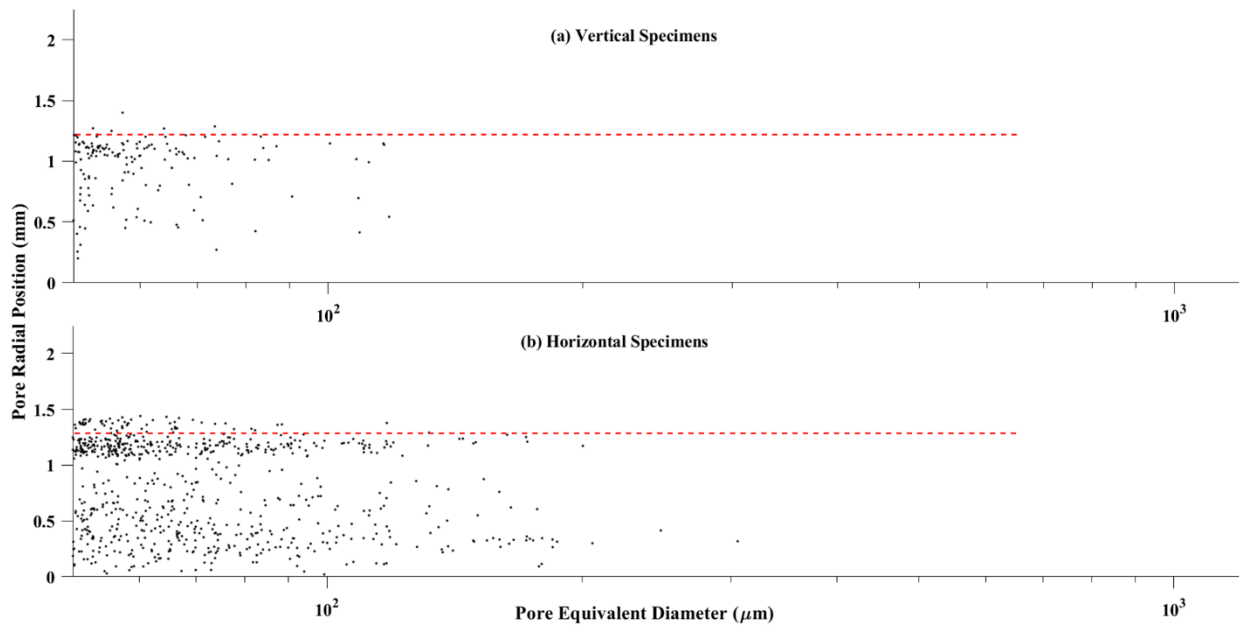


**Figure 5.16 Radial distance of the pores from the center of the specimen vs. pore equivalent diameter for E8M-5 specimens for V and H orientations. Pore radial position is with respect to the center of the part; E8M-5 components have a nominal radius of 1.25 mm.**

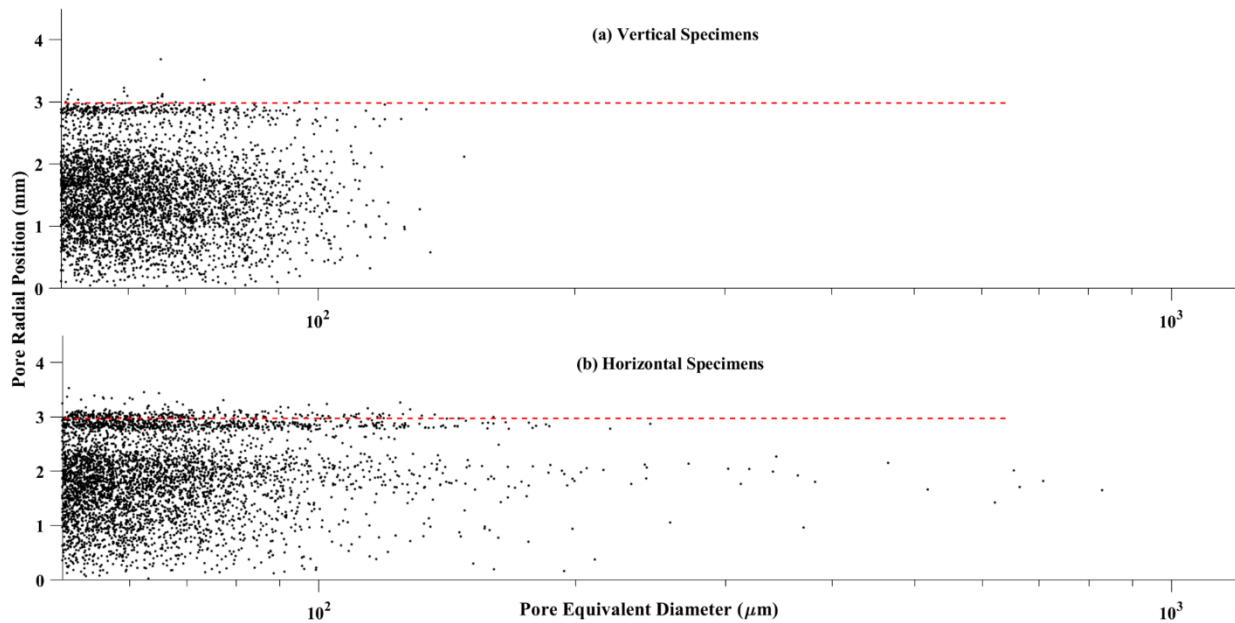


**Figure 5.17 Radial distance of the pores from the center of the specimen vs. pore equivalent diameter for E8-3 specimens for V and H orientations. Pore radial position is with respect to the center of the part; E8-3 components have a nominal radius of 3 mm.**

Figure 5.18 depicts the number of pores, for all pore classes, with respect to the cross-sectional area where (a) and (b) are the vertical and horizontal specimens, respectively. Once again, the only trend observed is that the H cylindrical specimens with the smallest (E8M-5, area: 1.9365 mm<sup>2</sup>) and largest cross-sectional area for (E8M-2, area: 7.0686 mm<sup>2</sup>) have no Class A pores. However, in Chapter 4 it was mentioned that an increase in specimen cross-sectional area showed no change in the % EL values. This strengthens the authors' conclusion that the increase in tensile properties, with an increase in specimen cross-sectional area, is not related to the pore space of the specimens.

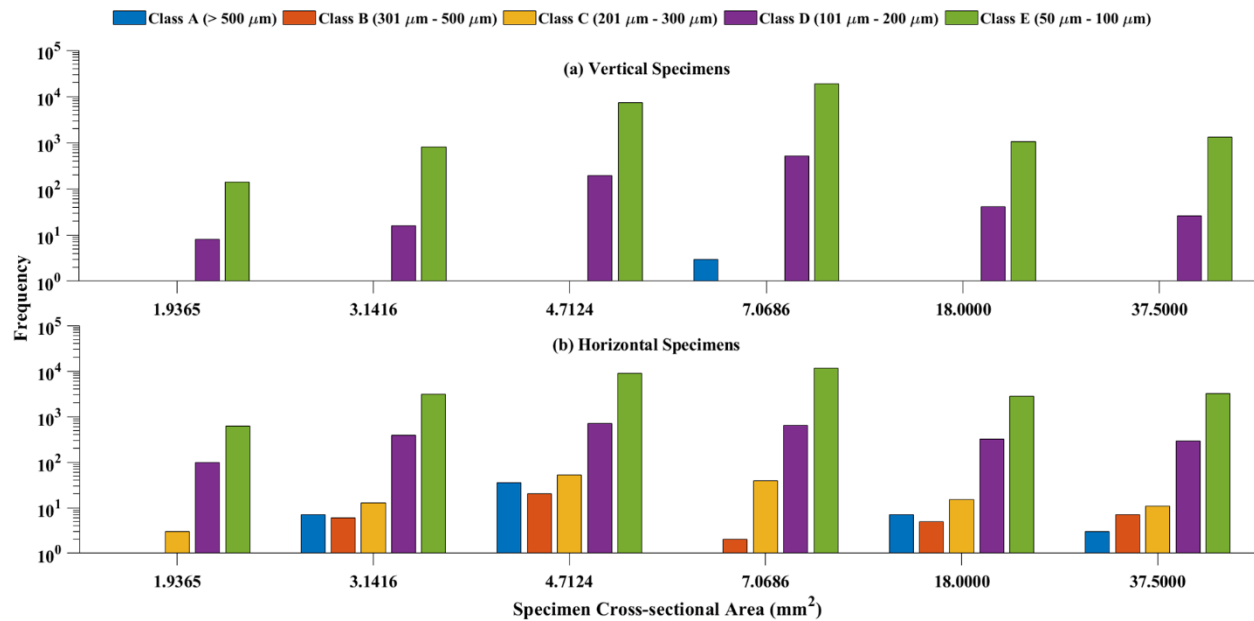


**Figure 5.18** Number of pores, for all pore classes, with respect to the cross-sectional area, where (a) and (b) are the vertical and horizontal specimens, respectively.

### 5.4.3 Effect of specimen surface area to volume ratio on pore space characteristics

In Chapter 4 it was noted that the UTS and YS decreased with an increasing surface area to volume ratio for all specimens. As explained in prior work (Chapter 4 Section 4.5.3.3) the surface area of the specimens was calculated based on the designed gauge diameter for the cylindrical specimens and based on the designed thickness and width for the flat specimens. The volume was then calculated using the gauge length. It was also observed that the samples having surface area to volume ratio between 0.5 /mm to 1.25 /mm exhibit lower elongation values. To understand whether these observation are linked to the pore space characteristics, this section looks at the impact of specimen surface area to volume ratio on the pore space characteristics. To categorize the pore defect distribution by specimen surface area to volume ratio; Figure 5.19 was created. It is worth mentioning again that a few sample types have identical surface area to volume ratios. E8M-4 and Flat (Small) specimens have a surface area to volume ratio of 1.00, E8M-3 and E8-3 have a surface area to volume ratio of 0.67. When looking at Figure 5.19, no trends in the pore space distribution, with respect to specimen surface area to volume ratio, are observed.

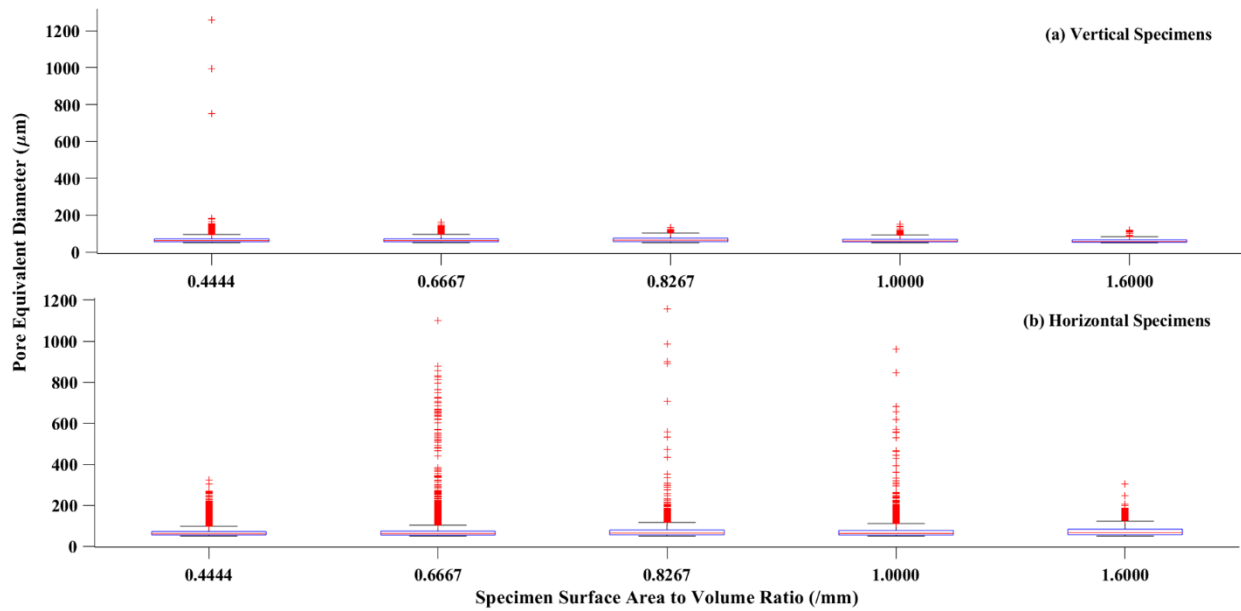


**Figure 5.19 Specimen surface area to volume ratio vs. pore equivalent diameter for all pores > 50 µm, where (a) and (b) are the vertical and horizontal specimens, respectively.**

Upon investigating the pores between 50 µm and 100 µm (Figure 5.12), similar observations can be made, i.e., there are no trends in the pore space distribution with respect to the specimen surface area to volume ratio. Therefore, it can be conclusively stated that the change in the tensile properties (UTS, YS and E) is not caused by the pores < 100 µm.

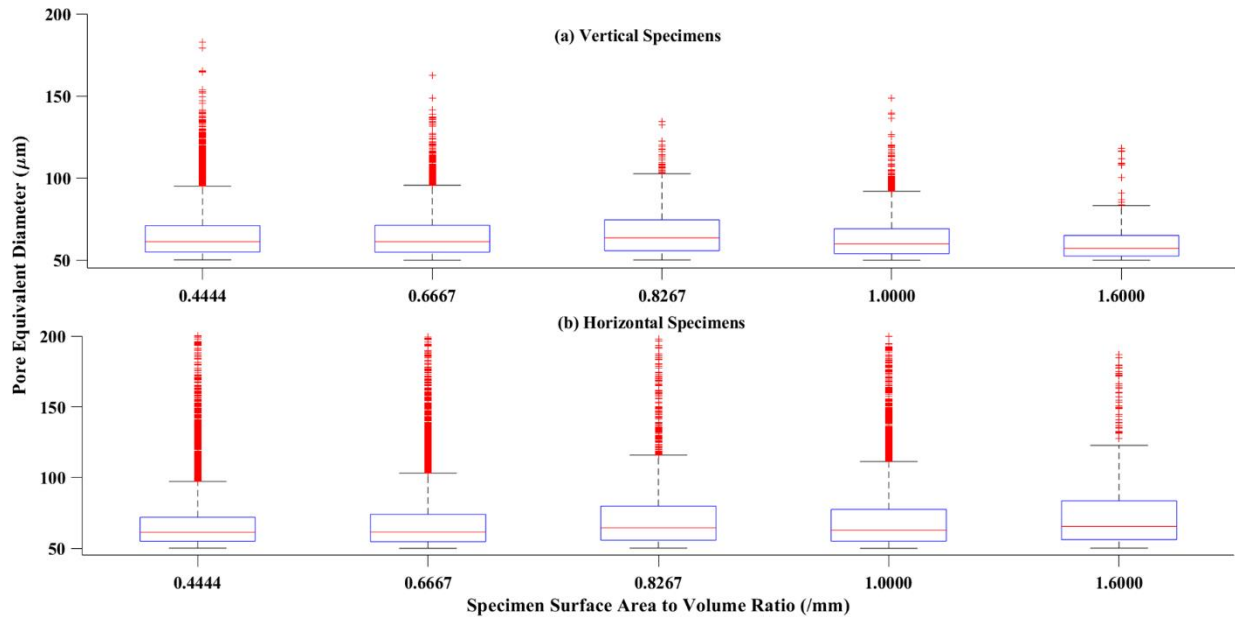


**Figure 5.20 Specimen surface area to volume ratio vs. pore equivalent diameter for all pores between 50  $\mu\text{m}$  and 200  $\mu\text{m}$  where (a) and (b) are the vertical and horizontal specimens, respectively.**

Figure 5.21 depicts the number of pores, for all pore classes, with respect to the surface area to volume ratio where (a) and (b) are the vertical and horizontal specimens, respectively. In Chapter 4 it was mentioned that specimens having a surface area to volume ratio between 0.5 /mm to 1.25 /mm had lower elongation values. The authors hypothesized that this change in elongation values is caused by the change in maximum pore size and is the same as what was seen when comparing just the effects of cross-sectional area in the previous section. This again indicates that the largest (E8M-2) and smallest (E8M-5) specimens, which correspond to the lowest and highest surface area to volume ratio, have smaller and more evenly spaced pores, giving them better elongation values. From Figure 5.21 this hypothesis can be verified. It is observed that the specimens with the smallest and largest surface area to volume ratio have no Class A pores. Additionally, it can be observed that specimens having surface area to volume ratios between 0.5 /mm to 1.25 /mm have pores belonging to all five classes. Once again, this leads us to the conclusion that Class A pores are the most detrimental pores when it comes to the elongation behavior of the specimens.

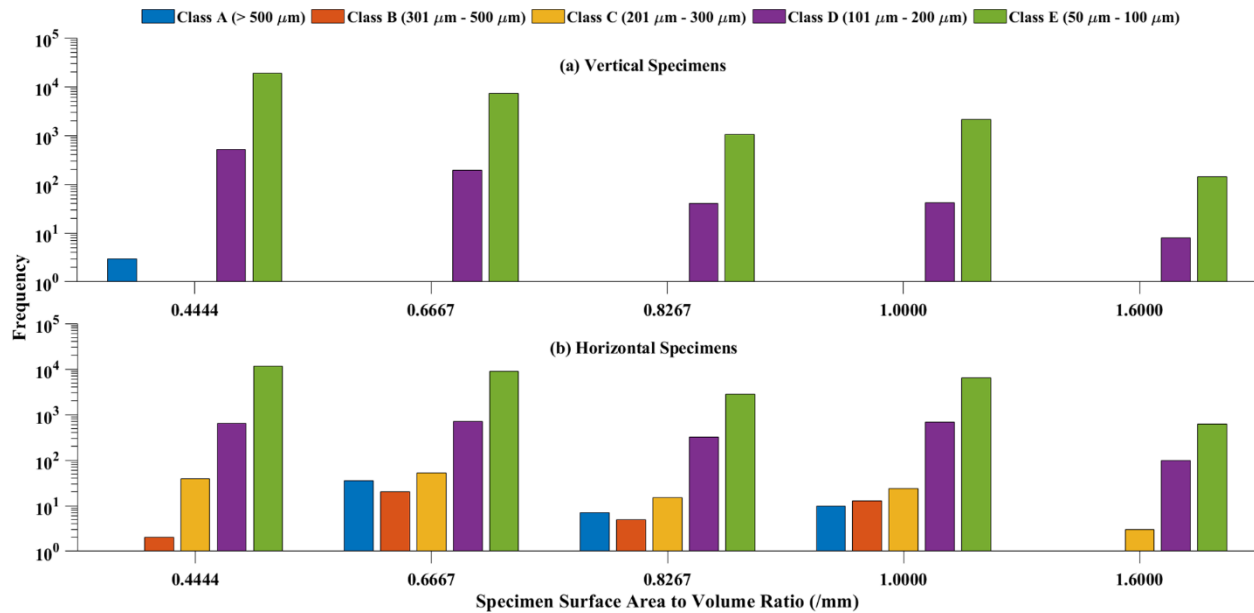


**Figure 5.21** Number of pores, for all pore classes, with respect to the specimen surface area to volume ratio, where (a) and (b) are the vertical and horizontal specimens, respectively.

#### 5.4.4 Effect of pore equivalent diameter on tensile properties

In prior work (Chapter 4) it was noted that the UTS, YS, and E were not affected by the maximum pore size, however, a strong correlation was observed for % EL of H specimens, such that an increase in maximum pore size led to a decrease in % EL. To further dive into this topic, this section looks at the effect of pore equivalent diameter on tensile properties. Figure 5.22, Figure 5.23, Figure 5.24, and Figure 5.25 depict the specimen ultimate tensile strength (UTS), yield strength (YS), elastic modulus (E), and % elongation vs. pore equivalent diameter, respectively. Through these figures, no significant trends can be observed between the UTS, YS, and E, and pore equivalent diameter. Similar to prior work (Chapter 4), there is a strong trend for % EL of H specimens, such that % EL values decrease with an increase in pore frequency of pores > 200 μm. The trend also follows the maximum pore size such that the % EL values decrease with an increase in pore size. One would expect that the presence of the largest pores (Class A pores) would be the most detrimental and therefore are probably more likely the cause of the low values for % EL.

Such a behavior (i.e., no dependence of pore equivalent diameter on the UTS, YS, and E) is not an unexpected result. From a solid mechanics standpoint, the bulk mechanical properties are based on the volumetric ratio of the elements making up a composite material (in this instance the composite is made up of the Ti-6Al-4V and the empty space). Because the bulk density of the specimens is  $\geq 99.28\%$ , as shown



in prior work (Chapter 4), it would be expected that a material that is 99 % dense would nominally have 99 % of the UTS, YS, and E of the bulk properties. This would be expected for a specimen with small uniformly-distributed pores. Large pores that make up a significant proportion of the cross-sectional area of a tensile specimen, could show more of an effect such that the reduced cross-sectional area leads to higher stress in the part with the same loading conditions. However, what is seen in the current work is that the specimens that would have this reduced cross-sectional area, i.e., the H specimens, show the opposite behavior where these parts show a better mechanical performance even though they have reduced cross-sectional area due to the presence of larger pores. This would indicate, as was hypothesized in prior work (Chapter 4), that it is not porosity but the grain size and microstructure that is having a more significant effect between the different orientation and tensile specimen types. However, there is an impact of the pore equivalent diameter on the % EL as these large pores act as stress concentrations and crack initiation points which would allow the part to fail more quickly under plastic deformation [35], [38], [281].

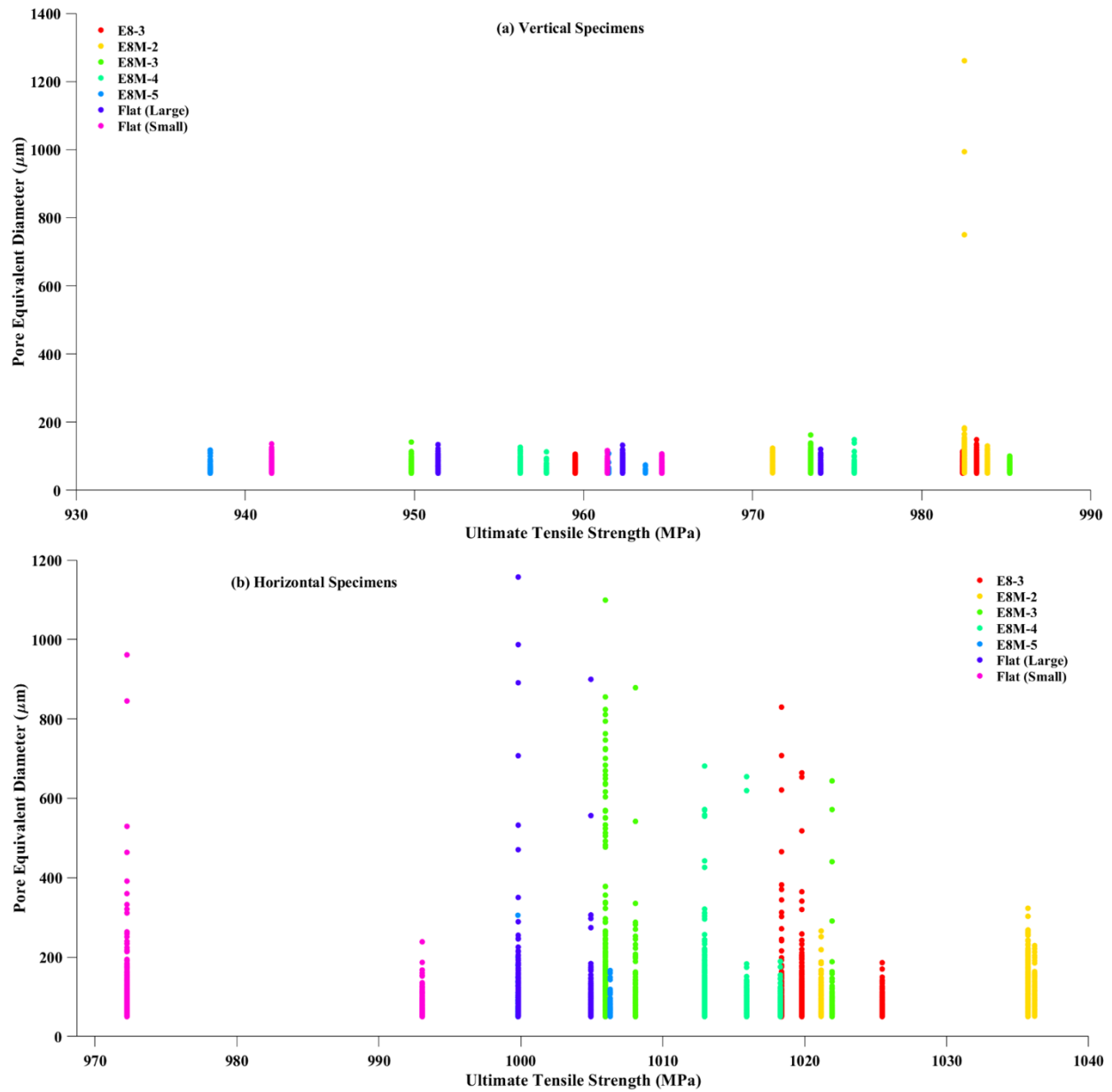


**Figure 5.22 Specimen ultimate tensile strength (UTS) vs. pore equivalent diameter for all pores > 50  $\mu\text{m}$ , where (a) and (b) are the vertical and horizontal specimens, respectively.**

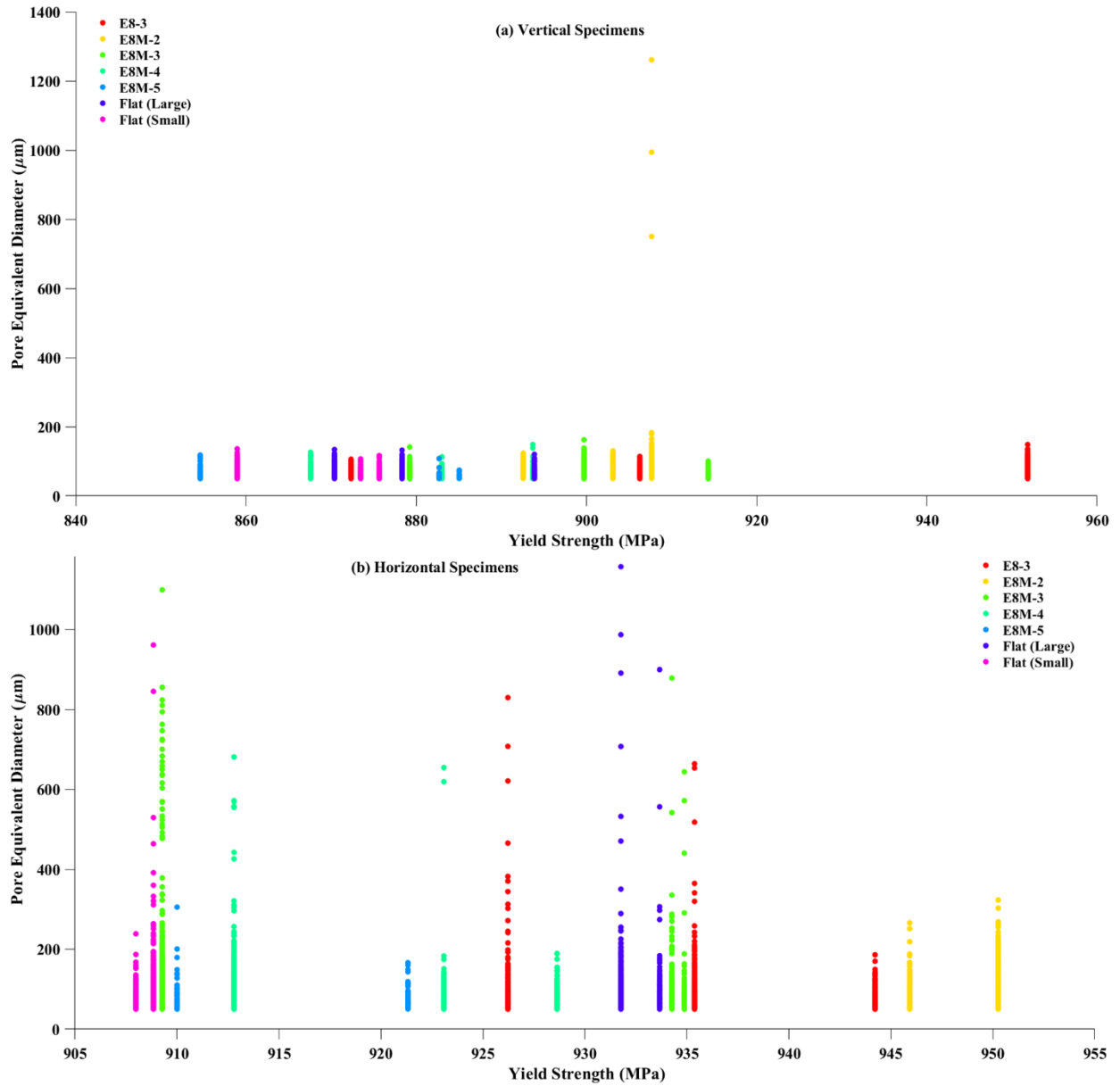


**Figure 5.23 Specimen yield strength (YS) vs. pore equivalent diameter for all pores > 50  $\mu\text{m}$ , where (a) and (b) are the vertical and horizontal specimens, respectively.**

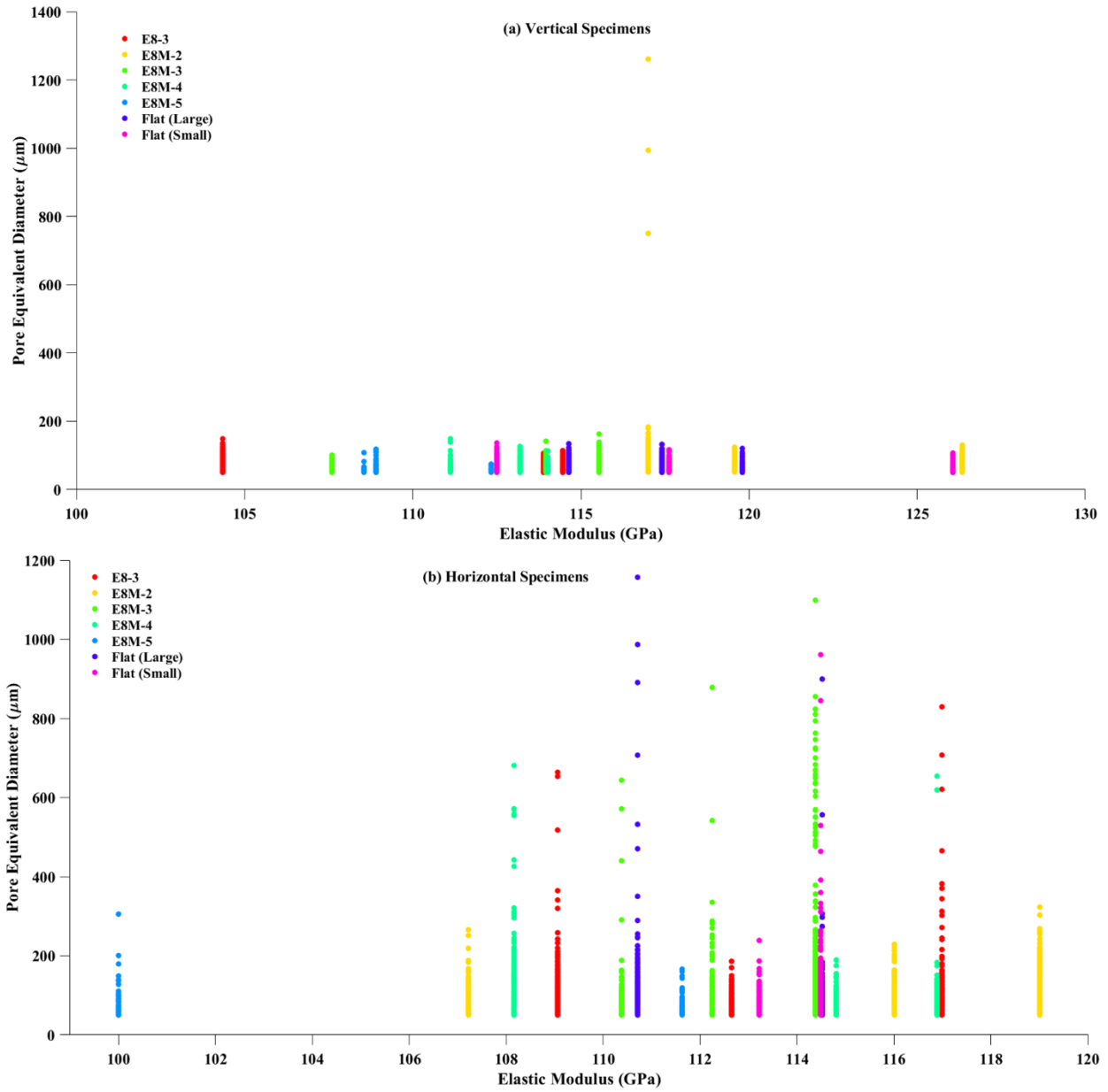


Figure 5.24 Specimen elastic modulus (E) vs. pore equivalent diameter for all pores > 50 μm, where (a) and (b) are the vertical and horizontal specimens, respectively.

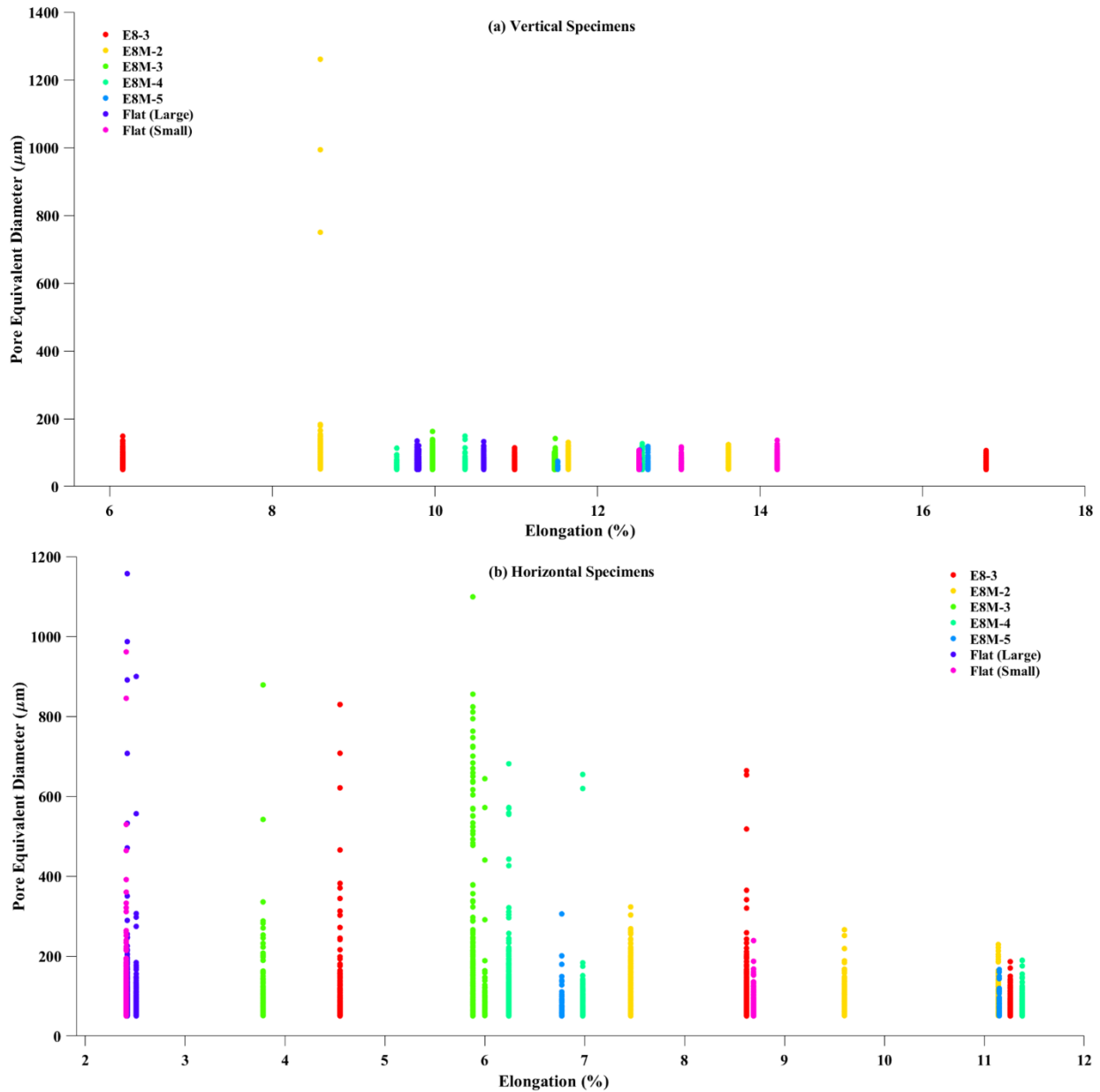


Figure 5.25 Specimen elongation (% EL) vs. pore equivalent diameter for all pores > 50 μm, where (a) and (b) are the vertical and horizontal specimens, respectively.

## 5.5 Conclusions

The current work looks at advancing the study conducted by the authors in prior work (Chapter 4), by employing X-ray computed tomography to assess the pore space characteristics of specimens built for tensile testing. The efforts will focus on establishing deeper correlations between the pore space characteristics (such as total volume, equivalent diameter, frequency, sphericity, aspect ratio, and radial

position) and the tensile specimen characteristics (such as geometry, orientation, cross-sectional area, surface area to volume ratio, and tensile behavior). Some of the main findings were:

- i. All pores for V specimens are  $< 200 \mu\text{m}$ , with the exception of E8M-2 specimen. Contrary to this, H specimens have a considerably larger number of pores that are  $> 200 \mu\text{m}$  and go up to  $1200 \mu\text{m}$ . In addition to this, it can be observed that for H specimens, although there are many pores  $< 200 \mu\text{m}$ , the pores  $> 200 \mu\text{m}$  contribute a much larger overall proportion of the pore volume.
- ii. The pore space  $< 100 \mu\text{m}$  is very similar across specimens manufactured in both directions. Therefore, the authors suspect that, if the processing parameters are kept the same, these pores will appear in specimens of any size and geometry, irrespective of their build orientation.
- iii. The majority of the pores  $< 100 \mu\text{m}$  for both orientations have a sphericity  $> 0.8$  and are categorized as gas pores, whereas majority of the pores  $> 200 \mu\text{m}$ , have a sphericity value  $< 0.6$  and therefore are categorized as lack-of-fusion pores. Pores between  $100 \mu\text{m} - 200 \mu\text{m}$  have mixed morphologies and are indicative of a transition between the two melting domains.
- iv. H specimens display all pore classes, but the V specimens only display Class D and Class E pores (with the exception of E8M – 2 V specimen). Furthermore, it was concluded that the % EL can be correlated with the Class A ( $> 500 \mu\text{m}$ ) pores and therefore, Class A pores are the most detrimental when it comes to the elongation behavior of the specimens.
- v. The subsurface pore population was significantly less for the H specimens having the largest and smallest cross-sectional area. Furthermore, no Class A pores were observed for these specimens.
- vi. The H specimens with the smallest and largest surface area to volume ratio have no Class A pores. Additionally, H specimens having surface area to volume ratios between  $0.5 /\text{mm}$  to  $1.25 /\text{mm}$  have pores belonging to all five classes.
- vii. The UTS, YS, and E were not affected by the pore equivalent diameter. The % EL was linked to the pore equivalent diameter such that specimens that showed absence of Class A pores had higher elongation values.
- viii. This work is expected to inform the scientific community about the true impact that porosity defects can have on the mechanical properties of EB-PBF specimens that are  $> 99\%$  dense.

## **Chapter 6**

### **Effect of varying preheating temperatures in electron beam powder bed fusion: Part I Assessment of the effective powder cake thermal conductivity**

This chapter is considered for publication as follows:

Shanbhag G, Vlasea M. “Effect of varying preheating temperatures in electron beam powder bed fusion: Part I Assessment of the effective powder cake thermal conductivity” *Journal of Manufacturing Processes*. *(Under Review)*.

## 6.1 Preface

One of the major barriers in adapting the existing EB-PBF process parameters to a new powder material system is controlling the preheating conditions such that every layer of powder results in enough partial sintering to create a coherent powder cake. To be able to understand the powder sintering process and adapt it to other materials, we must look at the degree of sintering and the effective thermal conductivity of the powder bed. An in-depth understanding of these characteristics will help tailor the preheating conditions and furthermore, make it easier to remove/de-powder intricate parts after build completion without compromising the advantages of the preheating phenomenon. This study evaluates the impact of preheating temperature on the in-situ powder cake properties. Three different preheat temperatures, 650 °C, 690 °C, and 730 °C, are employed to a Ti-6Al-4V powder cake and in each standalone build, unique powder-capture artefacts are fabricated to be able to analyze the in-situ powder cake properties using X-ray computed tomography. An empirically-derived model for thermal conductivity of the powder cake as a result of changing the preheating temperatures, was obtained. The results demonstrated that the effective thermal conductivity of the powder cake at a given preheating temperature strongly depends on the packing density, contact size ratio, and coordination number. An increase in preheating temperature, led to a linear increase in the packing density (from  $58.42 \pm 1.10$  % to  $61.87 \pm 0.96$  %), contact size ratio (from  $0.45 \pm 0.004$  to  $0.48 \pm 0.003$ ), coordination number (from  $3.36 \pm 0.05$  to  $3.58 \pm 0.05$ ) and the effective thermal conductivity (from  $.75 \pm 0.07$  W/m/K to  $2.11 \pm 0.07$  W/m/K) of the powder cake. The findings in this work will be deployed in Chapter 7 to assess and to correlate the effects of different powder conductivity and preheat temperature on the surface topography and geometric fidelity of components with simple and complex geometries.

## 6.2 Introduction

The energy source in electron beam powder bed fusion (EB-PBF) processes, is used for both partial sintering (during preheating) and fusing (during melting) powder particles together [88]. The electron beam interaction with metallic powder develops a charge distribution around the build plate. If this charge exceeds a critical limit, the repulsive forces between the negatively-charged powder particles can cause particle motion and result in an avalanche effect, also known as “smoke” or “smoking effect” [53]. As a result of smoking, a powder cloud is created, which can spread detrimentally throughout the build chamber and potentially up into the electron beam gun, all within a matter of milliseconds. In order to avoid this smoking effect, the powder needs to be partially sintered in all Arcam EB-PBF machines [54]. A few other EB-PBF machine manufacturers such as Freemelt and Wayland Technologies do not require the creation



of this partially sintered powder cake [297]. However, assessing these other machines is out of scope for the current thesis. This powder sintering is performed by using the Preheat Theme. There are two steps in preheating, Preheating 1 (PH1) and Preheating 2 (PH2). PH1 is required for securing the powder particles strongly such that the electron beam is able to sweep over the powder bed without the formation of any smoke. PH1 covers the entire build plate and enables the electron beam to jump between melt areas; making the electron beam jump safe. The estimated spot size of the beam in PH1 is 800  $\mu\text{m}$  [298]. PH2 is required to facilitate the melting of powder particles in select regions corresponding to the part cross-section at that layer and to prevent swelling in parts. PH2 covers each individual melt region (as shown in Figure 6.1) and uses a higher energy electron beam to provide mechanical anchoring of parts and supports (if any) [55]. The estimated spot size of the beam in PH1 is 300  $\mu\text{m}$  [298]. The PH1 and PH2 stages are followed by the melting of the powders at the location corresponding to the part slice, as controlled by the Melt Theme; the effect of the Melt Theme is out of scope for this study.

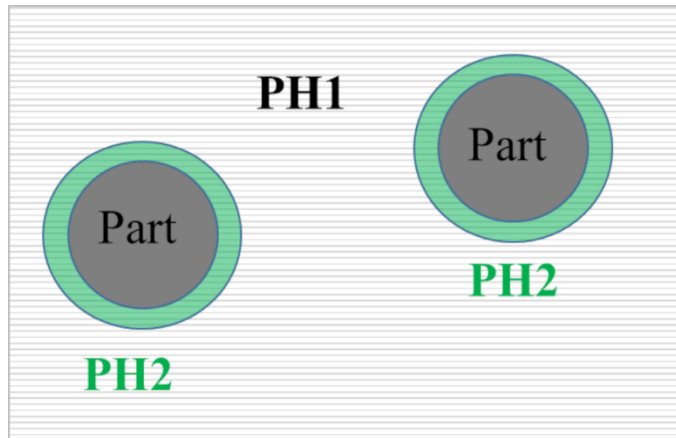


**Figure 6.1 Illustration of where the PH1 and PH2 theme regions are in effect, with respect to a part slice within a layer. PH1 and PH2 are applied to sinter the powder cake. The Melt Theme is applied to melt the cake and create the part layer.**

The reason for using a higher energy electron beam is to create a more uniform heat environment by lowering the difference in thermal conductivity between parts and powder. PH2 ensures that the electron beam is melt safe and can move on to the Melt Theme. The Preheat Theme can be controlled by varying the beam current (mA), beam speed (mm/s), number of repetitions, focus offset (mA) and scan order. The beam current controls the energy input during the heating process, the beam speed controls the exposure time of the beam, the focus offset controls the beam sharpness or beam diameter during preheating. An

additional solution to the smoking issue is introducing a small partial pressure of helium into the vacuum environment. This inert gas creates  $\text{He}^+$  ions above the powder bed that pick-up electrons from the powder bed and reduce the risk of smoke. However, the introduction of helium only takes place during the melting stage. In addition, He gas increases the cost of the process, thus increasing its use is generally prohibitive.

### 6.3 Preheating studies in EB-PBF of Ti-6Al-4V

Studies have shown that preheating can increase the mechanical strength, electrical and thermal conductivity of the sintered powder, as well as improve the beam-powder interaction efficiency [56]–[59]. Preheating has also been shown to reduce the formation of balling phenomena [56], [60] and lower the thermal gradient during melting, thus reducing distortion and warpage in the manufactured components [12], [58], [61]. However, Sigl et al. [62] identified a few drawbacks. They mentioned that (i) preheating increases the total build time and energy consumption, (ii) a powder recovery system (PRS) is required break up the powder cake to retrieve the final parts, and (iii) preheating may limit the small details in complex internal geometries as it is difficult to remove the partially sintered powder particles. The presence of partially sintered powder particles in intricate or complex internal geometries and features may lead to an increased surface roughness of the part as well.

Drescher et al. [54] looked into modifying PH1 to achieve a higher build efficiency. The procedure was to replace the default PH1 strategy with one that preheats only the area that is to be consecutively melted. Thus, the powder surrounding the part is not sintered as strongly and the powder cake is expected to be less cohesive. This would lead to the easy removal of partially sintered powder and a reduction of time for retrieving final parts, in turn increasing productivity. They concluded that modifying the PH1 step led to an increase in build efficiency by 23%. They reported that the mechanical properties and microstructure remained unchanged. However, the powder had an increase in oxygen content and higher brittleness. Leung et al. [298] studied the effect of applied preheat energy per unit area ( $E_a$ ) on the microstructure, hardness, and porosity of parts on an A2XX machine with a layer thickness of 70  $\mu\text{m}$  for Ti-6Al-4V. The applied preheat energy ( $E_a$ ) in the base sinter was calculated as shown in Equation 6.1.

$$E_a = \left( \frac{E_{line}}{L_0} \right) * N \quad \text{Equation 6.1}$$

where  $E_{line}$  is the line energy expressed as (Equation 6.2):

$$E_{line} = \frac{\text{accelerating voltage} * \text{beam current}}{\text{scan velocity}} \quad \text{Equation 6.2}$$

and  $L_0$  is the line offset and  $N$  is the number of scan repetitions. They observed that the thermal conductivity increases with an increase in  $Ea$ . Another observation was that the micro-hardness of the components reduces with increasing  $Ea$  due to microstructural coarsening of Ti-6Al-4V caused by annealing. They identified that an  $Ea$  value of  $411 \text{ kJ m}^{-2}$  was optimum as it produced parts with a high hardness and low dimensional deviations from the computer-aided design (CAD) model.

There is a need for identifying a suitable preheating strategy in order to address the disadvantages presented by Sigl et al. [62] and influence the powder cake properties for easy powder removal after the build has been completed. In order to do this, it is important to understand the effect of preheating and sintering on the powder particles and their thermal properties. The majority of the literature in this domain focuses on finite element (FE) modeling and simulation of the preheating and melting process [88], [192], [299]–[302] to understand the heat transfer phenomena in EB-PBF. However, Landau et al. [303] have identified some of the drawbacks of such FE models. They noted that such simulations require small time increments and when using FE models, the mesh must be sufficiently fine in order to properly simulate the melt pool shape. Therefore, modeling a complete hatching path may be too computationally expensive. Secondly, the preheating process takes place over a long time and therefore using the existing moving heat source based thermal models may not be entirely practical [303]. Hence literature on modeling usually implements preheating temperatures as an initial given condition, which is not truly representative of the thermal history of the powder cake.

One of the major barriers in adapting the existing EB-PBF process parameters to a new powder material system and particle size distribution is controlling the preheating conditions such that every layer of powder obtains enough partial sintering to create a coherent powder cake, while simultaneously ensuring that the powder cake can be reconditioned into free-flowing powder with appropriate qualities for powder reuse. To be able to understand the powder sintering process and adapt it to other materials, the degree of sintering, or more explicitly the size of the sinter necks and density of each preheated layer, must be determined to predict the thermal conductivity of the powder bed. This will help tailor the preheat temperature and other parameters that would make it easier to remove/de-powder parts after build completion without compromising the advantages of the preheating phenomenon.

## 6.4 Thermal conductivity studies of Ti-6Al-4V powder bed

Parts manufactured by powder-bed fusion (PBF) additive manufacturing (AM) processes, that are employed in critical sectors such as aerospace, biomedical, defense, marine, and automobile require rigorous qualification steps. As such, a strong understanding of the properties of the metal powder feedstock, as well as its behavior in the process is necessary. Specifically, researchers across the globe are modelling the heat transfer process [12], [57], [88], [192], [260], [299], [304]–[307] in PBF to comprehend the mechanisms behind the consolidation of metal powder particles. In order to do so, it is imperative to understand the thermal properties of metal powders; information on this aspect is currently limited. Inputs for thermal properties in such models are often estimated by analytical or empirical models, or directly taken from property tables and databases.

Some studies [308]–[310] have presented analytical models for calculation of the thermal conductivity in a powder bed based on geometrical considerations of the constitutive powder material system. Gusarov et al. [308] concluded that the conductivity depends on the relative density, coordination number, and the contact size of the particles. This model was created to understand the sintering and binding mechanism in the laser powder bed fusion (LPBF) process. In the work by Siu et al. [309], it was concluded that the conductivity highly depends on the contact angle between the spheres when packed in simple cubic, body centered cubic, or face centered cubic configuration. Although the model is difficult to generalize for complex powder particle organization, the findings capture the level of sensitivity expected as a function of packing configuration. In addition, Slavin et al. [310] concluded that the narrow gaps between adjacent particles significantly contribute to the thermal conductivity of a particle system consisting of irregularly shaped spheroidal particles. Such modeling works are important theoretical contributions, with inherent limitations in translating findings empirically, depending on the underlying model assumptions.

A few mathematical models relating the thermal conductivity of powder beds to the porosity and the gas type around the powder particles, were proposed. As such, Sih et al. [311] derived a model for a randomly packed metallic powder bed by enhancing a few variables in the Zehner-Schlünder's equation [312] to incorporate conductivity of gas, contributions from porosity, and particle contact area ratio. Yagi et al. [313] developed a model to relate the effective conductivity of a porous material to its volume void fraction. They conclude that at low temperatures the conductivity is affected only by convection, whereas at higher temperatures radiative heat transfer also plays a major role. Thümmeler et al. [314] also developed a model that emphasizes the importance of pore geometries on thermal conductivity and pointed out that it can be controlled by the amount of gas content in the pores. However, the EB-PBF process takes place under vacuum and therefore these models cannot be applied to this process.

Only a handful of studies demonstrated work on empirical measurements conducted explicitly to verify and improve thermal property information used in finite element (FE) models to simulate the heat transfer mechanism in AM processes. Rombouts et al. [315] evaluated the thermal conductivity of 316L stainless steel, iron, and copper powders of various particle shapes and size ranges using photopyroelectric measurements. The authors observed that the relative density is a critical factor for thermal conductivity of the powder bed, and it was concluded that beds of irregular particle shapes or particles with a wider size distribution were more conductive. Alkahari et al. [316] studied the effect of bulk density and particle diameter on the thermal conductivity of bimodal 316L stainless steel powder. A pulsed Yb: fiber laser was used to create a heat source on the top face of the powder bed, and measurements were taken with a thermocouple embedded below the top face. The data gathered from the thermocouple output was used to calculate the thermal conductivity. The authors observed that the thermal conductivity of metal powder increased with an increase in bulk density and particle diameter and that, not surprisingly, increased porosity led to a lower thermal conductivity. Arce [55] performed a comprehensive thermophysical evaluation of Ti-6Al-4V EB-PBF parts prepared from plasma rotating electrode process (PREP) and gas atomized (GA) powders as well as the powders themselves. The powder size distribution was 45-150  $\mu\text{m}$ . These experiments were conducted to provide more accurate inputs for an FE model to simulate the process. Arce used differential scanning calorimetry (DSC) to measure  $C_p$  and concluded that there was not a significant difference in measured  $C_p$  values between the EB-PBF and conventionally processed Ti-6Al-4V samples. The  $C_p$  values were observed to be between 0.5 – 0.6  $\text{J g}^{-1} \text{K}^{-1}$  measured at up to 800  $^{\circ}\text{C}$  for raw powders, as-built parts and conventional processed Ti-6Al-4V. The thermal diffusivity of powder and solid samples was measured by the laser flash method by holding the samples in sapphire containers inside the instrument. Differences in the results of the two types of powders was attributed to different particle size distributions. Thermal conductivity values were acquired and compared to cast and wrought material to show that there were no considerable differences in thermal conductivity between the EB-PBF samples and conventionally processed material (values summarized in Table 6.1). Cheng et al. [88], [192] calculated the thermal conductivity of both solid and powder-encapsulated Ti-6Al-4V EB-PBF parts (values given in Table 6.1) where the powder size distribution was 45-100  $\mu\text{m}$ . The authors observed that the thermal conductivity of the powder cake is < 15% of its solid counterpart. They found powder porosity to be a critical factor in the reduction of thermal conductivity. They found a value of 2.44  $\text{W m}^{-1} \text{K}^{-1}$  for a sample with 50% porosity and 10.17  $\text{W m}^{-1} \text{K}^{-1}$  for solid Ti-6Al-4V at 750  $^{\circ}\text{C}$ . They also measured (with the help of scanning electron microscopy) the diameter of the sinter neck formed after preheating; such diameter values were on the order of 1  $\mu\text{m}$  to 10  $\mu\text{m}$ . Smith et al. [59] studied the effect of changing process parameters such as number of

beam passes and line energy on the powder density, thermal diffusivity and thermal conductivity in EB-PBF, for a similar plasma-atomized (PA) powder size distribution of 45-105  $\mu\text{m}$ . The authors observed that the thermal diffusivity values increased with an increase in the number of beam passes over a certain area. However, the density did not change significantly with the number of beam passes, which led to the conclusion that the thermal conductivity is solely related to a morphological change; this was confirmed by electron microscopy where an increased connectivity due to necking and partial melting between particles was observed. Increased connectivity between particles is undesirable if the powder needs to be re-sieved and reused in the process.

**Table 6.1 Thermal conductivity values for powder ( $\text{W m}^{-1} \text{K}^{-1}$ ), as-built parts, wrought rods and for wrought Ti-6Al-4V material extracted from representative plots presented by Arce [55], Cheng et al. [88], [192] and Boivineau et al. [317]. PREP = Plasma Rotating Electrode Process and GA = Gas Atomized**

Sample type		Temperature (in $^{\circ}\text{C}$ )								
		20	100	200	300	400	500	600	700	750
Powder [55]	PREP	1	1	1	1	1	1	1.1	1.2	1.5
	GA	1	1	1	1	1	1	1.1	1.2	1.5
As-built Part [55]	PREP	7	8	8.5	9.5	10.5	11	13	13.9	14.5
	GA	7	8.1	8.6	10	11	12	13.5	14.3	15.5
As-built hollow part with encapsulated powder [88], [192]		2.7	-	-	-	2.8	-	-	-	4
As-built solid part [88], [192]		6.2	-	-	-	9	-	-	-	10
Wrought [317]		-	7	8	9	9.5	10	12	13	13.3

The above-mentioned literature indicates that the thermal conductivity for a powder bed is substantially different when compared to the same material obtained in its cast or wrought form. This can be attributed to the limited contact between powder particles and is furthermore influenced by complex packing conditions. Heat transfer through conduction in a solid part is faster than in powder as the vacuum gaps between powder particles work as insulators and slow down the heat transfer [307]. The conductivities are dependent on the porosity of the powder bed and the process environment. With an increase in porosity, the powder bed emissivity increases, and the effective powder bed thermal conductivity decreases. However, with the small amount of existing literature, it is challenging to predict the thermal properties of the powder in vacuum when exposed to elevated temperatures for any substantial duration [59]. Significant improvements in EB-PBF part quality outcomes and powder recovery efficiency may result from more accurate estimates of powder thermal conductivity derived from experiential measurements and evaluation

of the thermal properties of the powder system. Therefore, the current work will look at constructing an empirically-derived model for thermal conductivity of the powder cake in the EB-PBF process as a result of changing the preheating temperature.

## **6.5 Assessing the in-situ powder cake properties using powder-capture artefacts**

It is important to recognize that the effective thermal conductivity of a powder bed in EB-PBF depends on the neck size between the partially sintered powder particles. The diameter of this neck controls the rate of heat transfer. Tolochko et al. [318] have observed in LPBF that a decreased neck size means low thermal conductivity and vice versa. For the current work, the goal is to examine and elucidate how the preheat temperature affects the sinter neck size, layer-wise density, and thermal conductivity. As mentioned earlier, this information will help tailor the preheating temperature and other parameters that would make it easier to remove/de-powder parts after build completion without compromising the advantages of the preheating phenomenon. In order to study the effect of preheating on powder sintering, one needs to capture the immobilized powder cake that is formed by the two-stage preheating.

Manufacturing a powder encapsulation container during the EB-PBF process would assist in obtaining a sample of the immobilized metal powder cake during in-situ building conditions. A few studies in literature tried to capture such an immobilized powder cake. Liu et al [190] manufactured a hollow cube with an open top using LPBF. The part was manufactured such that the immobilized cake was inside the container that was being built. However, the authors did not mention the container removal, powder immobilization, nor the powder removal procedure. These procedures can have a high impact on the powder bed density measurements and therefore it is important to clearly describe them. The second disadvantage of this study is that the authors did not describe the procedure of determining the actual volume of the powder container. They computed the powder bed density value by assuming that the volume of the inner cavity of the container is equal to the nominal design volume, which has been shown to be an inaccurate assumption [319]. Jacob et al. [320] built a hollow cylinder with a closed top (which was a second component – unattached to the cylinder) using LPBF. The intent was to be able to end up with unaffected powder inside the powder encapsulation container and to infer the powder bed density via mass-volume estimates. The mass of captured powder was measured by punching a hole through the lid and removing all powder. The inner volume of specimens was evaluated by mass measurements of the empty specimen and of the specimen filled with a fluid of known density to infer the fluid-accessible volume. The drawbacks of this study were certain uncertainties such as accidental removal of powder by hole punching, remainder of powder inside while draining, surface tension effects of the measurement fluid, etc. Rogalsky et al. [319]

also built a hollow cylinder but with an open top. After the build was completed, tops were closed with a plastic lid with the intent to end up with unaffected powder inside the container. This study used XCT for quantitative analysis to determine the relative powder bed density as well as an infiltration method for experimental validation. However, since this study was conducted for LPBF with highly irregular powders, powder bed denudation and surface topography introduced uncertainties to the results.

This work introduces a method to assess and investigate the behavior of powder and powder layers during the EB-PBF process. A special powder capture artefact with an internal cavity, referred to as a capsule, was used to capture the immobilized powder cake during the EB-PBF process. This powder capture artefact design assists in protecting the powder cake in a way that is unaffected from the environment during the powder recovery stage. These artefacts are also manufactured in different locations on the build plate to measure the consistency of the powder bed condition. Furthermore, the assessment of the powder cake will assist in constructing an empirically-derived model for thermal conductivity of the powder cake in the EB-PBF process as a result of changing the preheating temperature. The findings in this work will be deployed in Chapter 7 to assess and to correlate the effects of different powder conductivity and preheating temperature on the surface topography and geometric fidelity of components with simple and complex geometries.

## **6.6 Materials and methods**

### **6.6.1 CAD file preparation, specimen design, and build layout**

SolidWorks (Dassault Systèmes, France) was used for designing and obtaining the specimen STL files. File preparation for manufacturing was then performed using Materialise Magics (Materialise, Belgium). The software was used for rescaling, positioning on a start plate, and support structure creation, where required. Slicing the files was then executed by Build Assembler (Arcam plug-in for Materialise Magics), which converts the information into an Arcam build file (.abf) that is imported to the machine.

Figure 6.2 (b) shows a CAD design of the powder-capture artefact. Inside the artefact, a small capsule was designed where powder was captured (Figure 6.2 (a)). Although two artefacts were manufactured (one stacked on top of the other as shown in Figure 6.2 (c)), XCT was performed only for the bottom artefacts. The top artefacts will be analysed as part of a future study.



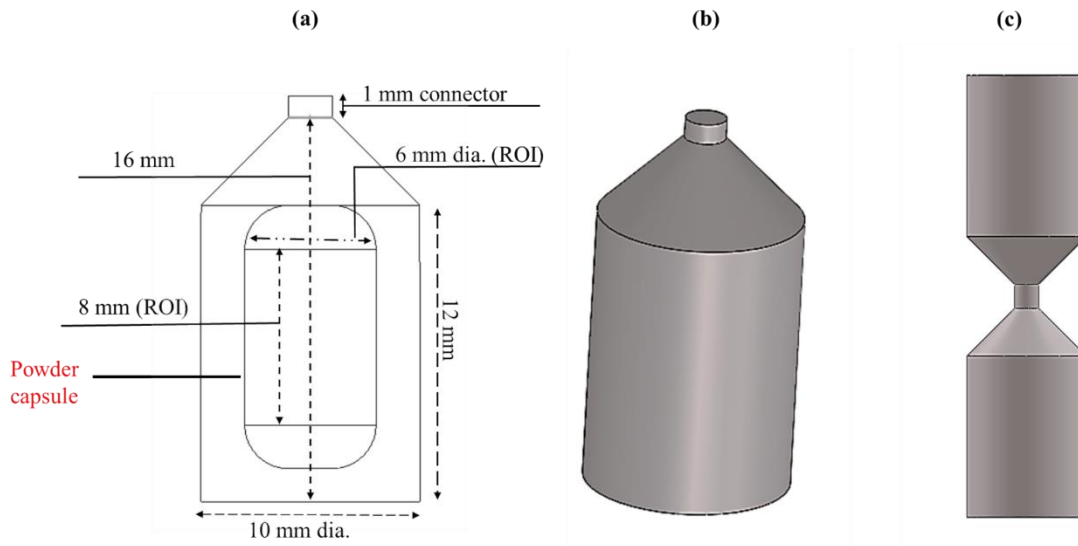


**Figure 6.2 (a) Wireframe diagram of the powder-capture artefact (b) Solid view of the cylindrical powder-capture artefact (c) 2 artefacts stacked and connected by a connector in the middle.**

The two stacked powder-capture artefacts are connected by a small 1 mm cylindrical connector. In the event that the two artefacts need to be separated, the connector can be easily cut or broken off. Note that, the artefact placed on top, appears upside down. This does not affect any analysis since the shape and orientation of the Region of Interest (ROI) remains the same with respect to the manufacturing coordinate system and the internal capsule design remains unchanged. Alongside every powder-capture artefact, there was a 15x15x30 mm part-quality artefact which was used to assess the surface topography, as described in Chapter 7. The position of the samples on the start plate of the machine and the naming strategy are shown in Figure 6.3(a). All samples have their longitudinal axis perpendicular to the build platform (parallel to the build direction / Z axis). A total of 9 powder-capture artefacts and 9 part-quality artefacts were manufactured. Figure 6.3(b) shows a modeler view of Materialise Magics – depicting all the specimens on the build plate.

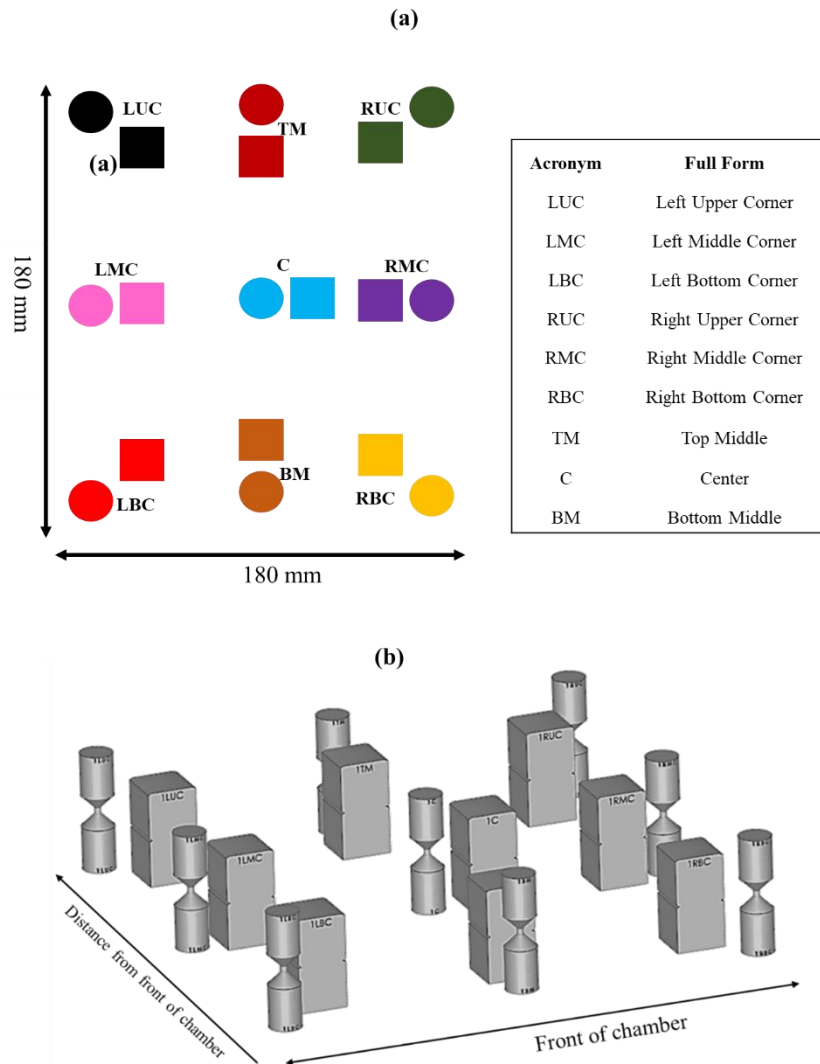


**Figure 6.3 (a) Top view of the build plate depicting powder-capture artefacts and part-quality artefacts (left) and Labeling strategy for all specimens based on their location on the build plate (right table) (b) Modeler view of Materialise Magics showing powder-capture artefacts and part-quality artefacts on the build plate.**

## 6.6.2 Additive manufacturing of samples

All samples were produced on an Arcam A2X (Arcam, GE Additive, Sweden) EB-PBF machine. The Ti-6Al-4V powder feedstock was supplied by Advanced Coatings & Processes (AP&C, Canada) and consisted of pre-alloyed, PA powder with a size distribution of 45  $\mu\text{m}$  to 105  $\mu\text{m}$ . The layer thickness was set to 50  $\mu\text{m}$ . The samples were built in accordance with the equipment manufacturer's default parameter settings (version 5.2.40), with the only modification being the preheating temperature. As mentioned in Section 6.2, preheating comprises of two stages: Preheat 1 and Preheat 2. In Preheat 1, the electron beam lightly sinters

the powder particles over the entire build area and in Preheat 2 the electron beam locally sinters the area where parts are supposed to be built. In the Arcam A2X model, the preheating temperature is monitored by a K-type thermocouple that is attached to the bottom of the build plate. The default preheat temperature for Ti-6Al-4V is set to 730 °C by the manufacturer. A total of three (3) separate builds were manufactured. The build height for all experiments was 37 mm. The only difference between the builds was the preheat temperature. The current study looks at three different preheating temperatures to understand the change in the in-situ properties of the powder cake. Table 6.2 shows the input preheat parameters used for each of these experiments. The line energy,  $E_{line}$  is expressed per Equation 6.2. It should be noted that the heat model in Arcam A2X automatically changes the required beam current to achieve the target preheat temperature.

**Table 6.2 Preheat Theme process parameters**

Preheat Parameters	Experiment 1		Experiment 2		Experiment 3	
	Preheat 1	Preheat 2	Preheat 1	Preheat 2	Preheat 1	Preheat 2
Preheat temperature (°C)	650		690		730	
Accelerating Voltage, $U_e$ (kV)	60	60	60	60	60	60
Beam current, $I_b$ (mA)	30	38	30	38	30	38
Scan velocity, $V_{sc}$ ( $ms^{-1}$ )	10	13	10	13	10	13
No. of scan repetitions	2	3	2	3	2	3
Line energy, $E_{line}$ ( $J.m^{-1}$ )	180	175.38	180	175.38	180	175.38
Line offset, $L_0$ (mm)	1.2	1.2	1.2	1.2	1.2	1.2

Al-Bermani et al. [92] observed that a coarser microstructure (leading to a decrease in mechanical properties) can be formed if the preheating temperature is above 951 K (or 677.85 °C). Therefore, it is important to investigate if the preheating temperature can be decreased from the default preheating temperature (i.e., 730 °C). Furthermore, it is essential to explore whether the decreased preheating temperature leads to better de-powdering and improved surface roughness, as illustrated in Chapter 7.

### 6.6.3 X-ray computed tomography (XCT)

The XCT-scanner (Xradia 520 Versa, Zeiss, Pleasanton, CA) was set to operate at 100 kV, 90  $\mu$ A, and resolution of 6  $\mu$ m. The acquisition files were obtained at 1001 projections (per 360 deg of rotation). Each artefact was first scanned, capturing the powder capsule at a 6  $\mu$ m voxel size. The scans focused on a 6 mm diameter by 6 mm tall sub-region (or ROI as shown in Figure 6.4) of the powder capsule.

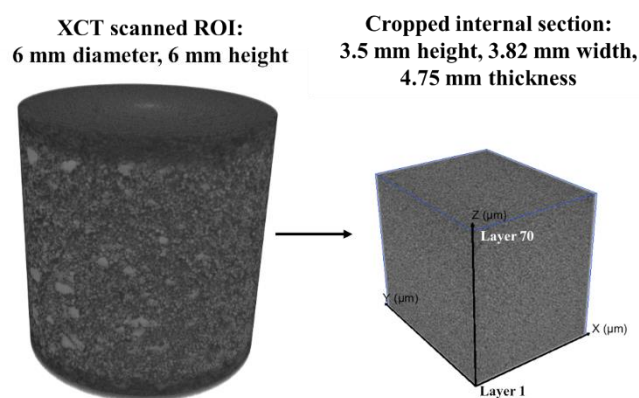


**Figure 6.4 Depiction of the cropped internal section from the original XCT scanned ROI**

The CT scans were reconstructed using the ZEISS Scout-and-Scan™ Control System Reconstruction Software package to produce a series of gray-scale images with 16-bit intensity ranges as shown in Figure 6.5(a). The image stack was then cropped in ImageJ to obtain a rectangular central region of length ( $Z$ ): 3.50 mm, width ( $X$ ): 3.82 mm, thickness ( $Y$ ): 4.75 mm (as shown in Figure 6.4) of the internal section of the sample. The printing layer thickness was set to 50  $\mu\text{m}$  and therefore the 3.5 mm translates to 70 printing layers. The cropping was done so as to only capture the powder cake during the steady-state part of manufacturing, when the capsule internal walls are vertical and away from the top and bottom edges, which may add uncertainty due to the different heating regime at those locations.

#### **6.6.4 Analysis of XCT data to extract particle coordination number, packing density, contact size ratio and sinter neck size**

Noise was reduced by down-sampling the gray-scale images to 8-bit in MATLAB. A gray-scale threshold value to isolate the solid portion of the specimen was chosen such that the thresholded images had a qualitative visual match to the gray-scale data pore structure. After down-sampling and thresholding, a black and white or B&W image (white = solid, black = pore) stack was obtained from MATLAB (Figure 6.5(b)). MATLAB code for down-sampling, thresholding, and obtaining the B&W image is provided in Appendix D. This B&W image stack obtained from MATLAB was then used as an input for subsequent processing in Python. PoreSpy, a Python Toolkit for quantitative analysis of porous media images, developed by Gostick et al. [321] was used for 3D analysis of the image stack. As a first step, PoreSpy performed a connected component analysis on the B&W image stack to obtain the layer-wise density by comparing the ratio of black and white voxels contained within the volume for each layer for the entire sample. Such a method for obtaining the layer-wise density was employed previously by the authors in

[322]. As a second step, a water shed segmentation was performed to isolate and label every particle. Detailed information on the watershed algorithm can be found in [323], [324]. Thirdly, particles in contact with the image border were removed. The removal of border particles was done to reduce any quantification errors in subsequent analysis. Lastly, interface areas (connected areas between identified particles) of the sintered regions were obtained. For specific information regarding each step, please refer to the Python code provided in Appendix E.

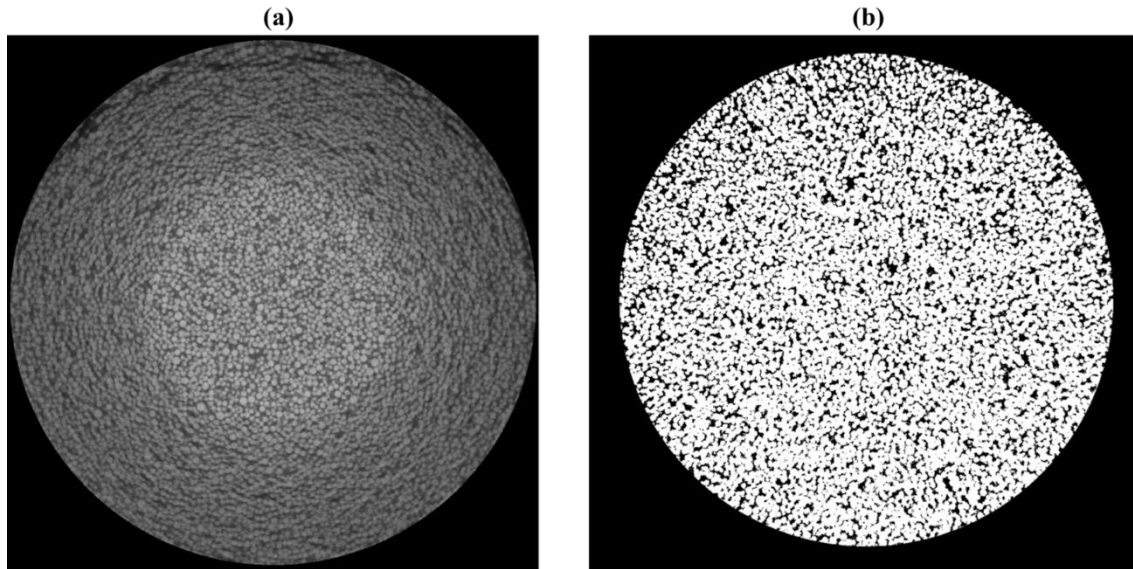


**Figure 6.5 (a) Grayscale image of a slice of powder artefact obtained by XCT reconstruction (b) Segmented image of a slice obtained by employing thresholding in MATLAB**

The particle space extracted based on the methodologies described above was used to extract the average particle coordination number (i.e., total number of particles that are in contact with an individual particle), the contact area between powder particles ( $\mu\text{m}^2$ ), the layer-wise powder bed density (%), the equivalent diameter of the powder particles ( $\mu\text{m}$ ), the X-, Y- and Z- coordinates of the powder particle centroids (in  $\mu\text{m}$ ), the sinter neck area between powder particles ( $\mu\text{m}^2$ ), the sinter neck diameter between powder particles ( $\mu\text{m}$ ), and sinter neck diameter to particle diameter ratio; the Python code used for processing is provided in Appendix E for further reference.

### **6.6.5 Inferred effective thermal conductivity**

The thermal conductivity can be calculated based on the methodology described by Gusarov et al. [308], [325], where they define the contact effective thermal conductivity between particles,  $\lambda_{eff}$ , as:

$$\frac{\lambda_{eff}}{\lambda} = \frac{pn}{\pi} x \quad \text{Equation 6.3}$$

where  $\lambda$  is the thermal conductivity of the corresponding bulk material (for Ti-6Al-4V the value is 6.7 W/m/K as per [75]),  $p$  is the packing density of the powder layer,  $n$  is the coordination number,  $x$  is the contact size ratio. The contact size ratio is defined as the ratio of the contact spot diameter (or sinter neck diameter) to the sphere diameter (or powder particle diameter). The effective thermal conductivity (W m<sup>-1</sup> K<sup>-1</sup>) of every powder layer of the capsule inside the powder capture artefact was then obtained from Python, as per Equation 6.3.

## 6.7 Results and Discussion

According to Gusarov et al. [308], [325], the effective thermal conductivity of a randomly packed powder bed depends on three in-situ properties: the packing density, the contact size ratio, and the coordination number. In this study, it is shown that these in-situ properties of the powder cake, in an EB-PBF machine, can be measured by using a special powder capsule inside a powder-capture artefact (as shown in Figure 6.2), trapping the powder cake inside of it. For simplicity, three samples were selected – one each from the top, middle and bottom of the build plate; and data pertaining to these is shown in the subsequent sections. Data related to all other samples can be found in Appendix F.

### 6.7.1 Packing density of powder layer, $p$

Figure 6.6 depicts the packing density of the powder layer (also known as layer-wise density) vs. layer number for the LUC, C, and RUC samples for all experiments mentioned in Table 6.2. The data for the remaining samples is presented in Appendix Figure F.1 in Appendix F. The average layer-wise density values lie between  $58.42 \pm 1.10$  % and  $59.57 \pm 1.48$  % for all Experiment 1 powder capsules (i.e., preheating temperature of 650 °C),  $59.40 \pm 1.70$  % and  $60.54 \pm 1.93$  % for all Experiment 2 powder capsules (i.e., preheating temperature of 690 °C) and  $60.83 \pm 0.99$  % and  $61.87 \pm 0.96$  % for all Experiment 3 powder capsules (i.e., preheating temperature of 730 °C) as shown in Table 6.3.

Firstly, it can be observed that with an increase in preheating temperature, the layer-wise density values increase. Secondly, the densities were predominantly uniform across the various locations sampled on the build platform, for a given preheating temperature. Thirdly, there is a clear indication that the layer-wise density for any specific capsule, across the 70 layers, had a global variation of approximately  $\pm 1.5\%$  with a clear density increase in the central region of the capsules. The reason for the density increase in the central region of the capsules is unclear at the moment and therefore will be investigated in a follow up study.

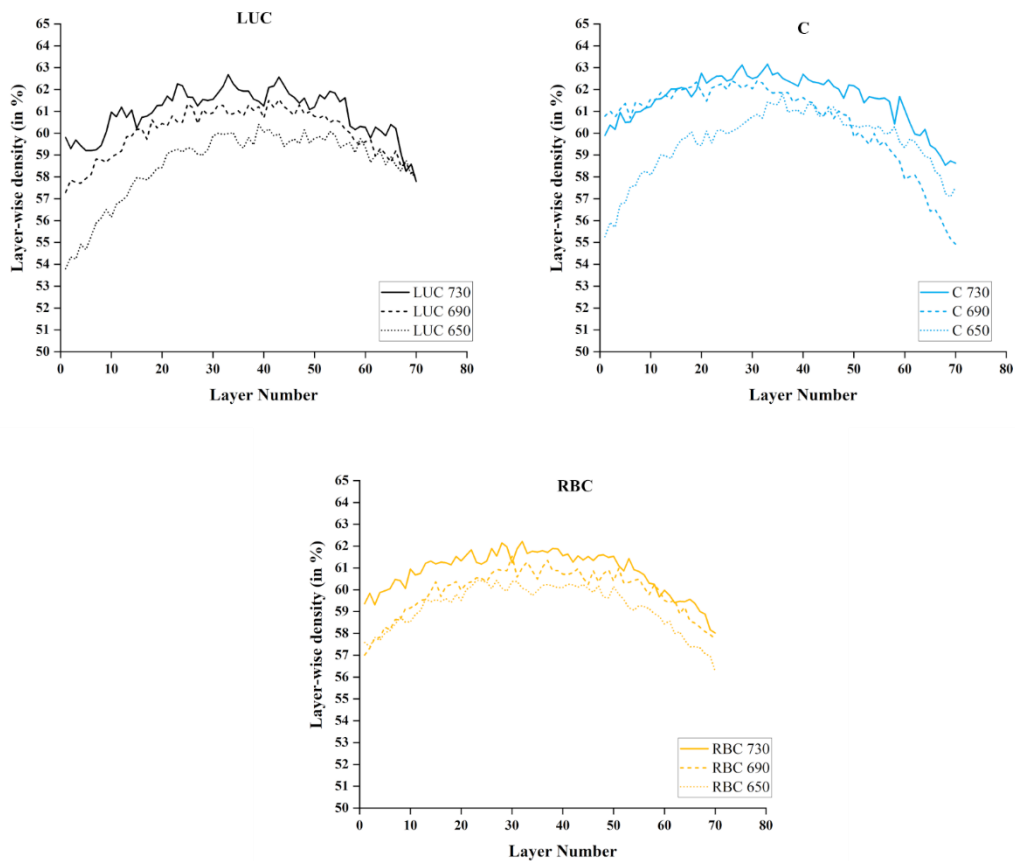


**Figure 6.6 Layer-wise density (in %) vs. Layer number for LUC, C, and RBC samples. The solid lines, dashed lines and dotted lines represent the behavior of the capsules processed at 730 °C, 690 °C, and 650 °C, respectively.**

In the EB-PBF process, a defocused electron beam (with an approximate spot size of 800  $\mu\text{m}$ ) is used to preheat the build plate to a desired sintering temperature and control the heat input and sintering mechanism. A few studies in literature have looked at influencing the sintering mechanism of the powder bed by changing the PH1 line energy [298], PH2 line energy [59], beam current [92], etc. Leung et al. [298] and Smith et al. [59] observed a slight increase in the packing density of the powder cake with an increase in the PH1 and PH2 line energy, respectively. However, the current study is one of the first studies that looks at influencing the heat input, sintering, and consequently the density of each powder layer by, controlling the preheating temperature. Powder particles that are in contact with each other start forming necks at the contact points. With an increase in the preheating temperature, the neck size increases. This

leads to further densification and reduction in the porosity. This also leads to an increase in the coordination number as seen in Table 6.3.

**Table 6.3 Table summarizing the average values and standard deviation for packing density, contact size ratio, eff. thermal conductivity and particle equivalent diameter, for all powder capsules**

Preheat temp. (°C)	Packing density, $p$ (%)			Contact size ratio, $x$			Effective thermal conductivity, $\lambda_{eff}$ (W/m/K)			Particle equivalent diameter ( $\mu\text{m}$ )			Average Coordination Number, $n$		
	650	690	730	650	690	730	650	690	730	650	690	730	650	690	730
Exp. No.	1	2	3	1	2	3	1	2	3	1	2	3	1	2	3
LUC	58.56 ± 1.63	60.01 ± 1.13	60.91 ± 1.09	0.44 ± 0.008	0.47 ± 0.004	0.47 ± 0.004	1.76 ± 0.11	1.94 ± 0.07	2.02 ± 0.07	54.51 ± 0.72	55.51 ± 0.55	56.44 ± 0.56	3.39 ± 0.08	3.49 ± 0.05	3.52 ± 0.05
LMC	59.45 ± 1.14	60.27 ± 1.16	61.87 ± 0.95	0.45 ± 0.004	0.47 ± 0.004	0.48 ± 0.003	1.84 ± 0.07	1.96 ± 0.08	2.11 ± 0.06	55.56 ± 0.60	55.48 ± 0.60	56.04 ± 0.50	3.43 ± 0.05	3.50 ± 0.05	3.58 ± 0.05
LBC	58.42 ± 1.10	59.40 ± 1.70	61.14 ± 0.98	0.45 ± 0.004	0.46 ± 0.010	0.48 ± 0.003	1.74 ± 0.06	1.89 ± 0.12	2.04 ± 0.06	56.64 ± 0.56	56.13 ± 0.73	56.22 ± 0.54	3.36 ± 0.05	3.44 ± 0.08	3.53 ± 0.04
TM	59.19 ± 1.44	60.13 ± 1.14	61.32 ± 0.96	0.45 ± 0.007	0.47 ± 0.004	0.48 ± 0.003	1.82 ± 0.10	1.95 ± 0.07	2.05 ± 0.06	54.03 ± 0.67	55.16 ± 0.53	56.77 ± 0.48	3.45 ± 0.07	3.50 ± 0.05	3.54 ± 0.05
C	59.57 ± 1.47	60.53 ± 1.93	61.55 ± 1.15	0.46 ± 0.005	0.47 ± 0.012	0.48 ± 0.004	1.87 ± 0.10	1.99 ± 0.15	2.08 ± 0.08	55.63 ± 0.57	55.47 ± 0.75	56.29 ± 0.55	3.44 ± 0.08	3.53 ± 0.09	3.57 ± 0.05
BM	58.69 ± 1.80	59.97 ± 1.13	61.29 ± 1.32	0.45 ± 0.011	0.47 ± 0.005	0.48 ± 0.006	1.77 ± 0.13	1.93 ± 0.07	2.05 ± 0.10	56.76 ± 0.81	56.77 ± 0.57	56.84 ± 0.53	3.37 ± 0.09	3.46 ± 0.05	3.54 ± 0.07
RUC	59.31 ± 1.11	59.62 ± 1.27	60.97 ± 1.00	0.45 ± 0.004	0.46 ± 0.006	0.47 ± 0.004	1.83 ± 0.06	1.88 ± 0.08	2.03 ± 0.06	54.94 ± 0.56	54.95 ± 0.62	56.24 ± 0.51	3.44 ± 0.05	3.46 ± 0.05	3.54 ± 0.05
RMC	58.94 ± 1.37	60.37 ± 1.39	61.65 ± 1.34	0.45 ± 0.007	0.47 ± 0.007	0.47 ± 0.006	1.80 ± 0.09	1.97 ± 0.10	2.06 ± 0.10	54.82 ± 0.65	55.58 ± 0.60	56.30 ± 0.65	3.42 ± 0.06	3.52 ± 0.06	3.57 ± 0.07
RBC	59.20 ± 1.05	59.88 ± 1.09	60.82 ± 0.98	0.45 ± 0.004	0.47 ± 0.004	0.47 ± 0.005	1.82 ± 0.06	1.92 ± 0.07	1.99 ± 0.06	57.04 ± 0.51	56.68 ± 0.62	56.62 ± 0.53	3.40 ± 0.05	3.46 ± 0.05	3.50 ± 0.04



It is important to evaluate whether the change in the preheating temperature also causes a change in the density of the solid part. Therefore, specimen C from Experiment 1, Experiment 2, and Experiment 3 was taken as a representative sample. A small section of the solid part, of the powder-capture artefact, was cropped (Figure 6.7) and its layer-wise density was evaluated.

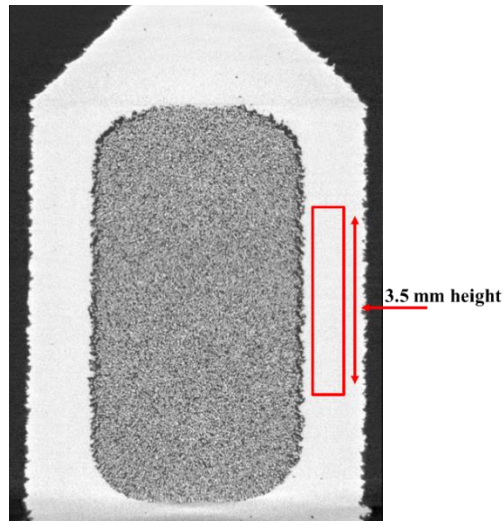


**Figure 6.7** Depiction of the solid part of the powder-capture artefact that was cropped and analyzed to obtain layer-wise density

It can be observed from Figure 6.8 that the layer-wise density for all three samples is quite consistent. The average layer-wise density values for the Experiment 1, Experiment 2, and Experiment 3 samples are 99.98%, 99.97% and 99.98% respectively. Hence it can be concluded that the change in preheating temperatures, between 650 °C and 730 °C, does not lead to a change in the density of the solid parts built in the powder cake.

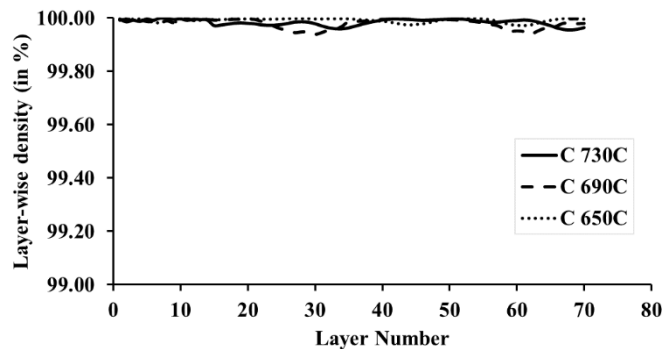


**Figure 6.8** Layer-wise density (in %) vs. Layer number C samples. The solid lines, dashed lines and dotted lines represent the behavior of the solid part, of the powder-capture artefact, processed at 730 °C, 690 °C, and 650 °C, respectively.

It is important to assess the impact of lower preheating temperatures since high preheating temperatures can cause excessive partial melting which may reduce the reusability of the powder [103], make de-powdering difficult [59], and lead to other disadvantages as described by Sigl et al. [62]. Furthermore, Suard et al. [264] and Koike et al. [326] demonstrated that excessive partial melting leads to high surface roughness containing rippled structures and visible sintered powder grains, in EB-PBF. Here, it can be noted that a decrease of 80 °C in the preheating temperature led to a mere approximate decrease of 3% in the relative layer-wise density of the powder-cake and no change in density of the solid part.

### **6.7.2 Average Equivalent diameter of powder particles in the powder cake**

The particle size has a significant influence on the layer-wise powder bed density [327], [328] and furthermore on the thermal conductivity. Alkahari et al. [316] showed that, for their LPBF experiments, the thermal conductivity increased with an increase in powder particle diameter. This behavior was attributed to the conductive heat transfer mechanism between particles. They mentioned that during conduction from the heat source to the thermocouple measurement point, smaller powder particles experienced increased repetitive changes between solid and air as a medium, however, the larger particles behaved the other way around. As a result, heat transfer and consecutively the thermal conductivity, is higher for the larger powder particles [316]. Therefore, it is imperative to observe whether there is a change in the powder particle equivalent diameter with a change in the preheating temperature. This will help isolate all factors that cause changes (if any) in the effective thermal conductivity. In order to calculate the particle size, all particles were assumed to be completely spherical. Figure 6.9 depicts the layer-wise average equivalent powder particle diameter (in  $\mu\text{m}$ ) vs. layer number for the LUC, C, and RUC samples for all experiments. The data for all remaining samples is provided in Appendix Figure F.2 in Appendix F.

It is observed that the average equivalent diameter values lie between  $54.03 \pm 0.68 \mu\text{m}$  to  $57.05 \pm 0.52 \mu\text{m}$  for all Experiment 1 powder capsules,  $54.95 \pm 0.62 \mu\text{m}$  to  $56.77 \pm 0.58 \mu\text{m}$  for all Experiment 2 powder capsules, and  $56.04 \pm 0.51 \mu\text{m}$  to  $56.84 \pm 0.53 \mu\text{m}$  for all Experiment 3 powder capsules (as shown in Table 6.3). From Table 6.3 and Figure 6.9, it can be stated that the average equivalent diameter is quite consistent for all preheating temperatures and across all capsule locations.

Therefore, a change in the layer-wise density or thermal conductivity associated with the preheating temperature cannot be correlated to the powder particle equivalent diameter. Another observation from Figure 6.9 is that there is an increase in the average equivalent diameter in the central region of the capsules. Upon close observation we can see that the global variation across the 70 layers (Table 6.3) is approximately less than 1%. Such a variation is considered to be negligible for the current study.

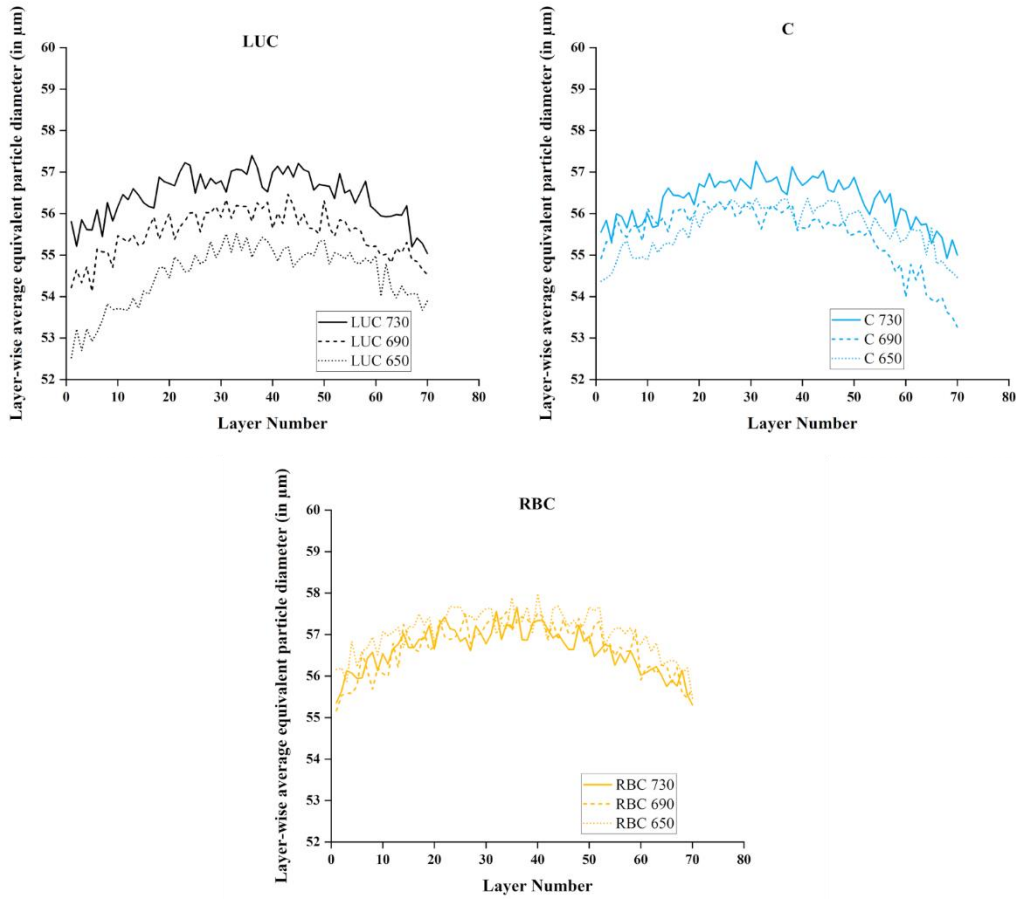


**Figure 6.9 Layer-wise average equivalent powder particle diameter (in  $\mu\text{m}$ ) vs. Layer number for LUC, C, and RBC samples. The solid lines, dashed lines and dotted lines represent the behavior of the capsules processed at 730 °C, 690 °C, and 650 °C, respectively.**

### 6.7.3 Contact size ratio, $x$

The contact size ratio,  $x$ , is the ratio of the contact spot diameter (or sinter neck diameter) to the sphere diameter (or powder particle diameter). Obtaining this ratio is critical to identify the effective thermal conductivity according to the equation presented by Gusarov et al. [308], [325]. The contact size ratio shows how strongly the powder particles are sintered together. A higher contact size ratio value translates to better sintering. Consequently, a higher degree of sintering leads to a lower chance of repulsion by virtue of electrostatic charging [54]. Figure 6.10 depicts the layer-wise average contact size ratio vs. Layer number for the LUC, C, and RUC samples for all experiments. The data for the remaining samples is presented in Appendix Figure F.3 in Appendix F.

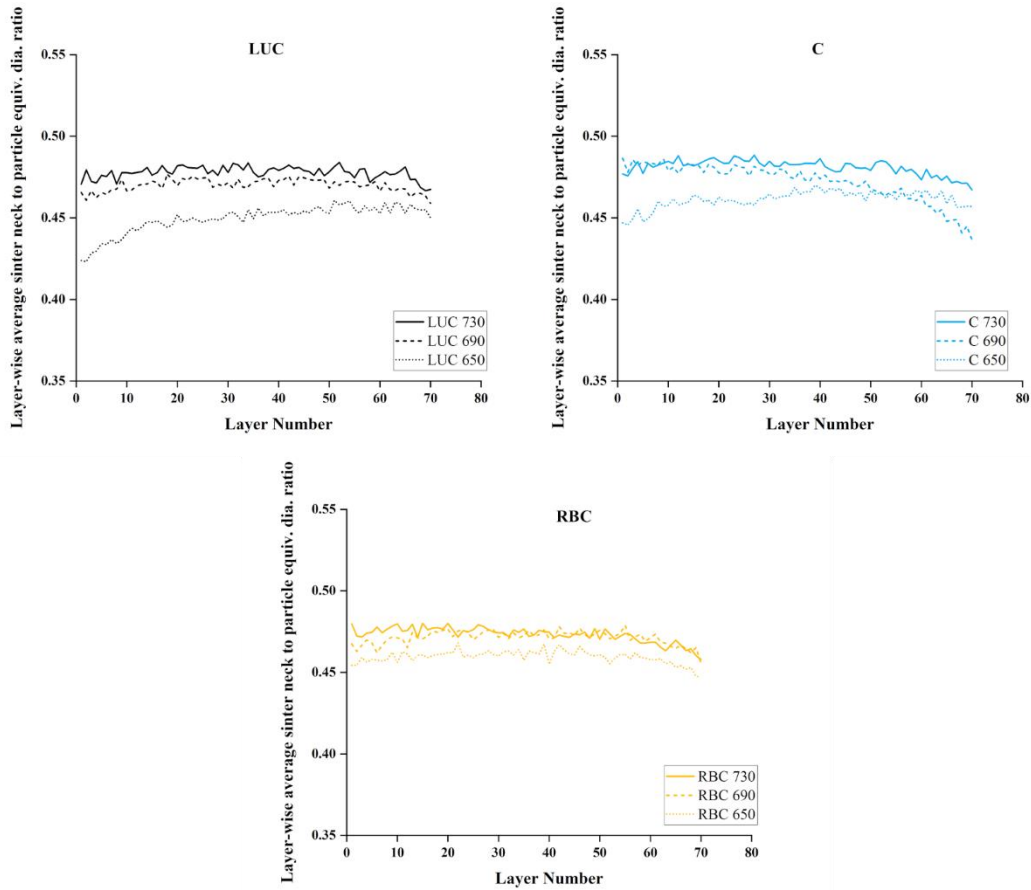


**Figure 6.10 Layer-wise average sinter neck diameter to particle equivalent diameter ratio vs. Layer number for LUC, C, and RBC samples. The solid lines, dashed lines and dotted lines represent the behavior of the capsules processed at 730 °C, 690 °C, and 650 °C, respectively.**

It is observed that the average contact size ratio values lie between  $0.45 \pm 0.004$  to  $0.46 \pm 0.005$  for all Experiment 1 capsules,  $0.46 \pm 0.006$  to  $0.47 \pm 0.005$  for all Experiment 2 capsules, and  $0.47 \pm 0.005$  to  $0.48 \pm 0.003$  for all Experiment 3 capsules (as shown in Table 6.3). It is observed that there is an increasing contact size ratio response as a function of increasing the preheating temperature. It is also observed that the contact size ratios were mostly uniform across the various locations sampled on the build platform, for a given preheating temperature.

In Figure 6.9 it is noted that the equivalent diameter range is quite consistent for all preheating temperatures. This means that the only variable changing in the contact size ratio is the sinter neck diameter. A previous study performed on assessing the powder sintering mechanism of EB-PBF powder beds [329] concluded that solid-state sintering is the dominant mechanism during the preheating procedure. In addition

to experimental studies from other authors [56], [57], [298], they also concluded that sintering of powder particles in EB-PBF Ti-6Al-4V only occurs between 873 K (600 °C) and 1003 K (730 °C). No true sintering occurs below 873 K [56], [329]. They also demonstrated that sinter necks grow faster with an increase in preheating temperatures. This is consistent with the current study where an increase in the contact size ratio is observed with an increase in preheating temperatures. Specifically, an increase of 80 °C in the preheating temperature led to an approximate increase of 5% in the contact size ratio. This increase in the sinter neck diameter can be attributed to the increase in layer-wise density with preheating temperature. As the density increases, the contact points between powder particles improve as more powder particles are touching their adjacent particles. As explained by Wheat et al. [328] there are two different types of sintering mechanisms within solid-state sintering: non-densifying and densifying sintering mechanisms (as shown in Figure 6.11). The authors hypothesize that the solid-state sintering mechanism taking place in EB-PBF is the densifying mechanism where mass from the particles moves from the core to the neck of the particles [330]. Furthermore, understanding which mechanism (lattice diffusion, grain boundary diffusion, or plastic flow) is causing densification is beyond the scope of the current study.

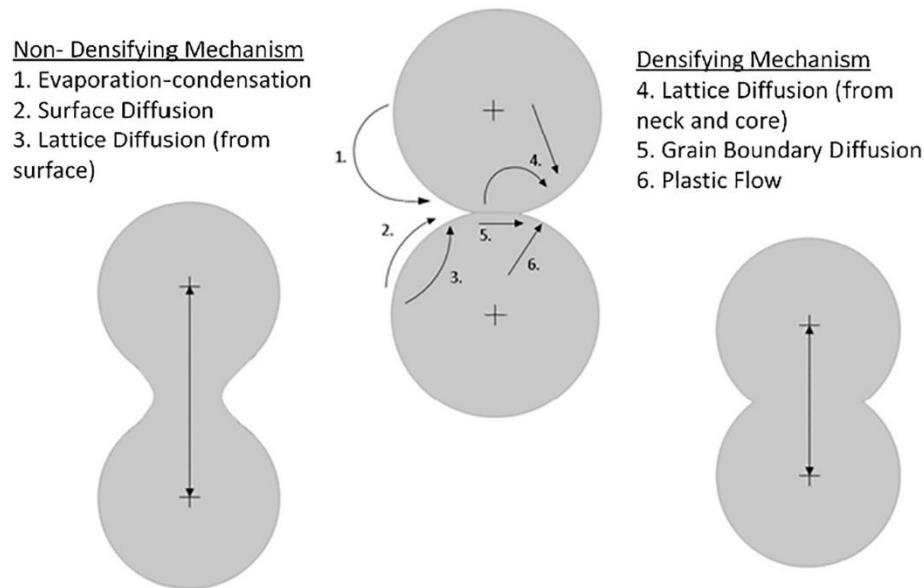


**Figure 6.11 Possible solid-state sintering mechanisms: non-densifying mechanisms (left) and densifying mechanisms (right). Reprinted with permission from Wheat et al. [328]**

To assess the correlation between density, coordination number, and contact size ratio; the values for a given experiment were averaged and plotted in Figure 6.12. The coefficient of determination (or R-squared)

values depict that a near linear relationship exists between the density, coordination number, and the contact size ratio.

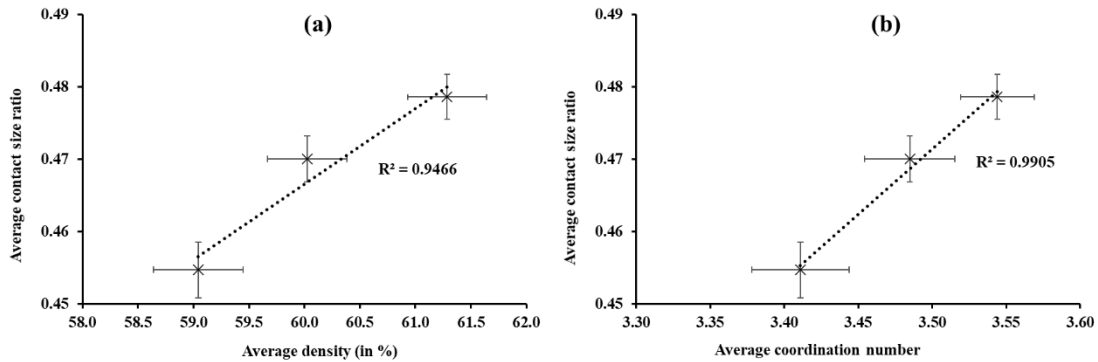


**Figure 6.12 Average (a) density (b) Coordination number vs. average contact size ratio for all experiments with linear trendlines and R-squared values. Error bars represent the standard deviation.**

#### 6.7.4 Effective thermal conductivity, $\lambda_{eff}$

Thermal conductivity is a measure of the rate of heat transfer through material [316]. The effective thermal conductivity,  $\lambda_{eff}$ , was calculated for every sinter neck in the powder cake. However, the layer-wise average effective thermal conductivity of LUC, C, and RBC samples, was used for demonstration in Figure 6.13. The data for the remaining samples is presented in Appendix Figure F.4 in Appendix F.

It is observed that the average effective thermal conductivity values lie between  $1.75 \pm 0.07$  W/m/K to  $1.87 \pm 0.10$  W/m/K for Experiment 1 capsules,  $1.88 \pm 0.09$  W/m/K to  $1.99 \pm 0.15$  W/m/K for all experiment 2 capsules and  $1.99 \pm 0.07$  W/m/K to  $2.11 \pm 0.07$  W/m/K for all Experiment 3 capsules (as shown in Table 6.3). An increase in preheating temperature leads to an increase in the effective thermal conductivity of the powder cake. Specifically, an increase of  $80^\circ\text{C}$  in the preheating temperature led to an approximate increase of 12% in the effective thermal conductivity.

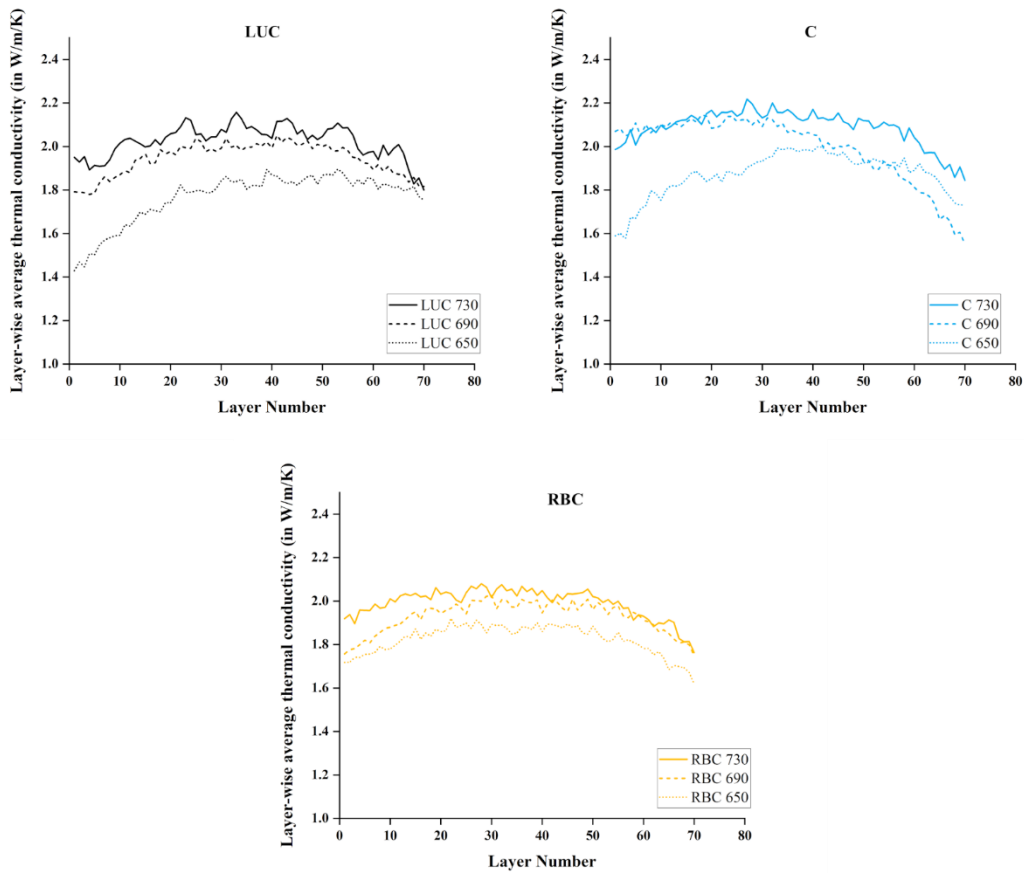


**Figure 6.13 Layer-wise average effective thermal conductivity vs. Layer number for LUC, C, and RBC samples. The solid lines, dashed lines and dotted lines represent the behavior of the capsules processed at 730 °C, 690 °C, and 650 °C, respectively.**

To assess the correlation between density, contact size ratio, coordination number, and the effective thermal conductivity; the values for a given experiment were averaged and plotted in Figure 6.14. The R-squared values depict that a near linear relationship exists for all the metrics.

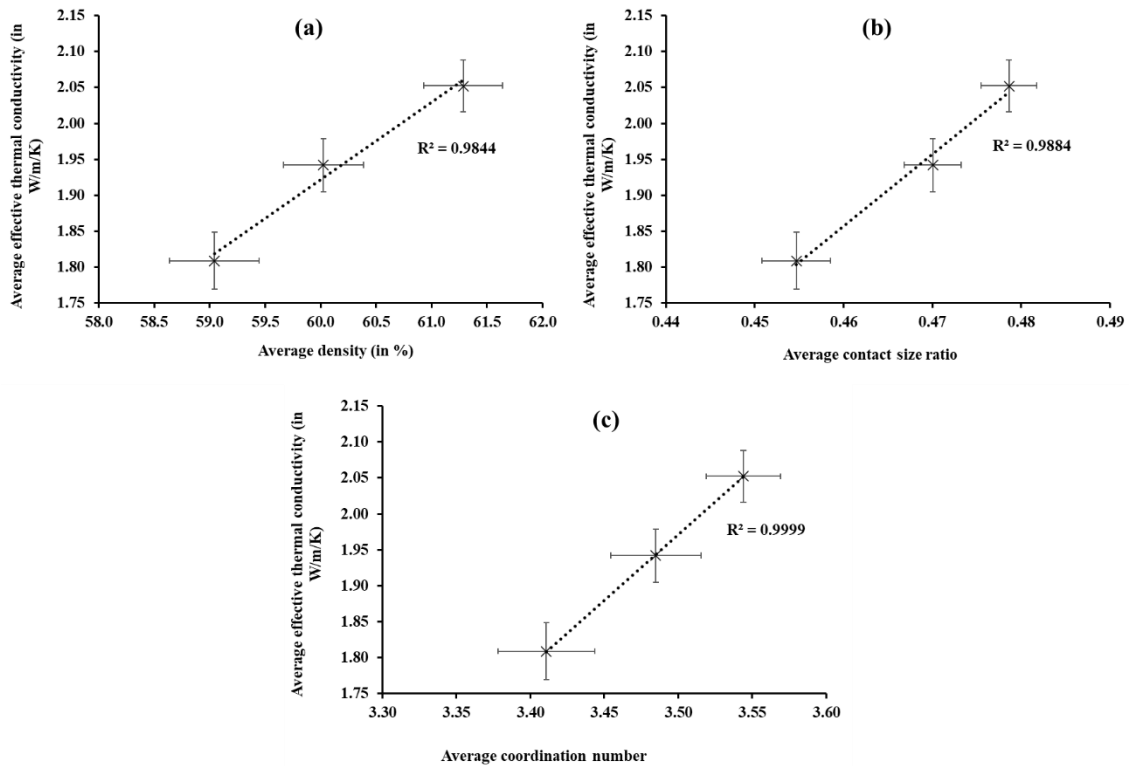


**Figure 6.14 Average (a) density (b) contact size ratio (c) coordination number vs. average effective thermal conductivity for all experiments with linear trendlines and R-squared values. Error bars represent the standard deviation.**

It is a well-known fact that the thermal conductivity of packed powder beds increases with temperature [331]–[334], however, the unanswered question is how well are these two metrics correlated.

### **6.7.5 Correlation between the preheating temperatures and density, contact size ratio and effective thermal conductivity of the powder capsules, respectively**

Stemming from the observations in Sections 6.7.1 - 6.7.4, some correlations were noticed between the preheating temperature and the various metrics such as layer-wise density, contact size ratio, coordination number, and effective thermal conductivity. Therefore, to quantify this interdependency, the packing density, contact size ratio, coordination number, and effective thermal conductivity values, as shown in Table 6.3, for a given experiment were averaged and plotted against the preheating temperatures in Figure 6.15. The R-squared values depict that a near linear relationship exists between the preheating temperatures and the various metrics.



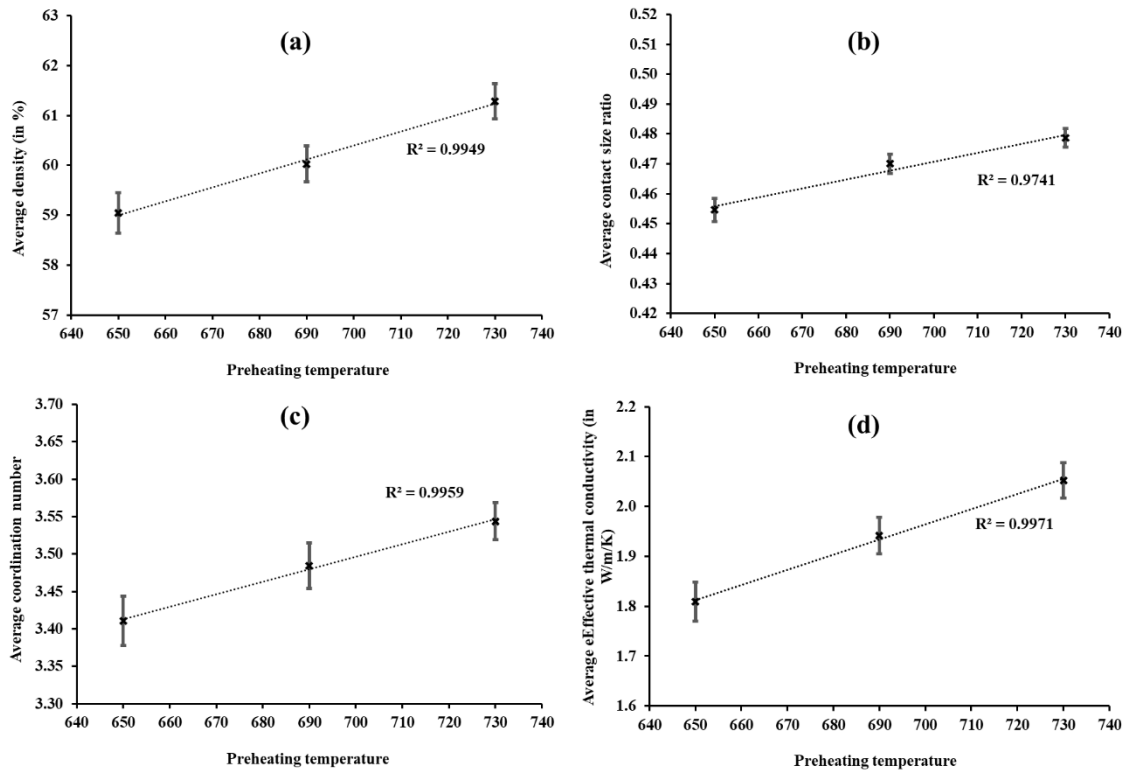


**Figure 6.15 Average (a) density, (b) contact size ratio, (c) coordination number, and (d) effective thermal conductivity, vs. preheating temperature for all experiments with linear trendlines and R-squared values.**

**Error bars represent the standard deviation.**

A linear equation was established from the experimentally-measured average values of the packing density (Equation 6.4), the contact size ratio (Equation 6.5), coordination number (Equation 6.6), and the effective thermal conductivity (Equation 6.7) for the three preheating temperatures.

$$p = 0.028 \times T + 40.784 \quad \text{Equation 6.4}$$

$$x = 0.0003 \times T + 0.2613 \quad \text{Equation 6.5}$$

$$n = 0.0017 \times T + 2.3318 \quad \text{Equation 6.6}$$

$$\lambda_{eff} = 0.003 \times T - 0.1648 \quad \text{Equation 6.7}$$

where  $p$  is the packing density,  $x$  is the contact size ratio defined as the ratio of the contact spot diameter (or sinter neck diameter) to the sphere diameter (or powder particle diameter),  $n$  is the coordination number,  $\lambda_{eff}$  is the effective thermal conductivity, and  $T$  is the preheating temperature. These equations can be

used to predict the density, contact size ratio, coordination number, and effective thermal conductivity of the powder bed when using preheating temperatures between 650 °C and 730 °C.

Maly et al. [335] have demonstrated that an increase in preheating temperature in Ti-6Al-4V samples, produced by LPBF, led to dramatic degradation of powder. An increase in the O<sub>2</sub> and H<sub>2</sub> content, beyond the ASTM defined limit, was observed. Al-Bermani et al. [92] have demonstrated that the yield strength and tensile strength decrease with an increase in the processing temperatures. Therefore, low preheating temperatures should be used for partially sintering the powder bed in EB-PBF. The current study shows that it is possible to use a reduced preheating temperature with very little change in the layer-wise density and effective thermal conductivity of the powder cake. Furthermore, the empirically-derived model for predicting the density, contact size ratio, coordination number, and effective thermal conductivity can be used to study the necking and sintering phenomenon for use in FE models. The authors believe that this work will aid in providing reliable empirical information into furthering the understanding behind the evolution of the input Ti-6Al-4V powder from its as-received powder feedstock state to preheated, partially sintered molten and finally its solid state.

## 6.8 Conclusions

The effect of varying preheating temperatures on the effective thermal conductivity of the Ti-6Al-4V powder cake, in EB-PBF, were observed. Some of the main findings were:

- i. The calculated average packing density, contact size ratio, coordination number, and effective thermal conductivity, of the powder-capsules, ranged from  $58.42 \pm 1.10$  % to  $61.87 \pm 0.96$  %,  $0.45 \pm 0.004$  to  $0.48 \pm 0.003$ ,  $3.36 \pm 0.05$  to  $3.58 \pm 0.05$ , and  $1.75 \pm 0.07$  W/m/K to  $2.11 \pm 0.07$  W/m/K, respectively when the preheating temperature was varied between 650 °C and 730 °C.
- ii. The effective thermal conductivity of the powder cake at a given preheating temperature strongly depends on the packing density, contact size ratio and coordination number.
- iii. The current study shows that it is possible to use a reduced preheating temperature since a mere change of 3% in the layer-wise density and 12% in the effective thermal conductivity, was observed, with an 80 °C decrease in the preheating temperature.
- iv. A decrease in the preheating temperature led to a linear decrease in the packing density, contact size ratio, coordination number, and consequently the effective thermal conductivity. Logarithmic regression equations were established from the empirically - derived thermal conductivity data. These equations can be used to predict the thermal conductivity of the powder cake, in EB-PBF, when using preheating temperatures between 650 °C and 730 °C.

## Chapter 7

# Effect of varying preheating temperatures in electron beam powder bed fusion: Part II Assessment of the surface topography and geometric fidelity

### 7.1 Preface

In electron beam powder bed fusion (EB-PBF), components are manufactured under a controlled vacuum and at an elevated temperature. This environment is beneficial, as it has the potential of having minimal impact on the chemical composition of the powders, it reduces the level of porosity when compared to other AM techniques that operate in an inert gas environment, and it results in lower residual stresses in the deposited material. In addition to this, the EB-PBF process enables faster build rates owing to the high-power and fast beam scanning. Due to these advantages, EB-PBF has enabled manufacturing of functional, highly geometrically-complex, and highly customized metallic parts in contrast to traditional manufacturing methods. One of the major drawbacks is the poor surface roughness of as-built components and the requirement of having a powder cake in the build bed. The surface topography is affected by the partially-sintered powder particles partially fused to the solidifying surface. Furthermore, the partially-sintered powder cake negatively affects the de-powdering and the geometric fidelity of intricate features. Therefore, it is essential to find ways of reducing the surface roughness of as-built EB-PBF parts, while retaining the basic thermal properties and cohesiveness of the powder cake. The quality of the surface and geometrical fidelity of manufactured parts are bound by the thermal properties of the powder bed. In Part I of this study (Chapter 6), it was observed that the effective thermal conductivity of the Ti-6Al-4V powder bed can be controlled and tuned by modifying the preheating temperature. To further leverage on this finding, it is important to assess whether the effective thermal conductivity can be tuned so as to improve the surface topography and geometric fidelity of as-built EB-PBF parts. This study shows that using the default parameters provided by the machine manufacturer, and without using any post-processing techniques apart from the blasting in the PRS, the Ra and Sa values can be tuned just by tuning the preheating temperature. A linear relationship between the surface roughness metrics and the preheating temperatures was observed. Furthermore, upon assessing the geometrical fidelity of complex geometries, it was found that a decrease in the preheating temperature led to a decrease in the amount of partially melted powder particles attached to the solidified structure. This led to better de-powdering and reduced geometrical deviation of the manufactured structures from their original CAD model.

## 7.2 Surface topography of EB-PBF parts

A robust understanding of the modalities available for control of the surface topography in electron beam powder bed fusion (EB-PBF) is imperative for industrial and biomedical applications. In the area of surface topography metrology for metal AM components, there is an increased interest in the extraction and measurement of localized surface features [336], [337] to characterize the process-material-geometry interactions by quantifying the performance at the micro-, macro-, and meso-scale. In the context of this work, (i) the macro-topography properties refer to the overall part geometric fidelity with consideration given to aspects such as, but not limited to part distortion, integrity, shrinkage, and swelling, (ii) the meso-topography properties refer to the feature primitive (for instance lattice cell architectures) geometric fidelity outcomes with consideration given to aspects such as, but not limited to build orientation, build location, build part density, as well as hierarchical or cellular architectures, (iii) the micro-topography properties refer to observing the effects of the interaction between the energy source and the material to explain the physics at the interaction zone and the resulting material properties. The focus of the work is at the meso- and macro-scale level.

Characterization of surfaces has evolved from subjective methods (a keen eye or fingernail and an experienced “metrologist” [338]), to qualitative methods (e.g., use of comparators), to quantitative methods (e.g., descriptions of a surface based on measurements) that continue to progress, as enabling technologies advance. Of those technologies, tracing a contact stylus across the surface has been the primary method of measurement for over a century and still has a strong hold in industry [339]. Over the past several decades, however, optical and areal methods have gained an increased interest [340]. A detailed history of these developments can be found elsewhere [338], [340], [341], but throughout these advances, the need for surface metrology has remained consistent. This need has centered on, 1) the ability to determine how a part will perform in a certain function, and 2) the ability to characterize the quality of a manufacturing process (i.e., has something in the process changed and must be addressed) [338].

The as-built parts for EB-PBF have relatively rough surfaces, when compared to conventionally machined surfaces or parts produced by other AM processes [70]–[74]. The range of Ra and Sa values of as-built EB-PBF components has been reported as 15 - 55  $\mu\text{m}$  [116], [342]–[346] and 15 - 70  $\mu\text{m}$  [14], [70], [123], [326], [347], [348], respectively, in literature. There are multiple reasons for such high Ra and Sa values of the EB-PBF samples. The drivers that influence surface topography are an interplay between numerous interdependent or correlated parameters. These primary drivers can be classified into three major categories – machine & feedstock characteristics, build file characteristics, and processing parameters [349].

The first category of factors that contribute towards introducing surface irregularities are the machine settings and feedstock characteristics. Machine settings include beam spot size, beam spot velocity and power, whereas powder morphology and size distribution are the feedstock characteristics. The electron beam spot diameter governs the minimum possible melt pool dimensions and, alongside the effects of partially-fused powder particles, contribute to the minimum feature size possible [350]. This is of importance when considering complex geometries prescribed by topology optimization methods as well as lattice structures. The powder feedstock for electron beam powder bed fusion (EB-PBF) can be in the form of spherical or irregular-shaped particles, with the size distribution typically in the range of 45  $\mu\text{m}$  to 150  $\mu\text{m}$ . A combination of layer thickness and partially fused powder particles are known to have an effect on the surface topography of EB-PBF parts [104]–[106], [259], [326]. Due to the design complexity afforded by the PBF processes, complex surfaces render part inspection difficult; furthermore, the design-dependence of surface quality outcomes may also reduce mechanical performance by providing crack initiation sites and reducing fatigue properties and fracture toughness [292]. Overall, the size and shape of powder particles adhered to the exterior surfaces of the part impact the surface topography. In addition, irregular-shaped powders can affect the flowability and uniform distribution of powder across the build platform, further influencing surface topography irregularities.

The second category of factors that contribute towards introducing surface irregularities are the build file characteristics. The geometry, orientation, and location of a given feature in a part along with the beam path strategy are the significant build file characteristics that contribute to surface topography variability. In EB-PBF support structures assist with uniform heat dissipation to the build plate. In the absence of properly-designed or insufficient supports, processes can result in various defects. One such defect is known as super-elevation of edges. It occurs when a part curls or warps upwards out of the powder layer [351]. This can interfere with the rake during spreading. Upon contact with the curled/warped surface, the rake may be damaged and may lead to a non-uniform powder layer density. This non-uniform powder layer may lead to additional defects such as lack-of-fusion or over-melting due to the impact of variation on beam-powder interaction. This can also lead to deterioration of surface topography [352].

The third major contributor to surface irregularities are the processing parameters. Processing parameters such as current, preheat energy, number of scan repetitions, power, scan speed, and powder layer thickness have a direct impact on surface topography through their effects on phenomena such as balling [352], powder ejecta [353], and adherence of partially fused powder particles [259], [354]. In EB-PBF, powder ejecta is attributed to the electrostatic repulsion of powder particles [37]. The electrons transmit energy and electrical charge upon interaction with the powder particles. When the repulsive forces

exceed the binding force between the powder particles in the powder bed, powder ejection may occur leading to denudation and in some cases the balling effect [53]. Layer thickness is also an important parameter as parts are manufactured in a layer-by-layer fashion. These layer-wise processes can often display ridged surfaces corresponding to the deposited powder layer [355]; this is known as the stair-stepping effect and is distinctly observed on sloped and freeform surfaces [113]. The effect of stair-stepping strongly depends on the layer thickness and the build angle with respect to the building platform [356].

It is important to find ways of reducing and controlling the surface roughness for as-built EB-PBF parts. Koptuyug et al. [116] have mentioned that the long-term performance of implants in the human body are determined by the surface topography. Improved surface topography will be beneficial when manufacturing complex and intricate geometries such as lattice structures for biomedical implants since as-built surfaces can be used without significant post-processing, thus lowering the manufacturing cost [26]. Galati et al. [357] and Wang et al. [261] have mentioned that the process window for improving surface roughness in EB-PBF by changing process parameters is very small. Furthermore, Klingvall et al. [63] looked at optimizing the scanning strategy, number of contours, distance between contours, etc., in EB-PBF, and noticed no influence on the surface roughness values.

Thus far, the effect of preheating temperatures on the surface topography (meso-scale part properties) and geometric fidelity (macro-scale part properties) of as-built EB-PBF parts, has not been analyzed. Therefore, it is essential to see the influence of preheating temperatures, controlled by the virtue of the Preheat Theme parameters, on improving the surface topography for the manufactured parts. Based on the results obtained in Chapter 6, the authors hypothesize that a decrease in the preheating temperatures will lead to an improved surface finish. The first goal of this study is to increase the body of knowledge in EB-PBF by quantifying the surface topography for a fixed set of EB-PBF process parameters with varying preheating temperatures. The second goal is to deploy this preheat strategies towards printing complex lattice architectures with good geometric fidelity and adequate de-powdering; the motivation for such is highlighted below.

### **7.3 Lattice architectures produced by EB-PBF and challenges in geometric fidelity**

With the advent of AM technologies, there has been renewed interest in fabrication of structures with controllable internal pore architectures to be used in biomedical applications, specifically to be able to mimic the complex architecture of tissues and organs [155]. Porous structures have been proven to have enhanced cell adhesion, migration, and proliferation as well as tissue ingrowth, nutrient delivery, and vascularization [156]–[158] when used as implants and scaffolds. There have been many studies on

fabrication of porous structures for biomedical applications using EB-PBF AM techniques. Harrysson et al. [29] stated that EB-PBF is capable of manufacturing porous bone replacement and augmentation implants and scaffolds that can be used for knees, hips, elbows, fingers, shoulders, and bone plates. Majority of these works focus on conventional lattice-based geometries, such as diamond [159]–[161], cubic [147], [162], [163], octahedral [164], [165], or rhombic dodecahedron [166], [167]. There have been several studies in literature specifically focusing on manufacturing porous Ti-6Al-4V structures using EB-PBF. Cansizoglu et al. [168] successfully fabricated non-stochastic hexagonal lattices with varying densities ranging from 5 % to 11% of solid fraction of Ti-6Al-4V. Parthasarathy et al. [147], [169] manufactured porous cellular cranioplasty plates which had up to 60% porosity. Murr et al. [170] manufactured knee implants with an inner dense material and an outer lattice structure. This geometry promoted cell propagation onto the implant. Heintl et al. [171] produced freeform open-cell structures and also demonstrated the possibility of locally varying the density of lattices. Horn et al. [166] manufactured open-cell rhombic dodecahedron structures with varying densities.

Another type of porous structures that are biologically desirable, due to the ease of controllability of the internal pore architectures, are triply periodic minimal surfaces (TPMS) [172], [173]. TPMS structures can be periodic along three independent directions and have zero mean curvature of the surface [174], [175]. Porous TPMS architectures are manufactured by using repeating unit cells with the minimum possible area [155]. TPMS structures have several advantages, over strut-based lattices, such as high surface area-to-volume ratio [155], improved mechanical and biological properties due to the geometrical continuity and topological smoothness [176], enhanced cell adhesion, migration, and proliferation [177], and superior fatigue properties [178]. These advantages make them ideal for use as scaffolds [155], [163]. Despite all these advantages, there have not been many studies on the fabrication of TPMS using Ti-6Al-4V EB-PBF. Some of the reasons for the limited number of studies could be that (i) TPMS structures consist of curved inner channels and therefore powder removal is a challenging task when dealing with such intricate structures [179], (ii) it is very challenging to produce intricate geometries that have high dimensional accuracy and low deviations from the intended geometrical models, especially since rough surfaces and dross are commonly observed in intricate geometries and (iii) removing the partially sintered powder particles from the intricate surfaces is difficult. According to the ASTM F3335 – 20 standard on Assessing the Removal of Additive Manufacturing Residues in Medical Devices Fabricated by Powder Bed Fusion, it is imperative to remove the partially sintered powder particles from the surfaces of these complex structures that may be used in biomedical applications as these may come loose during implantation, potentially affecting patient outcomes [358]. These topographical defects are caused due to heat trapping

and over melting of the thermally insulating powder cake that surrounds and supports these structures [66]. The as-built surfaces of EB-PBF components are relatively rough. Partly fused and loosely attached powder particles are always present on the surfaces if no post-processing is performed. Even with parameter optimization, thin and porous structures may have significantly rough surfaces [116].

Studies on the geometric fidelity of TPMS structures in metal AM remain scarce [349], specifically in EB-PBF. There is an opportunity to deploy the scientific insights related to the customization of powder cake properties by virtue of tuning the preheating temperature and assessing its influence on the surface topography and geometric fidelity of components. Therefore, this study looks into fabricating two classes of components, so-called part-quality artefacts and TPMS structures, with varying preheating temperatures. The goal is to see whether the change in preheating temperature leads to an improvement in the surface topography, dimensional fidelity, and de-powdering characteristics of the manufactured parts, from the CAD model.

## **7.4 Materials and methods**

### **7.4.1 Additive manufacturing of the part-quality artefacts**

The details regarding the design and fabrication of the part-quality artefacts can be found in prior work (Section 6.6.1 of Chapter 6). In brief, a total of nine (9) 15x15x30 mm part-quality artefacts were manufactured, in every build, to assess the surface topography. All artefacts had their longitudinal axis perpendicular to the build platform (parallel to the build direction / Z axis). A total of three (3) separate builds were manufactured, with a preheat temperature setting of 650 °C (Experiment 1), 690 °C (Experiment 2), and 730 °C (Experiment 3) respectively. The build height for all experiments was 37 mm. The only difference between the builds was the preheat temperature.

### **7.4.2 Surface topography evaluation for the part-quality artefacts**

There are many different parameters used to characterize the surface roughness of a part. The ASME B46.1 standard [257] defines and describes all of the different parameters used for quantifying the surface roughness. For the purpose of this study, the Ra and Sa parameters were evaluated. Ra is the arithmetic average of the absolute values of the profile height deviations from the mean line, recorded within the sampling length. Simply put, Ra is the average of a set of individual measurements of a surface's peaks and valleys along a linear path, as shown in Figure 7.1 (a). Sa is the extension of Ra and is used to estimate the waviness of a surface. Sa is expressed as, an absolute value, the difference in height of each point compared



to the arithmetical mean of the surface, as shown in Figure 7.1 (b). These values are usually measured in micrometers ( $\mu\text{m}$ ) [359]. The following equations describe Ra and Sa respectively.

$$Ra = \frac{1}{l_r} \int_0^{l_r} |Z(x)| dx \quad \text{Equation 7.1}$$

$$Sa = \frac{1}{A} \iint_A |Z(x,y)| dx dy \quad \text{Equation 7.2}$$

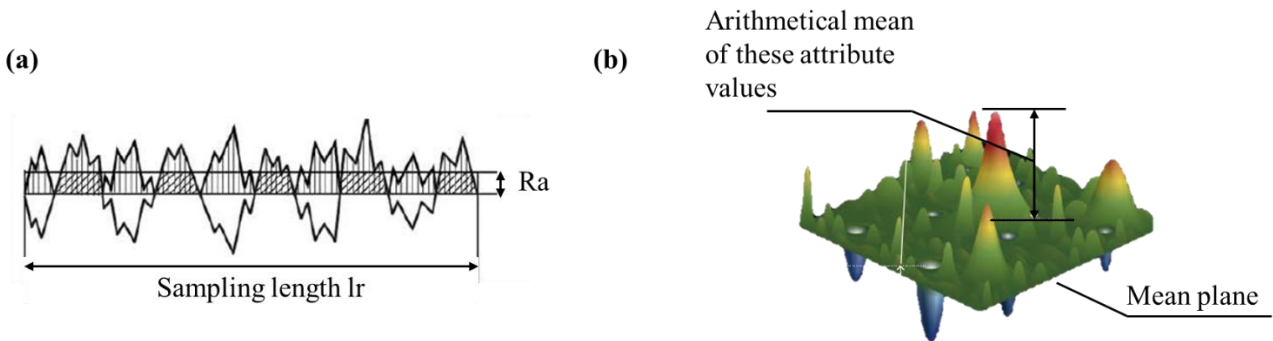


**Figure 7.1 Schematic describing the (a) Ra and (b) Sa measurements for calculating surface roughness [359]**

The steps for the main operations for acquisition of the different parameters is shown in Figure 7.2. The Ra and Sa values of the part-quality artefacts were determined using a coaxial laser confocal microscope (VK-X250, Keyence, Japan).

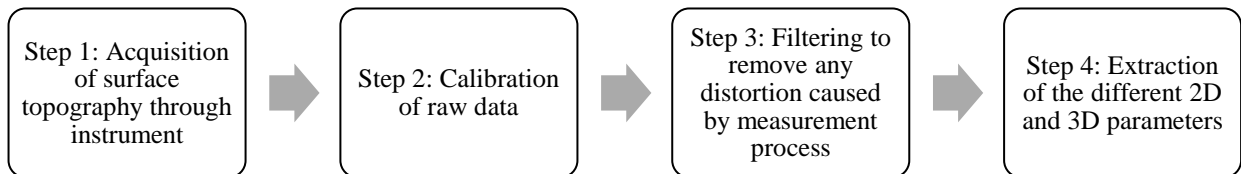


**Figure 7.2 Flowchart showing the steps for the main operations for acquisition of surface roughness parameters**

All 4 vertical surfaces (also referred to as skins) of the manufactured part-quality artefacts were analyzed. Skin 1 is the surface that was facing the front of the chamber during fabrication (green in Figure 7.3). Skin 2 is the surface adjacent to Skin 1 on the right (red in Figure 7.3). Skin 3 is the surface opposite to Skin 1 and faces the back of the chamber (blue in Figure 7.3). Skin 4 is the surface opposite to Skin 2 and to the left of Skin 1 (yellow in Figure 7.3). Six measurements were taken across the surface of each skin at locations equidistant from each other. The first 40 built layers (2 mm) from the plate were ignored

to account for any contamination caused by the fusing of titanium on a stainless-steel plate. A surface scanning area of nearly  $1400\ \mu\text{m}$  by  $1000\ \mu\text{m}$  was scanned for each measurement (i.e., each patch) and the measurements were conducted at a vertical feature resolution of  $10\ \mu\text{m}$ . Surface roughness analysis was performed with a laser scanning surface analysis software (Keyence VK-H1XME). Figure 7.3 illustrates an example of the profilometry, showing a 2D surface profile and a 3D topographic map. In the 2D profile, a surface with less peak-to-valley height corresponds to a lower  $R_a$  value. In the 3D profile, the presence of both dark blue and red colors corresponds to a large variation in the peak-to-valley height value leading to a high  $S_a$  value.

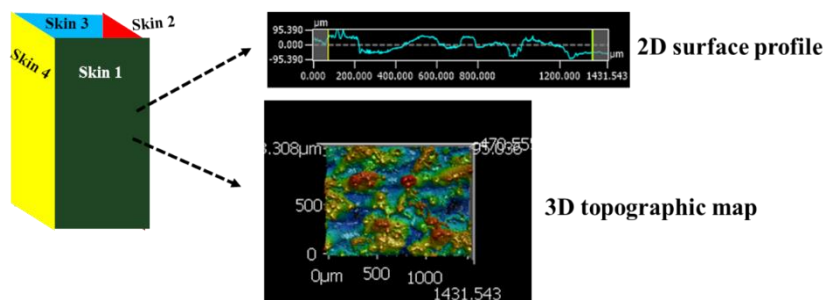


**Figure 7.3 Schematic showing an example a 2D surface profile and 3D topographic map, used to calculate the  $R_a$  and  $S_a$  values; respectively.**

### 7.4.3 Additive manufacturing of TPMS structures

In this work a diamond TPMS structure was investigated. A total of 3 specimen types with varying cell size and porosities were manufactured. More details on the cell size, height, wall thickness, and volume fraction cellular architecture density of the structures, are presented in Table 7.1. The TPMS structured were designed using nTopology (New York, United States) software. The inputs in the software were diameter and height of the TPMS disk and the cell size and wall thickness of the TPMS. Table 7.1 shows an image for the unit cell, corresponding CAD model, and manufactured part for the various TPMS designs along with the nomenclature.

All specimens were manufactured using an Arcam A2X EB-PBF machine. The Ti-6Al-4V powder feedstock was supplied by Advanced Coatings & Processes (AP&C, Canada) and consisted of pre-alloyed, PA powder with a size distribution of  $45\ \mu\text{m}$  to  $105\ \mu\text{m}$ . The layer thickness was set to  $50\ \mu\text{m}$ . The samples were built in accordance with the equipment manufacturer’s default “Net theme” settings (version 5.2.40). A total of three (3) separate builds were manufactured. The principal difference between the builds was the preheat temperature. Preheat parameters mentioned in prior work (Table 6.2 of Chapter 6) were used; in

brief a total of three (3) separate builds were manufactured. The only difference between the builds was the preheat temperature. The preheat temperatures used for Experiment 1, Experiment 2, and Experiment 3 were 650 °C, 690 °C, and 730 °C, respectively.

**Table 7.1 TPMS Diamond specimen types and their associated dimensions**

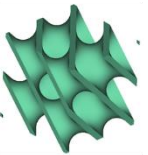
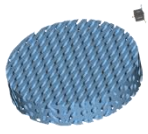
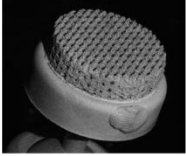
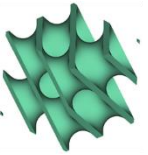
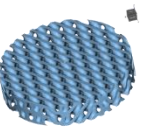
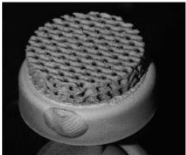
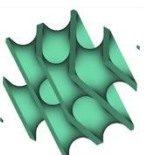
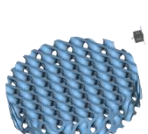
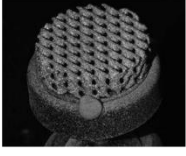
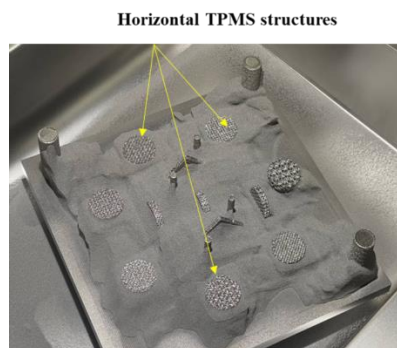
TPMS Type	Disk Diameter (in mm)	Disk Height (in mm)	Cell size (in mm)	Wall Thickness (in mm)	TPMS Density (in %)	Nomenclature	Unit cell	CAD model	Manufactured part
Diamond	25	5	4	1.1	0.645808	Diamond 4			
Diamond	25	5	5	1	0.466499	Diamond 5			
Diamond	25	6	6	1	0.387683	Diamond 6			

Figure 7.4 depicts the start plate containing the TPMS structures partially embedded in the powder cake. The specimens were removed (from the start plate) and de-powdered by using the PRS. No post-processing or heat treatment was performed. The specimens of interest for this work were manufactured horizontally, i.e., the long axis of the specimens was oriented parallel to the powder stacked layers (X direction).



**Figure 7.4 Depiction of the start plate containing the TPMS structures partially embedded in the powder cake**

#### 7.4.4 Geometric fidelity evaluation of the TPMS structures

X-ray computed tomography (XCT) is known to be the most common method of evaluating the geometric fidelity of intricate features [255], [349], [360], [361]. Therefore, a Zeiss Xradia 520 Versa X-ray computed tomography (XCT) scanner was used to scan the TPMS structures. A high-resolution scan was obtained at 10  $\mu\text{m}$  voxel size to capture the center of the TPMS structure. Data obtained from the XCT scans was analyzed using an image processing software (Dragonfly 3.0, Object Research Systems Inc., Montreal, QC). The scanned specimens were then manually best-fitted with the CAD model to qualitatively observe the geometrical deviations (the steps are depicted in Figure 7.5).

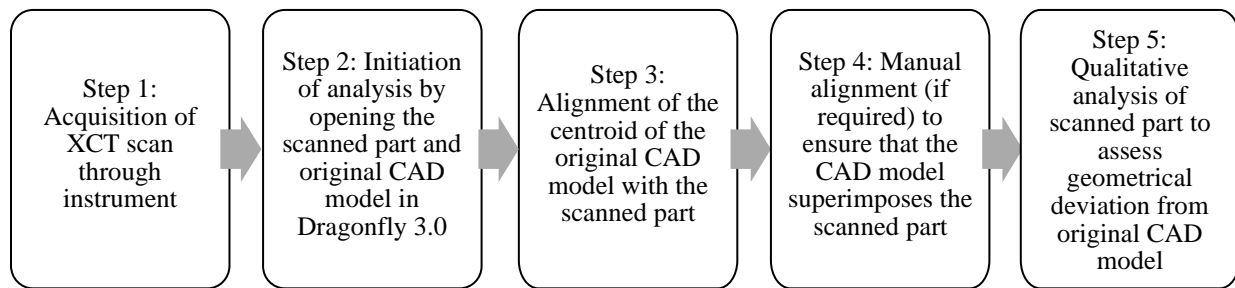


**Figure 7.5** Flowchart showing the steps for qualitative assessment of geometrical deviations

### 7.5 Results and Discussion

#### 7.5.1 Analysis of the part-quality artefacts

Figure 7.6 shows the average Ra values (in  $\mu\text{m}$ ) and Figure 7.7 shows the average Sa values (in  $\mu\text{m}$ ), for all skins (for all fabricated part-quality artefacts) across the build plate where (a), (b), and (c) represent artefacts manufactured during Experiment 1, 2, and 3, respectively. The colors green, red, blue, and yellow represent Skin 1, Skin 2, Skin 3, and Skin 4, respectively. The samples are labeled according to Figure 6.3. The plots shown in Figure 7.6 and Figure 7.7 were created in MATLAB. The MATLAB code that was written to create these visualizations is provided in Appendix G.

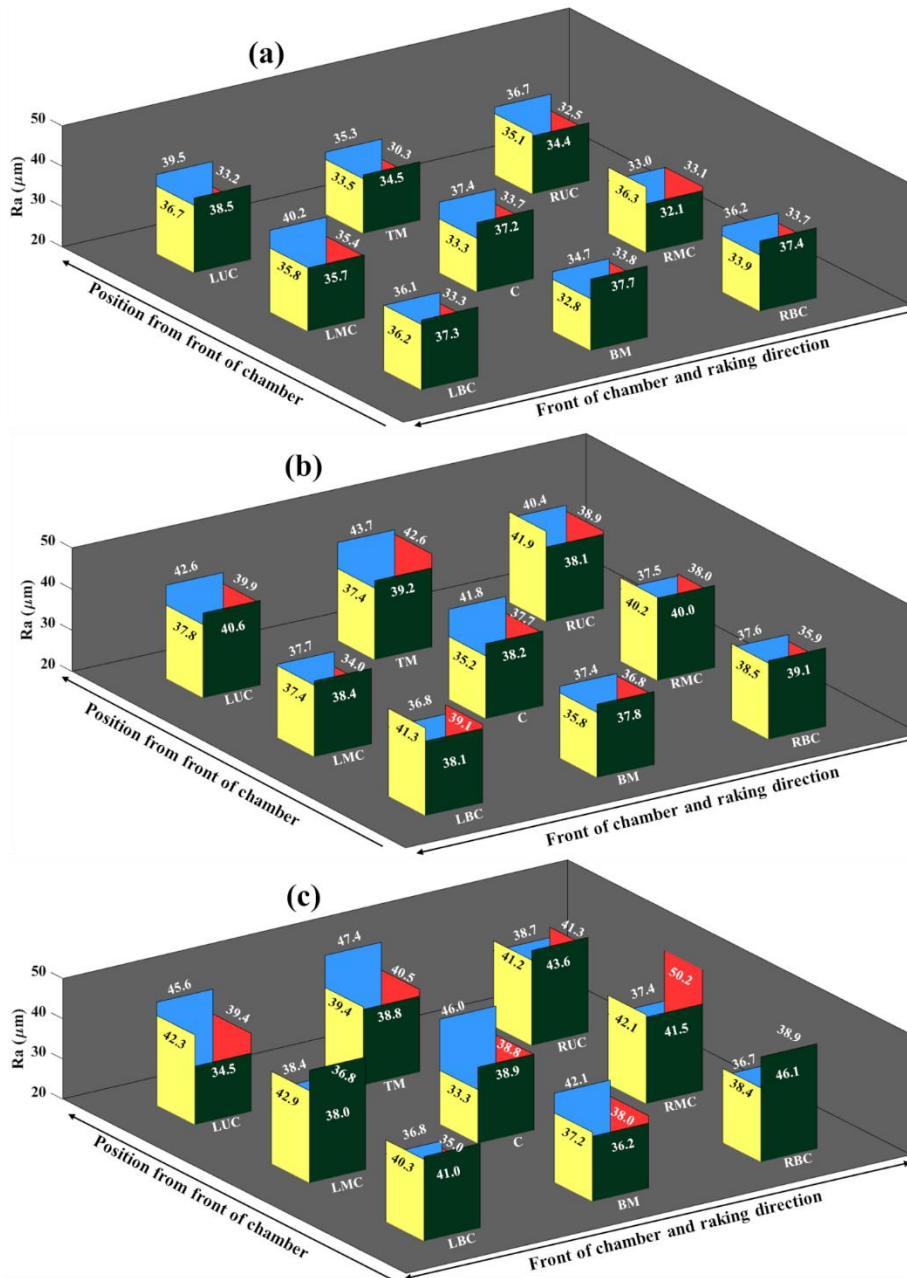


Figure 7.6 Average Ra values (in  $\mu\text{m}$ ) for all skins (for all fabricated part-quality artefacts) across the build plate where (a), (b), and (c) represent artefacts manufactured at 650 °C (Experiment 1), 690 °C (Experiment 2), and 730 °C (Experiment 3), respectively. The colors green, red, blue, and yellow represent Skin 1, Skin 2, Skin 3, and Skin 4, respectively.

From Figure 7.6 it is observed that the average Ra values lie between  $30.3 \pm 1.22 \mu\text{m}$  to  $40.2 \pm 2.09 \mu\text{m}$  for Experiment 1 artefacts,  $34.0 \pm 1.70 \mu\text{m}$  to  $43.7 \pm 1.29 \mu\text{m}$  for all Experiment 2 artefacts and  $33.2 \pm$

1.42  $\mu\text{m}$  to  $50.2 \pm 3.07 \mu\text{m}$  for all Experiment 3 artefacts. From Figure 7.7 it is also observed that the average Sa values lie between  $33.2 \pm 1.16 \mu\text{m}$  to  $44.9 \pm 3.29 \mu\text{m}$  for Experiment 1 artefacts,  $37.0 \pm 1.67 \mu\text{m}$  to  $52.7 \pm 4.26 \mu\text{m}$  for all Experiment 2 artefacts and  $36.3 \pm 5.06 \mu\text{m}$  to  $59.5 \pm 5.38 \mu\text{m}$  for all Experiment 3 artefacts.

The most noteworthy observation from Figure 7.6 and Figure 7.7 is that a decrease in preheating temperature led to a decrease in the Ra and Sa values. On an average, a decrease of  $80 \text{ }^\circ\text{C}$  in the preheating temperature led to a bulk 13% and 18% decrease in the Ra and Sa values, respectively.

The quality of the surface and dimensional accuracy are bound by the thermal properties of the powder bed [362]. A higher preheating temperature leads to over melting of the powder cake [180], [181], as demonstrated in Chapter 6. As the amount of heat input or energy density increases, the amount of particles simultaneously sintered on the surface of components increases, which in turn is expected to lead to difficulty in de-powdering and retrieval of parts post-build, thereby increasing the surface roughness of the parts and reducing the geometric fidelity of final components.

Another observation from Figure 7.6 and Figure 7.7 is that for each of the three experiments, there is a considerable difference observed between the Ra and Sa values for all skins, respectively. The difference in surface topology when comparing the Skins 1 to 4 can be attributed to the interaction between the energy source and the powder density neighboring the part border. The powder density at the border is influenced by the raking mechanism used when a new powder layer is spread. In the present study, the direction of raking is parallel to the Skins 1 and Skins 3, which were shown to have the highest values for Ra and Sa. The raking system may introduce grooves parallel to the direction of spread, which contribute to differences in local powder bed density within an entire layer along Skin 1 and 3 in when compared to the Skin 2 at the powder front and Skin 4 at the tail end of the powder spread for each part.

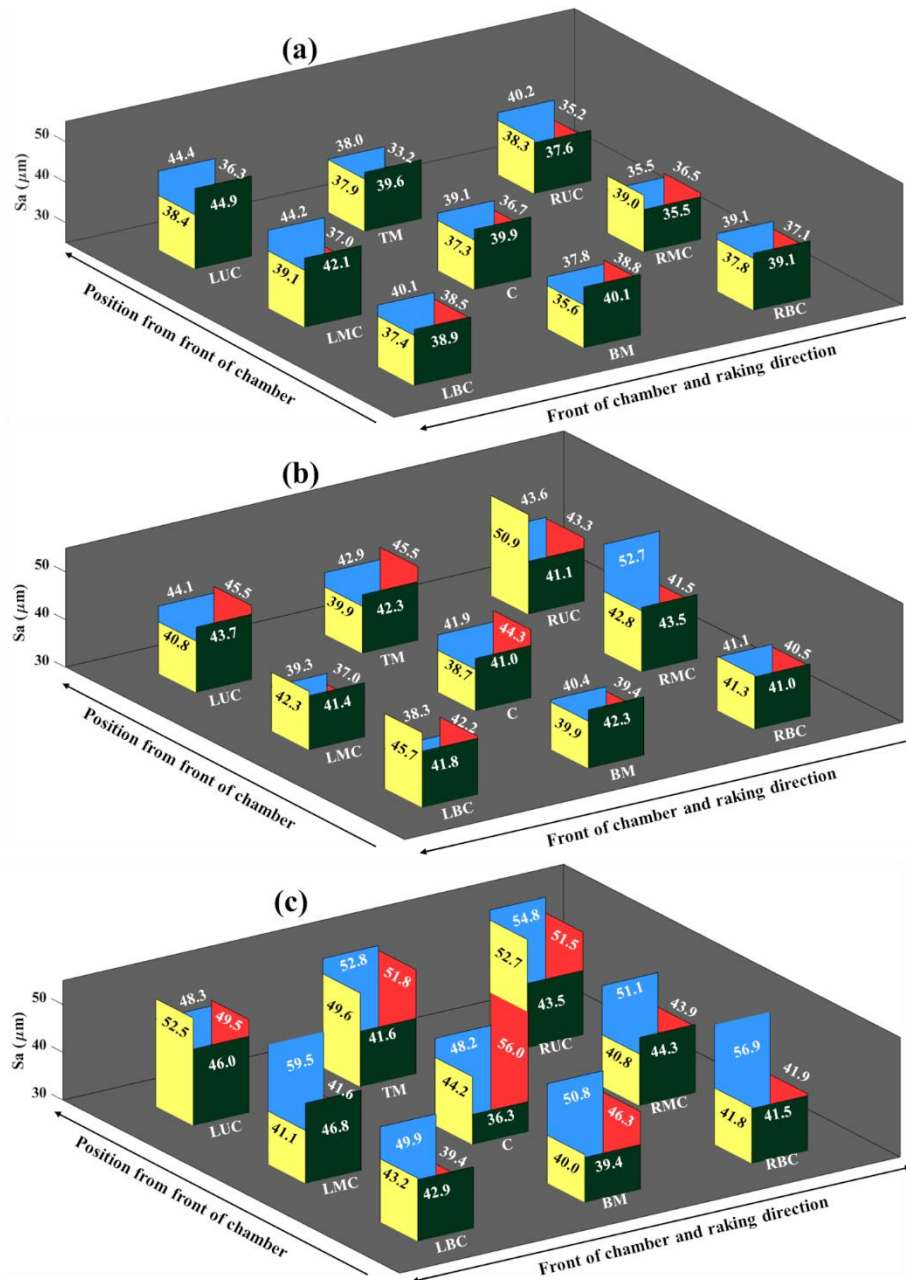


Figure 7.7 Average Sa values (in  $\mu\text{m}$ ) for all skins (for all fabricated part-quality artefacts) across the build plate where (a), (b), and (c) represent artefacts manufactured at 650 °C (Experiment 1), 690 °C (Experiment 2), and 730 °C (Experiment 3), respectively. The colors green, red, blue, and yellow represent Skin 1, Skin 2, Skin 3, and Skin 4, respectively.

To be able to quantify the change in Ra and Sa values with changing preheating temperatures, the values for a given experiment were averaged and plotted against the preheating temperatures as shown in Figure 7.8. The coefficient of determination (or R-squared) values depict that a near linear relationship exists between the preheating temperatures and the Ra and Sa values for each skin. A linear equation was established, for all skins, from the experimentally measured values of Ra and Sa for the three preheating temperatures. The equations below describe such:

$$\text{Skin 1 Ra} = 0.061 \times T - 3.4338 \quad \text{Equation 7.3}$$

$$\text{Skin 2 Ra} = 0.0833 \times T - 20.384 \quad \text{Equation 7.4}$$

$$\text{Skin 3 Ra} = 0.0556 \times T + 0.6582 \quad \text{Equation 7.5}$$

$$\text{Skin 4 Ra} = 0.0604 \times T - 4.0437 \quad \text{Equation 7.6}$$

$$\text{Skin 1 Sa} = 0.0343 \times T + 17.741 \quad \text{Equation 7.7}$$

$$\text{Skin 2 Sa} = 0.1285 \times T - 46.795 \quad \text{Equation 7.8}$$

$$\text{Skin 3 Sa} = 0.1582 \times T - 64.143 \quad \text{Equation 7.9}$$

$$\text{Skin 4 Sa} = 0.0904 \times T - 20.585 \quad \text{Equation 7.10}$$

where  $T$  is the preheating temperature. These equations can be used to predict the Ra and Sa values of the various skins (w.r.t build location) when using preheating temperatures between 650 °C and 730 °C. Caution should be taken in doing so, as only three points were used to construct the interpolation function.

During the past two decades, significant efforts have been made to adjust and tune the surface topography of implants to be able to enhance the initial bonding between the implant and the biological tissue [81]. Ponader et al. [81] mentioned that the proliferation of hFOB cells was reduced on surfaces having a high Ra value. Apart from biomedical implants, Chan et al. [107] and Edwards et al. [108] have indicated that the fatigue life of Ti-6Al-4V parts fabricated by AM techniques can be diminished due to high surface roughness values. In industrial applications, rough surfaces for this material system lead to corrosion and fracture of conduits [109].



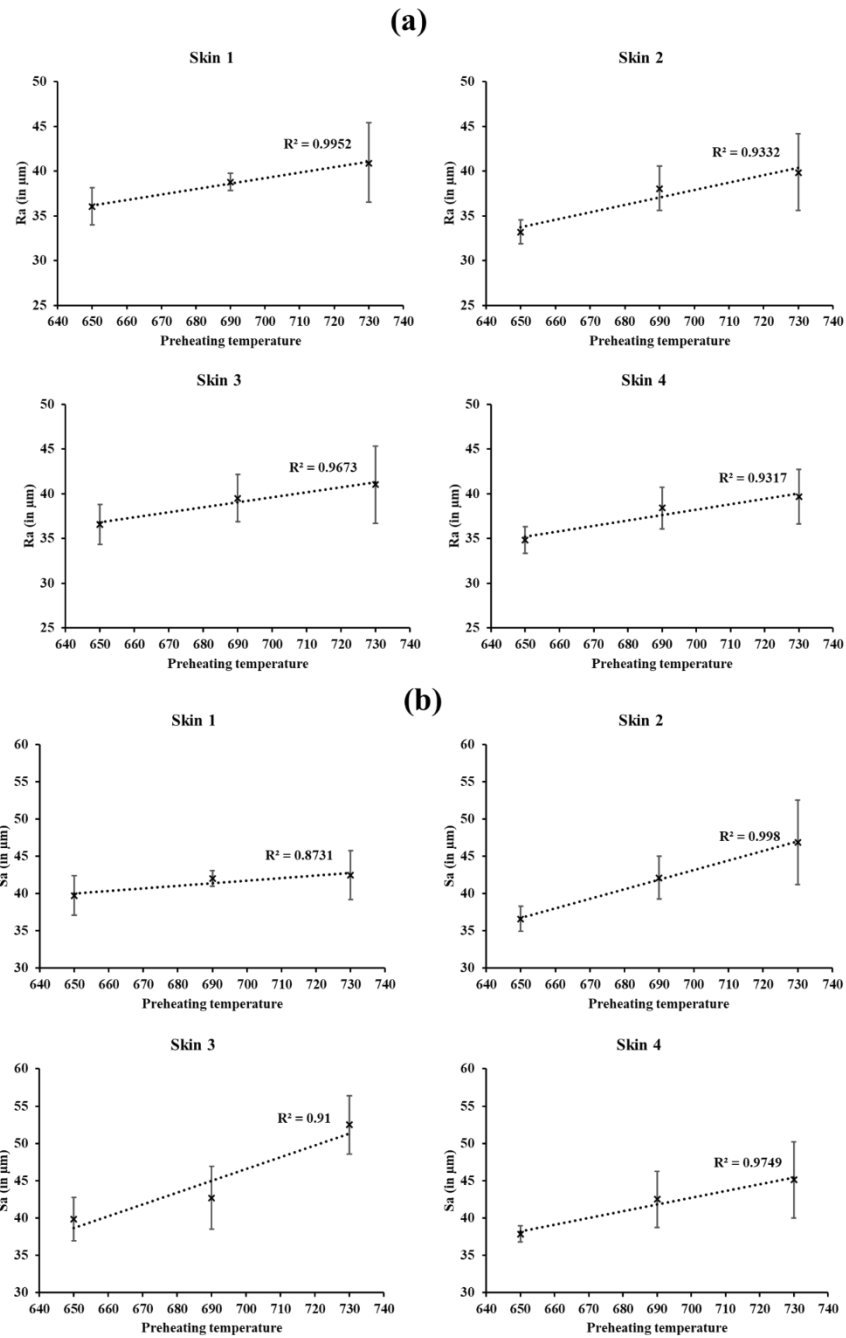


**Figure 7.8 Average (a) Ra and (b) Sa values for every skin for all experiments with linear trendlines. Error bars represent the standard deviation.**

It is essential to find ways of controlling or reducing the surface roughness of EB-PBF parts without changing many processing parameters, and/or by incorporating post-processing techniques. It is important

to note that in PBF, it has been shown that reducing the particle size distribution of the feedstock powders also correlates with better surface quality [363], [364], however this is not possible to explore in EB-PBF because the typical particle size distribution for all EB-PBF machines is 45  $\mu\text{m}$  to 105  $\mu\text{m}$  [117]. This study shows that the Ra and Sa values can be improved, without using any post-processing techniques apart from the blasting in the PRS, by simply tuning the preheating temperature of the powder cake. Altogether, parts produced by EB-PBF, can be controlled to fine-tune the density, contact size ratio, and thermal conductivity of the preheated powder cake and, as a result, can impart a noticeable effect on the surface roughness of the solidified parts.

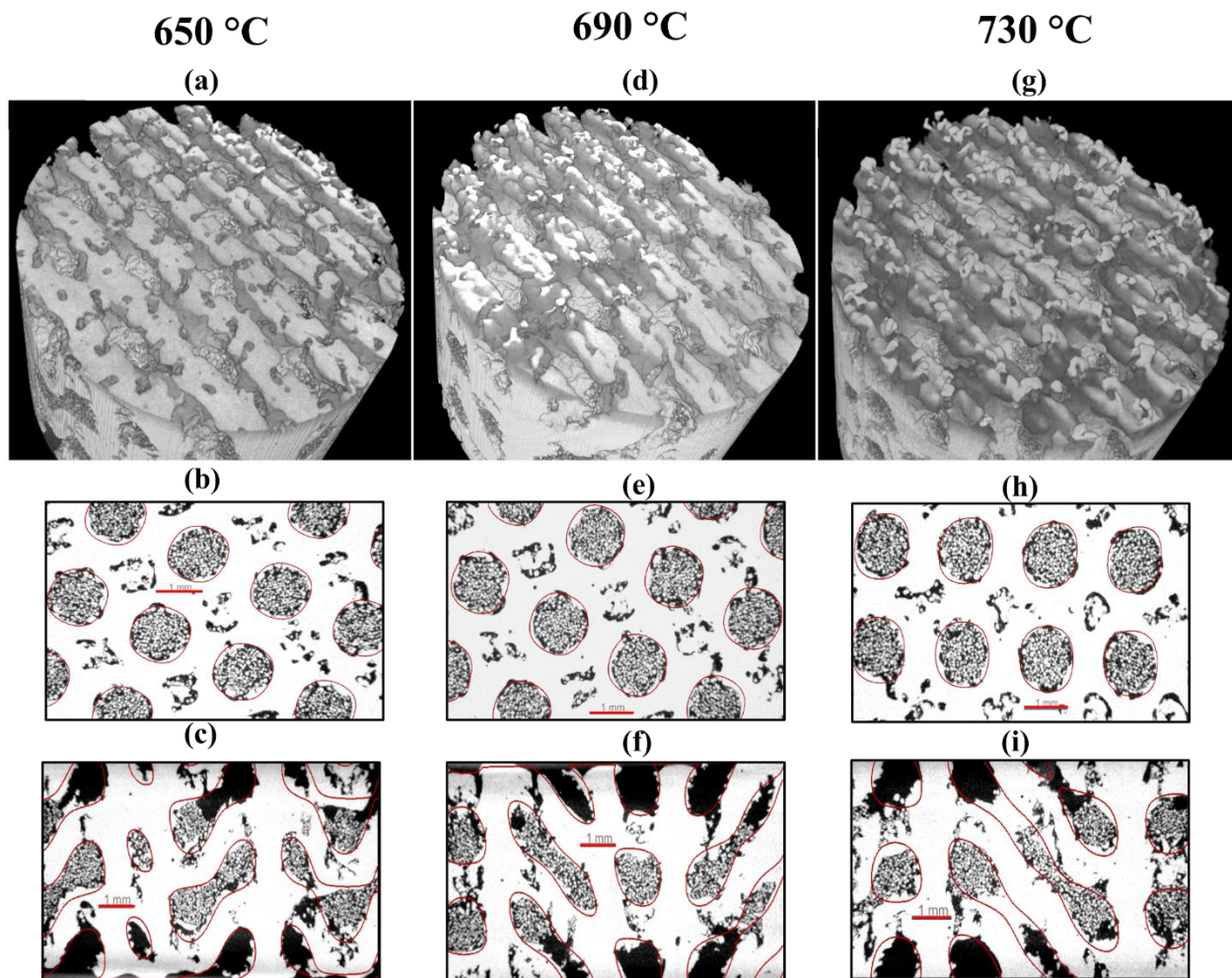
### 7.5.2 Analysis of the TPMS structures

Figure 7.9 shows select 2D and 3D XCT visualizations of Diamond 4 TPMS structures manufactured during Experiment 1 ((a), (b), (c)), Experiment 2 ((d), (e), (f)), and Experiment 3 ((g), (h), (i)). Figure 7.9 (a), (b), and (c) are the 3D visuals for each experiment and the images shown below them (i.e., (b), (c), (e), (f), (h), and (i)) are 2D comparisons of the slices along the XY and XZ plane of the corresponding 3D visuals.

Figure 7.9 (a), (d), and (g) show the top surfaces of the Diamond 4 TPMS structures manufactured during Experiment 1, 2, and 3, respectively. From these figures, it can be observed that the top surface appears to be smooth for the Experiment 1 (650 °C) structure. However, for the Experiment 2 (690 °C) structure, some partially-melted powder particles attached to the surface are observed, and the quantity of these partially melted powder particles increases for the Experiment 3 (730 °C) structure. In prior work (Chapter 6), it was observed that an increase in the preheating temperature enhances the particle sintering phenomenon. The interaction between the beam exposure at the border of the part and the solidified powder cake causes an increase in the surface roughness (as seen in Section 7.5.1) as a direct result of increased partial melting and attachment of the powder particles to the solidified area of the manufactured surface [259], [260]. Therefore, it can also be hypothesized that an increase in preheating temperature will cause poor de-powdering due to the difficulty in removing the partially melted powder particles that are attached to the solid surface of the TPMS structures.

To qualitatively assess the deviation of geometry of the manufactured structures with their as-designed CAD geometry, Figure 7.9 (b), (c), (e), (f), (h), and (i) shows the best fit alignment of the various TPMS structures' slices with the original CAD model. The red line in these figures is the original CAD. From a qualitative perspective, the deviation of the manufactured structures from the original CAD geometry appears to be increasing with an increase in preheating temperature. A quantitative analysis of this deviation is part of future work, and it is out of scope at the present time.

A significant challenge with the analysis of the Diamond 4 structure is that the internal pore architectures had retained powder, even after cleaning via the Powder Recovery System (PRS). This is due to the very small feature size that does not enable proper cleaning of the intricate architectures. In order to substantially remove the retained powder, other post-processing techniques, such as forced chemical processing may need to be adopted [365]. Despite this challenge, it was observed that de-powdering, using the PRS, became easier and faster with a decrease in preheating temperature. This was attributed to the fact that the reduced preheating temperature will lead to low contact size ratio and smaller sinter necks (refer to Chapter 6 for more details), thus leading to easy break-off of powder particles attached to the solidified material.



**Figure 7.9** 2D and 3D XCT visualizations of Diamond 4 TPMS structures manufactured during Experiment 1 ((a), (b), (c)), Experiment 2 ((d), (e), (f)), and Experiment 3 ((g), (h), (i)).

Figure 7.10 and Figure 7.11 show the 2D and 3D XCT visualizations of Diamond 5 and Diamond 6 TPMS structures, respectively, manufactured during Experiment 1 ((a), (b), (c)), Experiment 2 ((d), (e), (f)), and Experiment 3 ((g), (h), (i)). Figure 7.10 and Figure 7.11 (a), (b), and (c) are the 3D visuals for each experiment and the images shown below them are 2D comparisons of slices along the XY and XZ plane of the corresponding 3D visuals.

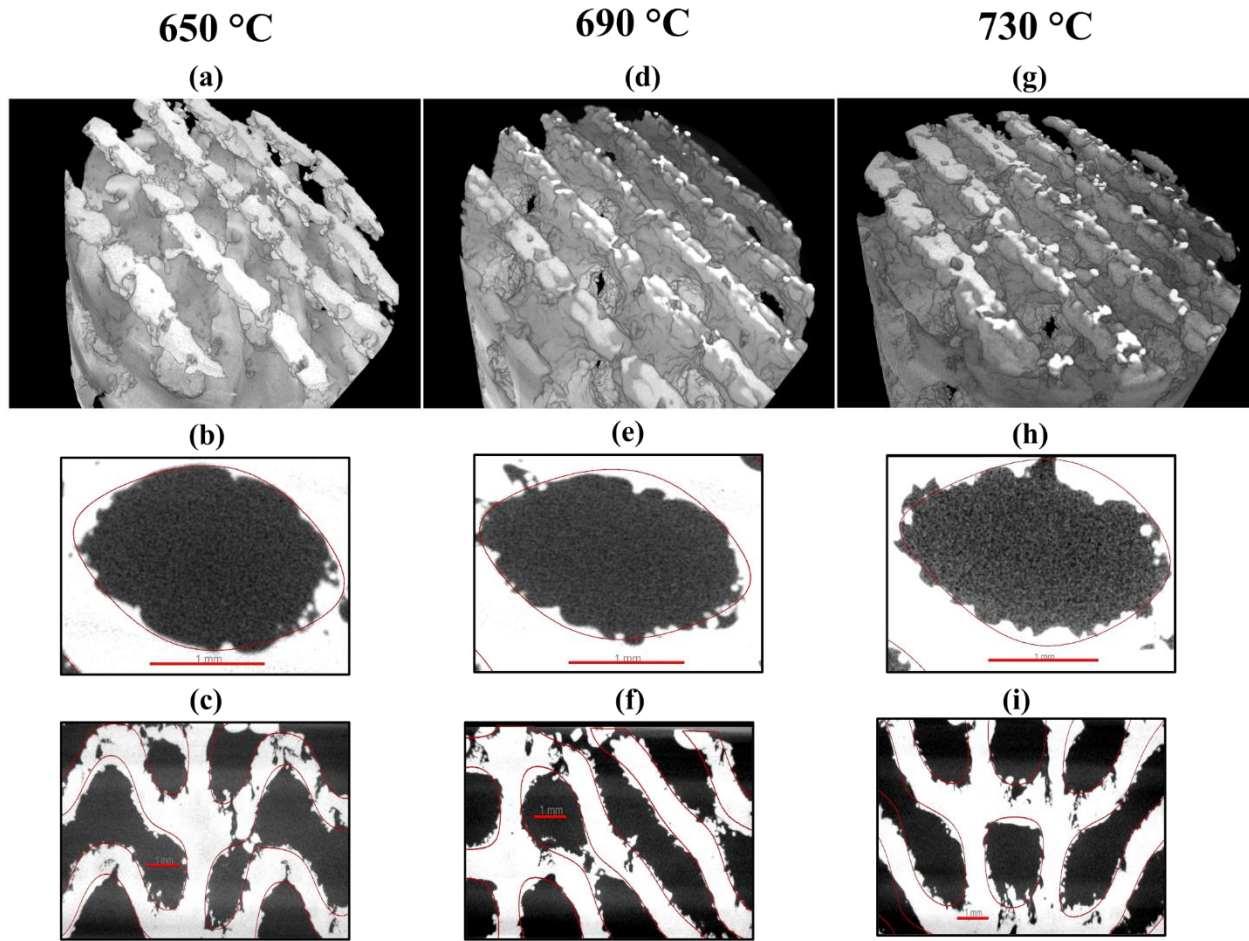


**Figure 7.10 2D and 3D XCT visualizations of Diamond5 TPMS structures manufactured during Experiment 1 ((a), (b), (c)), Experiment 2 ((d), (e), (f)), and Experiment 3 ((g), (h), (i)).**

Similarly to Figure 7.9, Figure 7.10 (a), (d), and (g) show the top surfaces of the Diamond 5 TPMS structures manufactured during Experiment 1, 2, and 3, respectively and Figure 7.11 (a), (d), and (g) show the top surfaces of the Diamond 6 TPMS structures manufactured during Experiment 1, 2, and 3, respectively. Similar results to the Diamond 4 structures was observed; qualitatively, an increase in partially

melted powder particles attached to the surface of the TPMS structures was observed with an increase in the preheating temperature.

Upon visual assessment of the deviation of geometry of the manufactured structures with their as-designed CAD geometry in Figure 7.10 ((b), (c), (e), (f), (h), and (i)) and Figure 7.11 ((b), (c), (e), (f), (h), and (i)), it can be observed that the deviation of the manufactured structures from the original CAD geometry keeps increasing with an increase in preheating temperature.

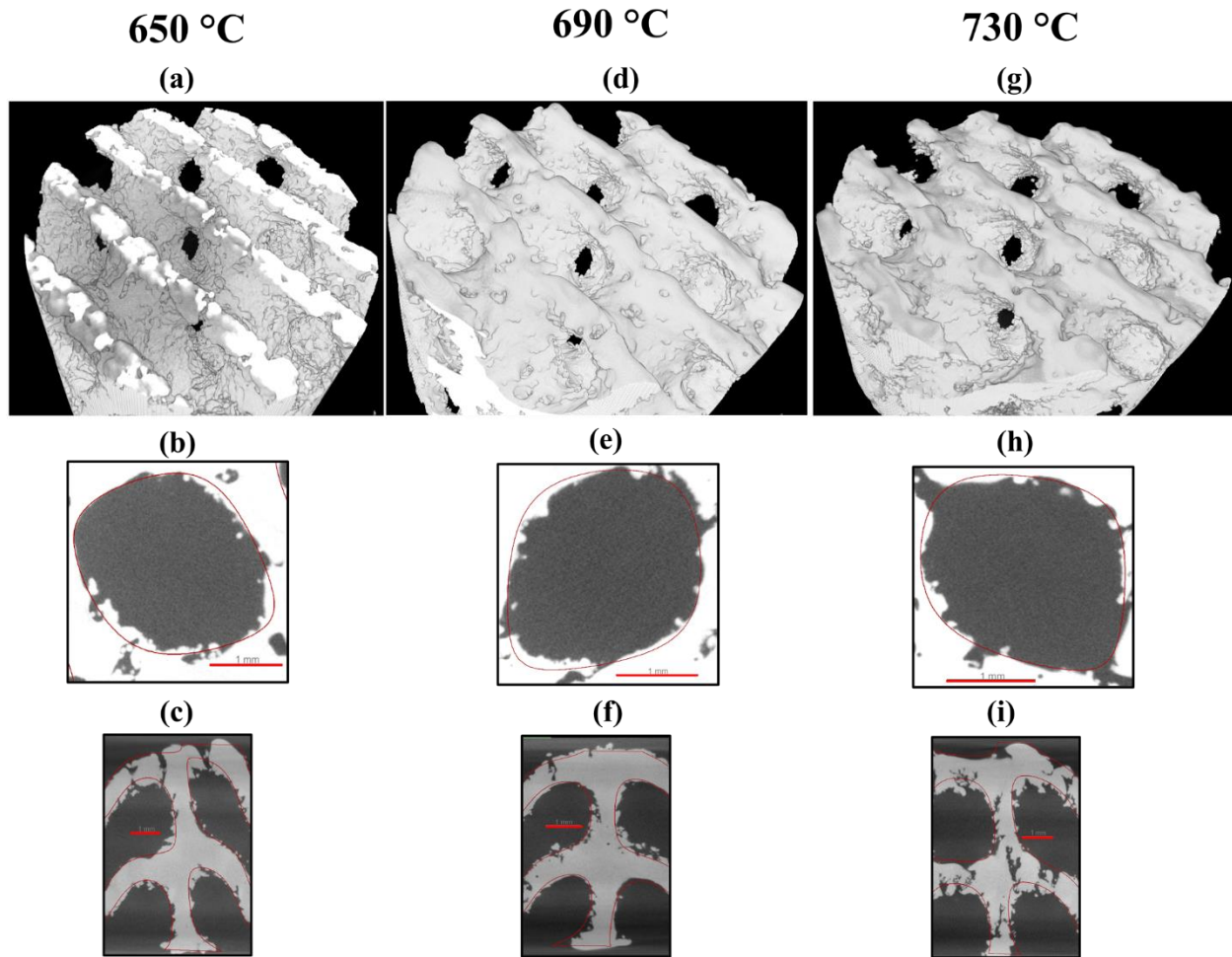


**Figure 7.11 2D and 3D XCT visualizations of Diamond 6 TPMS structures manufactured during Experiment 1 ((a), (b), (c)), Experiment 2 ((d), (e), (f)), and Experiment 3 ((g), (h), (i)).**

The geometric fidelity is determined by the physics phenomena happening at the boundary of the Melt Theme zone (pertinent to manufacturing the part) and the Preheat Theme zone (pertinent to producing the powder cake). The thermal conductivity of the powder cake was shown to increase as a function of

increasing the preheat temperature (Chapter 6). As a result, it is hypothesized that the heat transfer phenomena is better coupled between the higher density powder cake and the part; as such, there may be a possibility that this facilitates powder material fusion at the surface, which leads to larger deviations from the original CAD geometry.

The geometric deviation of the cross-sectional shape and size of the TPMS structures may have a significant impact on the moment of inertia and load-bearing area of the fine features and ultimately impact the elastic modulus (E) of the structure [366]. It was shown in prior work (Chapter 4) that an increase in the cross-sectional area can lead to an increase in the strength of the part. Therefore, the geometric deviation may also affect the strength of the structure [367]; either increasing it or decreasing it, depending on whether the manufactured cross-section is smaller or larger than the original CAD model. Various researchers have looked at compensating for geometrical errors [368], [369], however, geometric deviation associated with surface roughness is difficult to compensate for [370]. Additionally, this surface roughness leads to issues surrounding tensile properties, as was described in prior work Chapter 5, and fatigue life as described in literature [104], [105]. Therefore, it is important to reduce the surface roughness in order to improve the dimensional accuracy and obtain low geometric deviations of the manufactured part from their corresponding CAD models. The knowledge gained from the prior work (Chapter 6) and current work on surface roughness and geometrical deviation evaluation, can be used to further optimize the preheating temperature to be able to gain better geometric fidelity.

## 7.6 Conclusions

The effect of varying preheating temperatures on the surface topography and geometric fidelity of simple and complex geometries in EB-PBF were observed. Additionally, the preheating temperature appears to have an impact on the de-powdering outcomes for complex-shaped lattice architectures. Some of the main findings were:

- i. The calculated Ra and Sa values for the part-quality artefacts ranged from  $30.3 \pm 1.22 \mu\text{m}$  to  $50.2 \pm 3.07 \mu\text{m}$  and  $33.2 \pm 1.16 \mu\text{m}$  to  $59.5 \pm 5.38 \mu\text{m}$  respectively when the preheating temperature was varied at 650 °C, 690 °C, and 730 °C respectively.
- ii. Logarithmic regression equations were established from the measured surface roughness data. These equations can be used to predict the surface roughness of parts fabricated by EB-PBF when using preheating temperatures of 650 °C, 690 °C, and 730 °C respectively.

- iii. The current study shows that a decrease of 80 °C in the preheating temperature led to a 13% and 18% decrease in the Ra and Sa values, respectively with a mere change of 3% in the layer-wise powder cake density and 12% in the effective thermal conductivity (as identified in Chapter 6).
- iv. A decrease in the preheating temperature can reduce the amount of partially-fused powder particles attached to the solidified material. This improves de-powdering of retained powder from intricate features of TPMS structures.
- v. A decrease in the preheating temperature has been shown to reduce the surface roughness, without dramatic changes in the packing density of the powder cake and seemingly no impact on the density of the corresponding solid part. This can be beneficial for researchers looking at improving fatigue performance of as-built parts.

## Chapter 8

### Conclusions and Future Work

The focus of this thesis is to advance the scientific body of knowledge in understanding the interconnected relationships between the powder properties, bulk powder behavior, in-situ performance, and part properties (as shown in Figure 1.1). While each chapter provides a conclusion specific to the chapters content, this chapter aims to summarize the main conclusions and proposed future work for continuation of this thesis.

#### 8.1 Thesis Conclusions and recommendations for future work

The main conclusions of this thesis and recommendations for future work are summarized below and categorized as per the objectives identified in Chapter 1:

##### **Objective 1: Understanding the effect of reuse on powder properties and the EB-PBF process**

Investigation into the effect of plasma-atomized Grade 5 Ti-6Al-4V powder reuse on the powder properties as well as properties of powder blends led to the following conclusions:

1. Upon comparing the influence of multiple reuse cycles, as well as powder blends created from reused powder on various powder characteristics such as the morphology, size distribution, flow properties, packing properties, and chemical composition, it was found that there was an increase in measured response in powder size distribution, tapped density, Hausner ratio, Carr index, basic flow energy, specific energy, dynamic angle of repose, oxygen, and nitrogen content, while the bulk density remained largely unchanged.
2. The input feedstock powder contributes to ~ 28 % of the total cost of the build. Therefore, the cost of the EB-PBF process heavily relies on the reusability of powders and may not be cost-affordable for complex applications if the un-melted powder in the build bed is not reused. Thus, the evaluation of the maximum number of allowable powder reuse cycles is an essential factor to assess process affordability for a specific part or application. In EB-PBF there is a possibility of reusing 95–98% of the powder that is not melted. The current work presents a set of powder suitability criteria which help users in determining which tests are relevant for their own work (or application) based on the information that is provided for each characterization technique. Furthermore, the suitability criteria enables users to quantitatively evaluate the relative drift in powder properties from a user-defined initial benchmark powder.



3. The powder metrics measured are very different in nature and may impact the PBF process and final part properties in different ways. For instance, powder metrics variations may have opposite effects, i.e., some characteristics may lead to an improved behavior in the AM process, others may lead to a deterioration of the AM process behavior, while some powder metrics may have limited effect. Variability is still relatively high for some of the powder measurement techniques, and are influenced by the testing equipment type, the testing conditions, the powder storage and handling conditions, the operator skill, the calibration of instruments, and many other factors. Care must be exercised in interpreting each powder metric result individually. A unified powder quality formula and score called the EB-PBF Suitability Factor was established to help compare the degree of deterioration of the reused powder. This may help other researchers in understanding how to compare their own reused powders to a reference powder.

The work detailed in this thesis strengthens the opportunity to explore future work in areas such as:

1. Investigation of the effects of reuse cycles on part quality such as, surface topography, part density, oxygen levels, microstructure, and mechanical properties. Furthermore, the effect of powder flowability on powder spreading with a rake, should be investigated.
2. Investigation of the powder cake organization as a function of reuse cycles to assess changes in powder thermal properties (if any).

**Objective 2: Understanding the tensile behavior and pore space characteristics of EB-PBF components:** This thesis focused on a systematic investigation of tensile properties for EB-PBF as-built Ti-6Al-4V by evaluating, assessing, and reporting the impact on tensile test results with respect to (i) the changes in specimen geometry, (ii) the change in specimen size, (iii) the change in build orientation, and (iv) the internal porous defects observed via XCT. Furthermore, deeper correlations between the pore space characteristics (such as total volume, equivalent diameter, frequency, sphericity, aspect ratio, and radial position) and the tensile specimen characteristics (such as geometry, orientation, cross-sectional area, surface area to volume ratio, and tensile behavior), were established. The findings support the following conclusions:

1. Horizontally-built (H) specimens showed higher Ultimate Tensile Strength (UTS) and Yield Strength (YS), and lower elongation at fracture (% EL) values when compared to Vertically-built (V) specimens.
2. H specimens had the highest variability in layer-wise pore fraction. It was observed that the single field of view scans for H specimens were not representative of the Full Gauge due to the presence of large unevenly distributed defects. This observation was extended to conclude that a single tensile specimen size and geometry may not accurately represent the mechanical properties of all features of an EB-PBF

as-built Ti-6Al-4V component. This impacts part qualification since a load-bearing feature from a part would not necessarily have the same mechanical properties if the qualifying tensile specimen differed from it in overall size, shape, and orientation. Furthermore, H specimens had a considerably larger number of pores that were  $> 200 \mu\text{m}$  and went up to  $1200 \mu\text{m}$ , whereas all pores for V specimens were  $< 200 \mu\text{m}$ , with the exception of E8M-2 specimen. The pore space  $< 100 \mu\text{m}$  was very similar across specimens manufactured in both directions. Therefore, the authors suspect that, if the processing parameters are kept the same, these pores will appear in specimens of any size and geometry, irrespective of their build orientation.

3. An increase in specimen cross-sectional area led to an increase in the UTS, YS, and Elastic Modulus (E) values. Furthermore, the subsurface pore population was significantly less, for the H specimens having the largest and smallest cross-sectional area. It is therefore very important to take the size and geometry into account when comparing results in literature and assessing the performance of tensile specimens.
4. An increase in the specimen surface area to volume ratio led to a decrease in the UTS and YS values. This indicates that cylindrical specimens with a smaller diameter and flat specimens with a larger width and/or smaller thickness, will have decreased performance. For H specimens, those with a very low, or very high surface area to volume ratio had a lower maximum pore size, which resulted in higher elongation values. These specimens also had higher minimum layer solid fractions, indicating that they have smaller, more evenly spaced pores compared to the other specimen types. Furthermore, the H specimens with the smallest and largest surface area to volume ratio had no pores  $> 500 \mu\text{m}$  whereas, all H specimens having surface area to volume ratios between  $0.5 /\text{mm}$  to  $1.25 /\text{mm}$  had pores from  $50 \mu\text{m}$  to  $500+ \mu\text{m}$ .
5. The specimen maximum pore size did not affect the UTS, YS, and E. However, a strong correlation was observed between the % EL and the maximum pore size for horizontal specimens, such that with the % EL decreases with an increase in maximum pore size. Furthermore, the % EL was linked to the pore equivalent diameter such that specimens that showed absence of pores  $> 500 \mu\text{m}$  had higher elongation values.
6. The analytical tools developed to evaluate pore characteristics and their effect on part mechanical properties are expected to be generalizable in nature and can be leveraged to other materials and PBF processes.

7. The scientific outcomes of such studies are expected to translate to a direct and immediate value to the standards community and to industry towards addressing the knowledge gap in quality assessment of the EB-PBF process.

The work detailed in this thesis strengthens the opportunity to explore future work in areas such as:

1. Systematic investigation of tensile properties for EB-PBF machined specimens by evaluating, assessing, and reporting the impact on tensile test results with respect to (i) the changes in specimen geometry, (ii) the change in specimen size, (iii) the change in build orientation, and (iv) the internal porous defects observed via XCT; and furthermore, comparing these to the results obtained for as-built specimens. This would assist in de-coupling the effects of machining on the tensile performance.
2. Development of adaptive pore classifiers and machine learning performance predictors. Pore classifiers may help reveal groups or classes of pores that are not inherently apparent when looking at the equivalent diameter alone. Furthermore, based on the size of datasets, it is important to explore mechanical performance predictors further to explore how all classes of pores can be correlated to mechanical properties.
3. Statistical analysis can be applied to prove or disprove the hypothesis regarding the effect of (i) the changes in specimen geometry, (ii) the change in specimen size, (iii) the change in build orientation, and (iv) the pore space characteristics on the tensile properties.

**Objective 3: Understanding the in-situ powder cake properties and its effects on the surface topography, geometric dimensional deviations, and de-powdering, in the EB-PBF process:** The effect of varying preheating temperatures on the effective thermal conductivity of the Ti-6Al-4V powder cake, surface topography and geometric fidelity of simple and complex geometries, in EB-PBF, were observed. Some of the main findings were:

1. The effective thermal conductivity of the powder cake at a given preheating temperature strongly depends on the packing density, contact size ratio, and coordination number.
2. An increase in the preheating temperature led to a linear increase in the packing density, contact size ratio, coordination number, effective thermal conductivity, and surface roughness. Logarithmic regression equations were established from the empirically - derived thermal conductivity data and the measured surface roughness data. These equations can be used to predict the average packing density, contact size ratio, coordination number, and the thermal conductivity of the powder cake, and surface roughness of fabricated parts, in EB-PBF, when using preheating temperatures between 650 °C and 730 °C. Furthermore, these empirically-derived models can be used to study the necking and sintering phenomenon for use in FE models.

3. The current study shows that a decrease of 80 °C in the preheating temperature led to a 13% and 18% decrease in the Ra and Sa values, respectively with a mere change of 3% in the layer-wise density and 12% in the effective thermal conductivity. Therefore, it can be stated that a decrease in the preheating temperature can drastically reduce the surface roughness without dramatic changes in the packing density of the powder cake. This can be beneficial for researchers looking at improving fatigue performance of parts.
4. Furthermore, upon assessing the geometrical fidelity it was found that a decrease in the preheating temperature led to a decrease in the amount of partially melted powder particles attached to the solidified structure. This in turn led to better de-powdering and reduced geometrical deviation of the manufactured structures from their original CAD model.
5. The authors believe that the current work will aid in providing reliable empirical information into furthering the understanding behind the evolution of the input Ti-6Al-4V powder from its as-received powder feedstock state to preheated, partially sintered molten and finally its solid state.

The work detailed in this thesis strengthens the opportunity to explore future work in areas such as:

1. Investigation of the powder cake organization as a function of reuse cycles to assess changes in powder thermal properties (if any).
2. Investigation of the effect of varying preheating temperatures on manufactured part properties such as oxygen levels, and microstructure.
3. Quantification of the extent of de-powdering and geometric dimensional deviations with increase of preheating temperature.

## 8.2 Research Contributions

### 8.2.1 Articles in peer-reviewed journals

1. **Shanbhag G**, Vlasea M. “The effect of reuse cycles on Ti-6Al-4V powder properties processed by electron beam powder bed fusion.” *Journal of Manufacturing Letters*. August 2020. <https://doi.org/10.1016/j.mfglet.2020.07.007>
2. Wheat, E., **Shanbhag, G.**, and Vlasea, M. "The Master Sinter Curve and Its Application to Binder Jetting Additive Manufacturing." *ASME. Journal of Manufacturing Science & Engineering*. October 2020. <https://doi.org/10.1115/1.4047140>
3. **Shanbhag G**, Vlasea M. “Variation of Powder Properties Induced by Reuse Cycles in Electron Beam Powder Bed Fusion.” *Journal of Materials, Special Issue: Materials Research Considerations for Metal*

Powder and Wire-Based Additive Manufacturing Processing. August 2021.  
<https://doi.org/10.3390/ma14164602>

4. **Shanbhag G**, Wheat E, Moylan S, Vlasea M. “Effect of specimen geometry and orientation on tensile properties of Ti-6Al-4V manufactured by electron beam powder bed fusion.” *Journal of Additive Manufacturing. (Under Review)*
5. **Shanbhag G**, Wheat E, Moylan S, Vlasea M. “Data related to Effect of specimen geometry and orientation on tensile properties of Ti-6Al-4V manufactured by electron beam powder bed fusion.” *Journal of Data in Brief. (Under Review)*
6. **Shanbhag G**, Vlasea M. “Effect of varying preheating temperatures in electron beam powder bed fusion: Part I Assessment of the effective powder cake thermal conductivity.” *Journal of Manufacturing Processes (Under Review)*

## **8.2.2 Conference proceedings, presentations, posters, magazines, and AM awards**

### **8.2.2.1 Conference Oral Presentations**

1. **Shanbhag G**, Wheat E, Moylan S, Vlasea M. “Effect of Sample Geometry and Orientation on Tensile Properties of Ti-6Al-4V manufactured by Electron Beam Melting” at Materials Science & Technology (MS&T) Conference (Online) in Oct 2020
2. **Shanbhag G**, Vlasea M. “Powder reuse cycles in electron beam melting and their effect on Ti-6Al-4V powder properties” at NSERC Holistic Innovation in Additive Manufacturing (HI-AM) Conference (Online) in Jun 2020
3. **Shanbhag G**, Vlasea M. “Design of a test artefact to evaluate critical design features for Ti-6Al-4V parts in electron-beam melting additive manufacturing” at NSERC Holistic Innovation in Additive Manufacturing (HI-AM) Conference – Vancouver, British Columbia, Canada in Jun 2019

### **8.2.2.2 Conference Poster Presentations**

1. **Shanbhag G**, Wheat E, Moylan S, Vlasea M. “Effect of specimen geometry and orientation on tensile properties of Ti-6Al-4V manufactured by electron beam powder bed fusion” at NSERC Holistic Innovation in Additive Manufacturing (HI-AM) Conference (Online) in Jun 2021
2. **Shanbhag G**, Brock L, Vlasea M. “The Copper Cooler: Heat Sink for CPUs” at RAPID + TCT 2019 Conference – Detroit, Michigan, USA in May 2019

3. **Shanbhag G**, Vlasea M. “Particle Packing Models – Current Understanding & Future Direction” at NSERC Holistic Innovation in Additive Manufacturing (HI-AM) Conference – Waterloo, Ontario, Canada in May 2018

#### 8.2.2.3 Conference Proceedings

1. **Shanbhag G**, Wheat E, Moylan S, Vlasea M. “Effect of specimen geometry and orientation on tensile properties of Ti-6Al-4V manufactured by electron beam powder bed fusion” at NSERC Holistic Innovation in Additive Manufacturing (HI-AM) Conference in Jun 2021
2. **Shanbhag G**, Vlasea M. “Powder reuse cycles in electron beam melting and their effect on Ti-6Al-4V powder properties” at NSERC Holistic Innovation in Additive Manufacturing (HI-AM) Conference (Online) in Jun 2020
3. **Shanbhag G**, Vlasea M. “Design of a test artefact to evaluate critical design features for Ti-6Al-4V parts in electron-beam melting additive manufacturing” at NSERC Holistic Innovation in Additive Manufacturing (HI-AM) Conference – Vancouver, British Columbia, Canada in Jun 2019
4. **Shanbhag G**, Vlasea M. “Particle Packing Models – Current Understanding & Future Direction” at NSERC Holistic Innovation in Additive Manufacturing (HI-AM) Conference – Waterloo, Ontario, Canada in May 2018

#### 8.2.2.4 Magazine articles

1. **Shanbhag G**, Brock L, Vlasea M. “Digital Manufacturing Challenge: Powering the World by an Innovative Design for CPU Heat Sinks” for Manufacturing Engineering magazine by SME in Sep 2019

#### 8.2.2.5 Additive manufacturing awards

1. **Shanbhag G**, Brock L, Vlasea M. “The Copper Cooler: Heat Sink for CPUs” – Digital Manufacturing Challenge Award valued at \$1000 by SME, Michigan, USA in Apr 2019
2. **Shanbhag G**, Rishmawi I, Vlasea M. “Modified Helicopter tail boom of Airbus H135 using aluminum 2024-T3” - Canada Makes 3D Challenge Runner-Up Award valued at \$1000 by Canada Makes, Quebec, Canada

## References

- [1] C. K. Chua, K. F. Leong, and C. S. Lim, *Rapid Prototyping: Principles and Applications*. World Scientific, 2010.
- [2] I. Gibson, D. Rosen, and B. Stucker, “Additive Manufacturing Technologies,” in *Additive Manufacturing Technologies*, Second., 2015, pp. 1–498.
- [3] ASTM, “52900:2015-Standard Terminology for Additive Manufacturing – General Principles – Terminology,” *ASTM Int.*, vol. i, pp. 1–9, 2015, doi: 10.1520/F2792-12A.2.
- [4] N. Hrabe and T. Quinn, “Effects of processing on microstructure and mechanical properties of a titanium alloy (Ti–6Al–4V) fabricated using electron beam melting (EBM), Part 2: Energy input, orientation, and location,” *Mater. Sci. Eng. A*, vol. 573, pp. 271–277, Jun. 2013, doi: 10.1016/j.msea.2013.02.065.
- [5] N. Hrabe and T. Quinn, “Effects of processing on microstructure and mechanical properties of a titanium alloy (Ti–6Al–4V) fabricated using electron beam melting (EBM), part 1: Distance from build plate and part size,” *Mater. Sci. Eng. A*, vol. 573, pp. 264–270, 2013, doi: 10.1016/j.msea.2013.02.064.
- [6] S. Gorsse, C. Hutchinson, M. Gouné, and R. Banerjee, “Additive manufacturing of metals: a brief review of the characteristic microstructures and properties of steels, Ti-6Al-4V and high-entropy alloys,” *Sci. Technol. Adv. Mater.*, vol. 18, no. 1, pp. 584–610, Dec. 2017, doi: 10.1080/14686996.2017.1361305.
- [7] S. Biamino *et al.*, “Electron beam melting of Ti–48Al–2Cr–2Nb alloy: Microstructure and mechanical properties investigation,” *Intermetallics*, vol. 19, no. 6, pp. 776–781, Jun. 2011, doi: 10.1016/j.intermet.2010.11.017.
- [8] J. J. Lewandowski and M. Seifi, “Metal Additive Manufacturing: A Review of Mechanical Properties,” *Annu. Rev. Mater. Res.*, vol. 46, no. 1, pp. 151–186, Jul. 2016, doi: 10.1146/annurev-matsci-070115-032024.
- [9] D. Cormier, O. Harrysson, T. Mahale, and H. West, “Freeform Fabrication of Titanium Aluminide via Electron Beam Melting Using Prealloyed and Blended Powders,” *Res. Lett. Mater. Sci.*, vol. 2007, pp. 1–4, 2007, doi: 10.1155/2007/34737.
- [10] F. A. Shah *et al.*, “Long-term osseointegration of 3D printed CoCr constructs with an interconnected open-pore architecture prepared by electron beam melting,” *Acta Biomater.*, vol. 36, pp. 296–309, May 2016, doi: 10.1016/j.actbio.2016.03.033.
- [11] L. E. Murr and S. M. Gaytan, “Electron Beam Melting,” in *Comprehensive Materials Processing*,

- vol. 10, Elsevier, 2014, pp. 135–161.
- [12] D. Cormier, O. Harrysson, and H. West, “Characterization of H13 steel produced via electron beam melting,” *Rapid Prototyp. J.*, vol. 10, no. 1, pp. 35–41, Feb. 2004, doi: 10.1108/13552540410512516.
- [13] C. Wang, X. Tan, E. Liu, and S. B. Tor, “Process parameter optimization and mechanical properties for additively manufactured stainless steel 316L parts by selective electron beam melting,” *Mater. Des.*, vol. 147, pp. 157–166, Jun. 2018, doi: 10.1016/j.matdes.2018.03.035.
- [14] T. Sanviemvongsak, D. Monceau, and B. Macquaire, “High temperature oxidation of IN 718 manufactured by laser beam melting and electron beam melting: Effect of surface topography,” *Corros. Sci.*, vol. 141, no. July, pp. 127–145, 2018, doi: 10.1016/j.corsci.2018.07.005.
- [15] B. Gustavsson, “Effect of Beam Scan Length on Microstructure Characteristics of EBM Manufactured Alloy 718,” 2018.
- [16] P. Nandwana *et al.*, “Recyclability Study on Inconel 718 and Ti-6Al-4V Powders for Use in Electron Beam Melting,” *Metall. Mater. Trans. B*, vol. 47, no. 1, pp. 754–762, Feb. 2016, doi: 10.1007/s11663-015-0477-9.
- [17] M. Romedenne, R. Pillai, M. Kirka, and S. Dryepondt, “High temperature air oxidation behavior of Hastelloy X processed by Electron Beam Melting (EBM) and Selective Laser Melting (SLM),” *Corros. Sci.*, vol. 171, p. 108647, Jul. 2020, doi: 10.1016/j.corsci.2020.108647.
- [18] L. E. Murr *et al.*, “Microstructures of Rene 142 nickel-based superalloy fabricated by electron beam melting,” *Acta Mater.*, vol. 61, no. 11, pp. 4289–4296, Jun. 2013, doi: 10.1016/j.actamat.2013.04.002.
- [19] K. A. Unocic, M. M. Kirka, E. Cakmak, D. Greeley, A. O. Okello, and S. Dryepondt, “Evaluation of additive electron beam melting of haynes 282 alloy,” *Mater. Sci. Eng. A*, vol. 772, p. 138607, Jan. 2020, doi: 10.1016/j.msea.2019.138607.
- [20] J. Ureña, M. Martínez, L. Portolés, S. Sanjuán, and J. Blasco, “Pure copper development at industrial scale by electron beam melting technology,” 2019.
- [21] M. A. Lodes, R. Guschlbauer, and C. Körner, “Process development for the manufacturing of 99.94% pure copper via selective electron beam melting,” *Mater. Lett.*, vol. 143, pp. 298–301, Mar. 2015, doi: 10.1016/j.matlet.2014.12.105.
- [22] J. Kowen, “Unrealised Potential: The story and status of Electron Beam Powder Bed Fusion,” *Metal Additive Manufacturing*, 2020. <https://www.metal-am.com/articles/unrealised-potential-the-story-and-status-of-electron-beam-powder-bed-fusion-3d-printing/> (accessed Aug. 09, 2021).



- [23] B. Kloeden, S. Biamino, U. Ackelid, B. Kieback, and T. Weissgaerber, “Properties of a TiAl turbocharger wheel produced by electron beam melting,” 2014.
- [24] A. L. Jardini *et al.*, “Customised titanium implant fabricated in additive manufacturing for craniomaxillofacial surgery,” *Virtual Phys. Prototyp.*, vol. 9, no. 2, pp. 115–125, Apr. 2014, doi: 10.1080/17452759.2014.900857.
- [25] A. L. Jardini *et al.*, “Cranial reconstruction: 3D biomodel and custom-built implant created using additive manufacturing,” *J. Cranio-Maxillofacial Surg.*, vol. 42, no. 8, pp. 1877–1884, Dec. 2014, doi: 10.1016/j.jcms.2014.07.006.
- [26] M. Cronskaer, L. E. Raennar, A. Koptioug, and M. Baekstroem, “Application of electron beam melting to titanium hip stem implants,” *Annals of DAAAM & Proceedings*, 2008. <https://www.thefreelibrary.com/Application+of+electron+beam+melting+to+titanium+hip+stem+implants.-a0225316135> (accessed Aug. 09, 2021).
- [27] A. Mazzoli, M. Germani, and R. Raffaelli, “Direct fabrication through electron beam melting technology of custom cranial implants designed in a PHANToM-based haptic environment,” *Mater. Des.*, vol. 30, no. 8, pp. 3186–3192, Sep. 2009, doi: 10.1016/j.matdes.2008.11.013.
- [28] S. L. Sing, J. An, W. Y. Yeong, and F. E. Wiria, “Laser and electron-beam powder-bed additive manufacturing of metallic implants: A review on processes, materials and designs,” *J. Orthop. Res.*, vol. 34, no. 3, pp. 369–385, Mar. 2016, doi: 10.1002/jor.23075.
- [29] K. R. Harrysson, O. L., Cormier, D. R., Marcellin-Little, D. J., & Jajal, “Direct Fabrication of Metal Orthopedic Implants Using Electron,” in *International Solid Freeform Fabrication Symposium*, 2003, pp. 439–446, doi: <http://dx.doi.org/10.26153/tsw/5604>.
- [30] T. Boissonneault, “Quebec forges ahead with 3D printed jawbone implant research with Arcam EBM tech,” *3D Printing Media Network*, Oct. 2018. <https://www.3dprintingmedia.network/quebec-3d-printed-jawbone-implant/> (accessed Aug. 09, 2021).
- [31] L. Dall’Ava, H. Hothi, A. Di Laura, J. Henckel, and A. Hart, “3D Printed Acetabular Cups for Total Hip Arthroplasty: A Review Article,” *Metals (Basel)*, vol. 9, no. 7, p. 729, Jun. 2019, doi: 10.3390/met9070729.
- [32] S. Zeidler and M. Öström, “From powder to spinal cage production: Added value for spinal implants through additive manufacturing,” *GE Additive*, 2020. [https://go.additive.ge.com/rs/706-JIU-273/images/GE\\_Additive-Added\\_Value\\_for\\_Spinal\\_Implants\\_through\\_AM.pdf](https://go.additive.ge.com/rs/706-JIU-273/images/GE_Additive-Added_Value_for_Spinal_Implants_through_AM.pdf) (accessed Aug. 09, 2021).
- [33] W. E. Frazier, “Metal Additive Manufacturing: A Review,” *J. Mater. Eng. Perform.*, vol. 23, no. 6,

- pp. 1917–1928, Jun. 2014, doi: 10.1007/s11665-014-0958-z.
- [34] L. E. Murr *et al.*, “Fabrication of Metal and Alloy Components by Additive Manufacturing: Examples of 3D Materials Science,” *J. Mater. Res. Technol.*, vol. 1, no. 1, pp. 42–54, Apr. 2012, doi: 10.1016/S2238-7854(12)70009-1.
- [35] P. Edwards, A. O’Conner, and M. Ramulu, “Electron Beam Additive Manufacturing of Titanium Components: Properties and Performance,” *J. Manuf. Sci. Eng.*, vol. 135, no. 6, p. 061016, Nov. 2013, doi: 10.1115/1.4025773.
- [36] L. Yang *et al.*, “Electron Beam Technology,” in *Additive Manufacturing of Metals: The Technology, Materials, Design and Production*, Springer International Publishing, 2017, pp. 63–79.
- [37] W. J. Sames V, “Additive Manufacturing of Inconel 718 using Electron beam melting: Processing, post-processing & Mechanical Properties,” Texas A&M University, 2015.
- [38] A. A. Antonysamy, “Microstructure , Texture and Mechanical Property Evolution during Additive Manufacturing of Ti6Al4V Alloy for Aerospace Applications [dissertation],” The University of Manchester, 2012.
- [39] C. Wen, *Metallic foam bone: Processing, modification and characterization and properties*. Elsevier Inc., 2016.
- [40] L. E. Murr *et al.*, “Microstructures and mechanical properties of electron beam-rapid manufactured Ti–6Al–4V biomedical prototypes compared to wrought Ti–6Al–4V,” *Mater. Charact.*, vol. 60, no. 2, pp. 96–105, Feb. 2009, doi: 10.1016/j.matchar.2008.07.006.
- [41] X. Gong, T. Anderson, and K. Chou, “Review on powder-based electron beam additive manufacturing technology,” *Manuf. Rev.*, vol. 1, p. 2, Apr. 2014, doi: 10.1051/mfreview/2014001.
- [42] A. Safdar, “A Study on Electron Beam Melted Ti-6Al-4V [dissertation],” Lund University, 2012.
- [43] A. Mohammadhosseini, D. Fraser, S. H. Masood, and M. Jahedi, “Microstructure and mechanical properties of Ti–6Al–4V manufactured by electron beam melting process,” *Mater. Res. Innov.*, vol. 17, no. sup2, pp. s106–s112, Dec. 2013, doi: 10.1179/1432891713Z.000000000302.
- [44] U. Ljungblad, “Method and apparatus for additive manufacturing,” US20150004045A1, 2013.
- [45] S. Liu and Y. C. Shin, “Additive manufacturing of Ti6Al4V alloy: A review,” *Mater. Des.*, vol. 164, p. 107552, Feb. 2019, doi: 10.1016/j.matdes.2018.107552.
- [46] ArcamEBM, “Manufacturing Unbound,” no. 5, p. 20, 2017, doi: 10.1080/03632415.2015.1027159.
- [47] Arcam AB, “Arcam Products.” <http://www.arcam.com/technology/products/>.
- [48] Arcam AB, “Arcam Level 1 Training Document,” 2018.
- [49] I. Gibson, D. W. Rosen, and B. Stucker, “Additive Manufacturing Technologies: Rapid Prototyping

- to Direct Digital Manufacturing,” *Media*, no. 3, pp. 193–198, 2010, doi: 10.1595/205651315X688406.
- [50] T. Douglas and S. Gilvert, “Costs and Cost Effectiveness of Additive Manufacturing,” *NIST Spec. Publ.*, no. 1176, 2014, doi: 10.6028/NIST.SP.1176.
- [51] U. Ackelid and P. Ohldin, “Freemelt.” <https://www.freemelt.com/>.
- [52] Wayland Additive, “Innovation in metal additive manufacturing.” <https://www.waylandadditive.com/neubeam/> (accessed Jul. 09, 2021).
- [53] T. Mahale, “Electron beam melting of advanced materials and structures,” North Carolina State University, 2009.
- [54] P. Drescher, M. Sarhan, and H. Seitz, “An Investigation of Sintering Parameters on Titanium Powder for Electron Beam Melting Processing Optimization,” *Materials (Basel)*, vol. 9, no. 12, p. 974, Dec. 2016, doi: 10.3390/ma9120974.
- [55] A. Neira-Arce, “Thermal Modeling and Simulation of Electron Beam Melting for Rapid Prototyping on Ti6Al4V Alloys,” North Carolina State University, 2012.
- [56] H. Weiwei, J. Wenpeng, L. Haiyan, T. Huiping, K. Xinting, and H. Yu, “Research on Preheating of Titanium Alloy Powder in Electron Beam Melting Technology,” *Rare Met. Mater. Eng.*, vol. 40, no. 12, pp. 2072–2075, Dec. 2011, doi: 10.1016/S1875-5372(12)60014-9.
- [57] X. Gong and K. Chou, “Characterization of Sintered Ti-6Al-4V Powders in Electron Beam Additive Manufacturing,” Jun. 2013, doi: 10.1115/MSEC2013-1131.
- [58] C. Körner, “Additive manufacturing of metallic components by selective electron beam melting — a review,” *Int. Mater. Rev.*, vol. 61, no. 5, pp. 361–377, Jul. 2016, doi: 10.1080/09506608.2016.1176289.
- [59] C. J. Smith, S. Tammas-Williams, E. Hernandez-Nava, and I. Todd, “Tailoring the thermal conductivity of the powder bed in Electron Beam Melting (EBM) Additive Manufacturing,” *Sci. Rep.*, vol. 7, no. 1, p. 10514, 2017, doi: 10.1038/s41598-017-11243-8.
- [60] M. F. Zäh, S. Lutzmann, M. Kahnert, and F. Walchshäusl, “Determination of Process Parameters for Electron Beam Sintering (EBS),” *COMSOL Conf. 2008*, pp. 12–18, 2008.
- [61] E. Rodriguez *et al.*, “Integration of a thermal imaging feedback control system in electron beam melting,” *23rd Annu. Int. Solid Free. Fabr. Symp. - An Addit. Manuf. Conf. SFF 2012*, no. Figure 1, pp. 945–961, 2012.
- [62] M. Sigl, S. Lutzmann, and M. F. Zaeh, “Transient physical effects in electron beam sintering,” in *Solid Freeform Fabrication Symposium*, 2006, pp. 464–477.

- [63] R. Klingvall Ek, L.-E. Rännar, M. Bäckstöm, and P. Carlsson, “The effect of EBM process parameters upon surface roughness,” *Rapid Prototyp. J.*, vol. 22, no. 3, pp. 495–503, Apr. 2016, doi: 10.1108/RPJ-10-2013-0102.
- [64] H. Gong, K. Rafi, N. V. Karthik, T. Starr, and B. Stucker, “Defect morphology in Ti-6Al-4V parts fabricated by Selective Laser Melting and Electron Beam Melting,” in *Solid Freeform Fabrication Symposium*, 2013, pp. 440–453.
- [65] S. Tamas-Williams, H. Zhao, F. Léonard, F. Derguti, I. Todd, and P. B. Prangnell, “XCT analysis of the influence of melt strategies on defect population in Ti-6Al-4V components manufactured by Selective Electron Beam Melting,” *Mater. Charact.*, vol. 102, pp. 47–61, 2015, doi: 10.1016/j.matchar.2015.02.008.
- [66] M. Suard, “Characterization and optimization of lattice structures made by Electron Beam Melting,” 2015.
- [67] N. Béraud, F. Vignat, F. Villeneuve, and R. Dendievel, “New trajectories in electron beam melting manufacturing to reduce curling effect,” *Procedia CIRP*, vol. 17, pp. 738–743, 2014, doi: 10.1016/j.procir.2014.02.038.
- [68] Y. H. Kok, X. P. Tan, N. H. Loh, S. B. Tor, and C. K. Chua, “Geometry dependence of microstructure and microhardness for selective electron beam-melted Ti-6Al-4V parts,” *Virtual Phys. Prototyp.*, vol. 11, no. 3, pp. 183–191, Jul. 2016, doi: 10.1080/17452759.2016.1210483.
- [69] J. K. Algardh *et al.*, “Thickness dependency of mechanical properties for thin-walled titanium parts manufactured by Electron Beam Melting (EBM) ®,” *Addit. Manuf.*, vol. 12, pp. 45–50, 2016, doi: 10.1016/j.addma.2016.06.009.
- [70] A. T. Sidambe, “Three dimensional surface topography characterization of the electron beam melted Ti6Al4V,” *Met. Powder Rep.*, vol. 72, no. 3, pp. 200–205, 2017, doi: 10.1016/j.mprp.2017.02.003.
- [71] Y. Y. Sun *et al.*, “The Influence of As-Built Surface Conditions on Mechanical Properties of Ti-6Al-4V Additively Manufactured by Selective Electron Beam Melting,” *JOM*, vol. 68, no. 3, pp. 791–798, Mar. 2016, doi: 10.1007/s11837-015-1768-y.
- [72] A. Triantaphyllou *et al.*, “Surface texture measurement for additive manufacturing,” *Surf. Topogr. Metrol. Prop.*, vol. 3, no. 2, 2015, doi: 10.1088/2051-672X/3/2/024002.
- [73] P. Wang *et al.*, “Recent Progress of Additive Manufactured Ti-6Al-4V by Electron Beam Melting,” in *Solid Freeform Fabrication Proceedings*, 2016, pp. 691–704.
- [74] P. Wang, X. Tan, M. L. S. Nai, S. B. Tor, and J. Wei, “Spatial and geometrical-based characterization of microstructure and microhardness for an electron beam melted Ti-6Al-4V

- component,” *Mater. Des.*, vol. 95, pp. 287–295, Apr. 2016, doi: 10.1016/j.matdes.2016.01.093.
- [75] G. Lütjering, J. C. C. Williams, G. Lütjering, and J. C. C. Williams, *Titanium*, 2nd ed. Berlin, Heidelberg: Berlin ; New York : Springer, 2007.
- [76] R. Ding, Z. X. Guo, and A. Wilson, “Microstructural evolution of a Ti–6Al–4V alloy during thermomechanical processing,” *Mater. Sci. Eng. A*, vol. 327, no. 2, pp. 233–245, Apr. 2002, doi: 10.1016/S0921-5093(01)01531-3.
- [77] T. Ahmed and H. J. Rack, “Phase transformations during cooling in  $\alpha+\beta$  titanium alloys,” *Mater. Sci. Eng. A*, vol. 243, no. 1, pp. 206–211, 1998, doi: [https://doi.org/10.1016/S0921-5093\(97\)00802-2](https://doi.org/10.1016/S0921-5093(97)00802-2).
- [78] M. Niinomi, “Mechanical biocompatibilities of titanium alloys for biomedical applications,” *J. Mech. Behav. Biomed. Mater.*, vol. 1, no. 1, pp. 30–42, Jan. 2008, doi: 10.1016/j.jmbbm.2007.07.001.
- [79] L. E. Murr *et al.*, “Microstructure and mechanical behavior of Ti–6Al–4V produced by rapid-layer manufacturing, for biomedical applications,” *J. Mech. Behav. Biomed. Mater.*, vol. 2, no. 1, pp. 20–32, Jan. 2009, doi: 10.1016/j.jmbbm.2008.05.004.
- [80] D. Vasudevan and P. Balashanmugam, “Study of thermal behaviour on titanium alloys (Ti-6Al-4V),” *J. Eng. Sci. Technol.*, vol. 12, pp. 2064–2077, Aug. 2017.
- [81] S. Ponader *et al.*, “Effects of topographical surface modifications of electron beam melted Ti-6Al-4V titanium on human fetal osteoblasts,” *J. Biomed. Mater. Res. Part A*, vol. 84A, no. 4, pp. 1111–1119, Mar. 2008, doi: 10.1002/jbm.a.31540.
- [82] A. Mohammadhosseini, D. Fraser, S. H. Masood, and M. Jahedi, “A Study of Morphology of Titanium Powder Used in Electron Beam Melting,” *Appl. Mech. Mater.*, vol. 541–542, pp. 160–163, Mar. 2014, doi: 10.4028/www.scientific.net/AMM.541-542.160.
- [83] G. E. Ryan, A. S. Pandit, and D. P. Apatsidis, “Porous titanium scaffolds fabricated using a rapid prototyping and powder metallurgy technique,” *Biomaterials*, vol. 29, no. 27, pp. 3625–3635, Sep. 2008, doi: 10.1016/j.biomaterials.2008.05.032.
- [84] D. M. Robertson, L. St. Pierre, and R. Chahal, “Preliminary observations of bone ingrowth into porous materials,” *J. Biomed. Mater. Res.*, vol. 10, no. 3, pp. 335–344, May 1976, doi: 10.1002/jbm.820100304.
- [85] X. Zhao *et al.*, “Comparison of the microstructures and mechanical properties of Ti-6Al-4V fabricated by selective laser melting and electron beam melting,” *Mater. Des.*, vol. 95, pp. 21–31, 2016, doi: 10.1016/j.matdes.2015.12.135.

- [86] M. J. Donachie, *Titanium: A Technical Guide, 2nd Edition*. ASM International, 2000.
- [87] D. Bhattacharyya, G. B. Viswanathan, S. C. Vogel, D. J. Williams, V. Venkatesh, and H. L. Fraser, “A study of the mechanism of  $\alpha$  to  $\beta$  phase transformation by tracking texture evolution with temperature in Ti-6Al-4V using neutron diffraction,” *Scr. Mater.*, vol. 54, no. 2, pp. 231–236, Jan. 2006, doi: 10.1016/j.scriptamat.2005.09.026.
- [88] B. Cheng, S. Price, J. Lydon, K. Cooper, and K. Chou, “On Process Temperature in Powder-Bed Electron Beam Additive Manufacturing: Model Development and Validation,” *J. Manuf. Sci. Eng.*, vol. 136, no. 6, Dec. 2014, doi: 10.1115/1.4028484.
- [89] A. Safdar, L.-Y. Wei, A. Snis, and Z. Lai, “Evaluation of microstructural development in electron beam melted Ti-6Al-4V,” *Mater. Charact.*, vol. 65, pp. 8–15, Mar. 2012, doi: 10.1016/j.matchar.2011.12.008.
- [90] S. Price, J. Lydon, K. Cooper, and K. Chou, “Temperature measurements in powder-bed electron beam additive manufacturing,” *ASME Int. Mech. Eng. Congr. Expo. Proc.*, vol. 2A, pp. 162–173, 2014, doi: 10.1115/IMECE2014-36661.
- [91] H. Galarraga, R. J. Warren, D. A. Lados, R. R. Dehoff, M. M. Kirka, and P. Nandwana, “Effects of heat treatments on microstructure and properties of Ti-6Al-4V ELI alloy fabricated by electron beam melting (EBM),” *Mater. Sci. Eng. A*, vol. 685, no. January, pp. 417–428, 2017, doi: 10.1016/j.msea.2017.01.019.
- [92] S. S. Al-Bermani, M. L. Blackmore, W. Zhang, and I. Todd, “The Origin of Microstructural Diversity, Texture, and Mechanical Properties in Electron Beam Melted Ti-6Al-4V,” *Metall. Mater. Trans. A*, vol. 41, no. 13, pp. 3422–3434, Dec. 2010, doi: 10.1007/s11661-010-0397-x.
- [93] B. Appolaire, L. Hélicher, and E. Aeby-Gautier, “Modelling of phase transformation kinetics in Ti alloys – Isothermal treatments,” *Acta Mater.*, vol. 53, no. 10, pp. 3001–3011, Jun. 2005, doi: 10.1016/j.actamat.2005.03.014.
- [94] M. Yan and P. Yu, “An Overview of Densification, Microstructure and Mechanical Property of Additively Manufactured Ti-6Al-4V — Comparison among Selective Laser Melting, Electron Beam Melting, Laser Metal Deposition and Selective Laser Sintering, and with Conventional Powder,” in *Sintering Techniques of Materials*, InTech, 2015.
- [95] S. M. Kelly, “Thermal and microstructure modeling of metal deposition processes with application to Ti-6Al-4V,” *Mater. Sci. Eng.*, vol. Doctoral, no. November, p. 319, 2004, [Online]. Available: [http://scholar.google.com/scholar?q=Thermal and microstructure modeling of metal deposition processes with application to Ti-6Al-4V&btnG=&hl=en&num=20&as\\_sdt=0%2C22](http://scholar.google.com/scholar?q=Thermal+and+microstructure+modeling+of+metal+deposition+processes+with+application+to+Ti-6Al-4V&btnG=&hl=en&num=20&as_sdt=0%2C22).

- [96] S. M. Gaytan *et al.*, “Comparison of Microstructures and Mechanical Properties for Solid and Mesh Cobalt-Base Alloy Prototypes Fabricated by Electron Beam Melting,” *Metall. Mater. Trans. A*, vol. 41, no. 12, pp. 3216–3227, Dec. 2010, doi: 10.1007/s11661-010-0388-y.
- [97] L. Zeng and T. R. Bieler, “Effects of working, heat treatment, and aging on microstructural evolution and crystallographic texture of  $\alpha$ ,  $\alpha'$ ,  $\alpha''$  and  $\beta$  phases in Ti–6Al–4V wire,” *Mater. Sci. Eng. A*, vol. 392, no. 1–2, pp. 403–414, Feb. 2005, doi: 10.1016/j.msea.2004.09.072.
- [98] F. X. Gil Mur, D. Rodríguez, and J. A. Planell, “Influence of tempering temperature and time on the  $\alpha'$ -Ti-6Al-4V martensite,” *J. Alloys Compd.*, vol. 234, no. 2, pp. 287–289, Feb. 1996, doi: 10.1016/0925-8388(95)02057-8.
- [99] J. Dawes, R. Bowerman, and R. Trepleton, “Introduction to the Additive Manufacturing Powder Metallurgy Supply Chain,” *Johnson Matthey Technol. Rev.*, vol. 59, no. 3, pp. 243–256, Jul. 2015, doi: 10.1595/205651315X688686.
- [100] P. K. Samal and J. W. Newkirk, *ASM Handbook, Volume 7: Powder Metallurgy*. ASM International, 2015.
- [101] Advanced Powders and Coatings, “Leading the Way in the Production of Plasma Atomized Spherical Metal Powders,” no. 450, 2015.
- [102] S. Vock, B. Klöden, A. Kirchner, T. Weißgärber, and B. Kieback, “Powders for powder bed fusion: a review,” *Prog. Addit. Manuf.*, vol. 4, pp. 383–397, 2019, doi: 10.1007/s40964-019-00078-6.
- [103] G. Shanbhag and M. Vlasea, “The effect of reuse cycles on Ti-6Al-4V powder properties processed by electron beam powder bed fusion,” *Manuf. Lett.*, vol. 25, pp. 60–63, 2020, doi: 10.1016/j.mfglet.2020.07.007.
- [104] D. Greitemeier, F. Palm, F. Syassen, and T. Melz, “Fatigue performance of additive manufactured TiAl6V4 using electron and laser beam melting,” *Int. J. Fatigue*, vol. 94, pp. 211–217, Jan. 2017, doi: 10.1016/j.ijfatigue.2016.05.001.
- [105] M. Kahlin, H. Ansell, and J. J. Moverare, “Fatigue behaviour of notched additive manufactured Ti6Al4V with as-built surfaces,” *Int. J. Fatigue*, vol. 101, pp. 51–60, Aug. 2017, doi: 10.1016/j.ijfatigue.2017.04.009.
- [106] N. Hrabe, T. Gnäupel-Herold, and T. Quinn, “Fatigue properties of a titanium alloy (Ti–6Al–4V) fabricated via electron beam melting (EBM): Effects of internal defects and residual stress,” *Int. J. Fatigue*, vol. 94, pp. 202–210, Jan. 2017, doi: 10.1016/j.ijfatigue.2016.04.022.
- [107] K. S. Chan, M. Koike, R. L. Mason, and T. Okabe, “Fatigue Life of Titanium Alloys Fabricated by Additive Layer Manufacturing Techniques for Dental Implants,” *Metall. Mater. Trans. A*, vol. 44,

- no. 2, pp. 1010–1022, Feb. 2013, doi: 10.1007/s11661-012-1470-4.
- [108] P. Edwards and M. Ramulu, “Fatigue performance evaluation of selective laser melted Ti–6Al–4V,” *Mater. Sci. Eng. A*, vol. 598, pp. 327–337, Mar. 2014, doi: 10.1016/j.msea.2014.01.041.
- [109] D. H. Abdeen and B. R. Palmer, “Effect of processing parameters of electron beam melting machine on properties of Ti-6Al-4V parts,” *Rapid Prototyp. J.*, vol. 22, no. 3, pp. 609–620, 2016, doi: 10.1108/RPJ-09-2014-0105.
- [110] C. Schmidt, D. Kaspar, M. R. Sarkar, L. E. Claes, and A. A. Ignatius, “A scanning electron microscopy study of human osteoblast morphology on five orthopedic metals,” *J. Biomed. Mater. Res.*, vol. 63, no. 3, pp. 252–261, 2002, doi: 10.1002/jbm.10185.
- [111] B. D. Boyan, C. H. Lohmann, D. D. Dean, V. L. Sylvia, D. L. Cochran, and Z. Schwartz, “Mechanisms Involved in Osteoblast Response to Implant Surface Morphology,” *Annu. Rev. Mater. Res.*, vol. 31, no. 1, pp. 357–371, Aug. 2001, doi: 10.1146/annurev.matsci.31.1.357.
- [112] K.-H. Frosch and K. M. Stürmer, “Metallic Biomaterials in Skeletal Repair,” *Eur. J. Trauma*, vol. 32, no. 2, pp. 149–159, Apr. 2006, doi: 10.1007/s00068-006-6041-1.
- [113] P. Thomsen, J. Malmström, L. Emanuelsson, M. René, and A. Snis, “Electron beam-melted, free-form-fabricated titanium alloy implants: Material surface characterization and early bone response in rabbits,” *J. Biomed. Mater. Res. Part B Appl. Biomater.*, vol. 90B, no. 1, pp. 35–44, Nov. 2008, doi: 10.1002/jbm.b.31250.
- [114] D. Deligianni, “Effect of surface roughness of the titanium alloy Ti–6Al–4V on human bone marrow cell response and on protein adsorption,” *Biomaterials*, vol. 22, no. 11, pp. 1241–1251, Jun. 2001, doi: 10.1016/S0142-9612(00)00274-X.
- [115] K. Suzuki, K. Aoki, and K. Ohya, “Effects of surface roughness of titanium implants on bone remodeling activity of femur in rabbits,” *Bone*, vol. 21, no. 6, pp. 507–514, Dec. 1997, doi: 10.1016/S8756-3282(97)00204-4.
- [116] A. Koptyug, C. Bergemann, R. Lange, V. E. Jaggi, L. E. Rännar, and J. B. Nebe, “Osteoblast ingrowth into titanium scaffolds made by electron beam melting,” *Mater. Sci. Forum*, vol. 783–786, no. May 2015, pp. 1292–1297, 2014, doi: 10.4028/www.scientific.net/msf.783-786.1292.
- [117] V. V. Popov *et al.*, “Powder Bed Fusion Additive Manufacturing Using Critical Raw Materials: A Review,” *Materials (Basel)*, vol. 14, no. 4, p. 909, Feb. 2021, doi: 10.3390/ma14040909.
- [118] J. A. Slotwinski, E. J. Garboczi, and K. M. Hebenstreit, “Porosity Measurements and Analysis for Metal Additive Manufacturing Process Control,” *J. Res. Natl. Inst. Stand. Technol.*, vol. 119, p. 494, Oct. 2014, doi: 10.6028/jres.119.019.



- [119] W. W. Wits, S. Carmignato, F. Zanini, and T. H. J. Vaneker, "Porosity testing methods for the quality assessment of selective laser melted parts," *CIRP Ann.*, vol. 65, no. 1, pp. 201–204, 2016, doi: 10.1016/j.cirp.2016.04.054.
- [120] A. Thompson, I. Maskery, and R. K. Leach, "X-ray computed tomography for additive manufacturing: a review," *Meas. Sci. Technol.*, vol. 27, no. 7, p. 072001, Jul. 2016, doi: 10.1088/0957-0233/27/7/072001.
- [121] C. J. Smith *et al.*, "Dimensional accuracy of Electron Beam Melting (EBM) additive manufacture with regard to weight optimized truss structures," *J. Mater. Process. Technol.*, vol. 229, pp. 128–138, 2016, doi: 10.1016/j.jmatprotec.2015.08.028.
- [122] S. M. Gaytan, L. E. Murr, F. Medina, E. Martinez, M. I. Lopez, and R. B. Wicker, "Advanced metal powder based manufacturing of complex components by electron beam melting," *Mater. Technol.*, vol. 24, no. 3, pp. 180–190, Sep. 2009, doi: 10.1179/106678509X12475882446133.
- [123] H. Galarraga, D. A. Lados, R. R. Dehoff, M. M. Kirka, and P. Nandwana, "Effects of the microstructure and porosity on properties of Ti-6Al-4V ELI alloy fabricated by electron beam melting (EBM)," *Addit. Manuf.*, 2016, doi: 10.1016/j.addma.2016.02.003.
- [124] P. A. Kobryn, E. H. Moore, and S. L. Semiatin, "The effect of laser power and traverse speed on microstructure, porosity, and build height in laser-deposited Ti-6Al-4V," *Scr. Mater.*, vol. 43, no. 4, pp. 299–305, Jul. 2000, doi: 10.1016/S1359-6462(00)00408-5.
- [125] H. Gong, K. Ra, H. Gu, G. D. J. Ram, T. Starr, and B. Stucker, "Influence of defects on mechanical properties of Ti-6Al-4V components produced by selective laser melting and electron beam melting," vol. 86, pp. 545–554, 2015, doi: 10.1016/j.matdes.2015.07.147.
- [126] R. Cunningham, S. P. Narra, T. Ozturk, J. Beuth, and A. D. Rollett, "Evaluating the Effect of Processing Parameters on Porosity in Electron Beam Melted Ti-6Al-4V via Synchrotron X-ray Microtomography," *Jom*, vol. 68, no. 3, pp. 765–771, 2016, doi: 10.1007/s11837-015-1802-0.
- [127] A. Yadollahi and N. Shamsaei, "Additive manufacturing of fatigue resistant materials: Challenges and opportunities," *Int. J. Fatigue*, vol. 98, pp. 14–31, May 2017, doi: 10.1016/j.ijfatigue.2017.01.001.
- [128] J. Z. Yi, Y. X. Gao, P. D. Lee, H. M. Flower, and T. C. Lindley, "Scatter in fatigue life due to effects of porosity in cast A356-T6 aluminum-silicon alloys," *Metall. Mater. Trans. A*, vol. 34, no. 9, pp. 1879–1890, Sep. 2003, doi: 10.1007/s11661-003-0153-6.
- [129] H. Zhu, B. Wu, D. Li, D. Zhang, and Y. Chen, "Influence of Voids on the Tensile Performance of Carbon/epoxy Fabric Laminates," *J. Mater. Sci. Technol.*, vol. 27, no. 1, pp. 69–73, Jan. 2011, doi:

- 10.1016/S1005-0302(11)60028-5.
- [130] M. Tang and P. C. Pistorius, “Oxides, porosity and fatigue performance of AlSi10Mg parts produced by selective laser melting,” *Int. J. Fatigue*, vol. 94, pp. 192–201, Jan. 2017, doi: 10.1016/j.ijfatigue.2016.06.002.
- [131] J.-P. Kruth, G. Levy, F. Klocke, and T. H. C. Childs, “Consolidation phenomena in laser and powder-bed based layered manufacturing,” *CIRP Ann.*, vol. 56, no. 2, pp. 730–759, 2007, doi: 10.1016/j.cirp.2007.10.004.
- [132] G. Nicoletto, G. Anzelotti, and R. Konečná, “X-ray computed tomography vs. metallography for pore sizing and fatigue of cast Al-alloys,” *Procedia Eng.*, vol. 2, no. 1, pp. 547–554, Apr. 2010, doi: 10.1016/j.proeng.2010.03.059.
- [133] A. Bauereiß, T. Scharowsky, and C. Körner, “Defect generation and propagation mechanism during additive manufacturing by selective beam melting,” *J. Mater. Process. Technol.*, vol. 214, no. 11, pp. 2522–2528, Nov. 2014, doi: 10.1016/j.jmatprotec.2014.05.002.
- [134] Y. Nikishkov, G. Seon, and A. Makeev, “Structural analysis of composites with porosity defects based on X-ray computed tomography,” *J. Compos. Mater.*, vol. 48, no. 17, pp. 2131–2144, Jul. 2014, doi: 10.1177/0021998313494917.
- [135] S. Khademzadeh, S. Carmignato, N. Parvin, F. Zanini, and P. F. Bariani, “Micro porosity analysis in additive manufactured NiTi parts using micro computed tomography and electron microscopy,” *Mater. Des.*, vol. 90, pp. 745–752, Jan. 2016, doi: 10.1016/j.matdes.2015.10.161.
- [136] M. A. Suhot, “The effect of voids on the flexural fatigue properties of carbon/epoxy composites [dissertation],” University of Southampton, 2010.
- [137] J. Lambert, A. R. Chambers, I. Sinclair, and S. M. Spearing, “3D damage characterisation and the role of voids in the fatigue of wind turbine blade materials,” *Compos. Sci. Technol.*, vol. 72, no. 2, pp. 337–343, Jan. 2012, doi: 10.1016/j.compscitech.2011.11.023.
- [138] P. Hermanek and S. Carmignato, “Reference object for evaluating the accuracy of porosity measurements by X-ray computed tomography,” *Case Stud. Nondestruct. Test. Eval.*, vol. 6, pp. 122–127, Nov. 2016, doi: 10.1016/j.csnedt.2016.05.003.
- [139] P. Hermanek and S. Carmignato, “Porosity measurements by X-ray computed tomography: Accuracy evaluation using a calibrated object,” *Precis. Eng.*, vol. 49, pp. 377–387, Jul. 2017, doi: 10.1016/j.precisioneng.2017.03.007.
- [140] P. Hermanek and S. Carmignato, “Establishment of metrological traceability in porosity measurements by x-ray computed tomography,” in *Developments in X-Ray Tomography XI*, Sep.

- 2017, p. 22, doi: 10.1117/12.2276942.
- [141] M. Benedetti, V. Fontanari, M. Bandini, F. Zanini, and S. Carmignato, “Low- and high-cycle fatigue resistance of Ti-6Al-4V ELI additively manufactured via selective laser melting: Mean stress and defect sensitivity,” *Int. J. Fatigue*, vol. 107, pp. 96–109, Feb. 2018, doi: 10.1016/j.ijfatigue.2017.10.021.
- [142] H. Villarraga, C. Lee, S. P. Charney, J. A. Tarbuton, and S. T. Smith, “Dimensional metrology of complex inner geometries built by additive manufacturing,” in *ASPE Spring Topical Meeting: Achieving Precision Tolerances in Additive Manufacturing*, 2015, no. May, pp. 164–169.
- [143] H. Villarraga, C. Lee, T. Corbett, J. A. Tarbuton, and S. T. Smith, “Assessing additive manufacturing processes with X-ray CT metrology,” in *ASPE Spring Topical Meeting: Achieving Precision Tolerances in Additive Manufacturing*, 2015, no. May, pp. 116–121.
- [144] H. Villarraga-Gómez, M. Seifi, Y. Uchiyama, and A. Ramsey, “Assessing the Structural Integrity of Additive Manufactured Metal Parts with X-ray CT,” in *ASPE/euspen Summer Topical Meeting - Dimensional Accuracy and Surface Finish in Additive Manufacturing*, 2016, no. June, pp. 1–6, doi: 10.13140/RG.2.1.1066.6486.
- [145] U. Ackelid and M. Svensson, “Additive Manufacturing of Dense Metal Parts by Electron Beam Melting,” in *Proceedings of the Materials Science and Technology Conference*, 2009, pp. 2711–2719.
- [146] H. Khalid Rafi., N. V. Karthik, T. L. Starr, and B. E. Stucker, “Mechanical property evaluation of Ti-6Al-4V parts made using Electron Beam Melting,” in *Solid Freeform Fabrication Symposium*, 2012, pp. 526–535.
- [147] J. Parthasarathy, B. Starly, S. Raman, and A. Christensen, “Mechanical evaluation of porous titanium (Ti6Al4V) structures with electron beam melting (EBM),” *J. Mech. Behav. Biomed. Mater.*, vol. 3, no. 3, pp. 249–259, Apr. 2010, doi: 10.1016/j.jmbbm.2009.10.006.
- [148] L. Facchini, E. Magalini, P. Robotti, and A. Molinari, “Microstructure and mechanical properties of Ti-6Al-4V produced by electron beam melting of pre-alloyed powders,” *Rapid Prototyp. J.*, vol. 15, no. 3, pp. 171–178, May 2009, doi: 10.1108/13552540910960262.
- [149] T. Machry, D. Eatock, J. Meyer, A. Antonysamy, A. Ho, and P. Prangnell, “Effect of microstructure on the tensile strength of Ti6Al4V specimens manufactured using additive manufacturing electron beam process,” *Powder Metall.*, vol. 59, no. 1, pp. 41–50, Jan. 2016, doi: 10.1080/00325899.2015.1123800.

- [150] R. S. Kircher, A. M. Christensen, and K. W. Wurth, “The Effects of Specimen Dimensions on the Mechanical Behavior of EBM Produced Ti6Al4V Alloys,” in *Solid Freeform Fabrication Symposium*, 2009, no. 1, pp. 398–405.
- [151] M. Koike *et al.*, “Evaluation of Titanium Alloys Fabricated Using Rapid Prototyping Technologies—Electron Beam Melting and Laser Beam Melting,” *Materials (Basel)*, vol. 4, no. 10, pp. 1776–1792, Oct. 2011, doi: 10.3390/ma4101776.
- [152] W. Everhart, J. Dinardo, and C. Barr, “The Effect of Scan Length on the Structure and Mechanical Properties of Electron Beam-Melted Ti-6Al-4V,” *Metall. Mater. Trans. A Phys. Metall. Mater. Sci.*, vol. 48, no. 2, pp. 697–705, 2017, doi: 10.1007/s11661-016-3866-z.
- [153] I. Ituarte, “The role of Additive Manufacturing in modern product development: a case study for consumer electronic industry,” Aalto University, 2013.
- [154] J. Tuomi *et al.*, “Medical applications of rapid prototyping - From applications to classification,” *Innov. Dev. Des. Manuf.*, pp. 701–704, Jan. 2010, doi: 10.1201/9780203859476.ch109.
- [155] D.-J. Yoo, “Advanced porous scaffold design using multi-void triply periodic minimal surface models with high surface area to volume ratios,” *Int. J. Precis. Eng. Manuf.*, vol. 15, no. 8, pp. 1657–1666, Aug. 2014, doi: 10.1007/s12541-014-0516-5.
- [156] E. Marin, S. Fusi, M. Pressacco, L. Paussa, and L. Fedrizzi, “Characterization of cellular solids in Ti6Al4V for orthopaedic implant applications: Trabecular titanium,” *J. Mech. Behav. Biomed. Mater.*, vol. 3, no. 5, pp. 373–381, Jul. 2010, doi: 10.1016/j.jmbbm.2010.02.001.
- [157] G. Ryan, A. Pandit, and D. P. Apatsidis, “Fabrication methods of porous metals for use in orthopaedic applications,” *Biomaterials*, vol. 27, no. 13, pp. 2651–2670, May 2006, doi: 10.1016/j.biomaterials.2005.12.002.
- [158] G. He, P. Liu, Q. Tan, and G. Jiang, “Flexural and compressive mechanical behaviors of the porous titanium materials with entangled wire structure at different sintering conditions for load-bearing biomedical applications,” *J. Mech. Behav. Biomed. Mater.*, vol. 28, pp. 309–319, Dec. 2013, doi: 10.1016/j.jmbbm.2013.08.016.
- [159] N. W. Hrabe, P. Heintl, B. Flinn, C. Körner, and R. K. Bordia, “Compression-compression fatigue of selective electron beam melted cellular titanium (Ti-6Al-4V),” *J. Biomed. Mater. Res. Part B Appl. Biomater.*, vol. 99B, no. 2, pp. 313–320, Nov. 2011, doi: 10.1002/jbm.b.31901.
- [160] S. J. Li *et al.*, “Compression fatigue behavior of Ti-6Al-4V mesh arrays fabricated by electron beam melting,” *Acta Mater.*, vol. 60, no. 3, pp. 793–802, Feb. 2012, doi: 10.1016/j.actamat.2011.10.051.
- [161] Y. J. Liu *et al.*, “Microstructure, defects and mechanical behavior of beta-type titanium porous

- structures manufactured by electron beam melting and selective laser melting,” *Acta Mater.*, vol. 113, pp. 56–67, Jul. 2016, doi: 10.1016/j.actamat.2016.04.029.
- [162] S. Hosseini, S. Mirdamadi, and A. Nemati, “Porous Ti6Al4V scaffolds for dental implants: Microstructure, mechanical, and corrosion behavior,” *Proc. Inst. Mech. Eng. Part L J. Mater. Des. Appl.*, vol. 230, no. 5, pp. 927–933, Oct. 2016, doi: 10.1177/1464420715588218.
- [163] J. Kadkhodapour *et al.*, “Failure mechanisms of additively manufactured porous biomaterials: Effects of porosity and type of unit cell,” *J. Mech. Behav. Biomed. Mater.*, vol. 50, pp. 180–191, Oct. 2015, doi: 10.1016/j.jmbbm.2015.06.012.
- [164] L. Mullen, R. C. Stamp, W. K. Brooks, E. Jones, and C. J. Sutcliffe, “Selective Laser Melting: A regular unit cell approach for the manufacture of porous, titanium, bone in-growth constructs, suitable for orthopedic applications,” *J. Biomed. Mater. Res. Part B Appl. Biomater.*, vol. 89B, no. 2, pp. 325–334, May 2009, doi: 10.1002/jbm.b.31219.
- [165] L. Xiao *et al.*, “Mechanical properties of open-cell rhombic dodecahedron titanium alloy lattice structure manufactured using electron beam melting under dynamic loading,” *Int. J. Impact Eng.*, vol. 100, pp. 75–89, 2017, doi: 10.1016/j.ijimpeng.2016.10.006.
- [166] T. J. Horn, O. L. A. Harrysson, D. J. Marcellin-Little, H. A. West, B. D. X. Lascelles, and R. Aman, “Flexural properties of Ti6Al4V rhombic dodecahedron open cellular structures fabricated with electron beam melting,” *Addit. Manuf.*, vol. 1–4, pp. 2–11, Oct. 2014, doi: 10.1016/j.addma.2014.05.001.
- [167] S. Babaei, B. H. Jahromi, A. Ajdari, H. Nayeb-Hashemi, and A. Vaziri, “Mechanical properties of open-cell rhombic dodecahedron cellular structures,” *Acta Mater.*, vol. 60, no. 6–7, pp. 2873–2885, Apr. 2012, doi: 10.1016/j.actamat.2012.01.052.
- [168] O. Cansizoglu, O. Harrysson, D. Cormier, H. West, and T. Mahale, “Properties of Ti–6Al–4V non-stochastic lattice structures fabricated via electron beam melting,” *Mater. Sci. Eng. A*, vol. 492, no. 1–2, pp. 468–474, Sep. 2008, doi: 10.1016/j.msea.2008.04.002.
- [169] J. Parthasarathy, B. Starly, and S. Raman, “A design for the additive manufacture of functionally graded porous structures with tailored mechanical properties for biomedical applications,” *J. Manuf. Process.*, vol. 13, no. 2, pp. 160–170, Aug. 2011, doi: 10.1016/j.jmapro.2011.01.004.
- [170] L. E. Murr *et al.*, “Next-generation biomedical implants using additive manufacturing of complex, cellular and functional mesh arrays,” *Philos. Trans. R. Soc. A Math. Phys. Eng. Sci.*, vol. 368, no. 1917, pp. 1999–2032, Apr. 2010, doi: 10.1098/rsta.2010.0010.
- [171] P. Heintz, A. Rottmair, C. Körner, and R. F. Singer, “Cellular Titanium by Selective Electron Beam

- Melting,” *Adv. Eng. Mater.*, vol. 9, no. 5, pp. 360–364, May 2007, doi: 10.1002/adem.200700025.
- [172] S. RAJAGOPALAN and R. ROBB, “Schwarz meets Schwann: Design and fabrication of biomorphic and durataxic tissue engineering scaffolds,” *Med. Image Anal.*, vol. 10, no. 5, pp. 693–712, Oct. 2006, doi: 10.1016/j.media.2006.06.001.
- [173] F. P. W. Melchels, K. Bertoldi, R. Gabbrielli, A. H. Velders, J. Feijen, and D. W. Grijpma, “Mathematically defined tissue engineering scaffold architectures prepared by stereolithography,” *Biomaterials*, vol. 31, no. 27, pp. 6909–6916, Sep. 2010, doi: 10.1016/j.biomaterials.2010.05.068.
- [174] E. A. Lord, A. L. Mackay, and S. Ranganathan, *New geometries for new materials*. Cambridge University Press, 2006.
- [175] M. M. Sychov, L. A. Lebedev, S. V. Dyachenko, and L. A. Nefedova, “Mechanical properties of energy-absorbing structures with triply periodic minimal surface topology,” *Acta Astronaut.*, vol. 150, pp. 81–84, Sep. 2018, doi: 10.1016/j.actaastro.2017.12.034.
- [176] D.-J. Yoo and K.-H. Kim, “An advanced multi-morphology porous scaffold design method using volumetric distance field and beta growth function,” *Int. J. Precis. Eng. Manuf.*, vol. 16, no. 9, pp. 2021–2032, Aug. 2015, doi: 10.1007/s12541-015-0263-2.
- [177] C. Yan, L. Hao, A. Hussein, and P. Young, “Ti–6Al–4V triply periodic minimal surface structures for bone implants fabricated via selective laser melting,” *J. Mech. Behav. Biomed. Mater.*, vol. 51, pp. 61–73, Nov. 2015, doi: 10.1016/j.jmbbm.2015.06.024.
- [178] M. Speirs, B. Van Hooreweder, J. Van Humbeeck, and J.-P. Kruth, “Fatigue behaviour of NiTi shape memory alloy scaffolds produced by SLM, a unit cell design comparison,” *J. Mech. Behav. Biomed. Mater.*, vol. 70, pp. 53–59, Jun. 2017, doi: 10.1016/j.jmbbm.2017.01.016.
- [179] S. Evsevlev *et al.*, “X-ray Computed Tomography Procedures to Quantitatively Characterize the Morphological Features of Triply Periodic Minimal Surface Structures,” *Materials (Basel)*, vol. 14, no. 11, p. 3002, Jun. 2021, doi: 10.3390/ma14113002.
- [180] I. Yadroitsev and I. Smurov, “Selective laser melting technology: From the single laser melted track stability to 3D parts of complex shape,” *Phys. Procedia*, vol. 5, pp. 551–560, 2010, doi: 10.1016/j.phpro.2010.08.083.
- [181] W. E. King *et al.*, “Laser powder bed fusion additive manufacturing of metals; physics, computational, and materials challenges,” *Appl. Phys. Rev.*, vol. 2, no. 4, p. 041304, Dec. 2015, doi: 10.1063/1.4937809.
- [182] J. E. Barnes, A. B. Kingsbury, and E. Bono, “Does " Low Cost " Titanium Powder Yield Low Cost Titanium Parts?,” *PowderMet 2016 Int. Conf. Powder Metall.*, no. January, 2016, doi:

- 10.1016/j.wear.2013.06.024.
- [183] T. DebRoy *et al.*, “Scientific, technological and economic issues in metal printing and their solutions,” *Nat. Mater.*, vol. 18, no. 10, pp. 1026–1032, Oct. 2019, doi: 10.1038/s41563-019-0408-2.
- [184] V. Petrovic and R. Niñerola, “Powder recyclability in electron beam melting for aeronautical use,” *Aircr. Eng. Aerosp. Technol.*, vol. 87, no. 2, pp. 147–155, Mar. 2015, doi: 10.1108/AEAT-11-2013-0212.
- [185] S. Chandrasekar *et al.*, “Investigating the effect of metal powder recycling in Electron beam Powder Bed Fusion using process log data,” *Addit. Manuf.*, vol. 32, p. 100994, Mar. 2020, doi: 10.1016/j.addma.2019.100994.
- [186] P. C. Angelo and R. Subramaniam, *Powder Metallurgy: Science, Technology And Applications*. Delhi: PHI Learning Pvt. Ltd., 2008, 2008.
- [187] R. M. German, *Powder metallurgy science*. Princeton, N.J.: Metal Powder Industries Federation, 1994.
- [188] V. V. Popov, A. Katz-Demyanetz, A. Garkun, and M. Bamberger, “The effect of powder recycling on the mechanical properties and microstructure of electron beam melted Ti-6Al-4 V specimens,” *Addit. Manuf.*, vol. 22, pp. 834–843, Aug. 2018, doi: 10.1016/j.addma.2018.06.003.
- [189] C. Wei *et al.*, “Microstructural and property evolution of Ti6Al4V powders with the number of usage in additive manufacturing by electron beam melting,” *Mater. Lett.*, vol. 221, pp. 111–114, Jun. 2018, doi: 10.1016/j.matlet.2018.03.124.
- [190] B. Liu, R. Wildman, C. Tuck, I. Ashcroft, and R. Hague, “Investigation the effect of particle size distribution on processing parameters optimisation in selective laser melting process,” in *Solid Freeform Fabrication Symposium*, 2011, pp. 227–238.
- [191] N. Karapatis and G. Egger, “Optimization of powder layer density in selective laser sintering,” in *Solid Freeform Fabrication Symposium*, 1999, pp. 255–264.
- [192] X. Gong, B. Cheng, S. Price, and K. Chou, “Powder-bed electron-beam-melting additive manufacturing: powder characterization, process simulation and metrology,” *Early Career Tech. Conf. Birmingham, AL*, no. November 2013, pp. 55–66, 2013.
- [193] J. A. Slotwinski, E. J. Garboczi, P. E. Stutzman, C. F. Ferraris, S. S. Watson, and M. A. Peltz, “Characterization of Metal Powders Used for Additive Manufacturing,” *J. Res. Natl. Inst. Stand. Technol.*, vol. 119, p. 460, Oct. 2014, doi: 10.6028/jres.119.018.
- [194] J. Clayton, D. Millington-Smith, and B. Armstrong, “The Application of Powder Rheology in

- Additive Manufacturing,” *JOM*, vol. 67, no. 3, pp. 544–548, Mar. 2015, doi: 10.1007/s11837-015-1293-z.
- [195] A. Strondl, O. Lyckfeldt, H. Brodin, and U. Ackelid, “Characterization and Control of Powder Properties for Additive Manufacturing,” *JOM*, vol. 67, no. 3, pp. 549–554, Mar. 2015, doi: 10.1007/s11837-015-1304-0.
- [196] ASTM, “F2924:14-Standard Specification for Additive Manufacturing Titanium-6 Aluminum-4 Vanadium with Powder Bed Fusion,” *ASTM Int.*, 2014, doi: 10.1520/F2924-14.
- [197] H. P. Tang, M. Qian, N. Liu, X. Z. Zhang, G. Y. Yang, and J. Wang, “Effect of Powder Reuse Times on Additive Manufacturing of Ti-6Al-4V by Selective Electron Beam Melting,” *J. Miner. Met. Mater. Soc.*, vol. 67, no. 3, pp. 555–563, Mar. 2015, doi: 10.1007/s11837-015-1300-4.
- [198] S. Ghods *et al.*, “Electron beam additive manufacturing of Ti6Al4V: Evolution of powder morphology and part microstructure with powder reuse,” *Materialia*, vol. 9, no. February, p. 100631, 2020, doi: 10.1016/j.mtla.2020.100631.
- [199] U. Ackelid, “Oxygen pick-up in the Ti6Al4V EBM process,” Marstrand, 2008.
- [200] A. Goyal *et al.*, “Development and physico-chemical characterization of microencapsulated flaxseed oil powder: A functional ingredient for omega-3 fortification,” *Powder Technol.*, vol. 286, pp. 527–537, Dec. 2015, doi: 10.1016/j.powtec.2015.08.050.
- [201] R. M. German, *Particle Packing Characteristics*. Princeton, N.J., USA: Metal Powder Industries Federation, 1989, 1989.
- [202] F. Medina, “Reducing metal alloy powder costs for use in powder bed fusion additive manufacturing: Improving the economics for production,” University of Texas El Paso, 2013.
- [203] M. Entezarian, F. Allaire, P. Tsantrizos, and R. A. L. Drew, “Plasma atomization: A new process for the production of fine, spherical powders,” *JOM*, vol. 48, no. 6, pp. 53–55, 1996, doi: 10.1007/BF03222969.
- [204] A. Simchi, “The role of particle size on the laser sintering of iron powder,” *Metall. Mater. Trans. B*, vol. 35, no. 5, pp. 937–948, Oct. 2004, doi: 10.1007/s11663-004-0088-3.
- [205] T. F. Teferra, “Engineering Properties of Food Materials,” in *Handbook of Farm, Dairy and Food Machinery Engineering*, Elsevier, 2019, pp. 45–89.
- [206] N. Hopkinson and P. Dicknes, “Analysis of rapid manufacturing—using layer manufacturing processes for production,” *Proc. Inst. Mech. Eng. Part C J. Mech. Eng. Sci.*, vol. 217, no. 1, pp. 31–39, Jan. 2003, doi: 10.1243/095440603762554596.
- [207] M. Baumers, P. Dickens, C. Tuck, and R. Hague, “The cost of additive manufacturing: machine



- productivity, economies of scale and technology-push,” *Technol. Forecast. Soc. Change*, vol. 102, no. C, pp. 193–201, 2016, [Online]. Available: <https://econpapers.repec.org/RePEc:eee:tefoso:v:102:y:2016:i:c:p:193-201>.
- [208] W. A. Grell *et al.*, “Effect of powder oxidation on the impact toughness of electron beam melting Ti-6Al-4V,” *Addit. Manuf.*, vol. 17, pp. 123–134, 2017, doi: 10.1016/j.addma.2017.08.002.
- [209] S. E. Brika, M. Letenneur, C. A. Dion, and V. Brailovski, “Influence of particle morphology and size distribution on the powder flowability and laser powder bed fusion manufacturability of Ti-6Al-4V alloy,” *Addit. Manuf.*, vol. 31, no. August 2019, p. 100929, 2020, doi: 10.1016/j.addma.2019.100929.
- [210] P. Moghimian *et al.*, “Metal powders in additive manufacturing: A review on reusability and recyclability of common titanium, nickel and aluminum alloys,” *Addit. Manuf.*, vol. 43, p. 102017, Jul. 2021, doi: 10.1016/j.addma.2021.102017.
- [211] Y. Sun, M. Aindow, and R. J. Hebert, “The effect of recycling on the oxygen distribution in Ti-6Al-4V powder for additive manufacturing,” *Mater. High Temp.*, vol. 35, no. 1–3, pp. 217–224, 2018, doi: 10.1080/09603409.2017.1389133.
- [212] C. L. A. Leung, S. Marussi, M. Towrie, R. C. Atwood, P. J. Withers, and P. D. Lee, “The effect of powder oxidation on defect formation in laser additive manufacturing,” *Acta Mater.*, vol. 166, pp. 294–305, Mar. 2019, doi: 10.1016/j.actamat.2018.12.027.
- [213] ISO, “13322-2 Particle size analysis — Image analysis methods — Part 2: Dynamic image analysis methods,” *Int. Organ. Stand.*, vol. 2, 2006, [Online]. Available: <https://www.iso.org/standard/38665.html>.
- [214] R. Freeman and X. Fu, “Characterisation of powder bulk, dynamic flow and shear properties in relation to die filling,” *Powder Metall.*, vol. 51, no. 3, pp. 196–201, Sep. 2008, doi: 10.1179/174329008X324115.
- [215] L. Cordova, M. Campos, and T. Tinga, “Revealing the Effects of Powder Reuse for Selective Laser Melting by Powder Characterization,” *JOM*, vol. 71, no. 3, pp. 1062–1072, Mar. 2019, doi: 10.1007/s11837-018-3305-2.
- [216] L. Grainger, “Investigating the effects of multiple re-use of Ti6Al4V powder in additive manufacturing (AM),” *White Pap. Renishaw*, pp. 1–10, 2016.
- [217] Granutools, “Linking Powder Rheology Characterization to Spreadability in Powder Bed-Based AM,” *AZO Materials*, 2020. <https://www.azom.com/article.aspx?ArticleID=19335> (accessed Apr. 23, 2021).

- [218] Granutools, “Effect of Recycling on the Spreadability of Metallic Powder,” *AZO Materials*, 2020. <https://www.azom.com/article.aspx?ArticleID=19313> (accessed Apr. 23, 2021).
- [219] N. Vluttert, “The absorption of moisture by metal powder in a humid environment and the effects on its composition,” 2016. <http://essay.utwente.nl/71620/> (accessed Apr. 23, 2014).
- [220] A. Montelione, S. Ghods, R. Schur, C. Wisdom, D. Arola, and M. Ramulu, “Powder Reuse in Electron Beam Melting Additive Manufacturing of Ti6Al4V: Particle Microstructure, Oxygen Content and Mechanical Properties,” *Addit. Manuf.*, vol. 35, p. 101216, Oct. 2020, doi: 10.1016/j.addma.2020.101216.
- [221] R. Shvab, E. Hryha, and L. Nyborg, “Surface chemistry of the titanium powder studied by XPS using internal standard reference,” *Powder Metall.*, vol. 60, no. 1, pp. 42–48, Jan. 2017, doi: 10.1080/00325899.2016.1271092.
- [222] J. H. Tan, W. L. E. Wong, and K. W. Dalgarno, “An overview of powder granulometry on feedstock and part performance in the selective laser melting process,” *Addit. Manuf.*, vol. 18, pp. 228–255, Dec. 2017, doi: 10.1016/j.addma.2017.10.011.
- [223] Y. Mizuno *et al.*, “Temperature dependence of oxide decomposition on titanium surfaces in ultrahigh vacuum,” *J. Vac. Sci. Technol. A Vacuum, Surfaces, Film.*, vol. 20, no. 5, pp. 1716–1721, Sep. 2002, doi: 10.1116/1.1500746.
- [224] A. Attalla, R. C. J. Bowman, B. D. Craft, C. M. Love, and R. L. Yauger, “Investigation of moisture in titanium metal powder by pulsed NMR,” May 1977. doi: 10.2172/7257103.
- [225] C. T. Sims, N. S. Stoloff, and W. C. Hagel, *Superalloys II: High-Temperature Materials for Aerospace and Industrial Power*. 1987.
- [226] N. M. Mehat, S. Kamaruddin, and A. R. Othman, “Hybrid Integration of Taguchi Parametric Design, Grey Relational Analysis, and Principal Component Analysis Optimization for Plastic Gear Production,” *Chinese J. Eng.*, vol. 2014, pp. 1–11, Jan. 2014, doi: 10.1155/2014/351206.
- [227] M. Galati and L. Iuliano, “A literature review of powder-based electron beam melting focusing on numerical simulations,” *Addit. Manuf.*, vol. 19, pp. 1–20, 2018, doi: <https://doi.org/10.1016/j.addma.2017.11.001>.
- [228] ASTM, “E8/E8M-16a-Standard Test Methods for Tension Testing of Metallic Materials,” *ASTM Int.*, pp. 1–30, 2016, doi: 10.1520/E0008\_E0008M-16A.
- [229] W. Everhart, E. Sawyer, T. Neidt, J. Dinardo, and B. Brown, “The effect of surface finish on tensile behavior of additively manufactured tensile bars,” *J. Mater. Sci.*, vol. 51, no. 8, pp. 3836–3845, 2016, doi: 10.1007/s10853-015-9702-9.

- [230] X. Tan *et al.*, “Graded microstructure and mechanical properties of additive manufactured Ti – 6Al – 4V via electron beam melting,” *Acta Mater.*, vol. 97, pp. 1–16, 2015, doi: 10.1016/j.actamat.2015.06.036.
- [231] P. Wang, M. L. S. Nai, W. J. Sin, and J. Wei, “Effect of building height on microstructure and mechanical properties of big-sized Ti-6Al-4V plate fabricated by electron beam melting,” in *MATEC Web of Conferences - International Conference on Material Science and Engineering Technology*, 2015, vol. 30, pp. 4–7, doi: 10.1051/mateconf/20153002001.
- [232] Y. Y. Sun, S. Gulizia, D. Fraser, C. H. Oh, S. L. Lu, and M. Qian, “Layer Additive Production or Manufacturing of Thick Sections of Ti-6Al-4V by Selective Electron Beam Melting (SEBM),” *J. Miner. Met. Mater. Soc.*, vol. 69, no. 10, pp. 1836–1843, 2017, doi: 10.1007/s11837-017-2462-z.
- [233] S. Raghavan, M. L. S. Nai, P. Wang, W. J. Sin, T. Li, and J. Wei, “Heat treatment of electron beam melted (EBM) Ti-6Al-4V: microstructure to mechanical property correlations,” *Rapid Prototyp. J.*, vol. 24, no. 4, pp. 774–783, 2018, doi: 10.1108/RPJ-05-2016-0070.
- [234] J. Dzugan *et al.*, “Effects of thickness and orientation on the small scale fracture behaviour of additively manufactured Ti-6Al-4V,” *Mater. Charact.*, vol. 143, no. April, pp. 94–109, 2018, doi: 10.1016/j.matchar.2018.04.003.
- [235] B. Wysocki, P. Maj, R. Sitek, J. Buhagiar, K. Kurzydłowski, and W. Świążkowski, “Laser and Electron Beam Additive Manufacturing Methods of Fabricating Titanium Bone Implants,” *Appl. Sci.*, vol. 7, no. 7, p. 657, Jun. 2017, doi: 10.3390/app7070657.
- [236] O. L. Rodriguez *et al.*, “Dynamic tensile behavior of electron beam additive manufactured Ti6Al4V,” *Mater. Sci. Eng. A*, vol. 641, pp. 323–327, 2015, doi: 10.1016/j.msea.2015.06.069.
- [237] C. de Formanoir, S. Michotte, O. Rigo, L. Germain, and S. Godet, “Electron beam melted Ti–6Al–4V: Microstructure, texture and mechanical behavior of the as-built and heat-treated material,” *Mater. Sci. Eng. A*, vol. 652, pp. 105–119, Jan. 2016, doi: 10.1016/j.msea.2015.11.052.
- [238] J. Bruno, A. Rochman, and G. Cassar, “Effect of Build Orientation of Electron Beam Melting on Microstructure and Mechanical Properties of Ti-6Al-4V,” *J. Mater. Eng. Perform.*, vol. 26, no. 2, pp. 692–703, Feb. 2017, doi: 10.1007/s11665-017-2502-4.
- [239] L. Ladani, J. Razmi, and S. F. Choudhury, “Mechanical Anisotropy and Strain Rate Dependency Behavior of Ti6Al4V Produced Using E-Beam Additive Fabrication,” vol. 136, no. July 2014, pp. 1–7, 2014, doi: 10.1115/1.4027729.
- [240] M. Fousová, D. Vojtěch, K. Doubrava, M. Daniel, and C. F. Lin, “Influence of inherent surface and internal defects on mechanical properties of additively manufactured Ti6Al4V alloy: Comparison

- between selective laser melting and electron beam melting,” *Materials (Basel)*., vol. 11, no. 4, 2018, doi: 10.3390/ma11040537.
- [241] Y. Zhai, H. Galarraga, and D. A. Lados, “Microstructure Evolution, Tensile Properties, and Fatigue Damage Mechanisms in Ti-6Al-4V Alloys Fabricated by Two Additive Manufacturing Techniques,” *Procedia Eng.*, vol. 114, pp. 658–666, 2015, doi: 10.1016/j.proeng.2015.08.007.
- [242] W. Everhart and J. Dinardo, “Process driven strengthening mechanisms in electron beam melted Ti-6Al-,” *Addit. Manuf.*, vol. 24, no. September, pp. 440–445, 2018, doi: 10.1016/j.addma.2018.09.031.
- [243] T. Scharowsky, V. Juechter, R. F. Singer, and C. Körner, “Influence of the Scanning Strategy on the Microstructure and Mechanical Properties in Selective Electron Beam Melting of Ti-6Al-4V,” *Adv. Eng. Mater.*, vol. 17, no. 11, pp. 1573–1578, 2015, doi: 10.1002/adem.201400542.
- [244] E. Tiferet *et al.*, “Mapping the tray of electron beam melting of Ti-6Al-4V: Properties and microstructure,” *Materials (Basel)*., vol. 12, no. 9, pp. 1–14, 2019, doi: 10.3390/ma12091470.
- [245] S. Draper, B. Lerch, R. Rogers, R. Martin, I. Locci, and A. Garg, “Materials Characterization of Electron Beam Melted Ti-6Al-4V,” in *Proceedings of the 13th World Conference on Titanium*, The Minerals, Metals & Materials Society, 2016, pp. 1433–1440.
- [246] C. Dharmendra, A. Hadadzadeh, B. S. Amirkhiz, A. Lloyd, and M. Mohammadi, “Deformation mechanisms and fracture of electron beam melted Ti-6Al-4V,” *Mater. Sci. Eng. A*, vol. 771, no. September 2019, p. 138652, 2020, doi: 10.1016/j.msea.2019.138652.
- [247] H. K. Rafi *et al.*, “Microstructures and Mechanical Properties of Ti6Al4V Parts Fabricated by Selective Laser Melting and Electron Beam Melting,” *J. Mater. Eng. Perform.*, vol. 22, no. 12, pp. 3872–3883, Dec. 2013, doi: 10.1007/s11665-013-0658-0.
- [248] S. L. Lu, H. P. Tang, Y. P. Ning, N. Liu, D. H. StJohn, and M. Qian, “Microstructure and Mechanical Properties of Long Ti-6Al-4V Rods Additively Manufactured by Selective Electron Beam Melting Out of a Deep Powder Bed and the Effect of Subsequent Hot Isostatic Pressing,” *Metall. Mater. Trans. A*, vol. 46, no. 9, pp. 3824–3834, Sep. 2015, doi: 10.1007/s11661-015-2976-3.
- [249] C. Pirozzi, S. Franchitti, R. Borrelli, F. Caiazza, V. Alfieri, and P. Argenio, “Study on the Factors Affecting the Mechanical Behavior of Electron Beam Melted Ti6Al4V,” *J. Mater. Eng. Perform.*, vol. 26, no. 9, pp. 4491–4499, 2017, doi: 10.1007/s11665-017-2894-1.
- [250] S. Yoder *et al.*, “Approach to qualification using E-PBF in-situ process monitoring in Ti-6Al-4V,” *Addit. Manuf.*, vol. 28, no. April, pp. 98–106, 2019, doi: 10.1016/j.addma.2019.03.021.
- [251] H. P. Tang *et al.*, “Microstructure, Mechanical Properties, and Flatness of SEBM Ti-6Al-4V Sheet

- in As-Built and Hot Isostatically Pressed Conditions,” *J. Miner. Met. Mater. Soc.*, vol. 69, no. 3, pp. 466–471, 2017, doi: 10.1007/s11837-016-2253-y.
- [252] A. Kirchner, B. Klöden, J. Luft, T. Weißgärber, and B. Kieback, “Process window for electron beam melting of Ti-6Al-4V,” *Powder Metall.*, vol. 58, no. 4, pp. 246–249, 2015, doi: 10.1179/0032589915Z.000000000244.
- [253] SAE International, “AMS 4928W: Titanium Alloy Bars, Wire, Forgings, Rings, and Drawn Shapes 6Al - 4V Annealed,” 2017, doi: <https://doi.org/10.4271/AMS4928W>.
- [254] H. Villarraga-Gómez, “Studies of dimensional metrology with X-ray CAT scan [dissertation],” University of North Carolina, 2018.
- [255] A. Du Plessis, I. Yadroitsev, I. Yadroitsava, and S. G. Le Roux, “X-Ray Microcomputed Tomography in Additive Manufacturing: A Review of the Current Technology and Applications,” *3D Print. Addit. Manuf.*, vol. 5, no. 3, pp. 227–247, Sep. 2018, doi: 10.1089/3dp.2018.0060.
- [256] MathWorks, “Image Processing Toolbox User’s Guide,” *Image Processing*, 2018. [https://www.mathworks.com/help/pdf\\_doc/images/images Ug.pdf](https://www.mathworks.com/help/pdf_doc/images/images Ug.pdf) (accessed Aug. 09, 2021).
- [257] ASME, *B46. 1 Surface Texture, Surface Roughness, Waviness and Lay*. 2009.
- [258] E. Muzangaza, “The effects of titanium Ti-6Al-4V powders manufactured using electron beam melting (EBM) - additive manufacturing on metallurgical evaluation [dissertation],” University of Birmingham, 2018.
- [259] G. Strano, L. Hao, R. M. Everson, and K. E. Evans, “Surface roughness analysis, modelling and prediction in selective laser melting,” *J. Mater. Process. Technol.*, vol. 213, no. 4, pp. 589–597, Apr. 2013, doi: 10.1016/j.jmatprotec.2012.11.011.
- [260] M. Jamshidinia, F. Kong, and R. Kovacevic, “Temperature Distribution and Fluid Flow Modeling of Electron Beam Melting® (EBM),” in *Volume 7: Fluids and Heat Transfer, Parts A, B, C, and D*, Nov. 2012, pp. 3089–3101, doi: 10.1115/IMECE2012-89440.
- [261] P. Wang, W. J. Sin, M. L. S. Nai, and J. Wei, “Effects of Processing Parameters on Surface Roughness of Additive Manufactured Ti-6Al-4V via Electron Beam Melting,” *Materials (Basel)*, vol. 10, no. 10, p. 1121, Sep. 2017, doi: 10.3390/ma10101121.
- [262] J. Karlsson, A. Snis, H. Engqvist, and J. Lausmaa, “Characterization and comparison of materials produced by Electron Beam Melting (EBM) of two different Ti-6Al-4V powder fractions,” *J. Mater. Process. Technol.*, vol. 213, no. 12, pp. 2109–2118, Dec. 2013, doi: 10.1016/j.jmatprotec.2013.06.010.
- [263] T. H. Vo, M. Museau, F. Vignat, F. Villeneuve, Y. Ledoux, and A. Ballu, “Typology of geometrical

- defects in Electron Beam Melting,” *Procedia CIRP*, vol. 75, pp. 92–97, 2018, doi: <https://doi.org/10.1016/j.procir.2018.04.033>.
- [264] M. Suard, P. Lhuissier, R. Dendievel, J.-J. Blandin, F. Vignat, and F. Villeneuve, “Towards stiffness prediction of cellular structures made by electron beam melting (EBM),” *Powder Metall.*, vol. 57, no. 3, pp. 190–195, Jul. 2014, doi: 10.1179/1743290114Y.0000000093.
- [265] T. DebRoy *et al.*, “Additive manufacturing of metallic components – Process, structure and properties,” *Prog. Mater. Sci.*, vol. 92, pp. 112–224, Mar. 2018, doi: 10.1016/j.pmatsci.2017.10.001.
- [266] H. Sharma *et al.*, “A critical evaluation of the microstructural gradient along the build direction in electron beam melted Ti-6Al-4V alloy,” *Mater. Sci. Eng. A*, vol. 744, pp. 182–194, Jan. 2019, doi: 10.1016/j.msea.2018.12.016.
- [267] D. R. Askeland, *The Science and Engineering of Materials*. Boston, MA: Springer US, 1996.
- [268] M. J. Birmingham, S. D. McDonald, M. S. Dargusch, and D. H. StJohn, “Grain-refinement mechanisms in titanium alloys,” *J. Mater. Res.*, vol. 23, no. 1, pp. 97–104, 2008, doi: DOI: 10.1557/JMR.2008.0002.
- [269] E. O. Hall, “The Deformation and Ageing of Mild Steel: III Discussion of Results,” *Proc. Phys. Soc. Sect. B*, vol. 64, no. 9, pp. 747–753, Sep. 1951, doi: 10.1088/0370-1301/64/9/303.
- [270] T. Vilaro, C. Colin, and J. D. Bartout, “As-Fabricated and Heat-Treated Microstructures of the Ti-6Al-4V Alloy Processed by Selective Laser Melting,” *Metall. Mater. Trans. A*, vol. 42, no. 10, pp. 3190–3199, Oct. 2011, doi: 10.1007/s11661-011-0731-y.
- [271] P.-H. Li, W.-G. Guo, W.-D. Huang, Y. Su, X. Lin, and K.-B. Yuan, “Thermomechanical response of 3D laser-deposited Ti–6Al–4V alloy over a wide range of strain rates and temperatures,” *Mater. Sci. Eng. A*, vol. 647, pp. 34–42, Oct. 2015, doi: 10.1016/j.msea.2015.08.043.
- [272] H. Gong, K. Rafi, H. Gu, T. Starr, and B. Stucker, “Analysis of defect generation in Ti6Al4V parts made using powder bed fusion additive manufacturing processes,” *Addit. Manuf.*, vol. 1–4, pp. 87–98, Oct. 2014, doi: 10.1016/j.addma.2014.08.002.
- [273] G. Lütjering, “Influence of processing on microstructure and mechanical properties of ( $\alpha$ + $\beta$ ) titanium alloys,” *Mater. Sci. Eng. A*, vol. 243, no. 1–2, pp. 32–45, Mar. 1998, doi: 10.1016/S0921-5093(97)00778-8.
- [274] P. Kobryn and S. Semiatin, “Microstructure and texture evolution during solidification processing of Ti–6Al–4V,” *J. Mater. Process. Technol.*, vol. 135, no. 2–3, pp. 330–339, Apr. 2003, doi: 10.1016/S0924-0136(02)00865-8.
- [275] ASTM, “52921:2019-Standard Terminology for Additive Manufacturing – Coordinate System and

- Test methodologies,” *ASTM Int.*, pp. 1–13, 2019, doi: 10.1520/ISOASTM52921-13R19.
- [276] G. Shanbhag, E. Wheat, S. Moylan, and M. Vlasea, “Effect of specimen geometry and orientation on tensile properties of Ti-6Al-4V manufactured by electron beam powder bed fusion (Under Review),” *Addit. Manuf.*, 2021.
- [277] H. Masuo *et al.*, “Influence of defects, surface roughness and HIP on the fatigue strength of Ti-6Al-4V manufactured by additive manufacturing,” *Int. J. Fatigue*, vol. 117, pp. 163–179, Dec. 2018, doi: 10.1016/j.ijfatigue.2018.07.020.
- [278] S. Romano, A. Brandão, J. Gumpinger, M. Gschweidl, and S. Beretta, “Qualification of AM parts: Extreme value statistics applied to tomographic measurements,” *Mater. Des.*, vol. 131, pp. 32–48, Oct. 2017, doi: 10.1016/j.matdes.2017.05.091.
- [279] S. Romano, A. Brückner-Foit, A. Brandão, J. Gumpinger, T. Ghidini, and S. Beretta, “Fatigue properties of AlSi10Mg obtained by additive manufacturing: Defect-based modelling and prediction of fatigue strength,” *Eng. Fract. Mech.*, vol. 187, pp. 165–189, Jan. 2018, doi: 10.1016/j.engfracmech.2017.11.002.
- [280] T. Persenot, G. Martin, R. Dendievel, J. Y. Buffière, and E. Maire, “Enhancing the tensile properties of EBM as-built thin parts: Effect of HIP and chemical etching,” *Mater. Charact.*, vol. 143, no. November 2017, pp. 82–93, 2018, doi: 10.1016/j.matchar.2018.01.035.
- [281] S. Leuders *et al.*, “On the mechanical behaviour of titanium alloy TiAl6V4 manufactured by selective laser melting: Fatigue resistance and crack growth performance,” *Int. J. Fatigue*, vol. 48, pp. 300–307, Mar. 2013, doi: 10.1016/j.ijfatigue.2012.11.011.
- [282] E. W. Hovig, A. S. Azar, M. F. Sunding, E. Andreassen, and K. Sørby, “High cycle fatigue life estimation of materials processed by laser powder bed fusion,” *Fatigue Fract. Eng. Mater. Struct.*, vol. 42, no. 7, pp. 1454–1466, Jul. 2019, doi: 10.1111/ffe.12982.
- [283] E. Brandl, U. Heckenberger, V. Holzinger, and D. Buchbinder, “Additive manufactured AlSi10Mg samples using Selective Laser Melting (SLM): Microstructure, high cycle fatigue, and fracture behavior,” *Mater. Des.*, vol. 34, pp. 159–169, Feb. 2012, doi: 10.1016/j.matdes.2011.07.067.
- [284] M. Saâdaoui, F. Khaldoun, J. Adrien, H. Reveron, and J. Chevalier, “X-ray tomography of additive-manufactured zirconia: Processing defects – Strength relations,” *J. Eur. Ceram. Soc.*, vol. 40, no. 8, pp. 3200–3207, Jul. 2020, doi: 10.1016/j.jeurceramsoc.2019.04.010.
- [285] H. Gong, V. K. Nadimpalli, K. Rafi, T. Starr, and B. Stucker, “Micro-CT Evaluation of Defects in Ti-6Al-4V Parts Fabricated by Metal Additive Manufacturing,” *Technologies*, vol. 7, no. 2, p. 44, 2019, doi: 10.3390/technologies7020044.

- [286] N. Ortega, S. Martínez, I. Cerrillo, A. Lamikiz, and E. Ukar, “Computed tomography approach to quality control of the Inconel 718 components obtained by additive manufacturing (SLM),” *Procedia Manuf.*, vol. 13, pp. 116–123, 2017, doi: 10.1016/j.promfg.2017.09.018.
- [287] A. Wu, M. M. LeBlanc, M. Kumar, G. F. Gallegos, D. W. Brownand, and W. E. King, “Effect of laser scanning pattern and build direction in additive manufacturing on anisotropy, porosity and residual stress,” 2014.
- [288] I. Cruz-Matías *et al.*, “Sphericity and roundness computation for particles using the extreme vertices model,” *J. Comput. Sci.*, vol. 30, pp. 28–40, Jan. 2019, doi: 10.1016/j.jocs.2018.11.005.
- [289] A. Safdar, H. Z. He, L. Wei, A. Snis, and L. E. Chavez de Paz, “Effect of process parameters settings and thickness on surface roughness of EBM produced Ti-6Al-4V,” *Rapid Prototyp. J.*, vol. 18, no. 5, pp. 401–408, Jul. 2012, doi: 10.1108/13552541211250391.
- [290] R. H. Morgan, A. J. Papworth, C. Sutcliffe, P. Fox, and W. O’neill, “High density net shape components by direct laser re-melting of single-phase powders,” *J. Mater. Sci.*, vol. 37, no. 15, pp. 3093–3100, 2002, doi: 10.1023/A:1016185606642.
- [291] S. Tammam-Williams, “XCT Analysis of the Defect Distribution and its Effect on the Static and Dynamic Mechanical Properties in Ti-6Al-4V Components Manufactured by Electron Beam Additive Manufacture,” 2015.
- [292] F. H. Kim and S. P. Moylan, “Literature review of metal additive manufacturing defects,” Gaithersburg, MD, May 2018. doi: 10.6028/NIST.AMS.100-16.
- [293] T. Sercombe, N. Jones, R. Day, and A. Kop, “Heat treatment of Ti-6Al-7Nb components produced by selective laser melting,” *Rapid Prototyp. J.*, vol. 14, no. 5, pp. 300–304, Sep. 2008, doi: 10.1108/13552540810907974.
- [294] K. Puebla, L. E. Murr, S. M. Gaytan, E. Martinez, F. Medina, and R. B. Wicker, “Effect of Melt Scan Rate on Microstructure and Macrostructure for Electron Beam Melting of Ti-6Al-4V,” *Mater. Sci. Appl.*, vol. 03, no. 05, pp. 259–264, 2012, doi: 10.4236/msa.2012.35038.
- [295] R. Snell *et al.*, “Methods for Rapid Pore Classification in Metal Additive Manufacturing,” *Jom*, vol. 72, no. 1, pp. 101–109, 2020, doi: 10.1007/s11837-019-03761-9.
- [296] E. Wycisk, S. Siddique, D. Herzog, F. Walther, and C. Emmelmann, “Fatigue Performance of Laser Additive Manufactured Ti-6Al-4V in Very High Cycle Fatigue Regime up to 109 Cycles,” *Front. Mater.*, vol. 2, Dec. 2015, doi: 10.3389/fmats.2015.00072.
- [297] S. Hendrixson, “NeuBeam 3D Printing Process Is an Update for Electron Beam Melting,” *Additive Manufacturing Media*, 2021. <https://www.additivemanufacturing.media/articles/neubeam-3d->



- printing-process-is-an-update-for-electron-beam-melting (accessed Sep. 13, 2021).
- [298] C. L. A. Leung, R. Tosi, E. Muzangaza, S. Nonni, P. J. Withers, and P. D. Lee, “Effect of preheating on the thermal, microstructural and mechanical properties of selective electron beam melted Ti-6Al-4V components,” *Mater. Des.*, vol. 174, p. 107792, Jul. 2019, doi: 10.1016/j.matdes.2019.107792.
- [299] N. Shen and K. Chou, “Thermal Modeling of Electron Beam Additive Manufacturing Process: Powder Sintering Effects,” in *ASME 2012 International Manufacturing Science and Engineering Conference*, Jun. 2012, pp. 287–295, doi: 10.1115/MSEC2012-7253.
- [300] N. Shen and K. Chou, “NUMERICAL THERMAL ANALYSIS IN ELECTRON BEAM ADDITIVE MANUFACTURING WITH PREHEATING EFFECTS,” in *Solid Freeform Fabrication Symposium*, 2012, pp. 774–784.
- [301] S. Price, B. Cheng, J. Lydon, K. Cooper, and K. Chou, “On Process Temperature in Powder-Bed Electron Beam Additive Manufacturing: Process Parameter Effects,” *J. Manuf. Sci. Eng.*, vol. 136, p. 61019, Dec. 2014, doi: 10.1115/1.4028485.
- [302] M. Galati, L. Iuliano, A. Salmi, and E. Atzeni, “Modelling energy source and powder properties for the development of a thermal FE model of the EBM additive manufacturing process,” *Addit. Manuf.*, vol. 14, pp. 49–59, 2017, doi: <https://doi.org/10.1016/j.addma.2017.01.001>.
- [303] E. Landau *et al.*, “Thermal characterization of the build chamber in electron beam melting,” *Addit. Manuf.*, vol. 36, no. April, p. 101535, 2020, doi: 10.1016/j.addma.2020.101535.
- [304] M. Shafiqur Rahman, P. J. Schilling, P. D. Herrington, and U. K. Chakravarty, “Thermal analysis of electron beam additive manufacturing using Ti-6Al-4V powder-bed,” *ASME Int. Mech. Eng. Congr. Expo. Proc.*, vol. 1, pp. 1–13, 2017, doi: 10.1115/IMECE2017-71663.
- [305] M. Jamshidinia, F. Kong, and R. Kovacevic, *The Coupled CFD-FEM Model of Electron Beam Melting® (EBM)*. 2013.
- [306] M. Jamshidinia, F. Kong, and R. Kovacevic, “Numerical modeling of heat distribution in the electron beam melting® of Ti-6Al-4V,” *J. Manuf. Sci. Eng. Trans. ASME*, vol. 135, no. 6, pp. 1–14, 2013, doi: 10.1115/1.4025746.
- [307] J. Romano, L. Ladani, and M. Sadowski, “Thermal Modeling of Laser Based Additive Manufacturing Processes within Common Materials,” *Procedia Manuf.*, vol. 1, pp. 238–250, 2015, doi: 10.1016/j.promfg.2015.09.012.
- [308] A. V. Gusarov, T. Laoui, L. Froyen, and V. I. Titov, “Contact thermal conductivity of a powder bed in selective laser sintering,” *Int. J. Heat Mass Transf.*, vol. 46, no. 6, pp. 1103–1109, Mar. 2003, doi: 10.1016/S0017-9310(02)00370-8.

- [309] W. W. M. Siu and S. H.-K. Lee, “Effective conductivity computation of a packed bed using constriction resistance and contact angle effects,” *Int. J. Heat Mass Transf.*, vol. 43, no. 21, pp. 3917–3924, Nov. 2000, doi: 10.1016/S0017-9310(00)00051-X.
- [310] A. J. Slavin, F. A. Londry, and J. Harrison, “A new model for the effective thermal conductivity of packed beds of solid spheroids: alumina in helium between 100 and 500°C,” *Int. J. Heat Mass Transf.*, vol. 43, no. 12, pp. 2059–2073, Jun. 2000, doi: 10.1016/S0017-9310(99)00290-2.
- [311] S. S. SIH and J. W. BARLOW, “The Prediction of the Emissivity and Thermal Conductivity of Powder Beds,” *Part. Sci. Technol.*, vol. 22, no. 4, pp. 427–440, Oct. 2004, doi: 10.1080/02726350490501682.
- [312] P. Zehner and E. U. Schlünder, “Wärmeleitfähigkeit von Schüttungen bei mäßigen Temperaturen,” *Chemie Ing. Tech.*, vol. 42, no. 14, pp. 933–941, Jul. 1970, doi: 10.1002/cite.330421408.
- [313] S. Yagi and D. Kunii, “Studies on effective thermal conductivities in packed beds,” *AIChE J.*, vol. 3, no. 3, pp. 373–381, Sep. 1957, doi: 10.1002/aic.690030317.
- [314] F. Thümmeler and R. Oberacker, *An introduction to powder metallurgy*. London: CRC Press, 1994.
- [315] M. Rombouts, L. Froyen, A. V. Gusarov, E. H. Bentefour, and C. Glorieux, “Photopyroelectric measurement of thermal conductivity of metallic powders,” *J. Appl. Phys.*, vol. 97, no. 2, p. 024905, Jan. 2005, doi: 10.1063/1.1832740.
- [316] M. R. Alkahari, T. Furumoto, T. Ueda, A. Hosokawa, R. Tanaka, and M. S. Abdul Aziz, “Thermal conductivity of metal powder and consolidated material fabricated via selective laser melting,” *Key Eng. Mater.*, vol. 523–524, pp. 244–249, 2012, doi: 10.4028/www.scientific.net/KEM.523-524.244.
- [317] M. Boivineau *et al.*, “Thermophysical properties of solid and liquid Ti-6Al-4V (TA6V) Alloy,” *Int. J. Thermophys.*, vol. 27, no. 2, 2006, doi: 10.1007/s10765-005-0001-6.
- [318] N. Tolochko, S. Mozzharov, T. Laoui, and L. Froyen, “Selective laser sintering of single- and two-component metal powders,” *Rapid Prototyp. J.*, vol. 9, no. 2, pp. 68–78, 2003, doi: 10.1108/13552540310467077.
- [319] A. Rogalsky, I. Rishmawi, L. Brock, and M. Vlasea, “Low cost irregular feed stock for laser powder bed fusion,” *J. Manuf. Process.*, vol. 35, pp. 446–456, 2018, doi: 10.1016/j.jmapro.2018.08.032.
- [320] G. Jacob, A. Donmez, J. Slotwinski, and S. Moylan, “Measurement of powder bed density in powder bed fusion additive manufacturing processes,” *Meas. Sci. Technol.*, vol. 27, no. 11, p. 115601, Nov. 2016, doi: 10.1088/0957-0233/27/11/115601.
- [321] J. Gostick *et al.*, “PoreSpy: A Python Toolkit for Quantitative Analysis of Porous Media Images,” *J. Open Source Softw.*, vol. 4, no. 37, p. 1296, May 2019, doi: 10.21105/joss.01296.

- [322] E. Wheat, G. Shanbhag, and M. Vlasea, “The Master Sinter Curve and Its Application to Binder Jetting Additive Manufacturing,” *J. Manuf. Sci. Eng.*, vol. 142, no. 10, Oct. 2020, doi: 10.1115/1.4047140.
- [323] R. C. Atwood, J. R. Jones, P. D. Lee, and L. L. Hench, “Analysis of pore interconnectivity in bioactive glass foams using X-ray microtomography,” *Scr. Mater.*, vol. 51, no. 11, pp. 1029–1033, Nov. 2004, doi: 10.1016/j.scriptamat.2004.08.014.
- [324] A. P. Mangan and R. T. Whitaker, “Partitioning 3D surface meshes using watershed segmentation,” *IEEE Trans. Vis. Comput. Graph.*, vol. 5, no. 4, pp. 308–321, 1999, doi: 10.1109/2945.817348.
- [325] A. V. Gusarov and E. P. Kovalev, “Model of thermal conductivity in powder beds,” *Phys. Rev. B - Condens. Matter Mater. Phys.*, vol. 80, no. 2, pp. 16–20, 2009, doi: 10.1103/PhysRevB.80.024202.
- [326] M. Koike, K. Martinez, L. Guo, G. Chahine, R. Kovacevic, and T. Okabe, “Evaluation of titanium alloy fabricated using electron beam melting system for dental applications,” *J. Mater. Process. Technol.*, vol. 211, no. 8, pp. 1400–1408, Aug. 2011, doi: 10.1016/j.jmatprotec.2011.03.013.
- [327] A. Alfaify, “The Effect of Changing Particle Size Distribution and Layer Thickness on the Density of Parts Manufactured Using the Laser Powder Bed Fusion Process,” University of Sheffield, 2019.
- [328] E. Wheat, M. Vlasea, J. Hinebaugh, and C. Metcalfe, “Sinter structure analysis of titanium structures fabricated via binder jetting additive manufacturing,” *Mater. Des.*, vol. 20, pp. 167–183, 2018, doi: 10.1016/j.dib.2018.08.135.
- [329] W. Yan, W. Ma, and Y. Shen, “Powder sintering mechanisms during the pre-heating procedure of electron beam additive manufacturing,” *Mater. Today Commun.*, vol. 25, p. 101579, Dec. 2020, doi: 10.1016/j.mtcomm.2020.101579.
- [330] M. N. Rahaman, “Kinetics and mechanisms of densification,” in *Sintering of Advanced Materials*, Elsevier, 2010, pp. 33–64.
- [331] C. M. Taylor and T. Childs, “Thermal experiments in direct metal laser sintering.”
- [332] I. Fedina, E. Litovsky, M. Shapiro, and A. Shavit, “Thermal conductivity of packed beds of refractory particles: Experimental results,” *J. Am. Ceram. Soc.*, vol. 80, no. 8, pp. 2100–2108, 1997, doi: 10.1111/j.1151-2916.1997.tb03094.x.
- [333] E. Tsotsas and H. Martin, “Thermal conductivity of packed beds: A review,” *Chem. Eng. Process. Process Intensif.*, vol. 22, no. 1, pp. 19–37, Jul. 1987, doi: 10.1016/0255-2701(87)80025-9.
- [334] M. Masoomi, J. W. Pegues, S. M. Thompson, and N. Shamsaei, “A numerical and experimental investigation of convective heat transfer during laser-powder bed fusion,” *Addit. Manuf.*, vol. 22, pp. 729–745, 2018, doi: <https://doi.org/10.1016/j.addma.2018.06.021>.

- [335] M. Malý *et al.*, “Effect of Process Parameters and High-Temperature Preheating on Residual Stress and Relative Density of Ti6Al4V Processed by Selective Laser Melting,” *Materials (Basel)*, vol. 12, no. 6, p. 930, Mar. 2019, doi: 10.3390/ma12060930.
- [336] N. Senin and L. Blunt, “Characterisation of Individual Areal Features,” in *Characterisation of Areal Surface Texture*, Berlin, Heidelberg: Springer Berlin Heidelberg, 2013, pp. 179–216.
- [337] N. Senin, A. Thompson, and R. Leach, “Feature-based characterisation of signature topography in laser powder bed fusion of metals,” *Meas. Sci. Technol.*, vol. 29, no. 4, p. 045009, Apr. 2018, doi: 10.1088/1361-6501/aa9e19.
- [338] X. Jiang, P. . Scott, D. . Whitehouse, and L. Blunt, “Paradigm shifts in surface metrology. Part I. Historical philosophy,” *Proc. R. Soc. A Math. Phys. Eng. Sci.*, vol. 463, no. 2085, pp. 2049–2070, Sep. 2007, doi: 10.1098/rspa.2007.1874.
- [339] L. D. Todhunter, R. K. Leach, S. D. A. Lawes, and F. Blateyron, “Industrial survey of ISO surface texture parameters,” *CIRP J. Manuf. Sci. Technol.*, vol. 19, pp. 84–92, 2017, doi: 10.1016/j.cirpj.2017.06.001.
- [340] R. Leach, *Fundamental Principles of Engineering Nanometrology*, 2nd ed. Elsevier, 2014.
- [341] D. J. Whitehouse, *Handbook of Surface Metrology*, 1st ed. CRC Press, 1994.
- [342] A. Mohammad, M. K. Mohammed, and A. M. Alahmari, “Effect of laser ablation parameters on surface improvement of electron beam melted parts,” *Int. J. Adv. Manuf. Technol.*, vol. 87, no. 1–4, pp. 1033–1044, 2016, doi: 10.1007/s00170-016-8533-4.
- [343] G. Stevenson, S. Rehman, E. Draper, E. Hernández-Nava, J. Hunt, and J. W. Haycock, “Combining 3D human in vitro methods for a 3Rs evaluation of novel titanium surfaces in orthopaedic applications,” *Biotechnol. Bioeng.*, vol. 113, no. 7, pp. 1586–1599, 2016, doi: 10.1002/bit.25919.
- [344] C. de Formanoir, M. Suard, R. Dendievel, G. Martin, and S. Godet, “Improving the mechanical efficiency of electron beam melted titanium lattice structures by chemical etching,” *Addit. Manuf.*, vol. 11, pp. 71–76, Jul. 2016, doi: 10.1016/j.addma.2016.05.001.
- [345] P. C. Liu *et al.*, “A study on the mechanical characteristics of the EBM-printed Ti-6Al-4V LCP plates in vitro,” *J. Orthop. Surg. Res.*, vol. 9, p. 106, 2014, doi: 10.1186/s13018-014-0106-3.
- [346] A. Townsend, N. Senin, L. Blunt, R. K. Leach, and J. S. Taylor, “Surface texture metrology for metal additive manufacturing: a review,” *Precis. Eng.*, vol. 46, pp. 34–47, Oct. 2016, doi: 10.1016/j.precisioneng.2016.06.001.
- [347] R. Pahuja, M. Ramulu, and M. Hashish, “Integration of jetting technology in metal additive manufacturing,” *24th Int. Conf. Water Jet.*, no. October 2019, pp. 23–35, 2018.

- [348] M. Thomas *et al.*, “Characterization of Multiperforated Plates Manufactured by SLM and EBM for Aeroengine Applications,” in *TMS 2017 146th Annual Meeting & Exhibition Supplemental Proceedings*, 2017, pp. 61–70.
- [349] M. McGregor, S. Patel, S. McLachlin, and M. Vlasea, “Architectural bone parameters and the relationship to titanium lattice design for powder bed fusion additive manufacturing,” May 2021, Accessed: Jul. 08, 2021. [Online]. Available: <https://arxiv.org/abs/2105.07945>.
- [350] Z. R. Francis, “The Effects of Laser and Electron Beam Spot Size in Additive Manufacturing Processes,” Carnegie Mellon University, 2017.
- [351] L. Scime and J. Beuth, “Anomaly detection and classification in a laser powder bed additive manufacturing process using a trained computer vision algorithm,” *Addit. Manuf.*, vol. 19, pp. 114–126, Jan. 2018, doi: 10.1016/j.addma.2017.11.009.
- [352] M. F. Zäh and S. Lutzmann, “Modelling and simulation of electron beam melting,” *Prod. Eng.*, vol. 4, no. 1, pp. 15–23, 2010, doi: 10.1007/s11740-009-0197-6.
- [353] A. R. Nassar, M. A. Gundermann, E. W. Reutzel, P. Guerrier, M. H. Krane, and M. J. Weldon, “Formation processes for large ejecta and interactions with melt pool formation in powder bed fusion additive manufacturing,” *Sci. Rep.*, vol. 9, no. 1, p. 5038, Dec. 2019, doi: 10.1038/s41598-019-41415-7.
- [354] F. Calignano, “Investigation of the accuracy and roughness in the laser powder bed fusion process,” *Virtual Phys. Prototyp.*, vol. 13, no. 2, pp. 97–104, Apr. 2018, doi: 10.1080/17452759.2018.1426368.
- [355] E. Attar, “Simulation of Selective Electron Beam Melting Processes,” University of Erlangen, 2011.
- [356] P. Delfs, M. Töws, and H.-J. Schmid, “Surface Roughness Optimized Alignment of Parts for Additive Manufacturing Processes,” *SFF Symp.*, pp. 1334–1344, 2015.
- [357] M. Galati, P. Minetola, and G. Rizza, “Surface Roughness Characterisation and Analysis of the Electron Beam Melting (EBM) Process,” *Materials (Basel)*, vol. 12, no. 13, p. 2211, Jul. 2019, doi: 10.3390/ma12132211.
- [358] ASTM, “F3335-20-Assessing the Removal of Additive Manufacturing Residues in Medical Devices Fabricated by Powder Bed Fusion,” *ASTM Int.*, pp. 1–7, 2020, doi: 10.1520/F3335-20.
- [359] KEYENCE CORPORATION, “Introduction to Surface Roughness Measurement,” *Keyence*, pp. 2–23, 2001, [Online]. Available: [www.keyence.com](http://www.keyence.com).
- [360] A. M. VilardeLL *et al.*, “Topology optimization and characterization of Ti6Al4V ELI cellular lattice structures by laser powder bed fusion for biomedical applications,” *Mater. Sci. Eng. A*, vol. 766, p.

- 138330, Oct. 2019, doi: 10.1016/j.msea.2019.138330.
- [361] I. Echeta, X. Feng, B. Dutton, R. Leach, and S. Piano, “Review of defects in lattice structures manufactured by powder bed fusion,” *Int. J. Adv. Manuf. Technol.*, vol. 106, no. 5–6, pp. 2649–2668, Jan. 2020, doi: 10.1007/s00170-019-04753-4.
- [362] P. W. Coopers, “3D printing and the new shape of industrial manufacturing,” *Pricewaterhouse Coopers LLP London, UK*, 2014.
- [363] M. Markl and C. Körner, “Multiscale Modeling of Powder Bed–Based Additive Manufacturing,” *Annu. Rev. Mater. Res.*, vol. 46, no. 1, pp. 93–123, Jul. 2016, doi: 10.1146/annurev-matsci-070115-032158.
- [364] A. B. Spierings, N. Herres, and G. Levy, “Influence of the particle size distribution on surface quality and mechanical properties in AM steel parts,” *Rapid Prototyp. J.*, vol. 17, no. 3, pp. 195–202, Apr. 2011, doi: 10.1108/13552541111124770.
- [365] H. Fayazfar, I. Rishmawi, and M. Vlasea, “Electrochemical-Based Surface Enhancement of Additively Manufactured Ti-6Al-4V Complex Structures,” *J. Mater. Eng. Perform.*, vol. 30, no. 3, pp. 2245–2255, Mar. 2021, doi: 10.1007/s11665-021-05512-x.
- [366] L. Liu, P. Kamm, F. García-Moreno, J. Banhart, and D. Pasini, “Elastic and failure response of imperfect three-dimensional metallic lattices: the role of geometric defects induced by Selective Laser Melting,” *J. Mech. Phys. Solids*, vol. 107, pp. 160–184, Oct. 2017, doi: 10.1016/j.jmps.2017.07.003.
- [367] C. Qiu *et al.*, “Influence of processing conditions on strut structure and compressive properties of cellular lattice structures fabricated by selective laser melting,” *Mater. Sci. Eng. A*, vol. 628, pp. 188–197, Mar. 2015, doi: 10.1016/j.msea.2015.01.031.
- [368] P. Lipinski, A. Barbas, and A.-S. Bonnet, “Fatigue behavior of thin-walled grade 2 titanium samples processed by selective laser melting. Application to life prediction of porous titanium implants,” *J. Mech. Behav. Biomed. Mater.*, vol. 28, pp. 274–290, Dec. 2013, doi: 10.1016/j.jmbbm.2013.08.011.
- [369] S. Van Bael, G. Kerckhofs, M. Moesen, G. Pyka, J. Schrooten, and J. P. Kruth, “Micro-CT-based improvement of geometrical and mechanical controllability of selective laser melted Ti6Al4V porous structures,” *Mater. Sci. Eng. A*, vol. 528, no. 24, pp. 7423–7431, Sep. 2011, doi: 10.1016/j.msea.2011.06.045.
- [370] M. Benedetti, A. du Plessis, R. O. Ritchie, M. Dallago, S. M. J. Razavi, and F. Berto, “Architected cellular materials: A review on their mechanical properties towards fatigue-tolerant design and fabrication,” *Mater. Sci. Eng. R Reports*, vol. 144, p. 100606, Apr. 2021, doi:

10.1016/j.mser.2021.100606.

## Appendices

### Appendix A. Chapter 4 Pore space analytics code

```
function DensityAnalytics ()

% Function calculates the density of a sample as a function of its height. It calculates the density in each
% image slice of a .tif stack.
% Function also finds approximate cross-sectional diameters from the data.

% The function requires:
% - imagescaling.m
% - saveastiff.m
% - Matlab Image Processing Toolbox (regionprops and regionprops3d)
% imagescaling.m and saveastiff.m provided at the end of densityanalytics.m

%% Section 0: Initialization

% Input the minimum and maximum greyscale values to complete 8-bit scaling

% E8M-2: 14000/56000
in.greymin = 14000;
in.greymax = 56000;

% E8M-3: 11000/52000
% E8-3: 15000/55000
% E8M-4: 11000/53000
% E8M-5: 7000/53000
% Flat Large: 19000/54000
% Flat Small: 17000/55000

% Input values for bilateral smoothing - same for all samples

in.spatialsigma = 3;
in.smoothing = 4e+03;

% Input in the image thresholding value

E8M-2: 155
% E8M-3: 155
% E8-3: 155
% E8M-4: 155
% E8M-5: 155
% Flat Large: 175
% Flat Small: 175

% Voxel size information
```



```

E8M-2: 10.5
% E8M-3: 8
% E8-3: 8
% E8M-4: 6.5
% E8M-5: 3.5
% Flat Large: 14
% Flat Small: 8

```

```

%% Section 1: File IO setup and Make Folders for Outputs

```

```

% Get file names/locations%% Section 1: File IO setup and Make Folders for Outputs

```

```

% Get file names/locations
[inFiles,inPath] = uigetfile('* .tif');
inName = char(strcat(inPath,inFiles));

```

```

% Generate base save name from input image file
saveNameBase = inFiles(1:end-4);

```

```

% Create the outpath and corresponding folder - creates an output folder
% where the data was taken from
% Ask the user to generate a folder name to output all of the files
out_folder_name = input('Provide a name for the output folder: ','s');
outPath = strcat(inPath,out_folder_name,"\");
% Make directory and add to path
[status, msg, msgID] = mkdir(char(outPath));
addpath(char(outPath)) ;

```

```

% Check if folder already existed and if it's okay to overwrite
folder_Check = 0;
while folder_Check == 0;
    if isempty(msg) % Empty return means that there was no folder
        folder_Check = 1;
    elseif msg == "Directory already exists."
        overwrite = input('Folder already exists, do you want to overwrite (y/n)?\n','s');
        if (overwrite ~= 'y') && (overwrite ~= 'n') % Did not enter y or n
            disp('You must enter y to overwrite or n to set a new output folder name\n');
        else
            if overwrite == 'y' % Overwrite in the existing folder
                folder_Check = 1;
            elseif overwrite == 'n' % Set a new output folder name
                workFolder = input('Provide a new name for the output folder: \n','s'); %Provide a new folder
name
                [status,msg,msgID] = mkdir(strcat(['outputs\',workFolder]));
            end
        end
    elseif not(isempty(msg)) && not(msg == "Directory already exists.")

```

```

        workFolder = input('Error making folder - Provide a new name for the output folder: \n','s'); %Provide
a new folder name
        [status,msg,msgID] = mkdir(strcat(['outputs\'',workFolder]));
    else
        folder_Check = 1; % Just in case checks return something weird
    end
end
end

%% Section 2: Open .tif and Perform Preprocessing

% Import the .tif stack into Matlab
[stack_in,Nframes] = imread_big(inName);
% stack = importstack(inName);

% Perform 8-bit scaling on the .tif stack and covert from 16bit to 8bit
% image.
stack8 = imagescaling(stack_in,in);
clear stack_in

% Perform a 2D bilateral filter on the image stack.
for j = 1:Nframes;
    stack8(:, :,j) = imbilatfilt(stack8(:, :,j));
end

% Perform thresholding on the image stack
stackBW = stack8 > imageThreshold;
clear stack8

%% Section 3: Perform 2D RegionProps Analysis and Calculate Bulk Density

density_data_2d = (0);
pore_area_2d = zeros(Nframes);
total_area_2d = zeros(Nframes);
stackFilled = [];
stackPores = [];
stackOpen = [];
img_data = { };

all_pore_area = 0;
all_filled_area = 0;

% Set up output data table
sample_data = { };
sample_data{1,1} = 'Sample Name';
sample_data{1,2} = saveNameBase;
% Bulk information
sample_data{3,1} = 'Bulk Density';
sample_data{4,1} = 'Bulk Porosity';

```

```

sample_data{5,1} = 'Effective Measured Diameter (mm)';
sample_data{5,2} = 0;
sample_data{6,1} = 'Average True Area (mm^2)';
sample_data{6,2} = 0;
sample_data{7,1} = 'Average Equivalent Diameter (mm)';
sample_data{7,2} = 0;
sample_data{8,1} = 'Average Filled Area (mm^2)';
sample_data{8,2} = 0;
% Per-layer information
sample_data{9,1} = 'Layer';
sample_data{9,2} = 'Height (mm)';
sample_data{9,3} = 'Density';
sample_data{9,4} = 'Porosity';
sample_data{9,5} = 'Minor Axis Length (mm)';
sample_data{9,6} = 'Major Axis Length (mm)';
sample_data{9,7} = 'Effective Measured Diameter (mm)';
sample_data{9,8} = 'True Area(mm^2)';
sample_data{9,9} = 'Equivalent Diameter (mm)';
sample_data{9,10} = 'Centroid X (mm)';
sample_data{9,11} = 'Centroid Y (mm)';
sample_data{9,12} = 'Filled Area(mm^2)';

% Run Segmentation and RegionProps analysis for each image in the stack
for i = 1:Nframes
    % Create a temp image for a single slice
    img_temp = stackBW(:, :, i);

    % Use regionprops to get layer information
    temp_data = regionprops(img_temp, 'all');
    names = fieldnames(temp_data);
    temp_data = struct2cell(temp_data);
    % Include the fieldnames with the cell data
    img_data{i} = horzcat(names, temp_data);

    % Use imfill to create an image with internal pore areas filled in
    img_filled = imfill(img_temp, 'holes');
    stackFilled(:, :, i) = img_filled;

    % Use bwdist to find maximum distance from sample edge
    % img_dist = bwdist(img_filled);
    % max_rad = max(img_dist(:));

    % Find column in regionprops data that has the largest area
    temp_mat = cell2mat(temp_data(1, :));
    max_area = max(temp_mat);
    %isMax = cellfun(@(x)isequal(x,a),temp_data);
    [~, index] = find(temp_mat == max_area);

```

```

% Create an img of just the pores
img_pores = xor(img_filled,img_temp);
stackPores(:, :, i) = img_pores;

% Calculate the pore area and total area
pore_area_2d = sum(img_pores(:));
total_area_2d = sum(img_filled(:));

% Add 2D pore/filled areas to totals
all_pore_area = all_pore_area + pore_area_2d;
all_filled_area = all_filled_area + total_area_2d;

% Compute the density and add it to the data array
density_data_2d(i) = (total_area_2d-pore_area_2d)/total_area_2d;

% Add in per-layer info into data table
sample_data{(9+i),1} = i; % layer
sample_data{(9+i),2} = (i*voxelSize/1000); % height
sample_data{(9+i),3} = density_data_2d(i); % density
sample_data{(9+i),4} = (1-density_data_2d(i)); % porosity
sample_data{(9+i),5} = temp_data{6,index}*voxelSize/1000; % minor axis length
sample_data{(9+i),6} = temp_data{5,index}*voxelSize/1000; % major axis length
sample_data{(9+i),7} = ((temp_data{6,index}+temp_data{5,index})/2)*voxelSize/1000; % effective
measured diameter
sample_data{(9+i),8} = temp_data{1,index}*voxelSize/1000*voxelSize/1000; % area
sample_data{(9+i),9} = temp_data{17,index}*voxelSize/1000; % equivalent diameter
centroid_temp = temp_data{2,index};
sample_data{(9+i),10} = centroid_temp(1)*voxelSize/1000; % centroid X
sample_data{(9+i),11} = centroid_temp(2)*voxelSize/1000; % centroid Y
sample_data{(9+i),12} = total_area_2d*voxelSize/1000*voxelSize/1000; % filled area

% Add in bulk info
sample_data{5,2} = sample_data{5,2} + sample_data{(9+i),7}; % average effective measured diameter
sample_data{6,2} = sample_data{6,2} + sample_data{(9+i),8}; % average true area
sample_data{7,2} = sample_data{7,2} + sample_data{(9+i),9}; % average equivalent diameter
sample_data{8,2} = sample_data{8,2} + sample_data{(9+i),12}; % average filled area

clear centroid_temp temp_data img_temp img_filled img_pores pore_area_2d total_area_2d max_rad

end

%% Section 4: Calculate bulk data and make an excel file
% Calculate Bulk Density
bulk_density = (all_filled_area - all_pore_area)/all_filled_area;
bulk_porosity = all_pore_area/all_filled_area;

% Add in bulk information to sample data table
sample_data{3,2} = bulk_density; % bulk density

```

```

sample_data{4,2} = bulk_porosity; % bulk porosity
sample_data{5,2} = sample_data{5,2}/Nframes; % average effective measured diameter
sample_data{6,2} = sample_data{6,2}/Nframes; % average true area
sample_data{7,2} = sample_data{7,2}/Nframes; % average equivalent diameter
sample_data{8,2} = sample_data{8,2}/Nframes; % average filled area

% save as excel file
save_name = strcat(outPath,saveNameBase,"_sampleData.xls");
xlswrite(save_name,sample_data);

%% Section 5: Generate Plots and Renders
% Generate a plot of density as a function of height
% Create a linear array for all layers
sampleHeight = linspace(1,Nframes,Nframes);
% Convert layers to size (mm)
sampleHeight = sampleHeight.*voxelSize./1000;
sampleHeight = sampleHeight';
figure
plot(sampleHeight, density_data_2d);
BD_text_Loc = [max(xlim) min(ylim)]+[-diff(xlim) diff(ylim)]*0.05;
xlabel('Sample Height (mm)');
ylabel('Relative Density');
title('Density Versus Sample Height');
% Determine max and min y limits
ymin = min(density_data_2d)-0.005;
ymax = max(density_data_2d)+0.005;
ylim([ymin ymax]);
% Add bulk density note
text(BD_text_Loc(1), BD_text_Loc(2), strcat("Bulk Density = ",num2str(bulk_density)),
'VerticalAlignment','top', 'HorizontalAlignment','right')
% Resize and save
set(gcf,'units','normalized','outerposition',[0 0 1 1]);
set(gcf, 'PaperPositionMode', 'auto');
saveas(gcf, strcat(outPath,saveNameBase,"_DensityAndHeight.fig"));
saveas(gcf, strcat(outPath,saveNameBase,"_DensityAndHeight.png"));
close all

%% Section 6: Cleanup and end function
% Save out tif stacks used during processing

% These are the default options in the code if not specified here
options.overwrite = true;
options.big = true;

% Save out BW thresholded images
stackBW = im2uint8(stackBW);
save_name = strcat(outPath,saveNameBase,"_stackBW.tif");

```

```

save_name = char(save_name);
saveastiff(stackBW,save_name,options);

% Save out pore images
stackPores = im2uint8(stackPores);
save_name = strcat(outPath,saveNameBase,"_stackPores.tif");
save_name = char(save_name);
saveastiff(stackPores,save_name,options);

% Save out filled images
stackFilled = im2uint8(stackFilled);
save_name = strcat(outPath,saveNameBase,"_stackFilled.tif");
save_name = char(save_name);
saveastiff(stackFilled,save_name,options);

% Clear the image stacks to reduce the workspace size
clear stackBW stackOpen stackFilled stackPores all_filled_area all_pore_area ans BD_text_Loc
folder_Check
clear j i msg msgID names options overwrite pore_area_2D status ymax ymin

% Save the workspace data
save_name = strcat(outPath,saveNameBase,"_workspaceData");
save(save_name, '-v7.3');

% Clear/close all remaining items
close all
clear all

end

function [stack8] = imagescaling(stack,in)

% This function is written to scale a 16 bit image to 8 bit range given a minimum and maximum scaling
value.

% Verify that input image is not already scaled to 8 bit range.
stackstats = whos('stack');
if strcmp(stackstats.class,'uint8')
    fprintf('WARNING: Input image stack already scaled to 8 bit range.\n');
end

% Make sure input stack is in correct data type
maxval = max(max(max(stack)));
if maxval <= 255
    stack = uint8(stack);
    in.greymmin = uint8(in.greymmin);
    in.greymax = uint8(in.greymax);
elseif maxval <= 65535

```

```

    stack = uint16(stack);
    in.greymmin = uint16(in.greymmin);
    in.greymax = uint16(in.greymax);
else
    stack = uint32(stack);
    in.greymmin = uint32(in.greymmin);
    in.greymax = uint32(in.greymax);
end

% set all values below and above the minval and maxval to minval and maxval
stack(stack<in.greymmin) = in.greymmin;
stack(stack>in.greymax) = in.greymax;

% subtract by the minval to align image data with 0
stack = stack-in.greymmin;
stackstats = whos('stack');

if strcmp(stackstats.class,'uint16') || strcmp(stackstats.class,'int16')
    % stretch the data to fill the full range.
    scale = single(65535)/single(in.greymax-in.greymmin);
    stack = uint16(single(stack)*scale);

    % convert the image to 8 bit scaling
    stack8 = uint8(stack/256);

elseif strcmp(stackstats.class,'uint8') || strcmp(stackstats.class,'int8')
    scale = single(256)/single(in.greymax-in.greymmin);
    stack8 = uint8(single(stack)*scale);

elseif strcmp(stackstats.class,'uint32') || strcmp(stackstats.class,'int32')
    scale = single(4294967296)/single(in.greymax-in.greymmin);
    stack8 = uint8(single(stack)*scale);
end

function res = saveastiff(data, path, options)
% options.color
% : true or FALSE
% : If this is true, third dimension should be 3 and the data is saved as a color image.
% options.compress
% : 'no', 'lzw', 'jpeg' or 'adobe'.
%   Compression type.
%   'no' : Uncompressed(Default)
%   'lzw' : lossless LZW
%   'jpeg' : lossy JPEG (When using JPEG compression, ImageWidth,
%   ImageLength, and RowsPerStrip must be multiples of 16.)
%   'adobe' : lossless Adobe-style
% options.message
% : true or FALSE.

```

```

% If this is false, all messages are skipped.
% options.append
% : true or FALSE
% If path is exist, the data is appended to an existing file.
% If path is not exist, this options is ignored.
% options.overwrite
% : true or FALSE
% Overwrite to an existing file.
% options.big
% : true or FALSE,
% Use 64 bit addressing and allows for files > 4GB
%
% Defalut value of 'options' is
% options.color = false;
% options.compress = 'no';
% options.message = false;
% options.append = false;
% options.overwrite = false;
% options.big = false;
%
% res : Return value. It is 0 when the function is finished with no error.
% If an error is occured in the function, it will have a positive
% number (error code).
%
% Copyright (c) 2012, YoonOh Tak
% All rights reserved.
% Redistribution and use in source and binary forms, with or without
% modification, are permitted provided that the following conditions are
% met:
%
% * Redistributions of source code must retain the above copyright notice, this list of conditions and the
following disclaimer.
% * Redistributions in binary form must reproduce the above copyright notice, this list of conditions and
the following disclaimer in the documentation and/or other materials provided with the distribution
% * Neither the name of the Gwangju Institute of Science and Technology (GIST), Republic of Korea nor
the names of its contributors may be used to endorse or promote products derived from this software without
specific prior written permission.
% THIS SOFTWARE IS PROVIDED BY THE COPYRIGHT HOLDERS AND CONTRIBUTORS "AS
IS" AND ANY EXPRESS OR IMPLIED WARRANTIES, INCLUDING, BUT NOT LIMITED TO, THE
IMPLIED WARRANTIES OF MERCHANTABILITY AND FITNESS FOR A PARTICULAR
PURPOSE ARE DISCLAIMED. IN NO EVENT SHALL THE COPYRIGHT OWNER OR
CONTRIBUTORS BE LIABLE FOR ANY DIRECT, INDIRECT, INCIDENTAL, SPECIAL,
EXEMPLARY, OR CONSEQUENTIAL DAMAGES (INCLUDING, BUT NOT LIMITED TO,
PROCUREMENT OF SUBSTITUTE GOODS OR SERVICES; LOSS OF USE, DATA, OR PROFITS;
OR BUSINESS INTERRUPTION) HOWEVER CAUSED AND ON ANY THEORY OF LIABILITY,
WHETHER IN CONTRACT, STRICT LIABILITY, OR TORT (INCLUDING NEGLIGENCE OR
OTHERWISE) ARISING IN ANY WAY OUT OF THE USE OF THIS SOFTWARE, EVEN IF ADVISED
OF THE POSSIBILITY OF SUCH DAMAGE.

```



```

tStart = tic;
errcode = 0;
try
%% Init options parameter
if nargin < 3 % default options
    options.color = false;
    options.compress = 'no';
    options.message = false;
    options.append = false;
    options.overwrite = false;
end
if ~isfield(options, 'message'), options.message = false; end
if ~isfield(options, 'append'), options.append = false; end
if ~isfield(options, 'compress'), options.compress = 'no'; end
if ~isfield(options, 'color'), options.color = false; end
if ~isfield(options, 'overwrite'), options.overwrite = false; end
if isfield(options, 'big') == 0, options.big = false; end

if isempty(data), errcode = 1; assert(false); end
if (options.color == false && ndims(data) > 3) || ...
    (options.color == true && ndims(data) > 4)
    % Maximum dimension of a grayscale image is 3 of [height, width, frame]
    % Maximum dimension of a color image is 4 of [height, width, color, frame]
    errcode = 2; assert(false);
end

%% Get image informations
% http://www.awaresystems.be/imaging/tiff/tifftags/photometricinterpretation.html
if ~options.color
    if ndims(data) >= 4, errcode = 2; assert(false); end;
    [height, width, depth] = size(data);
    tagstruct.Photometric = Tiff.Photometric.MinIsBlack;
else
    if ndims(data) >= 5, errcode = 2; assert(false); end;
    [height, width, rgb, depth] = size(data);
    if rgb ~= 3 && rgb ~= 4, errcode = 3; assert(false); end;
    tagstruct.Photometric = Tiff.Photometric.RGB;
end
tagstruct.ImageLength = height;
tagstruct.ImageWidth = width;
tagstruct.RowsPerStrip = height; % http://www.awaresystems.be/imaging/tiff/tifftags/rowsperstrip.html
tagstruct.PlanarConfiguration = Tiff.PlanarConfiguration.Chunky; %
http://www.awaresystems.be/imaging/tiff/tifftags/planarconfiguration.html

%% Complex number
% http://www.awaresystems.be/imaging/tiff/tifftags/samplesperpixel.html

```

```

if ~options.color && isreal(data) % Grayscale image with real numbers
    tagstruct.SamplesPerPixel = 1;
    data = reshape(data, height, width, 1, depth);
elseif ~options.color && ~isreal(data) % Grayscale image with complex numbers
    tagstruct.SamplesPerPixel = 2;
    data = reshape([real(data) imag(data)], height, width, 2, depth);
elseif options.color && isreal(data) % Color image with real numbers
    tagstruct.SamplesPerPixel = rgb;
    if rgb == 4
        tagstruct.ExtraSamples = Tiff.ExtraSamples.AssociatedAlpha; % The forth channel is alpha channel
    end
    data = reshape(data, height, width, rgb, depth);
elseif options.color && ~isreal(data) % Color image with complex numbers
    tagstruct.SamplesPerPixel = rgb * 2;
    if rgb == 3
        tagstruct.ExtraSamples = repmat(Tiff.ExtraSamples.Unspecified, 1, 3);
    else
        tagstruct.ExtraSamples = repmat(Tiff.ExtraSamples.Unspecified, 1, 5);
    end
    data = reshape([real(data) imag(data)], height, width, rgb*2, depth);
end

%% Image compression
% http://www.awaresystems.be/imaging/tiff/tifftags/compression.html
switch lower(options.compress)
    case 'no'
        tagstruct.Compression = Tiff.Compression.None;
    case 'lzw'
        tagstruct.Compression = Tiff.Compression.LZW;
    case 'jpeg'
        tagstruct.Compression = Tiff.Compression.JPEG;
    case 'adobe'
        tagstruct.Compression = Tiff.Compression.AdobeDeflate;
    otherwise
        % Use tag nubmer in http://www.awaresystems.be/imaging/tiff/tifftags/compression.html
        tagstruct.Compression = options.compress;
end

%% Sample format
% http://www.awaresystems.be/imaging/tiff/tifftags/sampleformat.html
switch class(data)
    case {'uint8', 'uint16', 'uint32'}
        tagstruct.SampleFormat = Tiff.SampleFormat.UInt;
    case {'int8', 'int16', 'int32'}
        tagstruct.SampleFormat = Tiff.SampleFormat.Int;
        if options.color
            errcode = 4; assert(false);
        end
end

```

```

case {'single', 'double', 'uint64', 'int64'}
    tagstruct.SampleFormat = Tiff.SampleFormat.IEEEF;
otherwise
    % Void, ComplexInt, ComplexIEEFP
    errcode = 5; assert(false);
end

%% Bits per sample
% http://www.awaresystems.be/imaging/tiff/tifftags/bitspersample.html
switch class(data)
    case {'uint8', 'int8'}
        tagstruct.BitsPerSample = 8;
    case {'uint16', 'int16'}
        tagstruct.BitsPerSample = 16;
    case {'uint32', 'int32'}
        tagstruct.BitsPerSample = 32;
    case {'single'}
        tagstruct.BitsPerSample = 32;
    case {'double', 'uint64', 'int64'}
        tagstruct.BitsPerSample = 64;
    otherwise
        errcode = 5; assert(false);
end

%% Overwrite check
if exist(path, 'file') && ~options.append
    if ~options.overwrite
        errcode = 6; assert(false);
    end
end

%% Save path configuration
path_parent = pwd;
[pathstr, fname, fext] = fileparts(path);
if ~isempty(pathstr)
    if ~exist(pathstr, 'dir')
        mkdir(pathstr);
    end
    cd(pathstr);
end

%% Write image data to a file
if ~options.append % Make a new file
    s=whos('data');
    if s.bytes > 2^32-1 || options.big
        tfile = Tiff([fname, fext], 'w8'); % Big Tiff file
    else
        tfile = Tiff([fname, fext], 'w');
    end
end

```

```

end
for d = 1:depth
    tfile.setTag(tagstruct);
    tfile.write(data(:, :, :, d));
    if d ~= depth
        tfile.writeDirectory();
    end
end
end
else
    if ~exist([fname, fext], 'file') % Make a new file
        s=whos('data');
        if s.bytes > 2^32-1 || options.big
            tfile = Tiff([fname, fext], 'w8'); % Big Tiff file
        else
            tfile = Tiff([fname, fext], 'w');
        end
    else % Append to an existing file
        tfile = Tiff([fname, fext], 'r+');
        while ~tfile.lastDirectory(); % Append a new image to the last directory of an exiting file
            tfile.nextDirectory();
        end
        tfile.writeDirectory();
    end
end

for d = 1:depth
    tfile.setTag(tagstruct);
    tfile.write(data(:, :, :, d));
    if d ~= depth
        tfile.writeDirectory();
    end
end
end
tfile.close();
if exist('path_parent', 'var'), cd(path_parent); end

tElapsed = toc(tStart);
if options.message
    display(sprintf('File saved successfully. Elapsed time : %.3f s.', tElapsed));
end

%% Exception management
catch exception
    if exist('tfile', 'var'), tfile.close(); end
    switch errcode
        case 1
            if options.message, error '"data" is empty.'; end;
        case 2
            if options.message, error 'Data dimension is too large.'; end;
    end
end

```

```

case 3
    if options.message, error 'Third dimesion (color depth) should be 3 or 4.'; end;
case 4
    if options.message, error 'Color image cannot have int8, int16 or int32 format.'; end;
case 5
    if options.message, error 'Unsupported data type.'; end;
case 6
    if options.message, error 'File already exists.'; end;
otherwise
    if exist('fname', 'var') && exist('fext', 'var')
        delete([fname fext]);
    end
    if exist('path_parent', 'var'), cd(path_parent); end
    rethrow(exception);
end
    if exist('path_parent', 'var'), cd(path_parent); end
end
res = errcode;
end

```

## Appendix B. Chapter 5 Formatting code

```
function CT_Tensile_Analysis_Formatting_2()

% Code is intended to open up and create a table containing all of the data in the selected excel sheets
% Code is intended to process the data outputted from the PoreAnalytics_X
% code

% V2 code also includes mechanical property values.

%% Section 0 - Initialization

sampleKeySet = {'e8m-2','e8-3','e8m-3','e8m-4','e8m-5','FlatSmall','FlatLarge'};
sampleValueSet = {"Round","Round","Round","Round","Round","Flat","Flat"};
sampleShapeMap = containers.Map(sampleKeySet,sampleValueSet);

typeKeySet = {'e8m-2','e8-3','e8m-3','e8m-4','e8m-5','FlatSmall','FlatLarge'};
typeValueSet = {"E8M-2","E8-3","E8M-3","E8M-4","E8M-5","Flat (Small)","Flat (Large)"};
typeShapeMap = containers.Map(typeKeySet,typeValueSet);

voxelKeySet = {'e8m-2','e8-3','e8m-3','e8m-4','e8m-5','FlatSmall','FlatLarge'};
voxelValueSet = {9.5,6.5,6.5,5.0,3.0,6.5,13.0};
sampleVoxelMap = containers.Map(voxelKeySet,voxelValueSet);

% Surface area to volume ratio
savKeySet = {'e8m-2','e8-3','e8m-3','e8m-4','e8m-5','FlatSmall','FlatLarge'};
savValueSet = {0.4444,0.6667,0.6667,1.0000,1.6000,1.0000,0.8267};
sampleSavMap = containers.Map(savKeySet,savValueSet);

% add in specimen nominal diameter / length X width
sizeKeySet = {'e8m-2','e8-3','e8m-3','e8m-4','e8m-5','FlatSmall','FlatLarge'};
sizeValueSet =
{[9.0,NaN,NaN],[6.0,NaN,NaN],[6.0,NaN,NaN],[4.0,NaN,NaN],[2.5,NaN,NaN],[NaN,12.5,3.0],[NaN,6.0,3.0]};
sampleSizeMap = containers.Map(sizeKeySet,sizeValueSet);

% add in vertical vs horizontal
orientKeySet = {'C','T','Q','E','J','R','A','M','U','H','O','F'...
,'G','N','T','K','P','S','B','D','L'...
'4','10','11','1B','2B','3B','1','5','6','13','14','15'...
,'7','8','9','17','20','22','28','27','29'};
orientValueSet = {"Horizontal","Horizontal","Horizontal","Horizontal","Horizontal"...
,"Horizontal","Horizontal","Horizontal","Horizontal","Horizontal","Horizontal"...
,"Horizontal","Horizontal","Horizontal","Horizontal","Horizontal","Horizontal"...
,"Horizontal","Horizontal","Horizontal"...
"Vertical","Vertical","Vertical","Vertical","Vertical","Vertical","Vertical"...
,"Vertical","Vertical","Vertical","Vertical","Vertical"...
,"Vertical","Vertical","Vertical","Vertical","Vertical","Vertical"...
```

```

    , "Vertical", "Vertical", "Vertical" };
sampleOrientMap = containers.Map(orientKeySet, orientValueSet);

% Add in Modulus Values
ModKeySet = {'C','T','Q','E','J','R','A','M','U','H','O','F'...
    , 'G','N','I','K','P','S','B','D','L'...
    , '4','10','11','1B','2B','3B','1','5','6','13','14','15'...
    , '7','8','9','17','20','22','28','27','29'};
ModValueSet = {"114.49", "113.22", "111.67", "110.71", "114.52" ...
    , "112.75", "119.01", "107.22", "116.01", "114.38", "112.25", "110.38" ...
    , "109.06", "116.99", "112.65", "108.16", "116.89", "114.81" ...
    , "111.61", "111.63", "100.00" ...
    , "112.50", "126.06", "117.62", "117.41", "119.80", "114.64", "117.00" ...
    , "119.57", "126.34", "115.54", "113.96", "107.60" ...
    , "104.35", "113.89", "114.46", "113.19", "114.02", "111.12" ...
    , "108.91", "108.55", "112.33"};
ModMap = containers.Map(ModKeySet, ModValueSet);

% Add in Yield Strength Values
YieldKeySet = {'C','T','Q','E','J','R','A','M','U','H','O','F'...
    , 'G','N','I','K','P','S','B','D','L'...
    , '4','10','11','1B','2B','3B','1','5','6','13','14','15'...
    , '7','8','9','17','20','22','28','27','29'};
YieldValueSet = {"908.84", "907.98", "913.22", "931.76", "933.66" ...
    , "919.22", "950.26", "945.92", "950.26", "909.27", "934.26", "934.87" ...
    , "935.37", "926.22", "944.22", "912.79", "923.08", "928.63" ...
    , "924.97", "921.32", "910.00" ...
    , "858.98", "873.47", "875.66", "878.34", "893.89", "870.40", "907.66" ...
    , "892.57", "903.11", "899.71", "879.24", "914.31" ...
    , "951.83", "872.35", "906.27", "867.59", "883.02", "893.70" ...
    , "854.63", "882.69", "885.06"};
YieldMap = containers.Map(YieldKeySet, YieldValueSet);

% Add in Tensile Strength Values
TenKeySet = {'C','T','Q','E','J','R','A','M','U','H','O','F'...
    , 'G','N','I','K','P','S','B','D','L'...
    , '4','10','11','1B','2B','3B','1','5','6','13','14','15'...
    , '7','8','9','17','20','22','28','27','29'};
TenValueSet = {"972.26", "993.06", "999.19", "999.82", "1004.94" ...
    , "989.41", "1035.73", "1021.16", "1036.20", "1005.96", "1008.08", "1021.93" ...
    , "1019.80", "1018.37", "1025.46", "1012.95", "1015.91", "1018.29" ...
    , "1020.83", "1006.30", "999.80" ...
    , "941.56", "964.63", "961.41", "962.31", "974.02", "951.40", "982.52" ...
    , "971.18", "983.88", "973.43", "949.82", "985.20" ...
    , "983.24", "959.51", "982.42", "956.26", "957.81", "976.01" ...
    , "937.93", "961.49", "963.66"};
TenMap = containers.Map(TenKeySet, TenValueSet);

```

```

% Add in Elongation Values
EloKeySet = {'C','T','Q','E','J','R','A','M','U','H','O','F'...
            'G','N','I','K','P','S','B','D','L'...
            '4','10','11','1B','2B','3B','1','5','6','13','14','15'...
            '7','8','9','17','20','22','28','27','29'};
EloValueSet = {"2.41","8.69","7.75","2.42","2.51"...
              "2.51","7.46","9.60","11.14","5.88","3.78","6.00"...
              "8.62","4.55","11.26","6.24","6.98","11.38"...
              "12.36","11.15","6.77"...
              "14.21","12.51","13.03","10.60","9.80","9.78","8.59"...
              "13.61","11.64","9.97","11.48","11.47"...
              "6.16","16.78","10.98","12.55","9.53","10.37"...
              "12.62","12.52","11.51"};
EloMap = containers.Map(EloKeySet,EloValueSet);

%% Section 1: File IO setup

% Get file names/locations of xls files
[inFiles,inPath] = uigetfile('*.*xls','MultiSelect','on');

% Create the outputpath and corresponding folder - creates an output folder
% where the data was taken from
% Ask the user to generate a folder name to output all of the files
out_folder_name = input('Provide a name for the output folder: ','s');
outPath = strcat(inPath,out_folder_name,'\');
% Make directory and add to path
[status, msg, msgID] = mkdir(char(outPath));
addpath(char(outPath));

% Check if folder already existed and if it's okay to overwrite
folder_Check = 0;
while folder_Check == 0;
    if isempty(msg) % Empty return means that there was no folder
        folder_Check = 1;
    elseif msg == "Directory already exists."
        overwrite = input('Folder already exists, do you want to overwrite (y/n)?\n','s');
        if (overwrite ~= 'y') && (overwrite ~= 'n') % Did not enter y or n
            disp('You must enter y to overwrite or n to set a new output folder name\n');
        else
            if overwrite == 'y' % Overwrite in the existing folder
                folder_Check = 1;
            elseif overwrite == 'n' % Set a new output folder name
                workFolder = input('Provide a new name for the output folder: \n','s'); %Provide a new folder
name
                [status,msg,msgID] = mkdir(strcat(['outputs\'],workFolder));
            end
        end
    end
    elseif not(isempty(msg)) && not(msg == "Directory already exists.")

```



```

        workFolder = input('Error making folder - Provide a new name for the output folder: \n','s');
% Provide a new folder name
    [status,msg,msgID] = mkdir(strcat(['outputs\',workFolder]));
    else
        folder_Check = 1; % Just in case checks return something weird
    end
end

%% Section 2 - Open files

dataTable = table;

for i = 1:length(inFiles)
    % Get sample name and identifiers from .xls file
    inFullName = inFiles{i};
    inFullName = strcat(inPath,inFullName);

    inName = inFiles{i}
    inName = split(inName,'_');

    % Read in table
    inTableOpts = detectImportOptions(inFullName,'NumHeaderLines',2);
    inTable = readtable(inFullName,inTableOpts);

    % Get sample type
    sampleType = typeShapeMap(inName{1});
    inTable.Type = repmat(string(sampleType), size(inTable,1),1);

    % Get Sample ID
    sampleID = string(inName{2});
    inTable.ID = repmat(sampleID, size(inTable,1),1);

    % Make full sample name
    sampleName = strcat(string(inName{1}),"_",string(inName{2}));
    inTable.Name = repmat(sampleName, size(inTable,1),1);

    % Get round vs flat
    sampleShape = sampleShapeMap(inName{1});
    inTable.Shape = repmat(sampleShape, size(inTable,1),1);

    % Get sample size information
    sampleSize = sampleSizeMap(inName{1});
    sampleDia = sampleSize(1);
    inTable.Dia = repmat(sampleDia, size(inTable,1),1);
    sampleLength = sampleSize(2);
    inTable.Length = repmat(sampleLength, size(inTable,1),1);
    sampleWidth = sampleSize(3);
    inTable.Width = repmat(sampleWidth, size(inTable,1),1);

```

```

% Get nominal cross-section area
areaRound = pi().*inTable.Dia./4;
nanLoc = isnan(areaRound);
areaRound(nanLoc) = 0;
clear nanLoc

areaFlat = inTable.Length.*inTable.Width;
nanLoc = isnan(areaFlat);
areaFlat(nanLoc) = 0;

inTable.Area = (areaRound + areaFlat);

% Get sample orientation
sampleOrient = sampleOrientMap(inName{2});
inTable.Build_Orientation = repmat(sampleOrient, size(inTable,1),1);

% Get sample voxel size
sampleVoxel = sampleVoxelMap(inName{1});
inTable.VoxelSize = repmat(sampleVoxel, size(inTable,1),1);

% Get surface area to volume ratio
sampleSav = sampleSavMap(inName{1});
inTable.SAV = repmat(sampleSav, size(inTable,1),1);

% Get Sphericity from principal axes
inTable.SphericityAlt =
(inTable.PrincipalAxisC_um_.^2)./(inTable.PrincipalAxisA_um_.*inTable.PrincipalAxisB_um_).^^(1/3);

% Get aspect ratio
inTable.Aspect_Ratio = (inTable.PrincipalAxisC_um_)./(inTable.PrincipalAxisA_um_);

% Get Mechanical Properties
sampleMod = ModMap(inName{2});
inTable.Modulus = repmat(sampleMod, size(inTable,1),1);

sampleYield = YieldMap(inName{2});
inTable.Yield_Strength = repmat(sampleYield, size(inTable,1),1);

sampleTen = TenMap(inName{2});
inTable.Tensile_Strength = repmat(sampleTen, size(inTable,1),1);

sampleElo = EloMap(inName{2});
inTable.Elongation = repmat(sampleElo, size(inTable,1),1);

% Add data into main table
dataTable = [dataTable;inTable];
clear inFullName inName sampleName sampleShape inTableOpts inTable nanLoc

```

```

end

%% Section 4 - Classify Pores

% Pore Classification
% 501+ : A
% 301-500 : B
% 201-300 : C
% 101-200: D
% 50-100 : E
% 0-49 : F (not used for further analysis)

% aMin = 501.0;
% bMax = 500.0;
% bMin = 301.0;
% cMax = 300.0;
% cMin = 201.0;
% dMax = 200.0;
% dMin = 101.0;
% eMax = 100.0;
% eMin = 50.0;
% fMax = 49.0;

aLim = 500;
bLim = 300;
cLim = 200;
dLim = 100;
eLim = 50;

for i = 1:height(dataTable)
    psTemp = dataTable.EquivalentDiameter_um_(i);
    % Classify Pore
    if psTemp < eLim;
        dataTable.Class(i) = "F";
    elseif psTemp >= eLim & psTemp < dLim;
        dataTable.Class(i) = "E";
    elseif psTemp >= dLim & psTemp < cLim;
        dataTable.Class(i) = "D";
    elseif psTemp >= cLim & psTemp < bLim;
        dataTable.Class(i) = "C";
    elseif psTemp >= bLim & psTemp < aLim;
        dataTable.Class(i) = "B";
    elseif psTemp >= aLim;
        dataTable.Class(i) = "A";
    end
end

```

## Appendix C. Chapter 5 Plotting code

```
function CT_Tensile_Plots_V2()

%% Section 1: File IO setup and Make Folders for Outputs

% Get file names/locations
[inFiles,inPath] = uigetfile('*.mat');
inName = char(strcat(inPath,inFiles));

% Create the outpath and corresponding folder - creates an output folder
% where the data was taken from
% Ask the user to generate a folder name to output all of the files
out_folder_name = input('Provide a name for the output folder: ','s');
outPath = strcat(inPath,out_folder_name,'\');
% Make directory and add to path
[status, msg, msgID] = mkdir(char(outPath));
addpath(char(outPath)) ;

% Check if folder already existed and if it's okay to overwrite
folder_Check = 0;
while folder_Check == 0;
    if isempty(msg) % Empty return means that there was no folder
        folder_Check = 1;
    elseif msg == "Directory already exists."
        overwrite = input('Folder already exists, do you want to overwrite (y/n)?\n','s');
        if (overwrite ~= 'y') && (overwrite ~= 'n') % Did not enter y or n
            disp('You must enter y to overwrite or n to set a new output folder name\n');
        else
            if overwrite == 'y' % Overwrite in the existing folder
                folder_Check = 1;
            elseif overwrite == 'n' % Set a new output folder name
                workFolder = input('Provide a new name for the output folder: \n','s'); %Provide a new folder
name
                [status,msg,msgID] = mkdir(strcat(['outputs\'',workFolder]));
            end
        end
    elseif not(isempty(msg)) && not(msg == "Directory already exists.")
        workFolder = input('Error making folder - Provide a new name for the output folder: \n','s'); %Provide
a new folder name
        [status,msg,msgID] = mkdir(strcat(['outputs\'',workFolder]));
    else
        folder_Check = 1; % Just in case checks return something weird
    end
end

%% Section 2: Load in Data and Seperate into Different Tables
```

```

dataFull = load(inName);
dataTable = dataFull.dataTable;

clear dataFull

% Convert Mechanical properties from String to Double
dataTable.Modulus = cellfun(@str2num,dataTable.Modulus);
dataTable.Yield_Strength = cellfun(@str2num,dataTable.Yield_Strength);
dataTable.Tensile_Strength = cellfun(@str2num,dataTable.Tensile_Strength);
dataTable.Elongation = cellfun(@str2num,dataTable.Elongation);

% Add Nominal Radial Position
dataTable.NomRadPos = dataTable.RadialDistance_mm_./(dataTable.Dia./2);

% Exclude specimens that broke outside the gauge section and truncate <50
% um
dataMech = dataTable;
dataMech(dataMech.ID == "Q", :) = [];
dataMech(dataMech.ID == "B", :) = [];
dataMech(dataMech.ID == "R", :) = [];
dataMech(dataMech.EquivalentDiameter_um_ < 50, :) = [];

% All Horizontal and Vertical Data
dataVert = dataTable;
dataVert(dataVert.Build_Orientation == "Horizontal", :) = [];

dataHoriz = dataTable;
dataHoriz(dataHoriz.Build_Orientation == "Vertical", :) = [];

% All data - Truncated at 50 um
dataTrunc = dataTable;
dataTrunc(dataTrunc.EquivalentDiameter_um_ < 50, :) = [];

% Truncated data less than 50 um
dataTruncLT = dataTable;
dataTruncLT(dataTruncLT.EquivalentDiameter_um_ >= 50, :) = [];

% Horizontal and Vertical Data - Truncated at 50 um
dataVertT = dataTrunc;
dataVertT(dataVertT.Build_Orientation == "Horizontal", :) = [];

dataHorizT = dataTrunc;
dataHorizT(dataHorizT.Build_Orientation == "Vertical", :) = [];

% Horizontal and Vertical Mechanical Property Data
dataVertMech = dataMech;
dataVertMech(dataVertMech.Build_Orientation == "Horizontal", :) = [];

```

```

dataHorizMech = dataMech;
dataHorizMech(dataHorizMech.Build_Orientation == "Vertical", :) = [];

% Data For Round Specimens Only
dataRound = dataTrunc;
dataRound(dataRound.Shape == "Flat", :) = [];

% Round Vertical Data
dataRoundVert = dataRound;
dataRoundVert(dataRoundVert.Build_Orientation == "Horizontal", :) = [];

% Round Horizontal Data
dataRoundHoriz = dataRound;
dataRoundHoriz(dataRoundHoriz.Build_Orientation == "Vertical", :) = [];

% dataRound.NorDia = (dataRound.RadialDistance_mm_)/(dataRound.Dia).*2;

%% Section 3: Type - PSD - Box Plot
figure
subplot(2,1,1);
boxplot(dataVertT.EquivalentDiameter_um_,dataVertT.Type);
xlabel('Specimen Type');
ylabel('Pore Equivalent Diameter (\mum)');
set(gca,'fontname','times','TickDir','out','FontSize',16,'fontweight','bold','Xcolor','black','Ycolor','black');
subplot(2,1,2);
boxplot(dataHorizT.EquivalentDiameter_um_,dataHorizT.Type);
xlabel('Specimen Type');
ylabel('Pore Equivalent Diameter (\mum)');
set(gca,'fontname','times','TickDir','out','FontSize',16,'fontweight','bold','Xcolor','black','Ycolor','black');

set(gcf,'units','normalized','outerposition',[0 0 1 1]);
set(gcf, 'PaperPositionMode', 'auto');
saveas(gcf,strcat(outPath,out_folder_name,"_1_Type-PSD-Box.fig"));
saveas(gcf,strcat(outPath,out_folder_name,"_1_Type-PSD-Box.tif"));
close all

%% Section 4: Type - PSD - Box Plot - Limited Range
figure
subplot(2,1,1);
boxplot(dataVertT.EquivalentDiameter_um_,dataVertT.Type);
ylim([45 200]);
xlabel('Specimen Type');
ylabel('Pore Equivalent Diameter (\mum)');
set(gca,'fontname','times','TickDir','out','FontSize',16,'fontweight','bold','Xcolor','black','Ycolor','black');
subplot(2,1,2);
boxplot(dataHorizT.EquivalentDiameter_um_,dataHorizT.Type);
ylim([45 200]);
xlabel('Specimen Type');

```

```

ylabel('Pore Equivalent Diameter (\mum));
set(gca,'fontname','times','TickDir','out','FontSize',16,'fontweight','bold','Xcolor','black','Ycolor','black');

set(gcf,'units','normalized','outerposition',[0 0 1 1]);
set(gcf, 'PaperPositionMode', 'auto');
saveas(gcf, strcat(outPath, out_folder_name, "_2_Type-PSD-Box-Limited.fig"));
saveas(gcf, strcat(outPath, out_folder_name, "_2_Type-PSD-Box-Limited.tif"));
close all

%% Section 5: Area - PSD - Box Plot
figure
subplot(2,1,1);
boxplot(dataVertT.EquivalentDiameter_um_, dataVertT.Area);
xtickformat('% .3f');
xlabel('Specimen Cross-sectional Area (mm^2)');
ylabel('Pore Equivalent Diameter (\mum));
set(gca,'fontname','times','TickDir','out','FontSize',16,'fontweight','bold','Xcolor','black','Ycolor','black',...
'XTick',[1 2 3 4 5 6], 'XTickLabel',{ '1.964', '3.142', '4.712', '7.069', '18.000', '37.500'});
subplot(2,1,2);
boxplot(dataHorizT.EquivalentDiameter_um_, dataHorizT.Area);
xtickformat('% .3f');
xlabel('Specimen Cross-sectional Area (mm^2)');
ylabel('Pore Equivalent Diameter (\mum));
set(gca,'fontname','times','TickDir','out','FontSize',16,'fontweight','bold','Xcolor','black','Ycolor','black',...
'XTick',[1 2 3 4 5 6], 'XTickLabel',{ '1.964', '3.142', '4.712', '7.069', '18.000', '37.500'});

set(gcf,'units','normalized','outerposition',[0 0 1 1]);
set(gcf, 'PaperPositionMode', 'auto');
saveas(gcf, strcat(outPath, out_folder_name, "_3_Area-PSD-Box.fig"));
saveas(gcf, strcat(outPath, out_folder_name, "_3_Area-PSD-Box.tif"));
close all

%% Section 6: Area - PSD - Box Plot - Limited
figure
subplot(2,1,1);
boxplot(dataVertT.EquivalentDiameter_um_, dataVertT.Area);
xtickformat('% .3f');
ylim([45 200]);
xlabel('Specimen Cross-sectional Area (mm^2)');
ylabel('Pore Equivalent Diameter (\mum));
set(gca,'fontname','times','TickDir','out','FontSize',16,'fontweight','bold','Xcolor','black','Ycolor','black',...
'XTick',[1 2 3 4 5 6], 'XTickLabel',{ '1.964', '3.142', '4.712', '7.069', '18.000', '37.500'});
subplot(2,1,2);
boxplot(dataHorizT.EquivalentDiameter_um_, dataHorizT.Area);
xtickformat('% .3f');
ylim([45 200]);
xlabel('Specimen Cross-sectional Area (mm^2)');
ylabel('Pore Equivalent Diameter (\mum));

```

```
set(gca,'fontname','times','TickDir','out','FontSize',16,'fontweight','bold','Xcolor','black','Ycolor','black',...
    'XTick',[1 2 3 4 5 6],'XTickLabel',{ '1.964','3.142','4.712','7.069','18.000','37.500'});
```

```
set(gcf,'units','normalized','outerposition',[0 0 1 1]);
set(gcf, 'PaperPositionMode', 'auto');
saveas(gcf,strcat(outPath,out_folder_name,"_4_Area-PSD-Box-Limited.fig"));
saveas(gcf,strcat(outPath,out_folder_name,"_4_Area-PSD-Box-Limited.tif"));
close all
```

```
%% Section 7: Surface Area to Volume Ratio - PSD - Box Plot
```

```
figure
```

```
subplot(2,1,1);
```

```
boxplot(dataVertT.EquivalentDiameter_um_,dataVertT.SAV);
```

```
xtickformat('%.3f');
```

```
xlabel('Specimen Surface Area to Volume Ratio (/mm)');
```

```
ylabel('Pore Equivalent Diameter (\mum)');
```

```
set(gca,'fontname','times','TickDir','out','FontSize',16,'fontweight','bold','Xcolor','black','Ycolor','black',...
    'XTick',[1 2 3 4 5],'XTickLabel',{ '0.4444','0.6667','0.8267','1.0000','1.6000'})
```

```
subplot(2,1,2);
```

```
boxplot(dataHorizT.EquivalentDiameter_um_,dataHorizT.SAV);
```

```
xtickformat('%.3f');
```

```
xlabel('Specimen Surface Area to Volume Ratio (/mm)');
```

```
ylabel('Pore Equivalent Diameter (\mum)');
```

```
set(gca,'fontname','times','TickDir','out','FontSize',16,'fontweight','bold','Xcolor','black','Ycolor','black',...
    'XTick',[1 2 3 4 5],'XTickLabel',{ '0.4444','0.6667','0.8267','1.0000','1.6000'});
```

```
set(gcf,'units','normalized','outerposition',[0 0 1 1]);
```

```
set(gcf, 'PaperPositionMode', 'auto');
```

```
saveas(gcf,strcat(outPath,out_folder_name,"_5_SAV-PSD-Box.fig"));
```

```
saveas(gcf,strcat(outPath,out_folder_name,"_5_SAV-PSD-Box.tif"));
```

```
close all
```

```
%% Section 8: Surface Area to Volume Ratio - PSD - Box Plot - Limited
```

```
figure
```

```
subplot(2,1,1);
```

```
boxplot(dataVertT.EquivalentDiameter_um_,dataVertT.SAV);
```

```
xtickformat('%.3f');
```

```
ylim([45 200]);
```

```
xlabel('Specimen Surface Area to Volume Ratio (/mm)');
```

```
ylabel('Pore Equivalent Diameter (\mum)');
```

```
set(gca,'fontname','times','TickDir','out','FontSize',16,'fontweight','bold','Xcolor','black','Ycolor','black',...
    'XTick',[1 2 3 4 5],'XTickLabel',{ '0.4444','0.6667','0.8267','1.0000','1.6000'})
```

```
subplot(2,1,2);
```

```
boxplot(dataHorizT.EquivalentDiameter_um_,dataHorizT.SAV);
```

```
xtickformat('%.3f');
```

```
ylim([45 200]);
```

```
xlabel('Specimen Surface Area to Volume Ratio (/mm)');
```

```
ylabel('Pore Equivalent Diameter (\mum)');
```



```
set(gca,'fontname','times','TickDir','out','FontSize',16,'fontweight','bold','Xcolor','black','Ycolor','black',...
    'XTick',[1 2 3 4 5],'XTickLabel',{'0.4444','0.6667','0.8267','1.0000','1.6000'})
```

```
set(gcf,'units','normalized','outerposition',[0 0 1 1]);
set(gcf, 'PaperPositionMode', 'auto');
saveas(gcf,strcat(outPath,out_folder_name,"_6_SAV-PSD-Box-Limited.fig"));
saveas(gcf,strcat(outPath,out_folder_name,"_6_SAV-PSD-Box-Limited.tif"));
close all
```

```
%% Section 9: Modulus - PSD - Scatter
```

```
g = {dataMech.Type,dataMech.Build_Orientation};
figure
h = gscatter(dataMech.Modulus,dataMech.EquivalentDiameter_um_,g);
legend('Location','northwest');
xlabel('Specimen Elastic Modulus (GPa)');
ylabel('Pore Equivalent Diameter (\mum)');
set(gca,'fontname','times','TickDir','out','FontSize',16,'fontweight','bold','Xcolor','black','Ycolor','black');
numGroups = max(size(h));
for i = 1:numGroups
    jgroup=h(i);
    jgroup.MarkerSize = 20;
end
```

```
set(gcf,'units','normalized','outerposition',[0 0 1 1]);
set(gcf, 'PaperPositionMode', 'auto');
```

```
saveas(gcf,strcat(outPath,out_folder_name,"_7_MOD-PSD-Scatter.fig"));
saveas(gcf,strcat(outPath,out_folder_name,"_7_MOD-PSD-Scatter.tif"));
close all
```

```
%% Section 10: YS - PSD - Scatter
```

```
g = {dataMech.Type,dataMech.Build_Orientation};
figure
h = gscatter(dataMech.Yield_Strength,dataMech.EquivalentDiameter_um_,g);
legend('Location','northwest');
xlabel('Specimen Yield Strength (MPa)');
ylabel('Pore Equivalent Diameter (\mum)');
set(gca,'fontname','times','TickDir','out','FontSize',16,'fontweight','bold','Xcolor','black','Ycolor','black');
numGroups = max(size(h));
for i = 1:numGroups
    jgroup=h(i);
    jgroup.MarkerSize = 20;
end
```

```
set(gcf,'units','normalized','outerposition',[0 0 1 1]);
set(gcf, 'PaperPositionMode', 'auto');
```

```
saveas(gcf,strcat(outPath,out_folder_name,"_8_YS-PSD-Scatter.fig"));
```

```

saveas(gcf,strcat(outPath,out_folder_name,"_8_YS-PSD-Scatter.tif"));
close all

%% Section 11: TS - PSD - Scatter
g = {dataMech.Type,dataMech.Build_Orientation};
figure
h = gscatter(dataMech.Tensile_Strength,dataMech.EquivalentDiameter_um_,g);
legend('Location','northeast');
xlabel('Specimen Tensile Strength (MPa)');
ylabel('Pore Equivalent Diameter (\mum)');
set(gca,'fontname','times','TickDir','out','FontSize',16,'fontweight','bold','Xcolor','black','Ycolor','black');
numGroups = max(size(h));
for i = 1:numGroups
    jgroup=h(i);
    jgroup.MarkerSize = 20;
end

set(gcf,'units','normalized','outerposition',[0 0 1 1]);
set(gcf, 'PaperPositionMode', 'auto');

saveas(gcf,strcat(outPath,out_folder_name,"_9_TS-PSD-Scatter.fig"));
saveas(gcf,strcat(outPath,out_folder_name,"_9_TS-PSD-Scatter.tif"));
close all

%% Section 12: Elong - PSD - Scatter
g = {dataMech.Type,dataMech.Build_Orientation};
figure
h = gscatter(dataMech.Elongation,dataMech.EquivalentDiameter_um_,g);
legend('Location','northeast');
xlabel('Specimen Elongation (% )');
ylabel('Pore Equivalent Diameter (\mum)');
set(gca,'fontname','times','TickDir','out','FontSize',16,'fontweight','bold','Xcolor','black','Ycolor','black');
numGroups = max(size(h));
for i = 1:numGroups
    jgroup=h(i);
    jgroup.MarkerSize = 20;
end

set(gcf,'units','normalized','outerposition',[0 0 1 1]);
set(gcf, 'PaperPositionMode', 'auto');

saveas(gcf,strcat(outPath,out_folder_name,"_10_Elong-PSD-Scatter.fig"));
saveas(gcf,strcat(outPath,out_folder_name,"_10_Elong-PSD-Scatter.tif"));
close all

%% Section 13: Vertical - Modulus - PSD - Scatter
g = {dataVertMech.Type,dataVertMech.Build_Orientation};
figure

```

```

h = gscatter(dataVertMech.Modulus,dataVertMech.EquivalentDiameter_um_,g);
legend('Location','northwest');
xlabel('Specimen Elastic Modulus (GPa)');
ylabel('Pore Equivalent Diameter (\mum)');
set(gca,'fontname','times','TickDir','out','FontSize',16,'fontweight','bold','Xcolor','black','Ycolor','black');
numGroups = max(size(h));
for i = 1:numGroups
    jgroup=h(i);
    jgroup.MarkerSize = 20;
end

set(gcf,'units','normalized','outerposition',[0 0 1 1]);
set(gcf, 'PaperPositionMode', 'auto');

saveas(gcf,strcat(outPath,out_folder_name,"_11_Vert-MOD-PSD-Scatter.fig"));
saveas(gcf,strcat(outPath,out_folder_name,"_11_Vert-MOD-PSD-Scatter.tif"));
close all

%% Section 14: Vertical - YS - PSD - Scatter
g = {dataVertMech.Type,dataVertMech.Build_Orientation};
figure
h = gscatter(dataVertMech.Yield_Strength,dataVertMech.EquivalentDiameter_um_,g);
legend('Location','northwest');
xlabel('Specimen Yield Strength (MPa)');
ylabel('Pore Equivalent Diameter (\mum)');
set(gca,'fontname','times','TickDir','out','FontSize',16,'fontweight','bold','Xcolor','black','Ycolor','black');
numGroups = max(size(h));
for i = 1:numGroups
    jgroup=h(i);
    jgroup.MarkerSize = 20;
end

set(gcf,'units','normalized','outerposition',[0 0 1 1]);
set(gcf, 'PaperPositionMode', 'auto');

saveas(gcf,strcat(outPath,out_folder_name,"_12_Vert-YS-PSD-Scatter.fig"));
saveas(gcf,strcat(outPath,out_folder_name,"_12_Vert-YS-PSD-Scatter.tif"));
close all

%% Section 15: Vertical - TS - PSD - Scatter
g = {dataVertMech.Type,dataVertMech.Build_Orientation};
figure
h = gscatter(dataVertMech.Tensile_Strength,dataVertMech.EquivalentDiameter_um_,g);
legend('Location','northwest');
xlabel('Specimen Tensile Strength (MPa)');
ylabel('Pore Equivalent Diameter (\mum)');
set(gca,'fontname','times','TickDir','out','FontSize',16,'fontweight','bold','Xcolor','black','Ycolor','black');
numGroups = max(size(h));

```

```

for i = 1:numGroups
    jgroup=h(i);
    jgroup.MarkerSize = 20;
end

set(gcf,'units','normalized','outerposition',[0 0 1 1]);
set(gcf, 'PaperPositionMode', 'auto');

saveas(gcf,strcat(outPath,out_folder_name,"_13_Vert-TS-PSD-Scatter.fig"));
saveas(gcf,strcat(outPath,out_folder_name,"_13_Vert-TS-PSD-Scatter.tif"));
close all

%% Section 16: Vertical - Elongation - PSD - Scatter
g = { dataVertMech.Type,dataVertMech.Build_Orientation };
figure
h = gscatter(dataVertMech.Elongation,dataVertMech.EquivalentDiameter_um_,g);
legend('Location','northeast');
xlabel('Specimen Elongation (%)');
ylabel('Pore Equivalent Diameter (\mum)');
set(gca,'fontname','times','TickDir','out','FontSize',16,'fontweight','bold','Xcolor','black','Ycolor','black');
numGroups = max(size(h));
for i = 1:numGroups
    jgroup=h(i);
    jgroup.MarkerSize = 20;
end

set(gcf,'units','normalized','outerposition',[0 0 1 1]);
set(gcf, 'PaperPositionMode', 'auto');

saveas(gcf,strcat(outPath,out_folder_name,"_14_Vert-Elong-PSD-Scatter.fig"));
saveas(gcf,strcat(outPath,out_folder_name,"_14_Vert-Elong-PSD-Scatter.tif"));
close all

%% Section 17: Horizontal - Modulus - PSD - Scatter
g = { dataHorizMech.Type,dataHorizMech.Build_Orientation };
figure
h = gscatter(dataHorizMech.Modulus,dataHorizMech.EquivalentDiameter_um_,g);
legend('Location','northwest');
xlabel('Specimen Elastic Modulus (GPa)');
ylabel('Pore Equivalent Diameter (\mum)');
set(gca,'fontname','times','TickDir','out','FontSize',16,'fontweight','bold','Xcolor','black','Ycolor','black');
numGroups = max(size(h));
for i = 1:numGroups
    jgroup=h(i);
    jgroup.MarkerSize = 20;
end

set(gcf,'units','normalized','outerposition',[0 0 1 1]);

```

```

set(gcf, 'PaperPositionMode', 'auto');

saveas(gcf, strcat(outPath, out_folder_name, "_15_Horiz-MOD-PSD-Scatter.fig"));
saveas(gcf, strcat(outPath, out_folder_name, "_15_Horiz-MOD-PSD-Scatter.tif"));
close all

%% Section 18: Horizontal - YS - PSD - Scatter
g = {dataHorizMech.Type, dataHorizMech.Build_Orientation};
figure
h = gscatter(dataHorizMech.Yield_Strength, dataHorizMech.EquivalentDiameter_um_, g);
legend('Location', 'northeast');
xlabel('Specimen Yield Strength (MPa)');
ylabel('Pore Equivalent Diameter (\mum)');
set(gca, 'fontname', 'times', 'TickDir', 'out', 'FontSize', 16, 'fontweight', 'bold', 'Xcolor', 'black', 'Ycolor', 'black');
numGroups = max(size(h));
for i = 1:numGroups
    jgroup=h(i);
    jgroup.MarkerSize = 20;
end

set(gcf, 'units', 'normalized', 'outerposition', [0 0 1 1]);
set(gcf, 'PaperPositionMode', 'auto');

saveas(gcf, strcat(outPath, out_folder_name, "_16_Horiz-YS-PSD-Scatter.fig"));
saveas(gcf, strcat(outPath, out_folder_name, "_16_Horiz-YS-PSD-Scatter.tif"));
close all

%% Section 19: Horizontal - TS - PSD - Scatter
g = {dataHorizMech.Type, dataHorizMech.Build_Orientation};
figure
h = gscatter(dataHorizMech.Tensile_Strength, dataHorizMech.EquivalentDiameter_um_, g);
legend('Location', 'northeast');
xlabel('Specimen Tensile Strength (MPa)');
ylabel('Pore Equivalent Diameter (\mum)');
set(gca, 'fontname', 'times', 'TickDir', 'out', 'FontSize', 16, 'fontweight', 'bold', 'Xcolor', 'black', 'Ycolor', 'black');
numGroups = max(size(h));
for i = 1:numGroups
    jgroup=h(i);
    jgroup.MarkerSize = 20;
end

set(gcf, 'units', 'normalized', 'outerposition', [0 0 1 1]);
set(gcf, 'PaperPositionMode', 'auto');

saveas(gcf, strcat(outPath, out_folder_name, "_17_Horiz-TS-PSD-Scatter.fig"));
saveas(gcf, strcat(outPath, out_folder_name, "_17_Horiz-TS-PSD-Scatter.tif"));
close all

```

```

%% Section 20: Horizontal - Elong - PSD - Scatter
g = {dataHorizMech.Type,dataHorizMech.Build_Orientation};
figure
h = gscatter(dataHorizMech.Elongation,dataHorizMech.EquivalentDiameter_um_,g);
legend('Location','northeast');
xlabel('Specimen Elongation (%)');
ylabel('Pore Equivalent Diameter (\mum)');
set(gca,'fontname','times','TickDir','out','FontSize',16,'fontweight','bold','Xcolor','black','Ycolor','black');
numGroups = max(size(h));
for i = 1:numGroups
    jgroup=h(i);
    jgroup.MarkerSize = 20;
end

set(gcf,'units','normalized','outerposition',[0 0 1 1]);
set(gcf, 'PaperPositionMode', 'auto');

saveas(gcf,strcat(outPath,out_folder_name,"_18_Horiz-Elong-PSD-Scatter.fig"));
saveas(gcf,strcat(outPath,out_folder_name,"_18_Horiz-Elong-PSD-Scatter.tif"));
close all

%% Section 21: PSD - All distrib - Histogram
figure
edges1 = [0:1:50];
poreMax = max(dataTable.EquivalentDiameter_um_);
edges2 = [50:1:poreMax];
h1 = histogram(dataTruncLT.EquivalentDiameter_um_,edges1);
hold on
h2 = histogram(dataTrunc.EquivalentDiameter_um_,edges2);
xlim([0 200]);
yMax = max(max(h1.BinCounts),max(h2.BinCounts)) + 100;
ylim([0 yMax]);
legend('Pores < 50 \mum','Pores >= 50 \mum');
xlabel('Pore Equivalent Diameter (\mum)');
ylabel('Frequency');
set(gca,'fontname','times','TickDir','out','FontSize',16,'fontweight','bold','Xcolor','black','Ycolor','black');

set(gcf,'units','normalized','outerposition',[0 0 1 1]);
set(gcf, 'PaperPositionMode', 'auto');

saveas(gcf,strcat(outPath,out_folder_name,"_19_PSD-All-Hist.fig"));
saveas(gcf,strcat(outPath,out_folder_name,"_19_PSD-All-Hist.tif"));
close all
clear edges1 edges2

%% Section 22: PSD - Vol - Histogram
figure
edges1 = [0:1:1200];

```

```

edges2 = [0:2:1200];
% Calculate total volume for each pore equivalent diameter
[N,~] = histcounts(dataTrunc.EquivalentDiameter_um_,edges1);
diaVal = edges1';
diaVal(1,:) = [];
N = N';
totalVolVert = (pi()/6).*N.*(diaVal.^3);

yyaxis right
h = histogram(dataTrunc.EquivalentDiameter_um_,edges2,'DisplayStyle','stairs');
ylabel('Frequency');
set(gca,'fontname','times','TickDir','out','FontSize',16,'fontweight','bold','Xcolor','black','Ycolor','black');
hold on
yyaxis left
bar(diaVal,totalVolVert);
ylabel('Total Pore Voume (\mum^3)');

legend('Total Volume of Pores With Same Equivalent Diameter','Frequency of Pore Equivalent Diameter');
xlabel('Pore Equivalent Diameter (\mum)');
set(gca,'fontname','times','TickDir','out','FontSize',16,'fontweight','bold','Xcolor','black','Ycolor','black');

set(gcf,'units','normalized','outerposition',[0 0 1 1]);
set(gcf,'PaperPositionMode','auto');

saveas(gcf, strcat(outPath,out_folder_name,"_20_PSD-Vol-Hist.fig"));
saveas(gcf, strcat(outPath,out_folder_name,"_20_PSD-Vol-Hist.tif"));
close all

%% Section 23: Vertical/Horizontal PSD - Vol - Histogram
figure
subplot(2,1,1);
edges1 = [0:1:1200];
edges2 = [0:2:1200];
% Calculate total volume for each pore equivalent diameter
[N,~] = histcounts(dataVertT.EquivalentDiameter_um_,edges1);
diaVal = edges1';
diaVal(1,:) = [];
N = N';
totalVolVert = (pi()/6).*N.*(diaVal.^3);

yyaxis right
h = histogram(dataVertT.EquivalentDiameter_um_,edges2,'DisplayStyle','stairs');
ylabel('Frequency');
set(gca,'fontname','times','TickDir','out','FontSize',16,'fontweight','bold','Xcolor','black','Ycolor','black');
hold on
yyaxis left
bar(diaVal,totalVolVert);
ylabel('Total Pore Voume (\mum^3)');

```

```

legend('Total Volume of Pores With Same Equivalent Diameter','Frequency of Pore Equivalent Diameter');
xlabel('Pore Equivalent Diameter (\mum)');
set(gca,'fontname','times','TickDir','out','FontSize',16,'fontweight','bold','Xcolor','black','Ycolor','black');

set(gcf,'units','normalized','outerposition',[0 0 1 1]);
set(gcf, 'PaperPositionMode', 'auto');

subplot(2,1,2);
edges1 = [0:1:1200];
edges2 = [0:2:1200];
% Calculate total volume for each pore equivalent diameter
[N,~] = histcounts(dataHorizT.EquivalentDiameter_um_,edges1);
diaVal = edges1;
diaVal(1,:) = [];
N = N';
totalVolVert = (pi()/6).*N.*(diaVal.^3);

yyaxis right
h = histogram(dataHorizT.EquivalentDiameter_um_,edges2,'DisplayStyle','stairs');
ylabel('Frequency');
set(gca,'fontname','times','TickDir','out','FontSize',16,'fontweight','bold','Xcolor','black','Ycolor','black');
hold on
yyaxis left
bar(diaVal,totalVolVert);
ylabel('Total Pore Voume (\mum^3)');

legend('Total Volume of Pores With Same Equivalent Diameter','Frequency of Pore Equivalent Diameter');
xlabel('Pore Equivalent Diameter (\mum)');
set(gca,'fontname','times','TickDir','out','FontSize',16,'fontweight','bold','Xcolor','black','Ycolor','black');

set(gcf,'units','normalized','outerposition',[0 0 1 1]);
set(gcf, 'PaperPositionMode', 'auto');

saveas(gcf,strcat(outPath,out_folder_name,"_21_V+H-PSD-Vol-Hist.fig"));
saveas(gcf,strcat(outPath,out_folder_name,"_21_V+H-Vol-Hist.tif"));
close all

%% Section 24: Vertical/Horizontal - AR - PSD - Scatter
g1 = {dataVertT.Type,dataVertT.Build_Orientation};
g2 = {dataHorizT.Type,dataHorizT.Build_Orientation};
figure
subplot(2,1,1);
gscatter(dataVertT.EquivalentDiameter_um_,dataVertT.Aspect_Ratio,g1);
xlim([40 1200]);
legend('Location','northeast');
xlabel('Pore Equivalent Diameter (\mum)');
xticks([10^0 10^1 10^2]);

```



```

ylabel('Aspect Ratio');
set(gca,'fontname','times','TickDir','out','FontSize',16,'fontweight','bold','Xcolor','black','Ycolor','black','XScale','log');
subplot(2,1,2);
gscatter(dataHorizT.EquivalentDiameter_um_,dataHorizT.Aspect_Ratio,g2);
xlim([40 1200]);
legend('Location','northeast');
xlabel('Pore Equivalent Diameter (\mum)');
xticks([10^0 10^1 10^2]);
ylabel('Pore Aspect Ratio');
set(gca,'fontname','times','TickDir','out','FontSize',16,'fontweight','bold','Xcolor','black','Ycolor','black','XScale','log');

```

```

set(gcf,'units','normalized','outerposition',[0 0 1 1]);
set(gcf, 'PaperPositionMode', 'auto');

```

```

saveas(gcf,strcat(outPath,out_folder_name,"_22_AR-PSD-Scatter.fig"));
saveas(gcf,strcat(outPath,out_folder_name,"_22_AR-PSD-Scatter.tif"));
close all

```

```

%% Section 25: Vertical/Horizontal - Sphericity - Histogram

```

```

figure
h = histogram(dataHorizT.SphericityAlt);
hold on
h = histogram(dataVertT.SphericityAlt);
legend('Horizontal Specimens','Vertical Specimens','Location','northwest');
xlabel('Pore Sphericity');
ylabel('Frequency');
set(gca,'fontname','times','TickDir','out','FontSize',16,'fontweight','bold','Xcolor','black','Ycolor','black');

```

```

set(gcf,'units','normalized','outerposition',[0 0 1 1]);
set(gcf, 'PaperPositionMode', 'auto');

```

```

saveas(gcf,strcat(outPath,out_folder_name,"_23_H+V_Sphericity-Hist.fig"));
saveas(gcf,strcat(outPath,out_folder_name,"_23_H+V_Sphericity-Hist.tif"));
close all

```

```

%% Section 26: Vertical/Horizontal - PSD - Histogram

```

```

figure
edges = [0:1:1200];
h = histogram(dataHorizT.EquivalentDiameter_um_,edges);
hold on
h = histogram(dataVertT.EquivalentDiameter_um_,edges);
xlim([40 200]);
legend('Horizontal Specimens','Vertical Specimens','Location','northeast');
xlabel('Pore Equivalent Diameter (\mum)');
ylabel('Frequency');
set(gca,'fontname','times','TickDir','out','FontSize',16,'fontweight','bold','Xcolor','black','Ycolor','black');

```

```

set(gcf,'units','normalized','outerposition',[0 0 1 1]);
set(gcf, 'PaperPositionMode', 'auto');

saveas(gcf,strcat(outPath,out_folder_name,"_24_H+V-PSD-Hist.fig"));
saveas(gcf,strcat(outPath,out_folder_name,"_24_H+V-PSD-Hist.tif"));
close all

%% Section 27: Vertical/Horizontal - Sphericity - PSD - Scatter
g1 = {dataVertT.Type,dataVertT.Build_Orientation};
g2 = {dataHorizT.Type,dataHorizT.Build_Orientation};
figure
subplot(2,1,1);
gscatter(dataVertT.EquivalentDiameter_um_,dataVertT.SphericityAlt,g1);
xlim([40 1200]);
legend('Location','northeast');
xlabel('Pore Equivalent Diameter (\mum)');
xticks([10^0 10^1 10^2]);
ylabel('Pore Sphericity');
set(gca,'fontname','times','TickDir','out','FontSize',16,'fontweight','bold','Xcolor','black','Ycolor','black','XScale','log');
subplot(2,1,2);
gscatter(dataHorizT.EquivalentDiameter_um_,dataHorizT.SphericityAlt,g2);
xlim([40 1200]);
legend('Location','northeast');
xlabel('Pore Equivalent Diameter (\mum)');
xticks([10^0 10^1 10^2]);
ylabel('Pore Sphericity');
set(gca,'fontname','times','TickDir','out','FontSize',16,'fontweight','bold','Xcolor','black','Ycolor','black','XScale','log');

set(gcf,'units','normalized','outerposition',[0 0 1 1]);
set(gcf, 'PaperPositionMode', 'auto');

saveas(gcf,strcat(outPath,out_folder_name,"_25_Sphericity-PSD-Scatter.fig"));
saveas(gcf,strcat(outPath,out_folder_name,"_25_Sphericity-PSD-Scatter.tif"));
close all

%% Section 28: RadPos - PSD - Scatter
% E8-3
figure
subplot(2,1,1);
dataTemp = dataRoundVert(strcmp(dataRoundVert.Type,'E8-3'),:);
scatter(dataTemp.EquivalentDiameter_um_,dataTemp.RadialDistance_mm_,'.','MarkerEdgecolor','red');
xlim([0 1200]);
xticks([10^0 10^1 10^2]);
ylim([0 4.5]);
legend('E8-3, Vertical','Location','northeast');

```

```

xlabel('Pore Equivalent Diameter (\mum)');
xticks([10^0 10^1 10^2]);
ylabel('Pore Radial Position (mm)');
set(gca,'fontname','times','TickDir','out','FontSize',16,'fontweight','bold','Xcolor','black','Ycolor','black','XScale','log');
clear dataTemp

subplot(2,1,2);
dataTemp = dataRoundHoriz(strcmp(dataRoundHoriz.Type,'E8-3'),:);
scatter(dataTemp.EquivalentDiameter_um_,dataTemp.RadialDistance_mm_,','MarkerEdgecolor',[0 0.4470 0.7410]);
xlim([0 1200]);
xticks([10^0 10^1 10^2]);
ylim([0 4.5]);
legend('E8-3, Horizontal','Location','northeast');
xlabel('Pore Equivalent Diameter (\mum)');
xticks([10^0 10^1 10^2]);
ylabel('Pore Radial Position (mm)');
set(gca,'fontname','times','TickDir','out','FontSize',16,'fontweight','bold','Xcolor','black','Ycolor','black','XScale','log');
clear dataTemp

set(gcf,'units','normalized','outerposition',[0 0 1 1]);
set(gcf,'PaperPositionMode','auto');

saveas(gcf, strcat(outPath,out_folder_name,"_26_RadPos_e8-3.fig"));
saveas(gcf, strcat(outPath,out_folder_name,"_26_RadPos_e8-3.tif"));
close all

% E8M-2
figure
subplot(2,1,1);
dataTemp = dataRoundVert(strcmp(dataRoundVert.Type,'E8M-2'),:);
scatter(dataTemp.EquivalentDiameter_um_,dataTemp.RadialDistance_mm_,','MarkerEdgecolor','green');
;
xlim([0 1200]);
xticks([10^0 10^1 10^2]);
ylim([0 5.5]);
legend('E8M-2, Vertical','Location','northeast');
xlabel('Pore Equivalent Diameter (\mum)');
ylabel('Pore Radial Position (mm)');
set(gca,'fontname','times','TickDir','out','FontSize',16,'fontweight','bold','Xcolor','black','Ycolor','black','XScale','log');
clear dataTemp

subplot(2,1,2);
dataTemp = dataRoundHoriz(strcmp(dataRoundHoriz.Type,'E8M-2'),:);

```

```

scatter(dataTemp.EquivalentDiameter_um_,dataTemp.RadialDistance_mm_',','MarkerEdgecolor',[0.8500
0.3250 0.0980]);
xlim([0 1200]);
xticks([10^0 10^1 10^2]);
ylim([0 5.5]);
legend('E8M-2, Horizontal','Location','northeast');
xlabel('Pore Equivalent Diameter (\mum)');
ylabel('Pore Radial Position (mm)');
set(gca,'fontname','times','TickDir','out','FontSize',16,'fontweight','bold','Xcolor','black','Ycolor','black','XS
cale','log');
clear dataTemp

set(gcf,'units','normalized','outerposition',[0 0 1 1]);
set(gcf, 'PaperPositionMode', 'auto');

saveas(gcf, strcat(outPath,out_folder_name, "_27_RadPos_e8m-2.fig"));
saveas(gcf, strcat(outPath,out_folder_name, "_27_RadPos_e8m-2.tif"));
close all

% E8M-3
figure
subplot(2,1,1);
dataTemp = dataRoundVert(strcmp(dataRoundVert.Type,'E8M-3'),:);
scatter(dataTemp.EquivalentDiameter_um_,dataTemp.RadialDistance_mm_',','MarkerEdgecolor','blue');
xlim([0 1200]);
xticks([10^0 10^1 10^2]);
ylim([0 4.5]);
legend('E8M-3, Vertical','Location','northeast');
xlabel('Pore Equivalent Diameter (\mum)');
ylabel('Pore Radial Position (mm)');
set(gca,'fontname','times','TickDir','out','FontSize',16,'fontweight','bold','Xcolor','black','Ycolor','black','XS
cale','log');
clear dataTemp

subplot(2,1,2);
dataTemp = dataRoundHoriz(strcmp(dataRoundHoriz.Type,'E8M-3'),:);
scatter(dataTemp.EquivalentDiameter_um_,dataTemp.RadialDistance_mm_',','MarkerEdgecolor',[0.9290
0.6940 0.1250]);
xlim([0 1200]);
xticks([10^0 10^1 10^2]);
ylim([0 4.5]);
legend('E8M-3, Horizontal','Location','northeast');
xlabel('Pore Equivalent Diameter (\mum)');
ylabel('Pore Radial Position (mm)');
set(gca,'fontname','times','TickDir','out','FontSize',16,'fontweight','bold','Xcolor','black','Ycolor','black','XS
cale','log');
clear dataTemp

```

```

set(gcf,'units','normalized','outerposition',[0 0 1 1]);
set(gcf, 'PaperPositionMode', 'auto');

saveas(gcf,strcat(outPath,out_folder_name,"_28_RadPos_e8m-3.fig"));
saveas(gcf,strcat(outPath,out_folder_name,"_28_RadPos_e8m-3.tif"));
close all

% E8M-4
figure
subplot(2,1,1);
dataTemp = dataRoundVert(strcmp(dataRoundVert.Type,'E8M-4'),:);
scatter(dataTemp.EquivalentDiameter_um_,dataTemp.RadialDistance_mm_,','MarkerEdgecolor','cyan');
xlim([0 1200]);
xticks([10^0 10^1 10^2]);
ylim([0 3.0]);
legend('E8M-4, Vertical','Location','northeast');
xlabel('Pore Equivalent Diameter (\mum)');
ylabel('Pore Radial Position (mm)');
set(gca,'fontname','times','TickDir','out','FontSize',16,'fontweight','bold','Xcolor','black','Ycolor','black','XScale','log');
clear dataTemp

subplot(2,1,2);
dataTemp = dataRoundHoriz(strcmp(dataRoundHoriz.Type,'E8M-4'),:);
scatter(dataTemp.EquivalentDiameter_um_,dataTemp.RadialDistance_mm_,','MarkerEdgecolor',[0.4940 0.1840 0.5560]);
xlim([0 1200]);
xticks([10^0 10^1 10^2]);
ylim([0 3.0]);
legend('E8M-4, Horizontal','Location','northeast');
xlabel('Pore Equivalent Diameter (\mum)');
ylabel('Pore Radial Position (mm)');
set(gca,'fontname','times','TickDir','out','FontSize',16,'fontweight','bold','Xcolor','black','Ycolor','black','XScale','log');
clear dataTemp

set(gcf,'units','normalized','outerposition',[0 0 1 1]);
set(gcf, 'PaperPositionMode', 'auto');

saveas(gcf,strcat(outPath,out_folder_name,"_29_RadPos_e8m-4.fig"));
saveas(gcf,strcat(outPath,out_folder_name,"_29_RadPos_e8m-4.tif"));
close all

% E8M-5
figure
subplot(2,1,1);
dataTemp = dataRoundVert(strcmp(dataRoundVert.Type,'E8M-5'),:);

```

```

scatter(dataTemp.EquivalentDiameter_um_,dataTemp.RadialDistance_mm_',','MarkerEdgecolor','magenta');
xlim([0 1200]);
xticks([10^0 10^1 10^2]);
ylim([0 2.25]);
legend('E8M-5, Vertical','Location','northeast');
xlabel('Pore Equivalent Diameter (\mum)');
ylabel('Pore Radial Position (mm)');
set(gca,'fontname','times','TickDir','out','FontSize',16,'fontweight','bold','Xcolor','black','Ycolor','black','XScale','log');
clear dataTemp

```

```

subplot(2,1,2);
dataTemp = dataRoundHoriz(strcmp(dataRoundHoriz.Type,'E8M-5'),:);
scatter(dataTemp.EquivalentDiameter_um_,dataTemp.RadialDistance_mm_',','MarkerEdgecolor',[0.4660 0.6740 0.1880]);
xlim([0 1200]);
xticks([10^0 10^1 10^2]);
ylim([0 2.25]);
legend('E8M-5, Horizontal','Location','northeast');
xlabel('Pore Equivalent Diameter (\mum)');
ylabel('Pore Radial Position (mm)');
set(gca,'fontname','times','TickDir','out','FontSize',16,'fontweight','bold','Xcolor','black','Ycolor','black','XScale','log');
clear dataTemp

```

```

set(gcf,'units','normalized','outerposition',[0 0 1 1]);
set(gcf, 'PaperPositionMode', 'auto');

```

```

saveas(gcf, strcat(outPath, out_folder_name, "_30_RadPos_e8m-5.fig"));
saveas(gcf, strcat(outPath, out_folder_name, "_30_RadPos_e8m-5.tif"));
close all

```

```

%% Section 29: Class - Type - Bar

```

```

figure
subplot(2,1,1);
dataTemp = dataVertT(strcmp(dataVertT.Type,'E8-3'),:);
[~,counts1] = countClass(dataTemp.Class);
dataTemp = dataVertT(strcmp(dataVertT.Type,'E8M-2'),:);
[~,counts2] = countClass(dataTemp.Class);
dataTemp = dataVertT(strcmp(dataVertT.Type,'E8M-3'),:);
[~,counts3] = countClass(dataTemp.Class);
dataTemp = dataVertT(strcmp(dataVertT.Type,'E8M-4'),:);
[~,counts4] = countClass(dataTemp.Class);
dataTemp = dataVertT(strcmp(dataVertT.Type,'E8M-5'),:);
[~,counts5] = countClass(dataTemp.Class);
dataTemp = dataVertT(strcmp(dataVertT.Type,'Flat (Small)'),:);
[~,counts6] = countClass(dataTemp.Class);

```

```

dataTemp = dataVertT(strcmp(dataVertT.Type,'Flat (Large)'),:);
[~,counts7] = countClass(dataTemp.Class);
xVert = categorical({'E8-3','E8M-2','E8M-3','E8M-4','E8M-5','Flat (Small)','Flat (Large)'});
yVert = [counts1; counts2; counts3; counts4; counts5; counts6; counts7];
bar(xVert,yVert);
legend('Class A (> 500 \mum)','Class B (301 \mum - 500 \mum)','Class C (201 \mum - 300 \mum)','Class
D (101 \mum - 200 \mum)','Class E (50 \mum - 100 \mum)','Location','north','Orientation','horizontal');
xlabel('Specimen Type');
ylabel('Frequency');
yticks([10^0 10^1 10^2 10^3 10^4 10^5]);
set(gca,'fontname','times','TickDir','out','FontSize',16,'fontweight','bold','Xcolor','black','Ycolor','black',
'YScale','log');
subplot(2,1,2);
dataTemp = dataHorizT(strcmp(dataHorizT.Type,'E8-3'),:);
[~,counts8] = countClass(dataTemp.Class);
dataTemp = dataHorizT(strcmp(dataHorizT.Type,'E8M-2'),:);
[~,counts9] = countClass(dataTemp.Class);
dataTemp = dataHorizT(strcmp(dataHorizT.Type,'E8M-3'),:);
[~,counts10] = countClass(dataTemp.Class);
dataTemp = dataHorizT(strcmp(dataHorizT.Type,'E8M-4'),:);
[~,counts11] = countClass(dataTemp.Class);
dataTemp = dataHorizT(strcmp(dataHorizT.Type,'E8M-5'),:);
[~,counts12] = countClass(dataTemp.Class);
dataTemp = dataHorizT(strcmp(dataHorizT.Type,'Flat (Small)'),:);
[~,counts13] = countClass(dataTemp.Class);
dataTemp = dataHorizT(strcmp(dataHorizT.Type,'Flat (Large)'),:);
[~,counts14] = countClass(dataTemp.Class);
xHoriz = categorical({'E8-3','E8M-2','E8M-3','E8M-4','E8M-5','Flat (Small)','Flat (Large)'});
yHoriz = [counts8; counts9; counts10; counts11; counts12; counts13; counts14];
bar(xHoriz,yHoriz);
legend('Class A (> 500 \mum)','Class B (301 \mum - 500 \mum)','Class C (201 \mum - 300 \mum)','Class
D (101 \mum - 200 \mum)','Class E (50 \mum - 100 \mum)','Location','north','Orientation','horizontal');
xlabel('Specimen Type');
ylabel('Frequency');
yticks([10^0 10^1 10^2 10^3 10^4 10^5]);
set(gca,'fontname','times','TickDir','out','FontSize',16,'fontweight','bold','Xcolor','black','Ycolor','black',
'YScale','log');
clear dataTemp counts1 counts2 counts3 counts4 counts5 counts6 counts7 counts8
clear counts9 counts10 counts11 counts12 counts13 counts14

set(gcf,'units','normalized','outerposition',[0 0 1 1]);
set(gcf,'PaperPositionMode','auto');

saveas(gcf,strcat(outPath,out_folder_name,"_31_Class-Type-Bar.fig"));
saveas(gcf,strcat(outPath,out_folder_name,"_31_Class-Type-Bar.tif"));
close all

```

```
%% Section 30: Class - Area - Bar
```

figure

```
% There are only 6 areas based on the specimen types
areaVal = unique(dataTable.Area);
subplot(2,1,1);
dataTemp = dataVertT(dataVertT.Area == areaVal(1,:));
[~,counts1] = countClass(dataTemp.Class);
dataTemp = dataVertT(dataVertT.Area == areaVal(2,:));
[~,counts2] = countClass(dataTemp.Class);
dataTemp = dataVertT(dataVertT.Area == areaVal(3,:));
[~,counts3] = countClass(dataTemp.Class);
dataTemp = dataVertT(dataVertT.Area == areaVal(4,:));
[~,counts4] = countClass(dataTemp.Class);
dataTemp = dataVertT(dataVertT.Area == areaVal(5,:));
[~,counts5] = countClass(dataTemp.Class);
dataTemp = dataVertT(dataVertT.Area == areaVal(6,:));
[~,counts6] = countClass(dataTemp.Class);
xVert = categorical({'1.9365','3.1416','4.7124','7.0686','18.0000','37.5000'});
xVert = reordercats(xVert,{'1.9365','3.1416','4.7124','7.0686','18.0000','37.5000'});
yVert = [counts1; counts2; counts3; counts4; counts5; counts6];
bar(xVert,yVert);
ylim([10^0 10^5]);
legend('Class A (> 500 \mum)','Class B (301 \mum - 500 \mum)','Class C (201 \mum - 300 \mum)','Class
D (101 \mum - 200 \mum)','Class E (50 \mum - 100 \mum)','Location','north','Orientation','horizontal');
xlabel('Specimen Cross-sectional Area (mm^2)');
ylabel('Frequency');
yticks([10^0 10^1 10^2 10^3 10^4 10^5]);
set(gca,'fontname','times','TickDir','out','FontSize',16,'fontweight','bold','Xcolor','black','Ycolor','black',
'YScale','log');
subplot(2,1,2);
dataTemp = dataHorizT(dataHorizT.Area == areaVal(1,:));
[~,counts7] = countClass(dataTemp.Class);
dataTemp = dataHorizT(dataHorizT.Area == areaVal(2,:));
[~,counts8] = countClass(dataTemp.Class);
dataTemp = dataHorizT(dataHorizT.Area == areaVal(3,:));
[~,counts9] = countClass(dataTemp.Class);
dataTemp = dataHorizT(dataHorizT.Area == areaVal(4,:));
[~,counts10] = countClass(dataTemp.Class);
dataTemp = dataHorizT(dataHorizT.Area == areaVal(5,:));
[~,counts11] = countClass(dataTemp.Class);
dataTemp = dataHorizT(dataHorizT.Area == areaVal(6,:));
[~,counts12] = countClass(dataTemp.Class);
xHoriz = categorical({'1.9365','3.1416','4.7124','7.0686','18.0000','37.5000'});
xHoriz = reordercats(xHoriz,{'1.9365','3.1416','4.7124','7.0686','18.0000','37.5000'});
yHoriz = [counts7; counts8; counts9; counts10; counts11; counts12];
bar(xHoriz,yHoriz);
ylim([10^0 10^5]);
legend('Class A (> 500 \mum)','Class B (301 \mum - 500 \mum)','Class C (201 \mum - 300 \mum)','Class
D (101 \mum - 200 \mum)','Class E (50 \mum - 100 \mum)','Location','north','Orientation','horizontal');
```



```

xlabel('Specimen Cross-sectional Area (mm^2));
ylabel('Frequency');
yticks([10^0 10^1 10^2 10^3 10^4 10^5]);
set(gca,'fontname','times','TickDir','out','FontSize',16,'fontweight','bold','Xcolor','black','Ycolor','black',
'YScale','log');
clear dataTemp counts1 counts2 counts3 counts4 counts5 counts6 counts7 counts8
clear counts9 counts10 counts11 counts12

set(gcf,'units','normalized','outerposition',[0 0 1 1]);
set(gcf,'PaperPositionMode','auto');

saveas(gcf,strcat(outPath,out_folder_name,"_32_Class-Area-Bar.fig"));
saveas(gcf,strcat(outPath,out_folder_name,"_32_Class-Area-Bar.tif"));
close all

%% Section 31: Class - SAV - Bar
figure
% There are only 5 sa/v ratios based on the specimen types
savVal = unique(dataTable.SAV);
subplot(2,1,1);
dataTemp = dataVertT(dataVertT.SAV == savVal(1,:));
[~,counts1] = countClass(dataTemp.Class);
dataTemp = dataVertT(dataVertT.SAV == savVal(2,:));
[~,counts2] = countClass(dataTemp.Class);
dataTemp = dataVertT(dataVertT.SAV == savVal(3,:));
[~,counts3] = countClass(dataTemp.Class);
dataTemp = dataVertT(dataVertT.SAV == savVal(4,:));
[~,counts4] = countClass(dataTemp.Class);
dataTemp = dataVertT(dataVertT.SAV == savVal(5,:));
[~,counts5] = countClass(dataTemp.Class);
xVert = categorical({'0.4444','0.6667','0.8267','1.0000','1.6000'});
xVert = reordercats(xVert,{'0.4444','0.6667','0.8267','1.0000','1.6000'});
yVert = [counts1; counts2; counts3; counts4; counts5];
bar(xVert,yVert);
ylim([10^0 10^5]);
legend('Class A (> 500 \mum)','Class B (301 \mum - 500 \mum)','Class C (201 \mum - 300 \mum)','Class
D (101 \mum - 200 \mum)','Class E (50 \mum - 100 \mum)','Location','north','Orientation','horizontal');
xlabel('Specimen Surface Area to Volume Ratio (/mm^2));
ylabel('Frequency');
yticks([10^0 10^1 10^2 10^3 10^4 10^5]);
set(gca,'fontname','times','TickDir','out','FontSize',16,'fontweight','bold','Xcolor','black','Ycolor','black',
'YScale','log');
subplot(2,1,2);
dataTemp = dataHorizT(dataHorizT.SAV == savVal(1,:));
[~,counts6] = countClass(dataTemp.Class);
dataTemp = dataHorizT(dataHorizT.SAV == savVal(2,:));
[~,counts7] = countClass(dataTemp.Class);
dataTemp = dataHorizT(dataHorizT.SAV == savVal(3,:));

```

```

[~,counts8] = countClass(dataTemp.Class);
dataTemp = dataHorizT(dataHorizT.SAV == savVal(4),:);
[~,counts9] = countClass(dataTemp.Class);
dataTemp = dataHorizT(dataHorizT.SAV == savVal(5),:);
[~,counts10] = countClass(dataTemp.Class);
xHoriz = categorical({'0.4444','0.6667','0.8267','1.0000','1.6000'});
xHoriz = reordercats(xHoriz,{'0.4444','0.6667','0.8267','1.0000','1.6000'});
yHoriz = [counts6; counts7; counts8; counts9; counts10];
bar(xHoriz,yHoriz);
ylim([10^0 10^5]);
legend('Class A (> 500 \mum)','Class B (301 \mum - 500 \mum)','Class C (201 \mum - 300 \mum)','Class
D (101 \mum - 200 \mum)','Class E (50 \mum - 100 \mum)','Location','north','Orientation','horizontal');
xlabel('Specimen Surface Area to Volume Ratio (/mm^2)');
ylabel('Frequency');
yticks([10^0 10^1 10^2 10^3 10^4 10^5]);
set(gca,'fontname','times','TickDir','out','FontSize',16,'fontweight','bold','Xcolor','black','Ycolor','black',
'YScale','log');
clear dataTemp counts1 counts2 counts3 counts4 counts5 counts6 counts7 counts8
clear counts9 counts10 counts11 counts12

set(gcf,'units','normalized','outerposition',[0 0 1 1]);
set(gcf,'PaperPositionMode','auto');

saveas(gcf, strcat(outPath, out_folder_name, "_33_Class-SAV-Bar.fig"));
saveas(gcf, strcat(outPath, out_folder_name, "_33_Class-SAV-Bar.tif"));
close all

close all
%% End
close all
clear all
end

```

## Appendix D. MATLAB code for thresholding and converting a grayscale image stack to a B&W image stack

```
function Threshold_PowderCapsules_V1()
% Function converts a greyscale image to black and white and saves it.

% The function requires:
% - imagescaling.m
% - saveastiff.m

%% Section 0: Initialization
% Input the minimum and maximum greyscale values to complete 8-bit scaling
in.greymin = 10000;
in.greymax = 42000;

% Input values for bilateral smoothing
in.spatialsigma = 3;
in.smoothing = 4e+03;

% Input in the image thresholding value
imageThreshold = 125;

% Folder location of the Expanse Microtechnologies code
addpath(genpath('S:\Gitanjali\PowderAnalysisSuite-master'));

%% Section 1: File IO setup and Make Folders for Outputs

% Get file names/locations
[inFiles,inPath] = uigetfile('*.tif','*.tiff');
inName = char(strcat(inPath,inFiles));

% Create the outpath and corresponding folder - creates an output folder % where the data was taken from
% Ask the user to generate a folder name to output all of the files
out_folder_name = input('Provide a name for the output folder: ','s');
outPath = strcat(inPath,out_folder_name,'\');

% Make directory and add to path
[status, msg, msgID] = mkdir(char(outPath));
addpath(char(outPath));

% Check if folder already existed and if it's okay to overwrite
folder_Check = 0;
while folder_Check == 0;
    if isempty(msg)
% Empty return means that there was no folder
```

```

    folder_Check = 1;
elseif msg == "Directory already exists."
    overwrite = input('Folder already exists, do you want to overwrite (y/n)?\n','s');
    if (overwrite ~= 'y') && (overwrite ~= 'n')
% Did not enter y or n
        disp('You must enter y to overwrite or n to set a new output folder name\n');
    else
        if overwrite == 'y' % Overwrite in the existing folder
            folder_Check = 1;
        elseif overwrite == 'n' % Set a new output folder name
            workFolder = input('Provide a new name for the output folder: \n','s');
% Provide a new folder name
            [status,msg,msgID] = mkdir(strcat(['outputs\',workFolder]));
        end
    end
elseif not(isempty(msg)) && not(msg == "Directory already exists.")
    workFolder = input('Error making folder - Provide a new name for the output folder: \n','s'); % Provide
a new folder name
    [status,msg,msgID] = mkdir(strcat(['outputs\',workFolder]));
else
    folder_Check = 1;
% Just in case checks return something weird
end
end

%% Section 2: Open .tif and Perform Preprocessing

% Import the .tif stack into Matlab
[stack_in,Nframes] = imread_big(inName);
% stack = importstack(inName);

% Perform 8-bit scaling on the .tif stack and covert from 16bit to 8bit
% image.
stack8 = imagescaling(stack_in,in);
clear stack_in

% Perform a 2D bilateral filter on the image stack.
for j = 1:Nframes;
    stack8(:, :,j) = imbilatfilt(stack8(:, :,j));
end

% Perform thresholding on the image stack
stackBW = stack8 > imageThreshold;
clear stack8

%% Section 2: Save Data
% Save out tif stack

```

```
% Generate base save name from input image file
saveNameBase = inFiles(1:end-4);

% These are the default options in the code if not specified here
% options.color = FALSE;
% options.compress = 'no';
% options.message = FALSE;
% options.append = true;
options.override = true;
options.big = true;

% Save out BW thresholded images
stackBW = im2uint8(stackBW);
save_name = strcat(outPath,saveNameBase,"_stackBW.tif");
save_name = char(save_name);
saveastiff(stackBW,save_name,options);

% Clear/close all remaining items
close all
clear all

end
```

## Appendix E. Python code for obtaining preheated powder bed analytics

```
import porespy as ps
from porespy import filters
from porespy import metrics
import scipy as sp
import numpy as np
import sys
import os
import tkinter
from tkinter import filedialog
import matplotlib
import skimage
from collections import Counter
import xlswriter
import math

"""This script is meant to run the porespy analysis on an image stack for powder capsules."""

# Set the voxel size for the powder capsules
voxel_size = 6.0 # microns
thermal_cond = 6.7 # W/m/k

# Open stackBW file generated through Matlab
file_path = filedialog.askopenfilename()
# Get the folder path and set the working directory
idx = file_path.rfind('/')
folder_path = file_path[0:idx+1]
os.chdir(folder_path)

# Get the image name for saving excel file
file_name = folder_path + file_path[idx+1:-4]
xlsx_name = file_name + ".xlsx"

# Load stackBW
stackBW = skimage.io.imread(file_path)
stackBW = stackBW > 0

# Find the layer-wise density of the image stack
layer_density = ps.metrics.porosity_profile(stackBW, axis = 0)

# Perform watershed segmentation - Matlab code removes adjacent voxels
stack_PSSW = ps.filters.snow_partitioning(stackBW, sigma = 0)

# Clear particle touching the border
stack_PSSW = skimage.segmentation.clear_border(stack_PSSW)
```

```

# Create lists of the old and new numbers for remapping
old_num = np.array(np.unique(stack_PSSW))
new_num = np.array(range(len(old_num)))

# Create a dict for the elements to be replaced
num_dict = { }
for i_num in range(len(old_num)):
    num = old_num[i_num]
    num_dict[num] = new_num[i_num]

stack_shape = np.shape(stack_PSSW)
stack_flat = stack_PSSW.flatten()
stack_flat = np.array([num_dict[x] for x in stack_flat])
stack_PSSW = stack_flat.reshape(stack_shape)

del stack_flat

# Find the surface areas of the regions
surface_areas = ps.metrics.region_surface_areas(stack_PSSW, voxel_size = 1)

# Find the interface areas of the regions
interface_info = ps.metrics.region_interface_areas(stack_PSSW, surface_areas, voxel_size = 1)
interface_area = interface_info.area
interface_conn = interface_info.conns
conn_pairs = list(Counter(interface_info.conns[:,0]).items())
conn_pairs = dict(conn_pairs)

# Find the equivalent diameters and centroids of each particle
region_info = skimage.measure.regionprops(stack_PSSW)
region_info = np.array(region_info)
dia_centroid_info = np.empty((len(region_info),4))
for i in range(len(region_info)):
    info_temp = region_info[i]
    cent_temp = info_temp.centroid
    dia_centroid_info[i,0] = cent_temp[2] # X
    dia_centroid_info[i,1] = cent_temp[1] # y
    dia_centroid_info[i,2] = cent_temp[0] # Z
    dia_centroid_info[i,3] = info_temp.equivalent_diameter

# Make all analysis values in um/um^2 as opposed to voxels
# um values
dia_centroid_info = dia_centroid_info*voxel_size
# um^2 values
interface_area = interface_area*voxel_size*voxel_size

# Create xlsx and save out info
workbook = xlsxwriter.Workbook(xlsx_name)

```

```

worksheet1 = workbook.add_worksheet()
worksheet2 = workbook.add_worksheet()
worksheet3 = workbook.add_worksheet()

# Worksheet 1
worksheet1.write('A1', 'Particle')
worksheet1.write('B1', 'Connectivity')
worksheet1.write('C1', 'Average Sinter Neck Area (um^2)')
worksheet1.write('D1', 'Average Sinter Neck Diameter (um)')
worksheet1.write('E1', 'Equivalent Diameter (um)')
worksheet1.write('F1', 'Layer Density')
worksheet1.write('G1', 'Neck/Dia Ratio')
worksheet1.write('H1', 'Neck Thermal Conductivity')
worksheet1.write('I1', 'X Position (um)')
worksheet1.write('J1', 'Y Position (um)')
worksheet1.write('K1', 'Z Position (um)')
worksheet1.write('L1', 'Layer')

# Worksheet 2
worksheet2.write('A1', 'Layer')
worksheet2.write('B1', 'Density')
worksheet2.write('C1', 'Layer Count')
worksheet2.write('D1', 'Layer Average Sinter Neck Area (um^2)')
worksheet2.write('E1', 'Average Sinter Neck Diameter (um)')
worksheet2.write('F1', 'Layer Average Neck Thermal Conductivity')
worksheet2.write('G1', 'Layer Average Equivalent Diameter (um)')
worksheet2.write('H1', 'Layer Average Neck/Dia Ratio')

# Worksheet 3
worksheet3.write('A1', 'Particle A')
worksheet3.write('B1', 'Particle B')
worksheet3.write('C1', 'Contact area (um^2)')

# Initialize layer avg array
layer_avg_info = np.zeros([len(layer_density),6])

# Write values for each particle
row = 1
col = 0
part_list = interface_conn[:,0]
for i in range(len(dia_centroid_info)):
    # Check if particle is connected
    conn_idx = np.where(part_list == (i+1))
    conn_idx = np.array(conn_idx)
    # Particle is not connected
    if conn_idx.size == 0:
        # Particle
        part_ID = (i+1) # 0 is background, particles start at 1

```



```

worksheet1.write(row,col,part_ID)
# Connectivity
conn = 0
worksheet1.write(row,col+1,conn)
# Avg Sinter Neck Size
neck_area = 0
worksheet1.write(row,col+2,neck_area)
# Avg Sinter Neck Diameter
neck_dia = 0
worksheet1.write(row,col+3,neck_dia)
# Equivalent Diameter
equiv_dia = dia_centroid_info[i,3]
worksheet1.write(row,col+4,equiv_dia)
# Layer Density
layer_idx = int(dia_centroid_info[i,2]/voxel_size)
den = layer_density[layer_idx]
worksheet1.write(row,col+5,den)
# Neck/Dia Ratio
neck_ratio = 0
worksheet1.write(row,col+6,neck_ratio)
# Neck Thermal Conductivity
therm_calc = 0
worksheet1.write(row,col+7,therm_calc)
# XYZ Position
worksheet1.write(row,col+8,dia_centroid_info[i,0])
worksheet1.write(row,col+9,dia_centroid_info[i,1])
worksheet1.write(row,col+10,dia_centroid_info[i,2])
worksheet1.write(row,col+11,layer_idx)
# Add sinter neck/thermal cond/particle size
layer_avg_info[layer_idx,0] += 1
layer_avg_info[layer_idx,1] += neck_area
layer_avg_info[layer_idx,2] += neck_dia
layer_avg_info[layer_idx,3] += therm_calc
layer_avg_info[layer_idx,4] += equiv_dia
layer_avg_info[layer_idx,5] += neck_ratio
# Particle is Connected
else:
# Particle
part_ID = (i+1) # 0 is background, particles start at 1
worksheet1.write(row,col,part_ID)
# Connectivity
conn = conn_pairs[(i+1)]
worksheet1.write(row,col+1,conn)
# Avg Sinter Neck Size
neck_area = np.mean(interface_area[conn_idx])
worksheet1.write(row,col+2,neck_area)
# Avg Sinter Neck Diameter
neck_dia = math.sqrt(4*neck_area/math.pi)

```

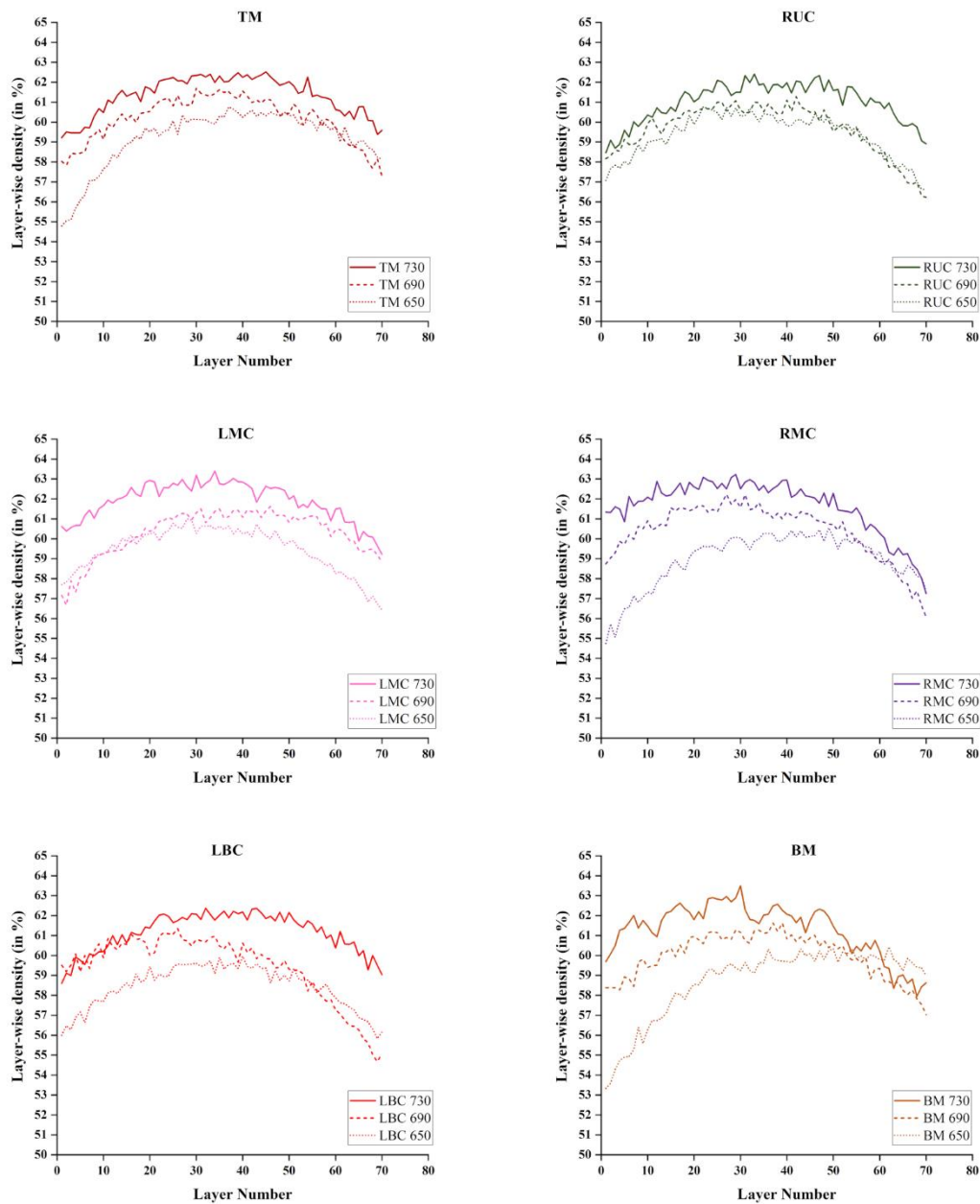
```

worksheet1.write(row,col+3,neck_dia)
# Equivalent Diameter
equiv_dia = dia_centroid_info[i,3]
worksheet1.write(row,col+4,equiv_dia)
# Layer Density
layer_idx = int(dia_centroid_info[i,2]/voxel_size)
den = layer_density[layer_idx]
worksheet1.write(row,col+5,den)
# Neck/Dia Ratio
neck_ratio = neck_dia/equiv_dia
worksheet1.write(row,col+6,neck_ratio)
# Neck Thermal Conductivity
therm_calc = (thermal_cond*neck_ratio*(den/100)*conn)/math.pi
worksheet1.write(row,col+7,therm_calc)
# XYZ Position
worksheet1.write(row,col+8,dia_centroid_info[i,0])
worksheet1.write(row,col+9,dia_centroid_info[i,1])
worksheet1.write(row,col+10,dia_centroid_info[i,2])
worksheet1.write(row,col+11,layer_idx)
# Add sinter neck/thermal cond/particle size
layer_avg_info[layer_idx,0] += 1
layer_avg_info[layer_idx,1] += neck_area
layer_avg_info[layer_idx,2] += neck_dia
layer_avg_info[layer_idx,3] += therm_calc
layer_avg_info[layer_idx,4] += equiv_dia
layer_avg_info[layer_idx,5] += neck_ratio
row += 1
# Worksheet 2 - Layer average information
row = 1
col = 0
layer = 1
for i in range(len(layer_density)):
    worksheet2.write(row,col,layer)
    worksheet2.write(row,col+1,layer_density[i])
    if layer_avg_info[i,0] == 0:
        worksheet2.write(row,col+2,0)
        worksheet2.write(row,col+3,0)
        worksheet2.write(row,col+4,0)
        worksheet2.write(row,col+5,0)
        worksheet2.write(row,col+6,0)
        worksheet2.write(row,col+7,0)
    else:
        worksheet2.write(row,col+2,layer_avg_info[i,0])
        worksheet2.write(row,col+3,(layer_avg_info[i,1]/layer_avg_info[i,0]))
        worksheet2.write(row,col+4,(layer_avg_info[i,2]/layer_avg_info[i,0]))
        worksheet2.write(row,col+5,(layer_avg_info[i,3]/layer_avg_info[i,0]))
        worksheet2.write(row,col+6,(layer_avg_info[i,4]/layer_avg_info[i,0]))
        worksheet2.write(row,col+7,(layer_avg_info[i,5]/layer_avg_info[i,0]))

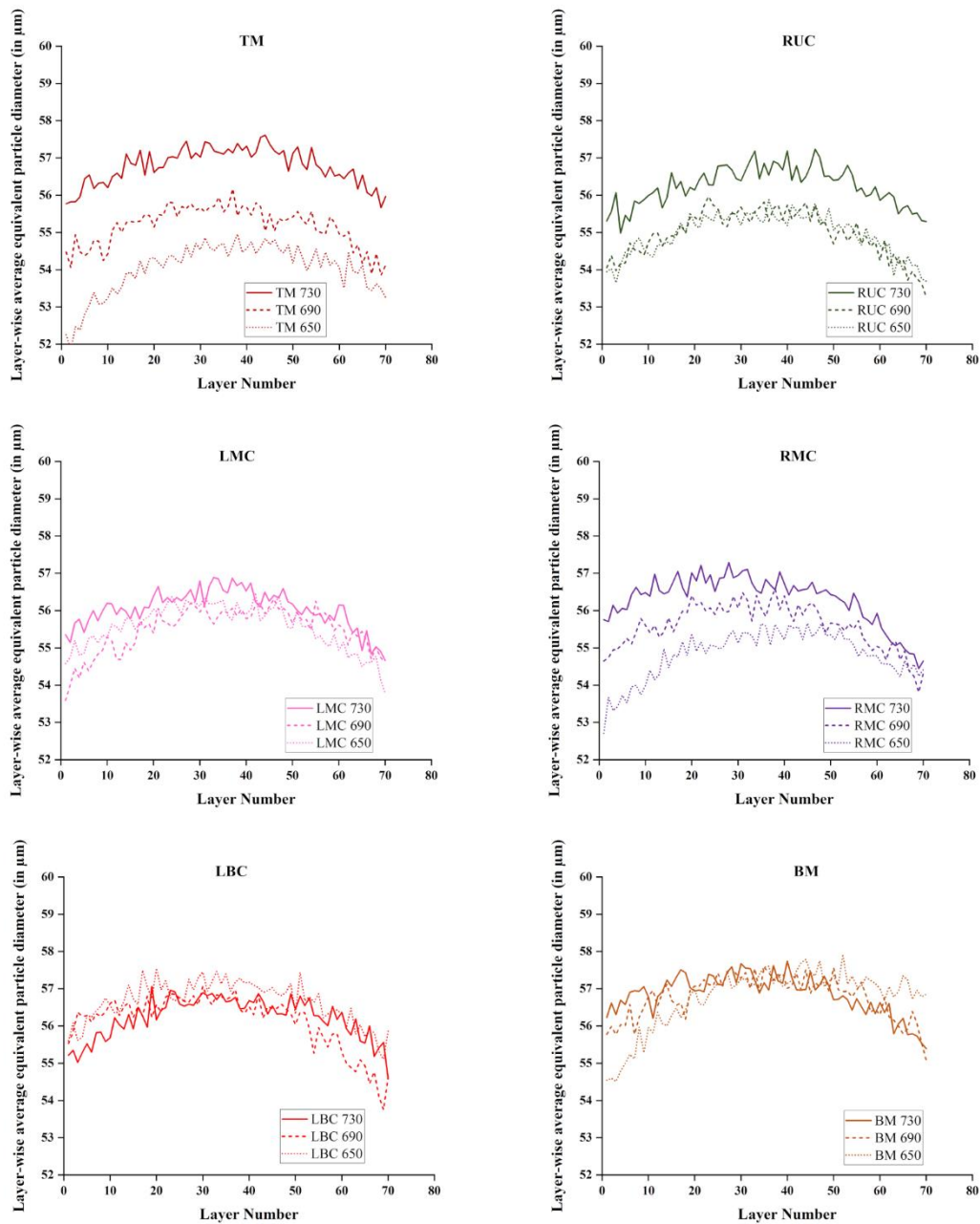
```

```
row += 1
layer += 1
# Worksheet 3 - Write values for all particle-particle pairs
row = 1
col = 0
for i in range(len(interface_area)):
    # Particle A
    worksheet3.write(row,col,interface_conn[i,0])
    # Particle B
    worksheet3.write(row,col+1,interface_conn[i,1])
    # Connection Area
    worksheet3.write(row,col+2,interface_area[i])
    row += 1
# Close workbook
workbook.close()
```

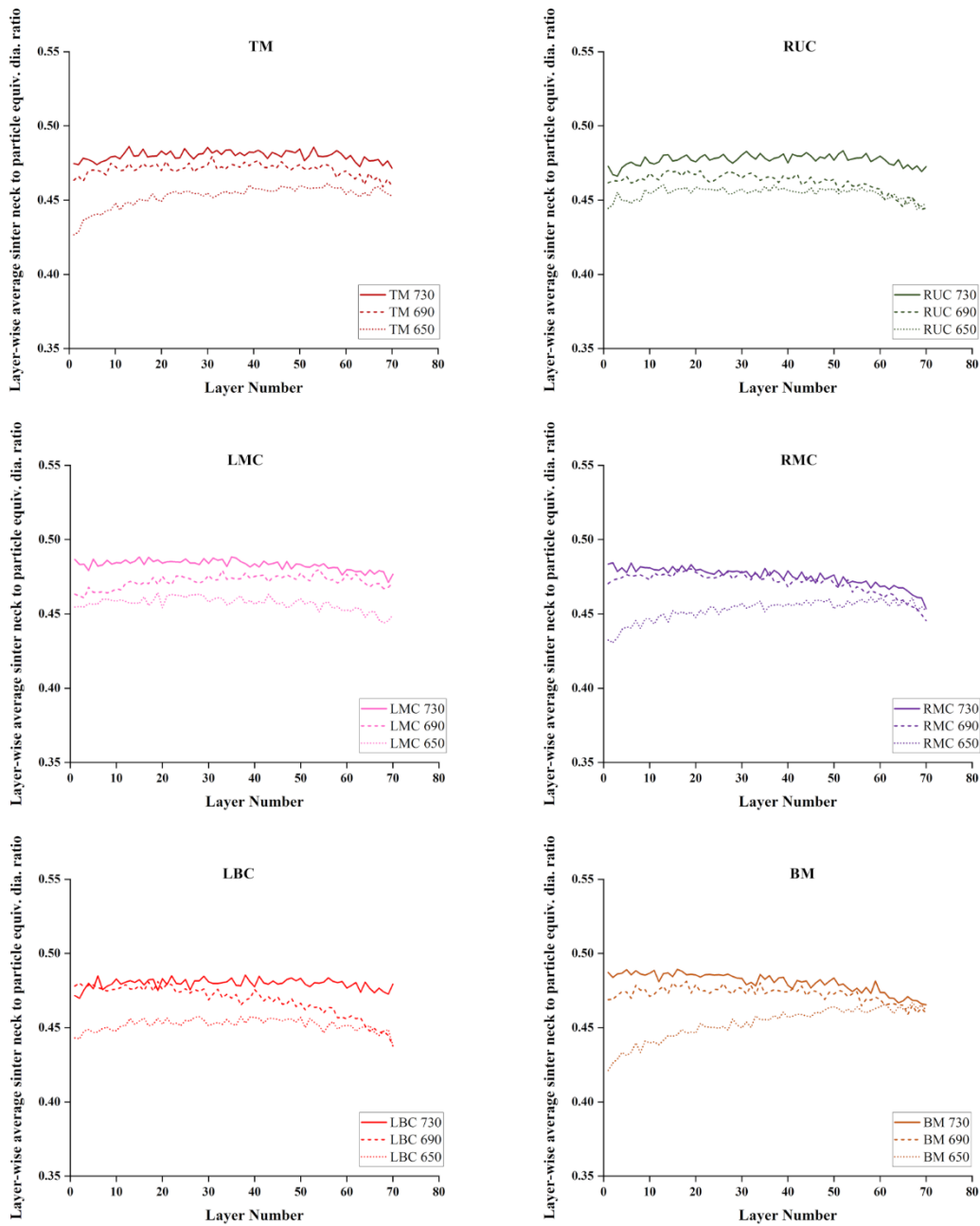
## Appendix F. Chapter 6 Supplementary Data



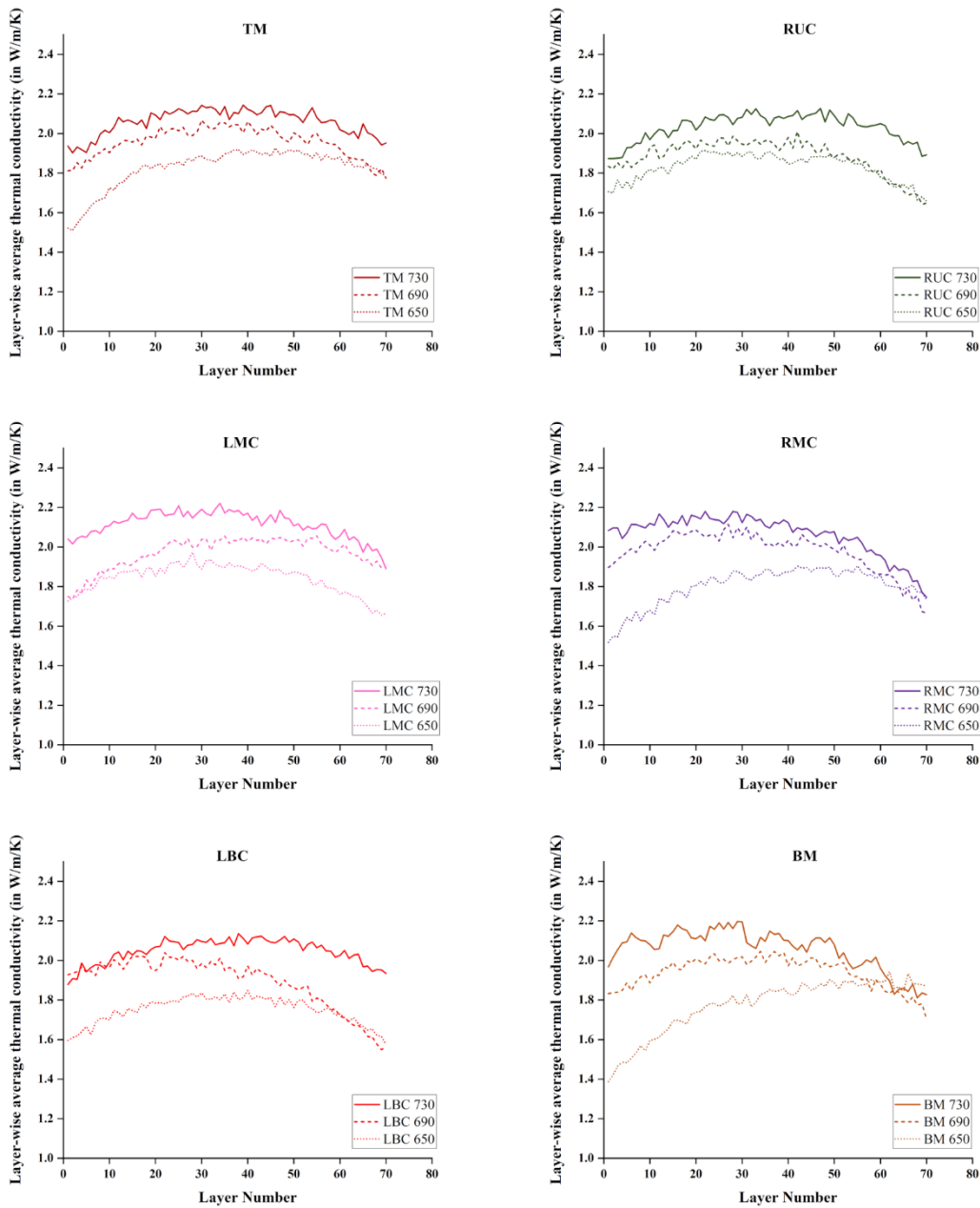
Appendix Figure F.1 Layer-wise density (in %) vs. Layer number for TM, RUC, LMC, RMC, LBC, and BM samples. The solid lines, dashed lines and dotted lines represent the behavior of the capsules processed at 730 °C, 690 °C, and 650 °C, respectively.



Appendix Figure F.2 Layer-wise average equivalent powder particle diameter (in  $\mu\text{m}$ ) vs. Layer number for TM, RUC, LMC, RMC, LBC, and BM samples. The solid lines, dashed lines and dotted lines represent the behavior of the capsules processed at 730  $^{\circ}\text{C}$ , 690  $^{\circ}\text{C}$ , and 650  $^{\circ}\text{C}$ , respectively.



Appendix Figure F.3 Layer-wise average sinter neck diameter to particle equivalent diameter ratio vs. Layer number for TM, RUC, LMC, RMC, LBC, and BM samples. The solid lines, dashed lines and dotted lines represent the behavior of the capsules processed at 730 °C, 690 °C, and 650 °C, respectively.



Appendix Figure F.4 Layer-wise average effective thermal conductivity vs. Layer number for TM, RUC, LMC, RMC, LBC, and BM samples. The solid lines, dashed lines and dotted lines represent the behavior of the capsules processed at 730 °C, 690 °C, and 650 °C, respectively.

## Appendix G. MATLAB code for Ra and Sa plot creation

```
function SurfaceRoughness_Plot()
%% Section 0: Initialization
close all;
colOff = 1;
rowOff = 1;

%% Section 1: Open Files and Make Folders for Outputs

% Get file names/locations
[inFiles,inPath] = uigetfile('MultiSelect', 'on','*.csv');

% Determine the number of files selected and initialize data array
[~,numFiles] = size(inFiles);

% Enter in Sample Group ID
sampleID = input('Enter sample group ID: ','s');

% Create the outpath and corresponding folder - creates an output folder
% where the data was taken from
% Ask the user to generate a folder name to output all of the files
out_folder_name = input('Provide a name for the output folder: ','s');
outPath = strcat(inPath,out_folder_name,"\");
% Make directory and add to path
[status, msg, msgID] = mkdir(char(outPath));
addpath(char(outPath)) ;

% Check if folder already existed and if it's okay to overwrite
folder_Check = 0;
while folder_Check == 0;
    if isempty(msg) % Empty return means that there was no folder
        folder_Check = 1;
    elseif msg == "Directory already exists."
        overwrite = input('Folder already exists, do you want to overwrite (y/n)?\n','s');
        if (overwrite ~= 'y') && (overwrite ~= 'n') % Did not enter y or n
            disp('You must enter y to overwrite or n to set a new output folder name\n');
        else
            if overwrite == 'y' % Overwrite in the existing folder
                folder_Check = 1;
            elseif overwrite == 'n' % Set a new output folder name
                workFolder = input('Provide a new name for the output folder: \n','s'); %Provide a new folder
                name
                [status,msg,msgID] = mkdir(strcat(['outputs\',workFolder]));
            end
        end
    elseif not(isempty(msg)) && not(msg == "Directory already exists.")
```



```

        workFolder = input('Error making folder - Provide a new name for the output folder: \n','s');
% Provide a new folder name
    [status,msg,msgID] = mkdir(strcat(['outputs\',workFolder]));
    else
        folder_Check = 1; % Just in case checks return something weird
    end
end

%% Section 2: Process raw data

% Read in Ra data from combined file
Index = find(contains(inFiles,'Ra'));
inName = char(strcat(inPath,inFiles(Index)));
RaData = csvread(inName,rowOff,colOff);
RaData = RaData(:,1:15);

% Read in Sa data from combined file
Index = find(contains(inFiles,'Sa'));
inName = char(strcat(inPath,inFiles(Index)));
SaData = csvread(inName,rowOff,colOff);
SaData = SaData(:,1:15);

% % Read in x data
% Index = find(contains(inFiles,'X'));
% inName = char(strcat(inPath,inFiles(Index)));
% xData = csvread(inName,rowOff,colOff);
% %xData = num2cell(inArray);
% % Read in y data
% Index = find(contains(inFiles,'Y'));
% inName = char(strcat(inPath,inFiles(Index)));
% yData = csvread(inName,rowOff,colOff);
% %yData = num2cell(inArray);
% % Read in z data
% Index = find(contains(inFiles,'Z'));
% inName = char(strcat(inPath,inFiles(Index)));
% zData = csvread(inName,rowOff,colOff);
% %zData = num2cell(inArray);

%% Section 3: Plot Ra data
% Determine the number of rows and columns in the Data
[numRow,numCol] = size(RaData);

% Set the colours for the fill3 plots
% colourArray =
['r','b','g','y','r','b','g','y','r','b','g','y','r','b','g','y','r','b','g','y','r','b','g','y','r','b','g','y'];
colourArray = {[0 51 25],[255 51 51],[51 153 255],[255 255 102],[0 51 25]...
    ,[255 51 51],[51 153 255],[255 255 102],[0 51 25],[255 51 51],[51 153 255]...
    ,[255 255 102],[0 51 25],[255 51 51],[51 153 255],[255 255 102],[0 51 25],...

```

```

[255 51 51],[51 153 255],[255 255 102],[0 51 25],[255 51 51],[51 153 255],...
[255 255 102],[0 51 25],[255 51 51],[51 153 255],[255 255 102],[0 51 25],...
[255 51 51],[51 153 255],[255 255 102],[0 51 25],[255 51 51],[51 153 255],[255 255 102]};

% Wireframe plot of data
% figure;
% for i=1:numRow
%   x = [RaData(i,1),RaData(i,4),RaData(i,7),RaData(i,10),RaData(i,13)];
%   y = [RaData(i,2),RaData(i,5),RaData(i,8),RaData(i,11),RaData(i,14)];
%   z = [RaData(i,3),RaData(i,6),RaData(i,9),RaData(i,12),RaData(i,15)];
%   plot3(x,y,z);
%   hold on
% end

% Shaded surface plot of data
figure;
for i=1:numRow
    x = [RaData(i,1),RaData(i,4),RaData(i,7),RaData(i,10)];
    y = [RaData(i,2),RaData(i,5),RaData(i,8),RaData(i,11)];
    z = [RaData(i,3),RaData(i,6),RaData(i,9),RaData(i,12)];
    fill3(x,y,z,(colourArray{i}/255));
    hold on
end

xlabel('Position Along Raking Direction (A.U.)');
ylabel('Position From Front of Chamber (A.U.)');
zlabel('Surface Roughness - Ra (\mum)');
xmax = unique(max(RaData(:,1)))+1
xlim([0 xmax]);
ymax = unique(max(RaData(:,2)))+1
ylim([0 ymax]);

% Set the colour of the xy (base) plane
fill3([0 xmax xmax 0],[0 0 ymax ymax],[0 0 0 0],[160 160 160]/255);

[caz,cel] = view([-31.1 52.4]);
% title("Surface Roughness - Ra");
set(gcf,'units','normalized','outerposition',[0 0 1 1]);
set(gcf, 'PaperPositionMode', 'auto');
saveas(gcf, strcat(outPath, sampleID, "_SurfaceRoughnessRa.fig"));
saveas(gcf, strcat(outPath, sampleID, "_SurfaceRoughnessRa.png"));
close all;

%% Section 4: Plot Sa data
% Determine the number of rows and columns in the Data
[numRow,numCol] = size(SaData);

% Set the colours for the fill3 plots

```

```

% colourArray =
['r','b','g','y','r','b','g','y','r','b','g','y','r','b','g','y','r','b','g','y','r','b','g','y','r','b','g','y'];
colourArray = {[0 51 25],[255 51 51],[51 153 255],[255 255 102],[0 51 25]...
,[255 51 51],[51 153 255],[255 255 102],[0 51 25],[255 51 51],[51 153 255]...
,[255 255 102],[0 51 25],[255 51 51],[51 153 255],[255 255 102],[0 51 25],...
[255 51 51],[51 153 255],[255 255 102],[0 51 25],[255 51 51],[51 153 255],...
[255 255 102],[0 51 25],[255 51 51],[51 153 255],[255 255 102],[0 51 25],...
[255 51 51],[51 153 255],[255 255 102],[0 51 25],[255 51 51],[51 153 255],[255 255 102]};

% Shaded surface plot of data
figure;
for i=1:numRow
    x = [SaData(i,1),SaData(i,4),SaData(i,7),SaData(i,10)];
    y = [SaData(i,2),SaData(i,5),SaData(i,8),SaData(i,11)];
    z = [SaData(i,3),SaData(i,6),SaData(i,9),SaData(i,12)];
    fill3(x,y,z,(colourArray{i}/255));
    hold on
end

xlabel('Position Along Raking Direction (A.U.)');
ylabel('Position From Front of Chamber (A.U.)');
zlabel('Surface Roughness - Sa (\num)');
xmax = unique(max(SaData(:,1)))+1
xlim([0 xmax]);
ymax = unique(max(SaData(:,2)))+1
ylim([0 ymax]);

% Set the colour of the xy (base) plane
fill3([0 xmax xmax 0],[0 0 ymax ymax],[0 0 0 0],[160 160 160]/255);

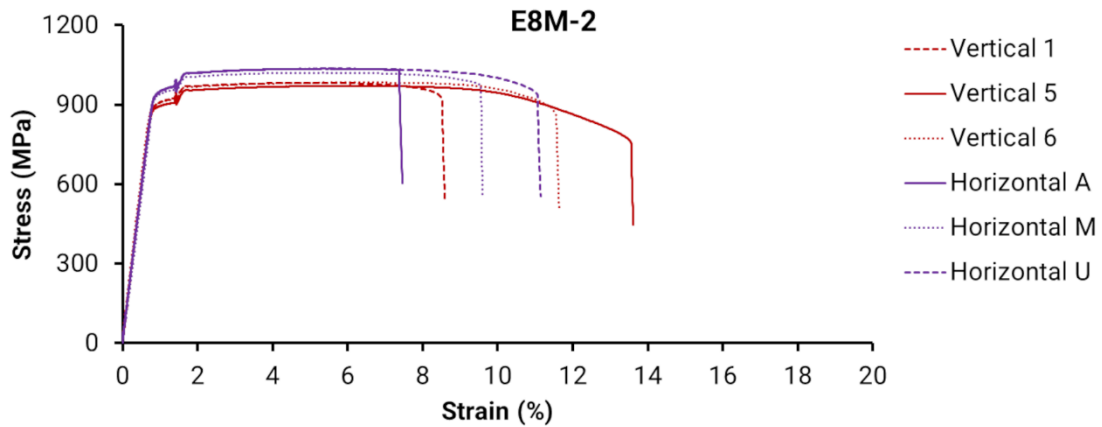
[caz,cel] = view([-31.1 52.4]);
% title("Surface Roughness - Ra");
set(gcf,'units','normalized','outerposition',[0 0 1 1]);
set(gcf, 'PaperPositionMode', 'auto');
saveas(gcf, strcat(outPath,sampleID, "_SurfaceRoughnessSa.fig"));
saveas(gcf, strcat(outPath,sampleID, "_SurfaceRoughnessSa.png"));

%% Section 5: End Function
clear all;
close all;

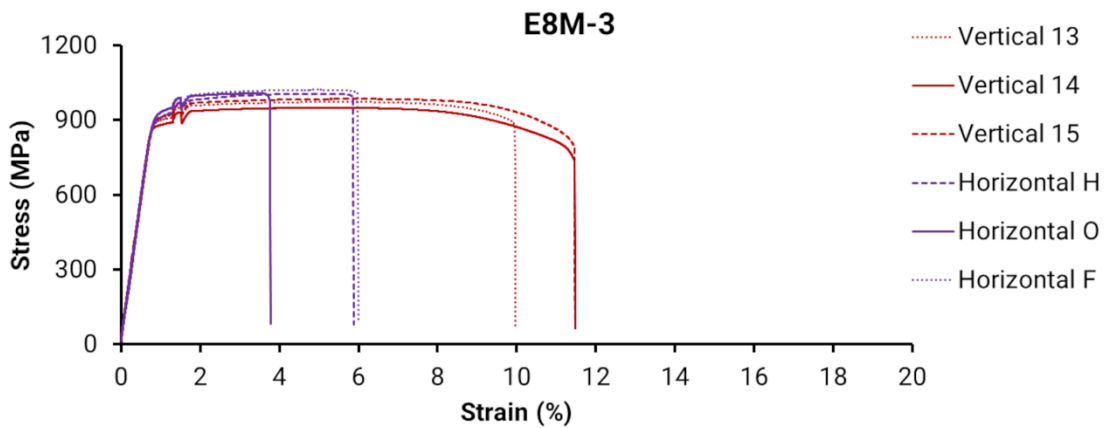
end

```

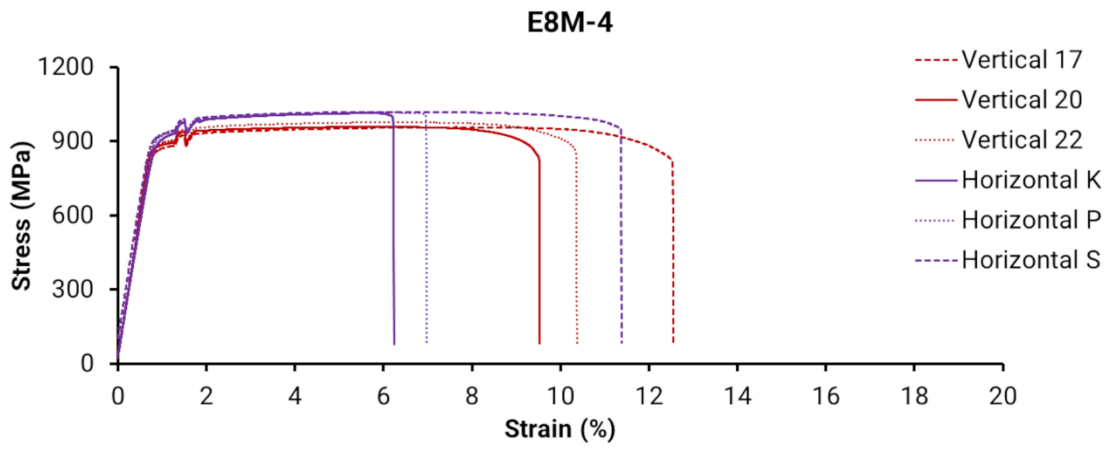
## Appendix H. Engineering stress-strain curves for Chapter 4 tensile specimens



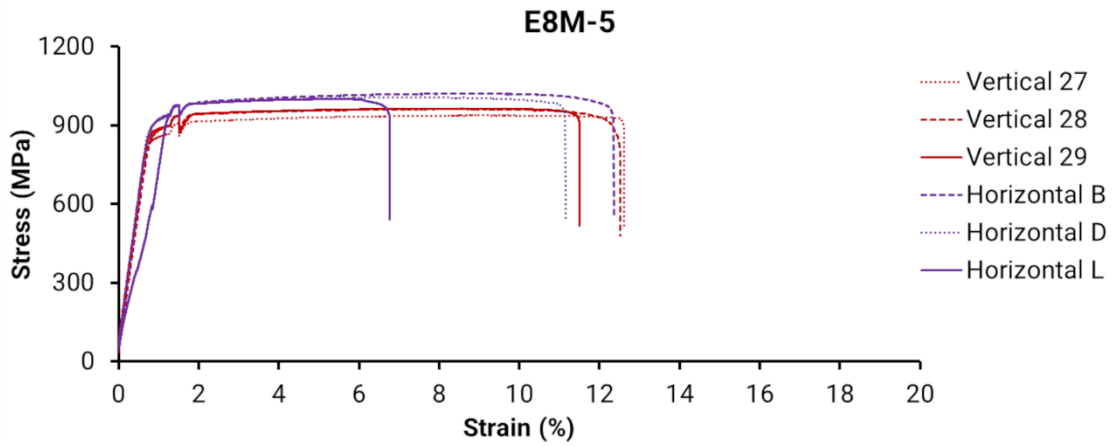
Appendix Figure H.1 Engineering stress-strain curves for all E8M-2 specimens



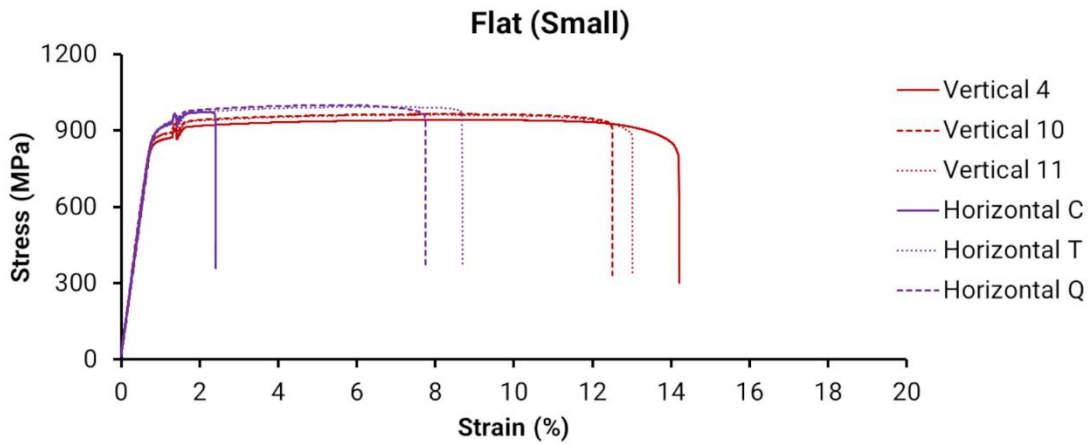
Appendix Figure H.2 Engineering stress-strain curves for all E8M-3 specimens



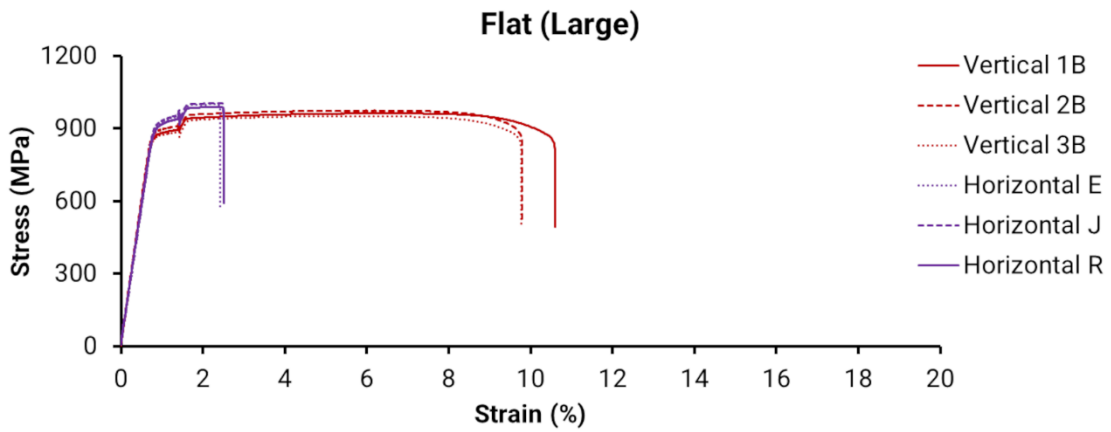
**Appendix Figure H.3 Engineering stress-strain curves for all E8M-4 specimens**



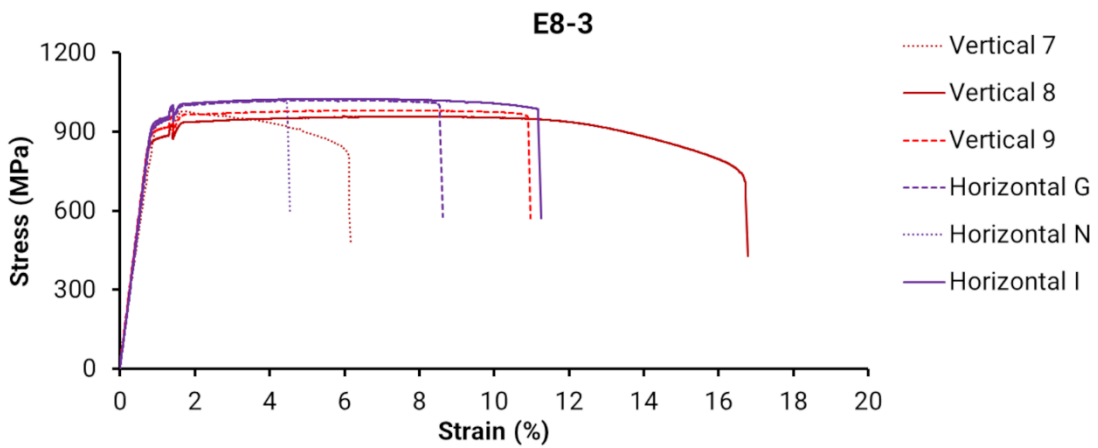
**Appendix Figure H.4 Engineering stress-strain curves for all E8M-5 specimens**



Appendix Figure H.5 Engineering stress-strain curves for all Flat (Small) specimens



Appendix Figure H.6 Engineering stress-strain curves for all Flat(Large) specimens



Appendix Figure H.7 Engineering stress-strain curves for all E8-3 specimens